Karlsruher Institut für Technologie

Lattice Design and Beam Optics Calculations for the new Large-Scale Electron-Positron-Collider FCC-ee

Zur Erlangung des akademischen Grades eines
DOKTORS DER NATURWISSENSCHAFTEN
von der Fakultät für Physik des
Karlsruher Instituts für Technologie (KIT)

genehmigte

DISSERTATION

von

Diplom-Physiker
Bastian Härer
aus Stuttgart-Bad Cannstatt

CERN-THESIS-2017-073
10/02/2017

Tag der mündlichen Prüfung:	10. Februar 2017
Hauptreferent:	**Prof. Dr. Anke-Susanne Müller**
Korreferent:	**Prof. Dr. Rüdiger Schmidt**

Zusammenfassung

Der Bau eines Teilchenbeschleunigers für Forschung in der Hochenergiephysik erfordert Jahrzehnte der Planung. Die "European Strategy Group for High Energy Physics" hat daher die Empfehlung ausgesprochen bereits heute, etwa 20 Jahre vor der geplanten Abschaltung des Large Hadron Colliders (LHC), mögliche Nachfolgeprojekte zu entwickeln. Die sogenannte *Future Circular Collider (FCC)* Design Studie untersucht den Nutzen und die Machbarkeit neuer Speicherringe für Teilchenkollisionen im Hinblick auf die Beantwortung aktueller Fragen der Teilchenphysik und die Suche nach Physik jenseits des Standard-Modells. Im Zuge der hier vorliegenden Dissertation wird die magnetische Bogenstruktur eines möglichen Electron-Positron Speicherrings entwickelt und optimiert, der unter dem Namen FCC-ee eines der Teilprojekte darstellt. Der geplante Umfang von 100 km erlaubt die Beobachtung von Teilchenkollisionen bis einer Schwerpunktenergie im Bereich von 90 bis 350 GeV mit tolerierbaren Synchrotronstrahlungsverlusten. Dieser Energiebereich ermöglicht nicht nur die Vermessung des W- und Z-Bosons mit sehr hoher Statistik, sondern auch zum ersten Mal Präzisionsmessungen des kürzlich nachgewiesenen Higgs-Bosons und des Top-Quarks.

Für die vorgestellten Studien werden zwei Maschinenmodelle mit unterschiedlicher Geometrie verwendet und in dem Programm MAD-X implementiert. Basierend auf einem Vergleich zweier gängiger Magnetstrukturen wird die Verwendung der sogenannten FODO-Struktur motiviert und so optimiert, dass die erforderlichen Strahlparameter für die höchste Teilchenenergie erreicht werden. Anders als bei Speicherringen mit hochenergetischen Leptonstrahlen allgemein üblich sind wegen des großen Umfangs von FCC-ee nur zwei Strecken mit Hohlraumresonatoren für die Energiezufuhr vorgesehen. Um die beachtliche Drift des Orbits als Folge des Energieverlustes in der Bogenstruktur und die damit verbundene Optikstörung zu vermeiden, werden verschiedene Lösungen zur Anpassung des Ablenkwinkels an die lokale Strahlenergie präsentiert.

Um die höchstmögliche Luminosität zu erreichen, werden die Strahlparameter für vier Strahlenergien individuell angepasst. Dies betrifft insbesondere die horizontale Gleichgewichtemittanz des Strahls, da sie von der Teilchenenergie abhängt. Um die Emittanz für kleine Strahlenergien zu erhöhen werden Möglichkeiten zur Modifikation der

Optik beruhend auf denselben Magnetstruktur erfolgreich entwickelt und implementiert. Eine nachfolgende Feinregulierung der Emittanz im Bereich von 10 % wird mit Hilfe von Dämpfungs- und Anregungswigglern unter akzeptablem Anstieg der Strahlungsleistung erreicht.

Bei höchster Energie verlieren die nicht kollidierenden Teilchen im Wechselwirkungspunkt bis zu 2 % ihrer Energie durch Beamstrahlung. Die Energieakzeptanz der Maschine muss daher beachtliche $\pm 2\,\%$ betragen, da diese Teilchen sonst verloren gehen. Dies erfordert die Korrektur der sehr starken chromatischen Fehler, die vor allem wegen der starken Fokussierung der Strahlen in den Quadrupolmagneten unmittelbar vor dem Wechselwirkungspunkt entstehen. Der Hauptteil der Arbeit umfasst daher eine systematische Studie von Sextupolschemata in den Bogenstrukturen zur Optimierung der Chromatizitätskorrektur. Dabei ist eine Korrektur des linearen Terms nicht ausreichend. Um das sehr ambitionierte Ziel von $\pm 2\,\%$ Energieakzeptanz zu erreichen, müssen höhere Ordnungen ebenfalls kompensiert werden. Hierzu werden die Sextupolmagnete in verschiedenen Familien eingeteilt. Das resultierende Sextupolschema wird dann an Hand der erreichten Energieakzeptanz bewertet. Zunächst wird ein Schema bestehend aus zwei Familien pro Bogen in der horizontalen Ebene und drei Familien pro Bogen in der vertikalen Ebene untersucht, das erlaubt die sogenannten W Funktionen zu korrigieren, die ein Maß für die chromatische Störung der Optik sind. Mit dieser Korrekturmethode wird kann die Energieakzeptanz von $\Delta p/p = \pm 0.04\,\%$ auf einen Bereich von $-0.3\,\%$ bis $+0.1\,\%$ vergrößert werden. Für eine höhere Flexibilität des Korrekturschemas wird die Anzahl der Sextupolfamilien anschließend auf sechs pro Bogen pro Ebene erhöht. Die Anzahl der Freiheitsgrade wird durch die individuelle Optimierung der Stärken der ersten zwölf Sextupolpaare nach der Wechselwirkungszone weiter erhöht. Mit diesem Sextupolschema kann die Energieakzeptanz auf mehr als $\pm 0.5\,\%$ erhöht werden. In Ergänzung zu diesen auf analytischen Annahmen basierenden Korrekturen wurde eine komplett numerische Optimierung der Sextupolstärken mit Hilfe des Downhill-Simplex-Algorithmus untersucht.

Zusammenfassend gesagt präsentiert diese Arbeit die Entwicklung einer flexiblen Magnetstruktur für höchste Luminositäten, mit der die Strahlparameter für alle vier vorgesehenen Strahlenergien erreicht werden können. In einer ersten Optimierung der Chromatizitätskorrektur wird eine beachtliche Vergrößerung der Energieakzeptanz erreicht. In Kombination mit einer lokalen Chromatizitätskorrektur nahe des Wechselwirkungspunktes sind die Zielwerte für die Energieakzeptanz dadurch in greifbarer Nähe.

Abstract

Following the recommendations of the European Strategy Group for High Energy Physics, CERN launched the Future Circular Collider Study (FCC) to investigate the feasibility of large-scale circular colliders for future high energy physics research. This thesis presents the considerations taken into account during the design process of the magnetic lattice in the arc sections of the electron-positron version FCC-ee. The machine is foreseen to operate at four different centre-of-mass energies in the range of 90 to 350 GeV. Different beam parameters need to be achieved for every energy, which requires a flexible lattice design in the arc sections. Therefore methods to tune the horizontal beam emittance without re-positioning machine components are implemented. In combination with damping and excitation wigglers a precise adjustment of the emittance can be achieved. A very first estimation of the vertical emittance arising from lattice imperfections is performed. Special emphasis is put on the optimisation of the chromaticity correction scheme based on a multi-family sextupole scheme in the arcs. In order to obtain a momentum acceptance of $\pm 2\,\%$, which is required because of the severe energy loss due to beamstrahlung, it is not sufficient to correct only the linear chromaticity. The very strong focussing in the final focus quadrupoles requires the correction of higher-order terms as well. Methods to deal with this issue are investigated. A systematic study of the higher-order chromaticity and the optimisation of the sextupole scheme to gain highest possible momentum acceptance is presented.

Symbols and Abbreviations

Arabic symbols:

a_1, b_1	first order chromatic derivatives of α and β
a_2, b_2	second order chromatic derivatives of α and β
A	transverse amplitude function of the betatron oscillation (m)
$\mathbf{B}$	magnetic induction (T)
c	speed of light (ms^{-1})
C	circumference of the design orbit (m)
C_q	$= \frac{55}{32\sqrt{3}} \frac{\hbar c}{m_0 c^2} = 3.832 \times 10^{-13}\,\mathrm{m}$, constant
C_γ	$= \frac{4\pi}{3} \frac{r_\mathrm{e}}{(m_\mathrm{e} c^2)^3} = 8.8460 \times 10^{-5}\,\frac{\mathrm{m}}{\mathrm{GeV}^3}$ m, constant
$D_{x,y}$	transverse dispersion functions (m)
e	unit electronic charge (As)
E	total particle or beam energy (eV)
$\mathbf{E}$	electric field strength (Vm^{-1})
f	focal length of quadrupole magnets (m) or revolution frequency (Hz)
$\mathbf{F}$	force (N)
F	$= \frac{\rho^2}{l_\mathrm{B}^3} \langle \mathcal{H} \rangle$, lattice form factor
$\mathcal{H}_{x,y}$	$= \beta_{x,y} D'^2_{x,y} + 2\alpha_{x,y} D_{x,y} D'_{x,y} + \gamma_{x,y} D^2_{x,y}$
$\mathcal{I}_{1,2,3,4,5}$	synchrotron integration integrals
$J_{x,y,s}$	damping partition numbers
k_1	normalised quadrupole strength (m^{-2})
k_2	normalised sextupole strength (m^{-3})
k_3	normalised octupole strength (m^{-4})
m_e	$= 0.510\,999\,\mathrm{MeV/c}^2$, electron rest mass
$\mathbf{M}$	transport matrix
N	number of particles in the bunch
L	length (m)
L^*	longitudinal distance between interaction point and first quadrupole (m)

$\mathcal{L}$	luminosity ($\mathrm{m^{-2}s^{-1}}$)
$\mathbf{p}$	particle momentum ($\mathrm{kgms^{-1}}$, $\mathrm{eVc^{-1}}$)
P_γ	synchrotron radiation power (W)
$Q_{x,y}$	transverse tune, number of betatron oscillation per turn
$Q'_{x,y}$	linear chromaticity
Q'', $Q^{(3)}$, $Q^{(4)}$	higher-order chromatic derivatives of the tune
r_e	classical electron radius (m)
$\sqrt{s}$	centre-of-mass energy
t	time (s)
T	revolution time (s)
u	variable used in calculations for any of the transverse coordinates x or y
U_0	energy loss per turn (eV)
$\mathbf{v}$	particle velocity (m/s)
$\mathbf{W}$	Montague W vector
W	Montague W function, absolute value of the W vector
x, y, s	coordinates of the curvilinear Frenet-Serret-Coordinate System (m, m, m)

Greek symbols:

α, β, γ	Twiss parameters
α_c	momentum compaction factor
α_f	fine structure constant
$\beta^*_{x,y}$	beta function at the interaction point (m)
γ	relativistic Lorentzfactor
δ	$= \Delta p/p$, relative energy deviation
Δ	difference to nominal value
ϵ	Courant-Snyder invariant (nm rad)
ϵ_0	permittivity of vacuum
$\epsilon_{x,y}$	(equilibrium) beam emittance (nm rad)
η_c	phase slip factor
θ	bending angle (rad, °)
$\mu_{x,y}$	phase advance of the betatron oscillation (rad, °)
ρ	local bending radius of the trajectory (m)
$\sigma_{x,y}$	transverse beam size (m)
Σ_p	cross section of physics event (b)
τ	damping time (s)

φ	phase advance of one unit cell (rad, °)
ψ	phase function of the betatron oscillation (rad, °)
ξ	beam-beam parameter
Υ	beamstrahlung parameter
ω_s	synchrotron oscillation frequency (Hz)

Abbreviations:

ANKA	Angströmquelle Karlsruhe
CLIC	Compact Linear Collider
ESS	Extended Straight Section in the FCC Racetrack Layout
FCC	Future Circular Collider
ILC	International Linear Collider
IP	interaction point
IR	interaction region
LARC	Long Arc in Racetrack Layout
LEP	Large Electron Positron Collider
LHC	Large Hadron Collider
LSS	Long Straight Section in the FCC Racetrack Layout
QF, QD	focussing, defocussing quadrupole
RF	radio-frequency
SARC	Short Arc in the FCC Racetrack Layout
SF, SD	focussing, defocussing sextupole

Contents

Introduction

This thesis presents the design of the magnet lattice and the calculations and optimisation of the particle beam optics for a new large-scale electron-positron-collider called *FCC-ee*. Following the recommendations of the European Strategy Group for High Energy Physics, three new large scale projects are under study to investigate the characteristics of the recently discovered Higgs particle in detail and to path the way for the investigation of the still open questions in particle physics in the frame of the Standard Model and beyond [1]. The so-called *Future Circular Collider Study (FCC)* combines the common effort of several international institutes and labs under the leadership of CERN and covers all three possible scenarios: a new proton-proton collider aiming for highest energies (FCC-hh), the electron-positron collider for high precision experiments (FCC-ee), which is the subject of this thesis, and an electron-proton version to provide deep inelastic scattering experiments between leptons and hadrons for the study of the quark structure of the proton (FCC-he).

The Future Circular Collider Study FCC is the next natural step in the attempt to answer today's questions in particle physics like dark matter, the matter/antimatter asymmetry or the origin of neutrino masses. In 2012 the existence of the so-called Higgs boson, predicted by Higgs, Brout and Englert, could be confirmed in collisions at the the Large Hadron Collider (LHC) [2, 3] and led shortly after to the award of the Nobel prize. LHC, the most powerful particle accelerator ever built, is designed for proton collisions at up to 14 TeV centre-of-mass energy [4]. It advanced our understanding of matter and the Standard Model and is still producing data for further analysis and the search for new physics. However, to explore today's key questions about the Standard Model and our universe a more powerful machine will be required that increases the energy threshold beyond LHC's capacities.

FCC-hh: In order to study physics observations at highest energies, a hadron collider pushing the energy frontier to 100 TeV centre-of-mass energy is proposed. The circumference is determined by the available dipole magnetic field [5], which is in the order of 16 to 20 T based on Nb_3Sn technology. The study therefore foresees an 80 to 100 km circumference tunnel in the Geneva area connected to the already existing CERN accelerator

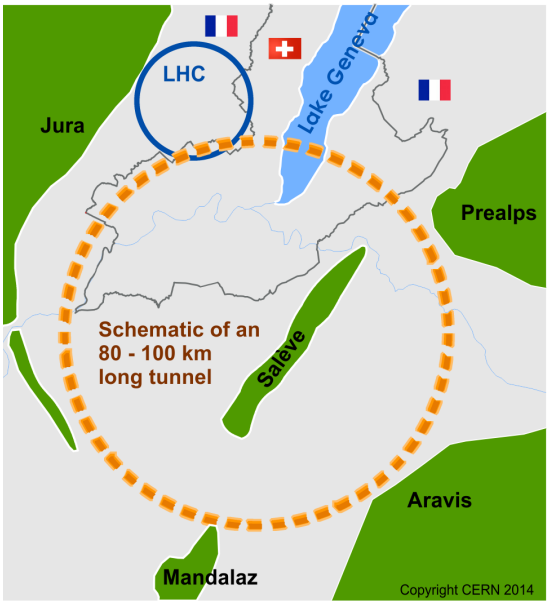

Figure 1: Illustration of a possible site for the FCC in the Geneva basin [6, 7].

infrastructure. A possible location for such a tunnel in the Geneva basin is illustrated in Fig. 1.

FCC-he: In continuation of the studies of deep inelastic scattering at HERA scenarios for electron-proton collisions are investigated in the context of the FCC Study as well. One interaction point of the hadron collider could be reserved for collisions with an electron beam provided by an energy recovery linac.

FCC-ee: In order to gain better knowledge about already discovered particles and draw conclusions about the properties of new physics an electron-positron collider is proposed for precision measurements. The last high-precision machine, the Large Electron Positron Collider (LEP), put the Standard Model on solid basis of empirical data by delivering precise measurements of the W and Z bosons, but was not powerful enough to produce Higgs bosons and to reach the $t\bar{t}$ threshold. Since the mass of the Higgs boson remained unknown, the linear collider projects *Compact Linear Collider* (CLIC) and *International Linear Collider* (ILC) were designed to reach high centre-of-mass energies up to the TeV range [8, 9]. At such high beam energies a linear machine layout is preferred, because of the vast energy loss due to synchrotron radiation in the arc sections of circular machines. However, the relatively low mass of the Higgs boson of $m_{\mathrm{H}} = 125\,\mathrm{GeV/c^2}$ and the large circumference of the FCC would allow the operation of an electron-positron collider with acceptable amount of synchrotron radiation losses. Therefore, the conceptual design study

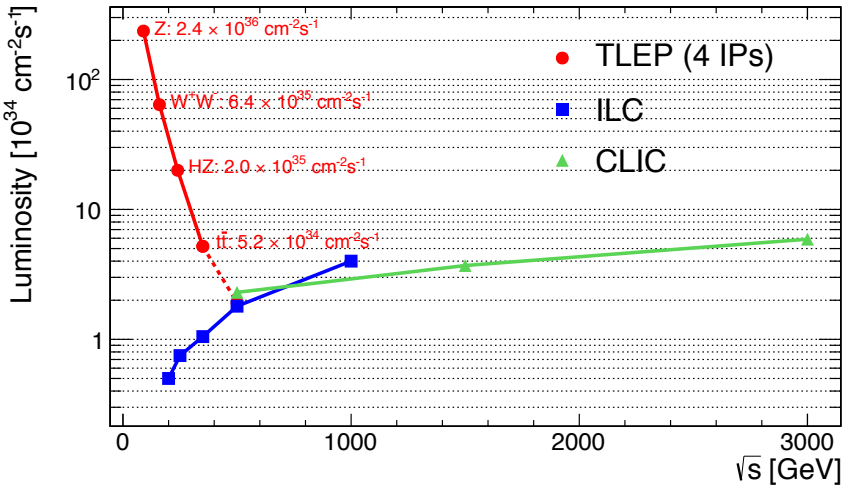

Figure 2: Expected luminosity of TLEP (FCC-ee) in units of $10^{34}\,\mathrm{cm}^{-2}\mathrm{s}^{-1}$ as a function of the centre-of-mass energy $\sqrt{s}$. The dashed line indicates a possible upgrade of TLEP to 500 GeV beam energy. The values of the linear collider projects ILC and CLIC are given for comparison [10].

also investigates a lepton collider featuring electron-positron collisions at centre-of-mass energy in the range from $\sqrt{s} = 90$ to 350 GeV for precision studies and observations of rare decay events [10, 11]. Within this energy range following production modes are of highest interest [12, 13]:

- the Z pole at 90 GeV: FCC-ee would serve as a very efficient factory of Z bosons allowing precise measurements of m_Z and Γ_Z as well as the search for extremely rare decays.
- the W pair production threshold at 160 GeV for high precision measurements of m_W
- the ZH production mode at 240 GeV: at this energy with maximum rate of Higgs boson production FCC-ee could precisely measure the characteristics of the recently found particle.
- operation at and above the $\mathrm{t\bar{t}}$ threshold at 350 GeV to allow the first precision measurements of the top quark.

In this energy range below 400 GeV circular colliders have much higher luminosity, because they can provide a higher collision rate and allow continuous top-up injection to compensate luminosity burn-off [13]. In addition, circular colliders offer the possibility to install several experiments, which increases the amount of collected data. Fig. 2 compares the expected luminosity of FCC-ee (TLEP) assuming four interaction points (IPs) to the values of ILC and CLIC. The expected luminosity of FCC-ee is up to two orders of magnitude larger than the ILC's. As a further advantage, for beam energies up to 80 GeV circular colliders allow the most precise measurement of the beam energy through resonant depolarisation of the transverse particle spin [14].

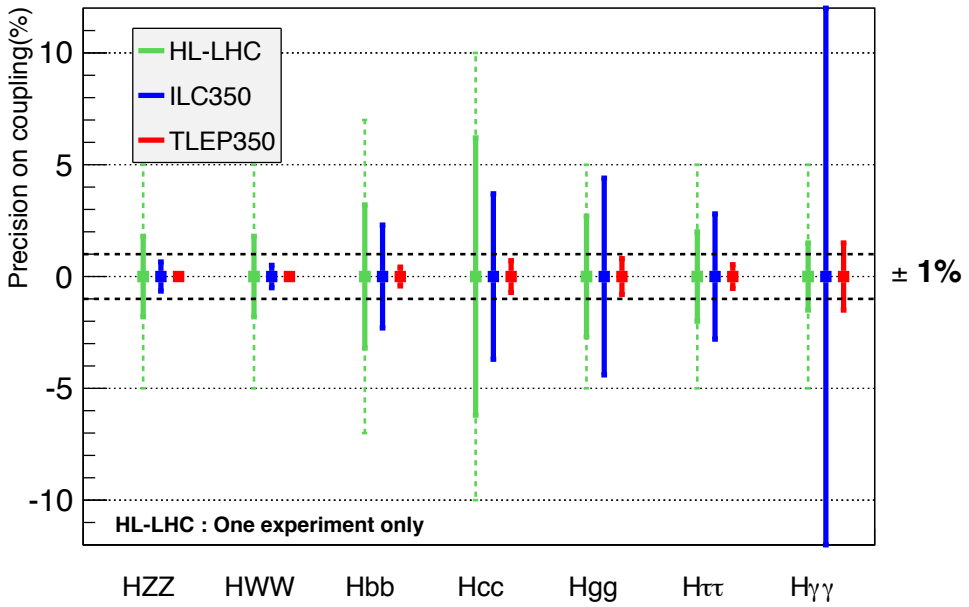

Figure 3: Comparison the relative uncertainties on the Higgs coupling for HL-LHC and the Higgs factories ILC and TLEP (FCC-ee). The dashed horizontal lines illustrate the 1 % band, relevant for sensitivity to multi-TeV new physics [10].

In summary, compared to hadron colliders, lepton machines provide a clean experimental environment in which the initial and final states are theoretically known very precisely. The huge data samples in combination with the precise knowledge of the centre-of-mass energy allow to measure the properties of the W and Z bosons with unprecedented precision [13]. In addition, high-precision measurements of the Higgs boson and the top quark could be performed for the first time. Fig. 3 shows a comparison of the relative uncertainties of the Higgs boson coupling for the HL-LHC, ILC and TLEP (FCC-ee) [10]. Coupling precision below the 1 % threshold would allow to draw conclusions to multi-TeV new physics [10]. For further information on the FCC-ee physics case see [10, 13, 15].

FCC-ee baseline parameter set and challenges for the lattice design: The ultimate performance limit for luminosity production in a lepton storage ring strongly depends on the energy of the colliding beams. Hence, the machine has to be designed and optimised for all four physics programmes individually while using the same machine hardware. For all cases a maximum synchrotron radiation power of $P_\gamma = 50\,\mathrm{MW}$ per beam was assumed leading to a considerably higher number of bunches and beam current at the lower beam energies. An excerpt of the resulting baseline parameter set optimised for highest possible luminosity is presented in Tab. 1 [16]. The full table is given in the Appendix in Tab. A2 as well as the previous version in Tab. A1.

Table 1: Excerpt of the baseline parameter set for the different physics programmes of FCC-ee [16]. The full table is given in the Appendix in Tab. A2.

	Z	Z	W	H	tt
Beam energy (GeV)	45.5	45.5	80	120	175
Beam current (mA)	1450	1450	152	30	6.6
Bunches/beam	30180	91500	5260	780	81
Bunch population (10^{11})	1	0.33	0.6	0.8	1.7
Horizontal emittance ϵ_x (nm)	0.2	0.09	0.26	0.61	1.3
Vertical emittance ϵ_y (pm)	1	1	1	1.2	2.5
Momentum comp. (10^{-5})	0.7	0.7	0.7	0.7	0.7
Betatron function at IP					
- Horizontal β^* (m)	0.5	1	1	1	1
- Vertical β^* (mm)	1	2	2	2	2
Synchrotron radiation power P_γ (MW)	50	50	50	50	50
Energy loss/turn (GeV)	0.03	0.03	0.33	1.67	7.55
Total RF voltage (GV)	0.4	0.2	0.8	3	10
Polarization time t_p (min)	11200	11200	672	89	13
Luminosity/IP for 2 IPs ($10^3 4\,\mathrm{cm}^{-2}\mathrm{s}^{-1}$)	207	90	19.1	5.1	1.3
Luminosity lifetime (min)	94	185	90	67	57
Beam-beam parameter ξ					
- Horizontal	0.025	0.05	0.07	0.08	0.08
- Vertical	0.16	0.13	0.16	0.14	0.12
Beamstrahlung critical	No/Yes	No	No	No	Yes

Out of the many challenges for the design of FCC-ee, the following ones concern the magnetic lattice and are therefore studied in detail in the context of this thesis:

- As the beam parameters are optimised for four different beam energies individually, the lattice needs to be flexible and easily allow modifications to obtain the beam parameters for the respective energy.
- The very high synchrotron radiation power requires a sophisticated absorber design to protect the machine components. Room for the absorbers must be reserved in the lattice and arrangements have been made to compensate for the energy loss of the particles while propagating through the arc sections.
- At 45.5 GeV beam energy the horizontal beam emittance reaches values below the nanometer range. In combination with the high bunch population the charge density in the bunches becomes very high, which might lead to large beam-beam tune shifts, intra-beam scattering or other collective effects. To prevent negative impact the emittance might have to be artificially increased.
- The small values of the vertical emittance in the range from 1.0 to 2.5 pm rad and the ambitious emittance ratio in the permille range correspond to the performance of

modern synchrotron light sources [17–19] and set serious constraints on the alignment tolerances of the machine components.

- The luminosity of previous storage ring colliders was mainly limited by the beam-beam tune shift [20]. At the largest beam energy of 175 GeV beamstrahlung created during the bunch crossing at the interaction point becomes most critical. The non-colliding particles in the bunch might lose up to 2 % of their energy leading to a required momentum acceptance of ±2 %. The effect of beamstrahlung was mainly discussed in context with linear colliders so far.
- The very small value of the vertical beta function $\beta_y^* = 2\,\text{mm}$ at the interaction point requires very strong focussing of the beam in the final doublet quadrupoles, which creates large chromatic perturbations of the optics for off-momentum particles. A satisfactory chromaticity correction scheme has to be established with stable motion for particles up to ±2 % momentum deviation. The global chromaticity correction scheme of the arc needs to be combined with a local chromaticity compensation scheme close to the interaction point.

In the context of this work the electron-positron collider version of FCC was studied with emphasis on the lattice, the beam optics and mainly the optimisation of the chromatic behaviour of the stored beam particles. In a lepton accelerator the magnetic lattice and optics, i.e. the periodic arrangement of the magnetic elements and the their strength and distance, directly affect the beam parameters which describe the characteristics of the particle beam such as beam size or particle density. A careful design of the lattice is therefore essential to obtain a certain luminosity of the collider.

The next chapters of this thesis will present the development of a possible lattice for the FCC-ee collider following above mentioned boundary conditions. The main focus is put on the investigation of the arc lattice, which in the case of lepton storage rings is essential to define the beam parameters. Starting from the layout of the basic lattice cell at the highest beam energy all lattice sections are derived which are required to implement a model of the whole machine. Methods will be presented that allow the modification of the horizontal beam emittance for lower energies while using the same hardware and possible lattice arrangements will be proposed that fulfill the requirements at each beam energy. To finalise the linear lattice design of FCC-ee a very first investigation of the vertical beam emittance and the alignment tolerances in the arcs and first results of the emittance fine-tuning with wigglers will be presented. In order to compensate for the large chromatic aberrations arising from the strong final focus quadrupoles a systematic study of global chromaticity compensation schemes was performed. Several sextupole arrangements in the arc sections were studied and different correction methods were implemented to optimise the momentum acceptance.

CHAPTER 1

Concepts of Accelerator Physics

This chapter gives a brief overview about the basics of accelerator physics. Further details can be found in the usual textbooks like [21] or [22]. A more comprehensive explanation to the topics relevant for this thesis will be given at the beginning of each chapter.

1.1 Frenet-Serret Coordinate System

The trajectory in a particle accelerator taken by a particle with design energy and no transverse momentum is called the design trajectory, or in the case of circular accelerators the design orbit. In order to keep the mathematical description of beam dynamics as simple as possible, the particle motion is described in reference to this design orbit in a right-handed orthogonal coordinate system moving along with the reference particle. This coordinate system is called the *Frenet-Serret Coordinate System* with the basis $\hat{x}$, $\hat{y}$, and $\hat{s}$. $\hat{s}$ always points tangentially along the path of the reference orbit and is used as independent variable. $\hat{x}$ is the horizontal coordinate pointing in the same direction as the radial vector. The vertical coordinate $\hat{y}$ is orthogonal to both $\hat{s}$ and $\hat{x}$ as illustrated in Fig. 1.1.

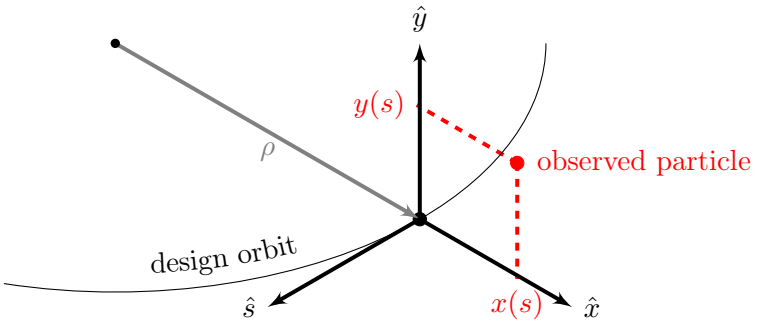

Figure 1.1: Frenet-Serret Coordinate System used in accelerator physics. $\hat{x}$, $\hat{y}$, and $\hat{s}$ form the right-handed orthogonal basis, ρ is the local bending radius.

1.2 Components of particle accelerators

Acceleration, guidance and focusing of the charged particles is performed with the Lorentz force

$$\mathbf{F}_\mathrm{L} = e(\mathbf{E} + \mathbf{v} \times \mathbf{B}) = \dot{\mathbf{p}}, \tag{1.1}$$

which emerges from both electric fields $\mathbf{E}$ and magnetic fields $\mathbf{B}$. If the particles have relativistic velocities the effects of magnetic fields are by a factor of c larger than the effect of electric fields. In other words a magnetic field of $B = 1\,\mathrm{T}$ corresponds to an electric field of $E = 3 \times 10^8\,\mathrm{V/m}$. Electric fields of this strengths are far beyond technical limits, therefore magnetic fields are usually used to bend and focus the beam in high energy storage rings. The guiding magnetic field can be expanded into a series of multipoles:

$$B_y = B_{y0} + \frac{\mathrm{d}B_y}{\mathrm{d}x}x + \frac{1}{2!}\frac{\mathrm{d}^2B_y}{\mathrm{d}x^2}x^2 + \frac{1}{3!}\frac{\mathrm{d}^3B_y}{\mathrm{d}x^3}x^3 \ldots \tag{1.2}$$

For optics design it is convenient to normalize the multipole strengths to the particle momentum to get an energy independent description of the focusing properties:

$$\begin{aligned}
\frac{e}{p}B_y(x) &= \frac{e}{p}B_{y0} + \frac{e}{p}\frac{\mathrm{d}B_y}{\mathrm{d}x}x + \frac{1}{2!}\frac{e}{p}\frac{\mathrm{d}^2B_y}{\mathrm{d}x^2}x^2 + \frac{1}{3!}\frac{e}{p}\frac{\mathrm{d}^3B_y}{\mathrm{d}x^3}x^3 \ldots \\
&= \frac{1}{\rho} + k_1 x + \frac{1}{2!}k_2 x^2 + \frac{1}{3!}\frac{e}{p}k_3 x^3 \ldots \\
&\quad \text{dipole} \quad \text{quadrupole} \quad \text{sextupole} \quad \text{octupole}
\end{aligned} \tag{1.3}$$

Each multipole has its particular effect on the particle beam: the homogeneous field of the dipole magnets is used to bend the particle trajectory and fix the geometry of the machine. Quadrupoles feature a linear field gradient, which is used to focus the beam. However, if they focus in one plane, they have a defocussing effect in the other. So a setup with quadrupole lenses of alternating polarity is required and their strengths and positions have to be adjusted to obtain an overall focusing effect in both planes. The configuration widely used in high-energy storage rings, the FODO layout with alternating quadrupoles in equal distance, is described in Sec. 2.2. Multipoles of higher orders are used to correct imperfections of the optics. Chromatic aberrations arising from momentum deviations, for example, are corrected by sextupole magnets.

The periodic sequence of magnetic elements is called the *magnetic lattice* of a particle accelerator. A *linear lattice* just contains dipole and quadrupole magnets.

Longitudinal electric fields in so-called *radio-frequency (RF) cavities* are used to increase the particle energy during the acceleration process. The advantage of a circular machine is, that the same accelerating structure can be used many times.

1.3 Linear transverse dynamics

1.3.1 Equations of motion, beta function, emittance and tune

The transverse motion of a single particle in an accelerator with periodic magnetic lattice can be described by Hill's equation

$$u'' + K_u(s)u = 0 \qquad (u = x, y) \tag{1.4}$$

assuming the existence of a closed orbit. K_u represents the focussing effect of dipoles and quadrupoles

$$K_x(s) = -k_1(s) + \frac{1}{\rho^2}, \tag{1.5a}$$

$$K_y(s) = \quad k_1(s). \tag{1.5b}$$

$k_1(s)$ is the normalized quadrupole strength and $1/\rho^2$ describes the geometric contribution to the weak focusing of the dipoles, which in a flat machine only arises in the horizontal plane. The solution of Hill's equation describes the trajectory of a single particle and is a transverse oscillation around the reference orbit, called the *betatron oscillation*:

$$u(s) = \sqrt{\epsilon}\sqrt{\beta(s)}\cos\left(\psi(s) + \phi\right) \tag{1.6a}$$

$$u'(s) = -\frac{\sqrt{\epsilon}}{\sqrt{\beta(s)}}\Big[\alpha(s)\cos(\psi(s) + \phi) + \sin(\psi(s) + \phi)\Big] \tag{1.6b}$$

The detailed derivation of this equations is given in [21]. ϵ is the so-called *Courant-Snyder invariant*, which is proportional to the area $A = \epsilon\pi$ of the phase space ellipse formed by the particles's potential states of motion at a specific point of the lattice. As illustrated in Fig. 1.2 the shape and orientation of the ellipse is described by the *Twiss parameters* β, α, and γ:

$$\gamma(s)u'^2(s) + 2\alpha(s)u(s)u'(s) + \beta(s)u^2(s) = \epsilon \tag{1.7}$$

$\beta(s)$ is the amplitude function of the betatron oscillation and depends on the focusing properties of the lattice. $\alpha(s) \equiv -\beta'(s)/2$ is proportional to the slope of the beta function and indicates the orientation of the ellipse in phase space.

$$\gamma(s) \equiv \frac{1 + \alpha^2(s)}{\beta(s)} \tag{1.8}$$

describes the angular envelope of the trajectory and is a measure for the divergence of the beam. Under the influence of conservative forces, according to Liouville's theorem, the phase space volume occupied by the particle beam stays constant. This means, while traveling through the lattice, the phase space ellipse gets deformed by bending and focusing

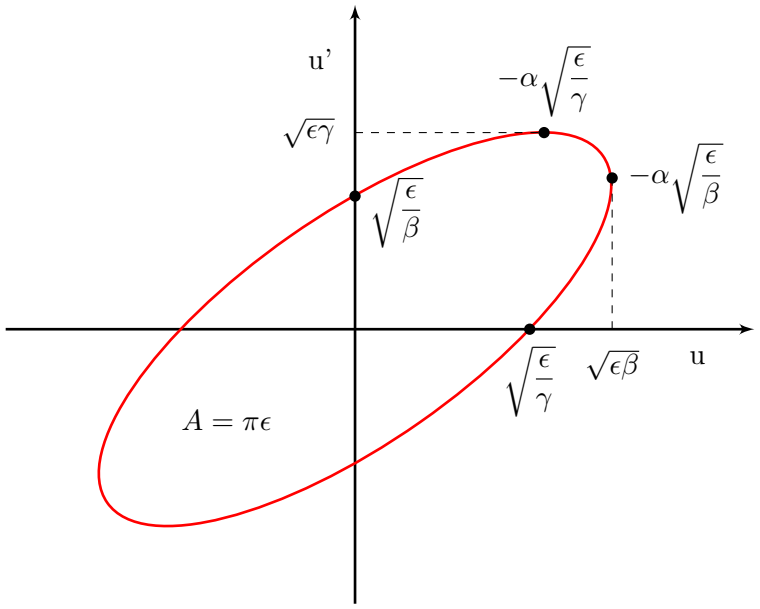

Figure 1.2: Ellipse representing the potential states of a particle in phase space.

elements, but its area stays constant. As immediate consequence a beam focussed to a narrow waist has a large divergence.

Considering a Gaussian shaped beam the particle at 1σ orbit offset defines the beam size

$$\sigma_u = \sqrt{\epsilon_u \beta_u} \tag{1.9}$$

and its Courant-Snyder invariant is equivalent with the so-called *beam emittance*, which describes the phase space volume occupied by the particles of the beam. In the case of more general particle distributions an alternative definition of emittance is often used [23, 24]:

$$\epsilon_{\mathrm{rms},u} = \sqrt{\langle u \rangle^2 \langle u' \rangle^2 - \langle u u' \rangle^2} \tag{1.10}$$

This statistical definition is not based on a more or less arbitrarily chosen contour of the phase space volume, but on the mean values of position and transverse momentum.

The difference of the phase functions at two points s_1 and s_2 in the lattice is called the *phase advance*

$$\mu = \psi(s_2) - \psi(s_1) = \int_{s_1}^{s_2} \frac{1}{\beta(s)} \, \mathrm{d}s. \tag{1.11}$$

The phase advance of the whole accelerator lattice divided by 2π gives the number of betatron oscillations in one revolution and is called the *tune*

$$Q_u = \frac{1}{2\pi} \oint \frac{1}{\beta_u(s)} \, \mathrm{d}s. \tag{1.12}$$

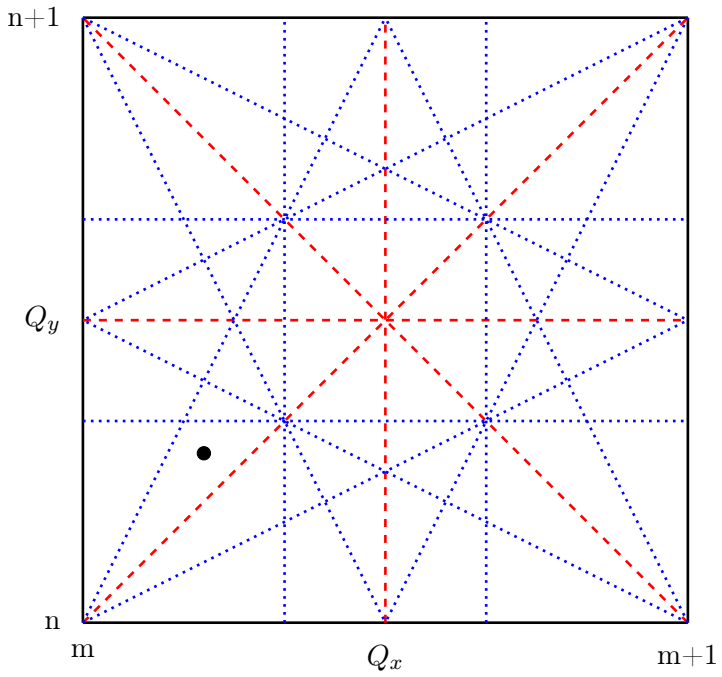

Figure 1.3: Tune diagram with optical resonances up to third order. The first order resonances are depicted with black continuous lines, the second order with red dashed lines and the third order resonances by dotted blue lines. A possible working point is marked by the black dot.

The tunes of both transverse planes define the so-called *working point* of the machine and have to be chosen very carefully. As in circular accelerators the stored particles encounter the same magnetic structure repeatedly, perturbations in the lattice can cause *optical resonances* that increase the amplitude of the betatron oscillation and hence can rapidly lead to the loss of the particles. Optical resonances of order l occur in both planes, if the resonance condition

$$lQ = p \quad (l, p \in \mathbb{Z}) \tag{1.13}$$

is fulfilled. If the lattice contains elements that introduce coupling between the transverse planes, like solenoids or skew elements, also *coupling resonances* depending on both the horizontal and the vertical tune arise for

$$mQ_x + nQ_y = p \quad (m, n, p \in \mathbb{Z}). \tag{1.14}$$

$|m| + |n|$ is the order of the resonance. All resonances up to the third order are visualised as lines in Fig. 1.3. During the lattice design process it is important to observe the working point and keep it sufficiently far from these lines.

1.3.2 Dispersion function

The design orbit is defined by the path of a particle with design momentum p and no transverse oscillations. The bending radius ρ of a charged particle in a homogeneous dipolar magnetic field depends on its momentum (compare Eq. (1.3)). The deflection is stronger for particles with low momentum than for particles with high momentum. In analogy to light optics this effect is called *dispersion*. As a consequence the equation of motion given by Eq. (1.4) needs to be extended. A particle with relative energy deviation $\delta = \Delta p/p$ satisfies the inhomogeneous Hill's equation

$$u'' + K(s)u = \frac{1}{\rho}\frac{\Delta p}{p}. \tag{1.15}$$

Its solution is a linear combination of the general solution (1.6b), here referred to as $u_\beta(s)$, and the particular solution of the inhomogeneous part $u_\delta(s)$:

$$u(s) = u_\beta(s) + u_\delta(s) \tag{1.16}$$

The particle with momentum deviation will no longer oscillate around the reference orbit but around a new dispersion orbit with a transverse offset, which is in first order proportional to the relative energy deviation δ. The so-called *dispersion function* is defined such, that it yields the closed orbit for a particle with 100 % energy deviation corresponding to $\delta = 1$. For any other energy deviation the dispersion orbit is

$$u_\delta(s) = D_u(s)\,\delta. \tag{1.17}$$

1.3.3 Momentum compaction factor

The dispersion orbit of particles with momentum offset introduced in the previous section has a different length than the design orbit. Since the bending radii decrease for particles with smaller momentum, the orbit moves to the inside of the ring and gets shorter. For particles with larger momentum the orbit becomes longer. In first order the change of orbit length is proportional to the energy deviation and quantified by the *momentum compaction factor* α_c:

$$\frac{\Delta C}{C} = \alpha_\mathrm{c}\frac{\Delta p}{p} \tag{1.18}$$

The momentum compaction factor is energy independent and constant for a given lattice. It can also be expressed using the first of the so-called *synchrotron radiation integrals*, that describe the modification of the beam parameters by the emission of synchrotron radiation:

$$\alpha_\mathrm{c} = \frac{1}{C}\oint \frac{D(s)}{\rho}\,\mathrm{d}s = \frac{\mathcal{I}_1}{C} \tag{1.19}$$

In the ultra-relativistic regime, where the particle velocity is close to the speed of light, the momentum compaction factor is approximately equal to the phase slip factor

$$\eta_\mathrm{c} = \alpha_\mathrm{c} - \frac{1}{\gamma^2} \approx \alpha_\mathrm{c}, \tag{1.20}$$

which describes the change of revolution time depending on the energy offset:

$$\frac{\Delta T}{T} = \eta_\mathrm{c} \frac{\Delta p}{p} \tag{1.21}$$

The phase slip factor and thus as well the momentum compaction factor is a key parameter in longitudinal dynamics, since it determines the arrival time at the RF cavities and together with the RF voltage the bunch length.

1.3.4 Chromaticity

Linear chromaticity

The deflection of a charged particle in magnetic fields depends on the particle's energy. This effect not only creates dispersion in bending magnets, but also modifies the effective focusing strength of quadrupoles, which is inversely proportional to the momentum. The change of focusing strength due to energy deviation is

$$\Delta k_1 = -\frac{e}{p^2} \frac{\mathrm{d}B_y}{\mathrm{d}x} \Delta p = -k_1\, \delta. \tag{1.22}$$

The quadrupole error results in a tune shift proportional to the energy offset:

$$\Delta Q = \frac{1}{4\pi} \int \beta(s) \Delta k_1(s)\ \mathrm{d}s = \left[-\frac{1}{4\pi} \int \beta(s) k_1(s)\ \mathrm{d}s \right] \delta \tag{1.23}$$

The derivative of the betatron tune with respect to the momentum deviation includes the effect of all quadrupoles in the lattice and is called the *natural chromaticity* of the accelerator

$$Q' = \frac{\mathrm{d}Q}{\mathrm{d}\delta} = -\frac{1}{4\pi} \int \beta(s) k_1(s)\ \mathrm{d}s. \tag{1.24}$$

Although the quadrupoles create positive chromaticity in their defocusing plane as well, the natural chromaticity is in general negative. As the beta functions at the quadrupoles reach maximum values in the focusing plane while having minimum values in the defocusing plane, the negative contribution from the focusing plane dominates.

In a FODO lattice (see Sec. 2.2) the value of the chromaticity equals approximately the negative value of the betatron tune. In collider storage rings the largest contribution to the chromaticity budget comes from the final focus quadrupoles. Their very large strengths drove up to 50 % of the chromaticity in past machines [4, 25].

Linear chromaticity correction with sextupoles

As explained in the previous section, non-zero chromaticity leads to tune shifts for particles with momentum offset. Those particles might encounter optical resonances, where their motion gets unstable and the particles might get lost. Since, especially in the case of a lepton beam with synchrotron radiation, a certain energy spread of the beam cannot be avoided, the chromaticity needs to be corrected.

For chromaticity correction the quadrupoles' focusing strength has to be re-established. As the focusing errors depend on the particle energy, the correction has to be energy-dependent as well. Such an energy-dependent focusing strength is provided by sextupole magnets in dispersive regions ($D_x \neq 0$). The sextupole field gradient is proportional to the transverse position of the particle.

$$\frac{e}{p}B_x = k_2\ x\ y \qquad \Rightarrow \qquad \frac{\partial B_x}{\partial y} = k_2\ x \tag{1.25a}$$

$$\frac{e}{p}B_y = \frac{1}{2}\ k_2\ (x^2 - y^2) \qquad \Rightarrow \qquad \frac{\partial B_y}{\partial x} = k_2\ x \tag{1.25b}$$

So in dispersive regions, where the transverse position of particles with energy deviation is determined by the dispersion orbit $x_\delta = D_x\delta$, they provide an additional focusing proportional to the energy deviation:

$$k_{1,\mathrm{sext}} = k_2\ D_x\ \delta \tag{1.26}$$

Particles with design momentum are not affected by the sextupoles, since their field gradient is zero on the reference orbit. For off-momentum particles the additional focusing restores the focal length of the quadrupole as illustrated in Fig. 1.4 and generates a second term in the chromaticity formula counteracting or increasing the chromatic perturbations:

$$Q' = -\frac{1}{4\pi}\int \Big[k_2(s)D_x(s) + k_1(s)\Big]\beta(s)\ \mathrm{d}s \tag{1.27}$$

Eq. (1.27) directly indicates good positions for the sextupoles for effective chromaticity correction: in order to reduce the sextupole strength a large value of the dispersion function is favored. Since sextupoles affect the optics of both transverse planes, the beta functions should be well-separated to avoid chromaticity increase in the secondary plane. Therefore the sextupoles are usually placed as close to the quadrupoles as possible, where the differ-

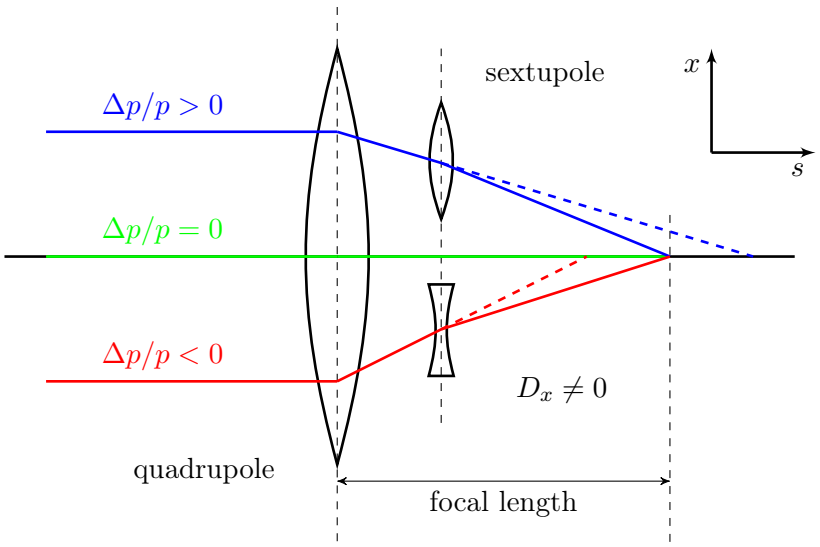

Figure 1.4: Linear chromaticity correction with a sextupole magnet in a dispersive region. The sextupole restores the focal length of the quadrupole for particles with momentum deviation $\Delta p/p \neq 0$.

ence of the beta functions is maximal. In addition, the sextupoles correct the chromaticity locally at the source of the chromatic perturbations. It follows, that a beam transport system can be made achromatic, if every quadrupole is paired with a sextupole of the strength $k_2 = k_1/D_x$. Although such a local chromaticity compensation is very effective, it cannot be achieved in circular accelerators, which include straight sections with vanishing dispersion. Instead, a global chromaticity correction scheme is required, in which the sextupoles of the arcs compensate the chromatic aberrations of the quadrupoles in the straight sections as well. As a consequence, the single lattice cell cannot be achromatic any more.

In state-of-the-art lepton colliders specifically designed chromaticity correction sections are installed close to the interaction point. Additional bending magnets create non-zero dispersion, which allows a local correction of the chromatic aberrations created by the final focus quadrupoles in addition to the global chromaticity correction in the arcs.

The chromaticity correction with sextupoles is unavoidable in large rings, but it has undesirable side-effects: non-linear fields are introduced to the lattice, which create geometric aberrations. This means the particle motion, previously a harmonic oscillation, becomes unstable for large betatron amplitude. This limit of stability is referred to as the *dynamic aperture* of the machine. Moreover, the sextupole fields can introduce coupling between the two transverse planes driving additional optical resonances. To minimize those effects, a large number of sextupoles with moderate strength is equally distributed around the ring instead of a few very strong sextupoles.

1.4 Synchrotron radiation

1.4.1 Synchrotron radiation power and energy loss per turn

Accelerated charged particles lose energy by emitting electromagnetic waves. The radiation created in particle accelerators is called *synchrotron radiation*, since it was observed in synchrotrons for the first time. While the effect is relatively small during longitudinal acceleration, considerable radiation losses are observed for acceleration in transverse direction. The synchrotron radiation power of a particle with charge e and energy E due to the bending forces of the dipole magnets is [26]

$$P_\gamma = \frac{cC_\gamma}{2\pi}\frac{E^4}{\rho^2} \tag{1.28}$$

with the speed of light c, the bending radius ρ representing the bending field $\frac{1}{\rho} = \frac{e}{p}B$ and the constant C_γ for electrons defined as

$$C_\gamma = \frac{e^2}{3\epsilon_0}\frac{1}{(m_\mathrm{e}c^2)^4} = 8.8460 \times 10^{-5}\,\frac{\mathrm{m}}{\mathrm{GeV}^3}. \tag{1.29}$$

m_e is the electron mass and ϵ_0 is the permittivity of vacuum. The radiated energy scales with the forth power of the particle energy, which means that the energy loss increases very quickly for large beam energies. It also scales inversely with the fourth power of the particle's rest mass. As a consequence, synchrotron radiation is mainly observed in electron storage rings. In order to reduce the losses the bending radius needs to be increased, which is why circular lepton colliders tend to have a large circumference.

The energy loss per turn is obtained by the integral of the radiation power for one revolution time T_0. Using $\mathrm{d}t = \frac{1}{c}\,\mathrm{d}s$ and the second synchrotron radiation integral [27]

$$\mathcal{I}_2 = \oint \frac{1}{\rho^2}\,\mathrm{d}s \tag{1.30}$$

the energy loss per turn is given by

$$U_0 = \int_0^{T_0} P_\gamma\,\mathrm{d}t = \frac{C_\gamma}{2\pi}E^4\mathcal{I}_2. \tag{1.31}$$

Synchrotron radiation is also created in quadrupoles in case of orbit offsets or large betatron amplitudes. Especially in the final focus quadrupoles of a collider, where the beam is very large and strongly focused, synchrotron radiation has to be controlled carefully to avoid background in the experiments.

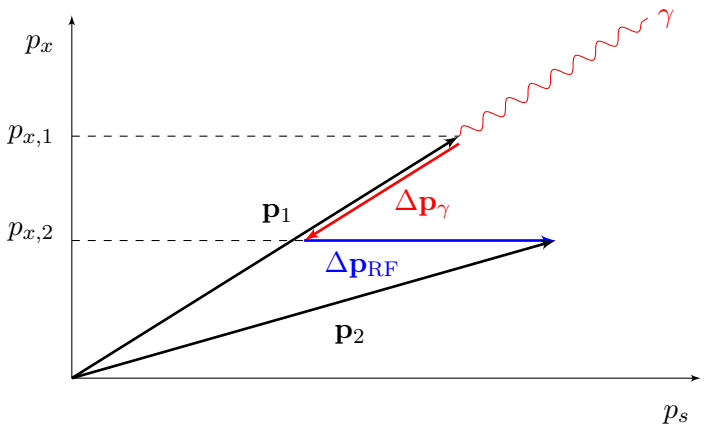

Figure 1.5: Decrease of transverse momentum by radiation damping. The emission of a photon reduces both longitudinal and transverse momentum, while the re-acceleration in the RF cavities only increases the longitudinal component.

1.4.2 Radiation damping

The emission of synchrotron radiation damps the particle oscillations both in the longitudinal and in the transverse planes. As the amount of emitted energy depends on the forth power of the particle momentum, particles with large momentum lose more energy due to synchrotron radiation than particles with a smaller momentum. This leads to a reduction of the energy spread of the beam and thus to a smaller amplitude of the longitudinal oscillation, also called the *synchrotron oscillation*.

The concept of transverse radiation damping is illustrated in Fig. 1.5. The synchrotron radiation photon is emitted into the forward direction of the particle movement reducing both longitudinal and transverse momentum. Since the particle only gains longitudinal momentum in RF system, a net loss of transverse momentum is achieved, which leads to a compression of the particles in phase space and consequently to a reduction of emittance.

The amplitudes of both synchrotron oscillation and betatron oscillations are damped exponentially:

$$A_i = A_{i,0}e^{-\alpha_i t} \quad \text{with } i = x, y, s \text{ and } \alpha_i = \frac{cC_\gamma}{4\pi C}E_0^3\mathcal{I}_2 J_i. \tag{1.32}$$

The parameters α_i are the damping decrements, the reciprocal of the damping times τ_i, and J_i are the damping partition numbers. Obviously, the damping times depend on the initial beam energy E_0 and become shorter when the synchrotron radiation losses increase.

According to Robinson's theorem [28] the sum of the damping partition numbers is four.

They can be expressed using the synchrotron radiation integrals $\mathcal{I}_2$ and $\mathcal{I}_4$ [26]:

$$J_x = 1 - \frac{\mathcal{I}_{4x}}{\mathcal{I}_2} \tag{1.33a}$$

$$J_y = 1 - \frac{\mathcal{I}_{4y}}{\mathcal{I}_2} \tag{1.33b}$$

$$J_s = 2 + \frac{\mathcal{I}_{4x} + \mathcal{I}_{4y}}{\mathcal{I}_2} \tag{1.33c}$$

The fourth synchrotron radiation integral is given by [27]

$$\mathcal{I}_{4u} = \oint \frac{D_u}{\rho_u} \left(\frac{1}{\rho_u^2} + 2k_1 \right) \mathrm{d}s. \tag{1.34}$$

1.4.3 Quantum excitation and equilibrium beam parameters

The emission of synchrotron radiation leads to damping of the particle motion. However, it also introduces noise to the beam, which is counteracting the damping process. Since synchrotron radiation is emitted in discrete quanta, this effect is called *quantum excitation*. The concept is illustrated in Fig. 1.6. First the particle oscillates around the design orbit with a small amplitude. After photon emission the particle has less energy and therefore oscillates around the dispersion orbit corresponding to its energy deviation δ. The new oscillation starts with a large betatron amplitude, which is equivalent to the transverse offset $x_\delta = D_x \delta$ of the dispersion orbit. The sudden change of betatron amplitude due to the energy loss leads to a modification of the phase space ellipse, which can be calculated by inserting the dispersion orbit x_δ into Eq. (1.7), the particle's Courant-Snyder invariant [29]:

$$\Delta\epsilon = \delta^2 \Big(\beta_u D_u'^2 + 2\alpha_u D_u D_u' + \gamma_u D_u^2 \Big) \tag{1.35}$$

It reasonable to define the so-called $\mathcal{H}$ *function*, which is specified by the guide field and includes all s-dependent quantities being evaluated at the time of photon emission:

$$\mathcal{H}_u(s) = \beta_u D_u'^2 + 2\alpha_u D_u D_u' + \gamma_u D_u^2 \tag{1.36}$$

Quantum excitation and radiation damping cause a permanent increase and decrease of oscillation amplitudes and the electron bunch eventually reaches an equilibrium situation. In the transverse planes the obtained *equilibrium beam emittance* is given by

$$\epsilon_u = C_\mathrm{q} \frac{\gamma^2}{J_u} \frac{\mathcal{I}_{5u}}{\mathcal{I}_2}, \tag{1.37}$$

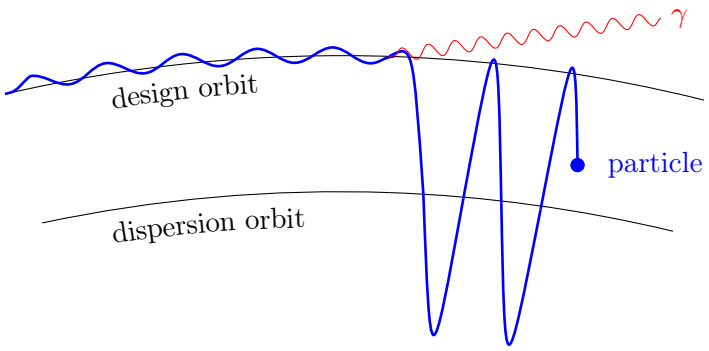

Figure 1.6: Transverse momentum and thus emittance increase by quantum excitation.

where C_q is a constant, that for electrons is given by $C_\mathrm{q} = \frac{55}{32\sqrt{3}} \frac{\hbar c}{m_0 c^2} = 3.832 \times 10^{-13}\,\mathrm{m}$.

$$\mathcal{I}_{5u} = \oint \frac{1}{|\rho_u|^3} \mathcal{H}_u \, \mathrm{d}s \tag{1.38}$$

is the fifth synchrotron radiation integral [27].

In a perfectly aligned planar lepton storage ring the vertical dispersion is equal to zero and the $\mathcal{H}$ function in $\mathcal{I}_{5y}$ vanishes. As a consequence the vertical emittance is dominated by radiation damping. The fundamental lower limit is determined by the vertical opening angle of the synchrotron radiation, which still excites small vertical oscillations, so that the equilibrium beam emittance does not reach zero.

In practice, magnet alignment errors create vertical dispersion and in addition coupling between the transverse planes transfers momentum to the vertical plane. Most storage rings therefore operate with a vertical emittance in the order of 1 % of the horizontal emittance [27]. With specifically designed low emittance lattices and state-of-the-art alignment techniques today's lightsources even reach the per mille range [18, 19].

In the longitudinal plane quantum excitation and radiation damping lead to the *equilibrium energy spread* in the beam, given by

$$\frac{\sigma_\mathrm{E}^2}{E^2} = C_\mathrm{q} \gamma^2 \frac{\mathcal{I}_3}{J_s \mathcal{I}_2} = C_\mathrm{q} \gamma^2 \frac{\mathcal{I}_3}{2\mathcal{I}_2 + \mathcal{I}_{4x} + \mathcal{I}_{4y}}, \tag{1.39}$$

which, because of the factor γ^2, increases with the beam energy squared. The longitudinal damping partition number can also be substituted from Eq. (1.33c) yielding an expression only dependent on the synchrotron radiation integrals $\mathcal{I}_2$, $\mathcal{I}_3$ and $\mathcal{I}_4$. The third synchrotron radiation integral is defined as [27]

$$\mathcal{I}_3 = \oint \frac{1}{|\rho^3|} \, \mathrm{d}s. \tag{1.40}$$

The energy spread directly leads to the *equilibrium bunch length*, which also depends on the phase slip factor η_c and the synchrotron oscillation frequency ω_s. It can also be expressed using the revolution frequency ω_0, the momentum compaction factor α_c and the RF voltage V_RF [22]:

$$\sigma_s = \frac{c|\eta_\mathrm{c}|}{\omega_s}\left(\frac{\sigma_\mathrm{E}}{E}\right) = \frac{\sqrt{2\pi}c}{\omega_0}\sqrt{\frac{\alpha_\mathrm{c}E}{heV_\mathrm{RF}\cos\phi_s}}\left(\frac{\sigma_\mathrm{E}}{E}\right) \tag{1.41}$$

1.4.4 Summary of synchrotron radiation integrals and related parameters

To summarise the discussions in the previous sections, the beam parameters in lepton storage rings are modified by the emission of synchrotron radiation. Assuming an uncoupled machine they can be expressed using the so-called synchrotron radiation integrals [27]

$$\begin{aligned}
\mathcal{I}_1 &= \oint \frac{D(s)}{\rho}\,\mathrm{d}s \\
\mathcal{I}_2 &= \oint \frac{1}{\rho^2}\,\mathrm{d}s \\
\mathcal{I}_3 &= \oint \frac{1}{|\rho^3|}\,\mathrm{d}s \\
\mathcal{I}_{4u} &= \oint \frac{D_u}{\rho_u}\left(\frac{1}{\rho_u^2} + 2k_1\right)\mathrm{d}s \\
\mathcal{I}_{5u} &= \oint \frac{1}{|\rho_u|^3}\mathcal{H}_u\,\mathrm{d}s
\end{aligned}$$

where u either stands for the transverse coordinate x or y and the $\mathcal{H}$ function is given by

$$\mathcal{H}_u(s) = \beta_u D_u'^2 + 2\alpha_u D_u D_u' + \gamma_u D_u^2.$$

The first synchrotron radiation integral is related to the momentum compaction factor

$$\alpha_\mathrm{c} = \frac{\mathcal{I}_1}{C}.$$

C is the machine circumference. The second integral determines the energy loss per turn

$$U_0 = \frac{C_\gamma}{2\pi}E^4\mathcal{I}_2$$

and in combination with the third synchrotron radiation integral the equilibrium energy spread

$$\frac{\sigma_\mathrm{E}^2}{E^2} = C_\mathrm{q}\gamma^2\frac{\mathcal{I}_3}{J_s\mathcal{I}_2}.$$

For electrons or positrons the constants C_q and C_γ have the values $C_\mathrm{q} = 3.832 \times 10^{-13}\,\mathrm{m}$ and $C_\gamma = 8.8460 \times 10^{-5}\,\frac{\mathrm{m}}{\mathrm{GeV}^3}$. The damping partition numbers

$$J_x = 1 - \frac{\mathcal{I}_{4x}}{\mathcal{I}_2}, \quad J_y = 1 - \frac{\mathcal{I}_{4y}}{\mathcal{I}_2} \quad \text{and} \quad J_s = 2 + \frac{\mathcal{I}_{4x} + \mathcal{I}_{4y}}{\mathcal{I}_2}$$

can be expressed using the second and forth integral and finally the equilibrium emittance is defined by the ratio of the fifth and second integral

$$\epsilon_u = C_\mathrm{q} \frac{\gamma^2}{J_u} \frac{\mathcal{I}_{5u}}{\mathcal{I}_2}.$$

1.5 Parameters and effects relevant in collider storage rings

1.5.1 Luminosity

The production rate of a certain physics event is determined by the product of the event's cross section Σ_p and the collider's *luminosity* $\mathcal{L}$:

$$\frac{\mathrm{d}N_\mathrm{p}}{\mathrm{d}t} = \mathcal{L}\ \Sigma_\mathrm{p} \tag{1.42}$$

The cross section is a measure of the probability for the occurrence of the event. The luminosity basically describes the density of the particle bunches at the collision point times the number of bunches and repetition rate. Since the cross section is constant, the luminosity has to be increased for a higher production rate. Especially for the observation of rare decay events with very small cross sections high luminosity is required to gain sufficient amount of statistics.

For head-on collision and Gaussian shaped bunches the luminosity is

$$\mathcal{L} = \frac{N_1 N_2 f n_\mathrm{b}}{4\pi \sigma_x^* \sigma_y^*}, \tag{1.43}$$

where N_1 and N_2 are the numbers of particles in the colliding bunches, f is the revolution frequency and n_b is the number of bunches per beam. σ_x^* and σ_y^* are the transverse beam sizes of the colliding bunches at the interaction point. To obtain highest luminosity both the number of bunches and the bunch population must be as high as possible. To further increase the luminosity the beam size at the collision point must be reduced either by smaller beam emittances or stronger focussing of the beam in the interaction region.

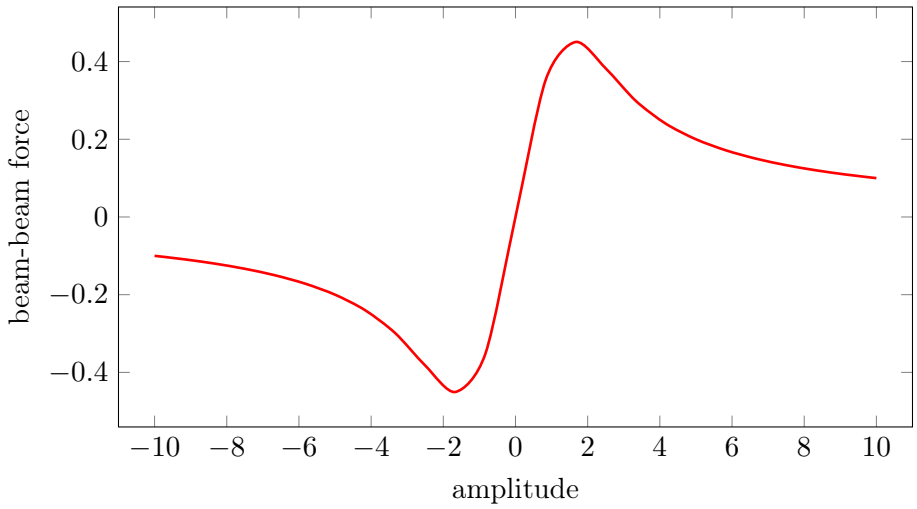

Figure 1.7: Beam-beam force for round beams ($\sigma_x = \sigma_y$) in arbitrary units according to [20]. The transverse amplitude is given in units of r.m.s. beam size.

1.5.2 Beam-beam tune shift

One of the most important performance limits of high intensity particle colliders is created by the interaction of the two particle beams at the collision point [20]. During a bunch crossing only a few particles of the bunch collide. Most particles cross the opposite bunch only affected by its electric field. The non-colliding particles experience a kick by the Lorentz force, which is repellant if the bunches have the same charge and attractive for opposite charge.

The electromagnetic beam-beam force is very non-linear [20] as shown in Fig. 1.7, which means the strength of this so-called *beam-beam effect* highly depends on the transverse particle amplitude. Considering a single particle deflected by a Gaussian charge distribution and small orbit offsets the beam-beam effect can be linearized and is then equivalent to an additional quadrupole term, which creates a tune shift. The magnitude of the tune shift depends on the phase advance between the interaction points and the so-called *beam-beam parameter*

$$\xi_u = \frac{N r_e \beta_u^*}{2\pi\gamma\sigma_u^*(\sigma_x^* + \sigma_y^*)}, \tag{1.44}$$

where β_u^* is the beta function at the interaction point. The beam-beam tune shift increases for large bunch population N and small beam sizes σ. At high energies with large Lorentz factor γ the tune shift becomes less relevant. Although it does not describe the non-linear nature of the beam-beam effect, the beam-beam parameter is often used as a scaling factor to quantify the strength of the beam-beam interaction. A more detailed model including the highly nonlinear effects for large orbit offsets and the effect of crossing angles is presented in [30].

As mentioned before, the beam-beam effect is one of the most important performance limits of a collider. It is aimed to be as small as possible to fit the working point including beam-beam tune shift in a resonance-free area in the tune diagram.

1.5.3 Beamstrahlung

At high particle energies the bending of the particle trajectories during beam-beam interaction at the collision point creates photon emission similar to synchrotron radiation, called *beamstrahlung*. The effects are described with the beamstrahlung parameter [26]

$$\Upsilon \approx \frac{5}{6} \frac{r_e^2 \gamma N}{\alpha_f \sigma_s (\sigma_x + \sigma_y)}, \tag{1.45}$$

where N is the number of particles per bunch and α_f is the fine structure constant. While $\Upsilon \ll 1$ corresponds to the classical limit, beamstrahlung effects occur for $\Upsilon \gg 1$. According to Eq. (1.45) a short bunch length, high bunch population and high energy enhance beamstrahlung. For high beam energies beamstrahlung is expected to be a luminosity limit in next-generation electron-positron colliders.

1.6 The Optics Code MAD-X

The *Methodical Accelerator Design (MAD)* scripting language [31] is a tool developed at CERN for lattice design and beam optics calculations of both circular accelerators and transfer lines. The current version MAD-X was first released in 2002 and is permanently maintained by the MAD group. MAD is accessible freely. The user's guide [32] and a detailed description of the physics model can be found on the webpage [31].

MAD-X was used for the complete lattice design and all beam optics calculations done in the framework of this thesis. It offers easy element definitions to set up lattice and geometry of the machine based on the Frenet-Serret Coordinate System introduced earlier in this chapter. After finding the closed orbit MAD-X calculates the global machine parameters like tunes and chromaticity, but also the optics functions such as beta functions and dispersion. MAD-X also calculates the synchrotron radiation integrals and the equilibrium beam parameters. Matching routines provide numerical optimisation tools to adjust magnet strengths in order to change the optics. The user can choose from a variety of methods and define his own constraints.

CHAPTER 2

Layout and global characteristics of the FCC-ee Lattice

This chapter presents the layouts that were considered during the studies for this thesis, and the lattice sections used to assemble them. Moreover, the machine parameters are compared for two different lattice designs of the arcs: on the one hand a FODO cell structure, which is the usual choice for high-energy particle colliders, and on the other hand a Double-Bend-Achromat based arc design, usually used for synchrotron radiation light sources. The last section focuses on constraints and requirements to deal with the large amount of synchrotron radiation power.

2.1 Layouts used for the studies

The studies presented in the context of this thesis are based on two different layouts for the FCC-ee collider. For general studies of beam dynamics a symmetric 12-fold layout was considered, ideal for lepton storage ring requirements dominated by synchrotron radiation. At a later stage the FCC baseline layout with a racetrack-like shape was implemented, which was developed in cooperation with the civil-engineering group following the boundary conditions of the Geneva valley and the requirements of the hadron machine.

2.1.1 12-fold Layout

The design of high energy lepton storage rings is constrained by the effects of synchrotron radiation. The constant energy loss in the dispersive arc sections makes the beam drift to the centre of the machine until it reaches the next straight section with an RF installation, where it gets re-accelerated and pushed outside again as soon as it enters the next dispersive arc. This orbit variation in addition to the regular orbit swing is known as the *sawtooth*

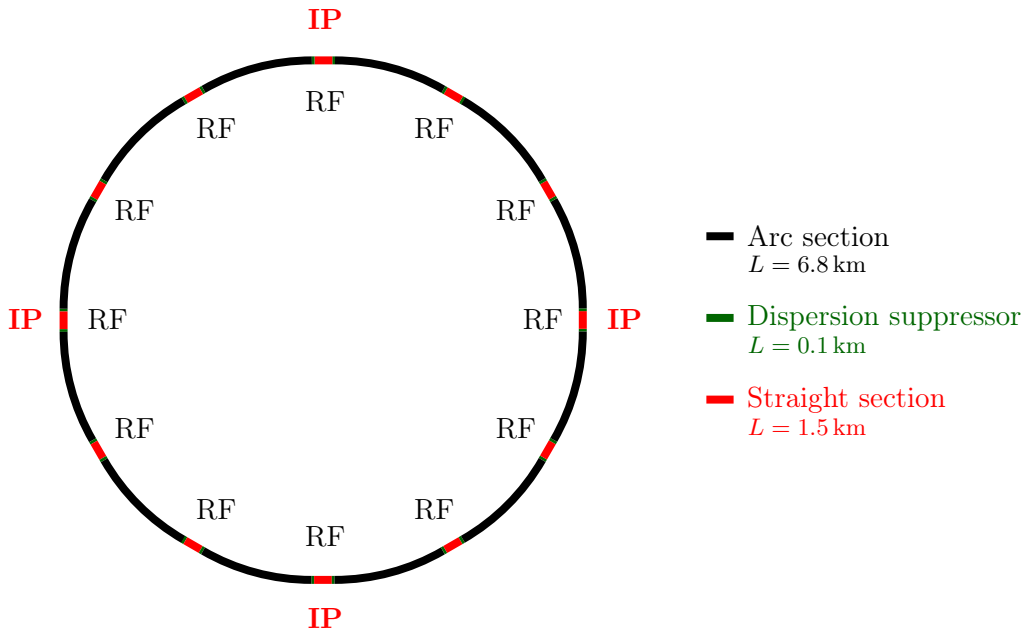

Figure 2.1: FCC-ee layout with a 12-fold symmetry used for general studies of a 100 km lepton collider ring.

effect and causes optics distortions. Since the beam does not pass the sextupole magnets in their centre any more, it experiences an additional quadrupolar term by the feed-down effect. In order to keep this perturbation on a reasonable level, many dispersion free straight sections with RF cavities should be evenly distributed around the ring.

The layout used for general studies of FCC-ee shown in Fig. 2.1 provides twelve straight sections with a length of 1.5 km each. The arcs in-between have a length of 6.8 km leading to an overall circumference of approximately 100 km (98.4 km). Alternatively, an 80 km version has been studied as well. The arc design includes dispersion suppressors at the beginning and at the end to provide a smooth transition to the dispersion-free straight sections. Additional dispersion suppressors in the middle of the arcs allow an easy installation of further RF sections, if required. Since this was not the case, the additional dispersion suppressors were removed for the studies of a global chromaticity correction scheme. In four of the straight sections mini-beta insertions are included producing small beam sizes for the experiments. These insertions are located in symmetric positions as well, to equally distribute the impact of the beam-beam effect and the chromaticity created by the final focus quadrupoles. Insertions for injection, beam dump and collimation have not yet been included in this very first design. To gain understanding of the very complex beam dynamics it is desired to keep the lattice as regular and symmetric as possible.

For the accommodation of many thousands of bunches [16, 33] two separate vacuum chambers are required. A common beam pipe, as it was realised for LEP, would limit

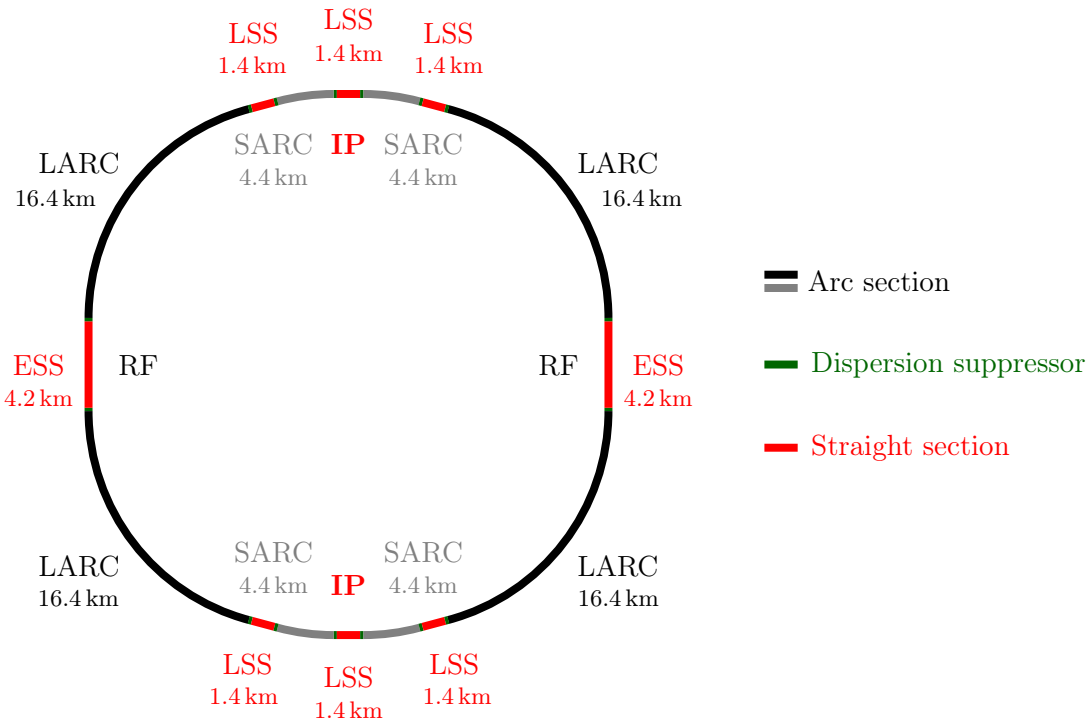

Figure 2.2: Second layout for FCC-ee used in the context of this thesis. The layout has a 100 km circumference and follows the official FCC baseline [16]. The Long Straight Sections (LSS) have a length of 1.4 km and the Extended Straight Sections (ESS) have a length of 4.2 km. Both types of arcs have the same bending radius, but different length: the Short Arcs (SARC) in-between two Long Straight Sections are 4.4 km long, while the Long Arcs (LARC) have length of 16.4 km.

the number of bunches to a few hundreds [16]. The two vacuum chambers will be placed side-by-side to conserve polarization and avoid vertical dispersion. However, in this early design stage only one single ring is implemented. This lattice will be referred to as the *12-fold Layout*.

2.1.2 Racetrack Layout

The second layout implemented within the context of this thesis follows the current machine baseline [16], which is compatible with the requirements of the FCC hadron collider summarized in [5] and [34]. Apart from technological aspects, geological factors of the Geneva basin were also considered.

As illustrated in Fig. 2.2, the layout comprises six straight sections with the length of 1.4 km (Long Straight Section, LSS) for two experimental insertions and injection sections. They are clustered in groups of three and connected by so-called Short Arcs (SARC) with the length of 4.4 km. Two additional straight sections (Extended Straight Section, ESS),

Table 2.1: Length of the lattice sections in the Racetrack Layout and the number of FODO cells they consist of.

Section	length (km)	FODO cells
Short Arc (SARC)	4.4	88
Long Arc (LARC)	16.4	328
Long Straight Section (LSS)	1.4	28
Extended Straight Section (ESS)	4.2	84

Table 2.2: Number of dipole, quadrupole and sextupole magnets in the lattices with 12-fold and Racetrack Layout.

	12-fold Layout	Racetrack Layout
# of dipole magnets	6528	6656
# of quadrupole magnets	4004	4008
# of sextupole magnets	3168/6336	6528

each 4.2 km long, will house the RF system. In spite of the above mentioned requirement of well-distributed RF sections, the RF cavities are concentrated in only two points to reduce the cost of the RF system. Arrangements to keep the sawtooth orbit on a reasonable level were investigated and will be presented in Sec. 2.4.2. The so-called Long Arcs (LARC) connecting the Long Straight Sections with the Extended Straight Sections have a length of 16.4 km.

This Layout will be called the *Racetrack Layout* in the following sections. The length of arcs and straight sections and the number of FODO cells they contain are summarised in Tab. 2.1. Tab. 2.2 presents the number of dipole quadrupole and sextupole magnets in the lattices with both 12-fold and Racetrack Layout.

2.2 Lattice modules in FCC-ee

The earlier presented layouts consist of so-called *arcs*, where the beam is bent in the horizontal plane, and *straight sections*. In-between arcs and straight sections special insertions, so-called *matching sections*, are required to guarantee a smooth transition of the optical functions. In both cases the lattice has a periodic sub-structure. The layout of the cell, on which the periodic lattice is based, has to be designed very carefully, because it defines the global parameters of the machine, such as tunes, chromaticity and emittance. The considerations taken into account for the basic cell design are specified in the following section.

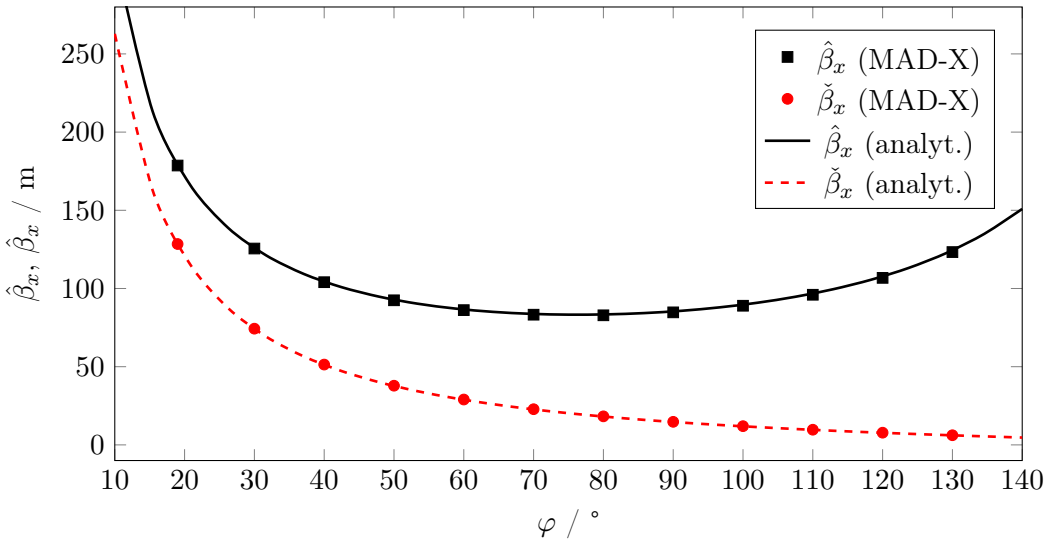

Figure 2.3: Maximum and minimum values of the beta function in an FCC-ee FODO cell for different phase advance per cell. The values calculated with MAD-X are in good agreement with the analytical expectation from Eq. (2.1).

2.2.1 FODO cells

Arcs and straight sections of the lattices implemented in the context of this thesis are based on a *FODO cell design*, which consists of equidistant quadrupoles of altering polarity. This setup provides the most space for dipole magnets and so leads to the smallest synchrotron radiation losses for a given machine size and particle energy. In addition, FODO cells are a preferred lattice arrangement for beam transport because their optical functions can be calculated easily in an analytical way.

Beta functions: The minimum and maximum values of the beta functions in the quadrupoles $\check{\beta}$ and $\hat{\beta}$ can be derived from the transfer matrix of a FODO cell, which is for example derived in [21] or [35]. They only depend on the cell length L and the FODO cell phase advance φ [35, 36]:

$$\hat{\beta} = L\,\frac{1+\sin(\varphi/2)}{\sin\varphi} \quad \text{and} \quad \check{\beta} = L\,\frac{1-\sin(\varphi/2)}{\sin\varphi} \tag{2.1}$$

For a given phase advance both $\check{\beta}$ and $\hat{\beta}$ are proportional to the cell length. The dependency on the phase advance is illustrated in Fig. 2.3, which shows both minimum and maximum values of the beta function for different phase advances from 20° to 130° in both planes. While $\check{\beta}$ decreases with rising values of the phase advance, $\hat{\beta}$ reaches a minimum at about 76°. As a consequence, for a given cell length a minimum beam size is obtained for a phase advance of 76° in both planes.

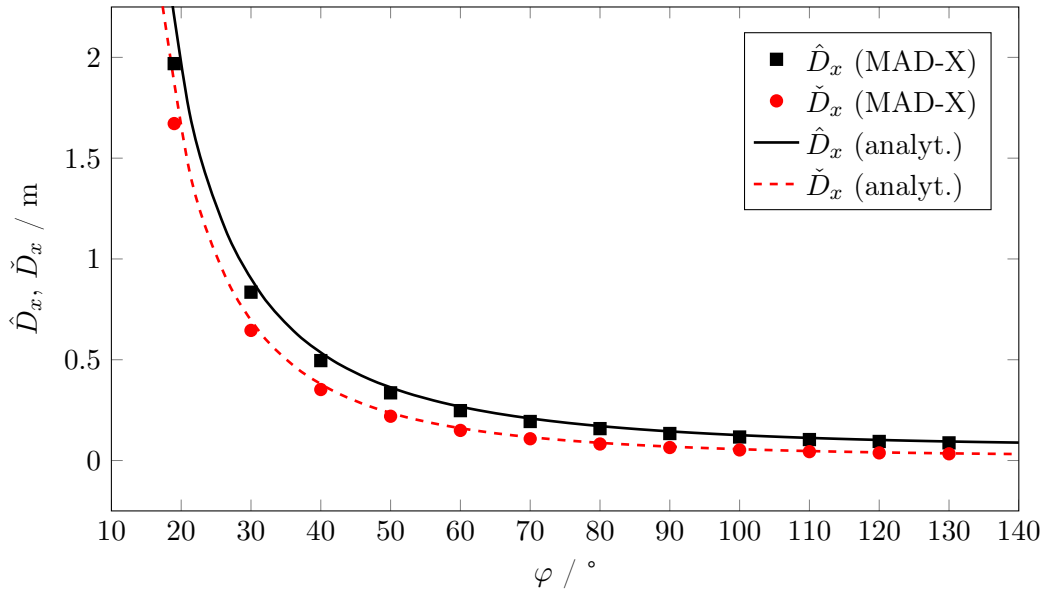

Figure 2.4: Maximum and minimum horizontal dispersion of an FCC-ee FODO cell for different FODO cell phase advance.

Horizontal dispersion: A transfer matrix can also be formed for the horizontal dispersion function, which allows the derivation of the minimum and maximum values $\check{D}_x$ and $\hat{D}_x$ in the FODO cell [36]:

$$\hat{D} = \frac{L^2}{\rho}\frac{\left(1+\frac{1}{2}\sin\left(\varphi/2\right)\right)}{4\sin^2\left(\varphi/2\right)} \quad \text{and} \quad \check{D} = \frac{L^2}{\rho}\frac{\left(1-\frac{1}{2}\sin\left(\varphi/2\right)\right)}{4\sin^2\left(\varphi/2\right)} \tag{2.2}$$

For a given bending radius ρ, which is determined by the beam energy and the acceptable amount of synchrotron radiation, $\hat{D}_x$ and $\check{D}_x$ can be tuned by modifying the cell length L or the phase advance φ. Larger dispersion is obtained by larger cell length or, as shown in Fig. 2.4, by smaller phase advance. In a longer cell the particles have more time to drift apart before they get focussed again and smaller phase advance is the direct consequence of weaker focussing. During the design process the tuning of the horizontal dispersion in the FODO cell is the key parameter to set the beam emittance, because via the $\mathcal{H}$ function in the fifth synchrotron radiation integral the dispersion defines the strength of the quantum excitation and thus the equilibrium beam emittance (see Sec. 1.4.3).

Beam emittance: As introduced in Sec. 1.4.3 the equilibrium beam emittance in an electron storage ring is given by

$$\epsilon_x = C_\mathrm{q}\frac{\gamma^2}{J_x}\frac{\mathcal{I}_{5x}}{\mathcal{I}_2}. \tag{2.3}$$

The synchrotron radiation integrals $\mathcal{I}_2$ and $\mathcal{I}_5$ can be approximated using the mean value of the $\mathcal{H}$ function, the bending angle θ, the bending radius ρ and length of the bending

magnet l_B (for details see [37]):

$$\epsilon_x = \frac{C_\mathrm{q}}{J_x}\gamma^2\theta^3 F \tag{2.4}$$

The factor $F = \frac{\rho^2}{l_\mathrm{B}^3}\langle\mathcal{H}\rangle$ describes the influence of a certain lattice design on the emittance and can in case of a FODO lattice be expressed as

$$F_\mathrm{FODO} = \frac{1}{2\sin\varphi}\frac{5+3\cos\varphi}{1-\cos\varphi}\frac{L}{2l_\mathrm{B}}. \tag{2.5}$$

If multiple dipole magnets are installed between two quadrupoles, the bending angle θ and the dipole length l_B correspond to the sum of the values of all bending magnets in a half cell.

Although expressed in a different way, this method of tuning the emittance is equivalent to the previously described matching of the dispersion, since the same parameters are used: cell length, bending angle and phase advance. However, Eq. (2.4) and Eq. (2.5) allow to estimate the expected equilibrium emittance from the parameters of one single FODO cell without establishing the whole lattice and are therefore a useful tool for the cell design.

In summary, the two steps to the design of a FODO cell are

1. choosing a phase advance, which is close to minimum beam size and suitable for an efficient chromaticity correction scheme (details will be discussed in Sec. 4.3), and
2. defining the cell length such, that the obtained dispersion leads to the required beam emittance.

The FCC-ee FODO cells

The design of the FODO cell for FCC-ee was realised according to the two steps described above. In agreement with good experience at LEP the phase advances $\varphi_x = 90°$ in the horizontal plane and $\varphi_y = 60°$ in the vertical plane were chosen as a starting point [38]. With this choice the factor from Eq. (2.5) becomes

$$F_\mathrm{FODO} = 2.5\ \frac{L}{l_\mathrm{B}}. \tag{2.6}$$

The choice of the cell length involved following considerations:

1. The FCC-ee lattice has to be optimised for operation at four different beam energies and the design parameter list from 2014 (Tab. A1 in the Appendix) requires different design values for the emittance in the range of $\epsilon_x = 2.0\,\mathrm{nm\,rad}$ at 175 GeV to 29.2 nm rad at 45 GeV beam energy. The basic cell was designed to obtain the smallest emittance at the maximum energy $E = 175\,\mathrm{GeV}$. As it will be shown in Sec. 3.3, it is easier to increase the emittance afterwards again than to decrease it, but even

more importantly, the lattice suffers from the strongest synchrotron radiation effects at this energy, which requires most optimisation for highest performance.

2. To compensate the impact of lattice imperfections like misalignments, field errors or coupling and emittance blow-up due to the beam-beam effect or beamstrahlung, it was decided to leave a factor of two margin between the emittance of the ideal lattice and the design value.
3. About 25 % of the overall circumference, in this case 100 km, is reserved for straight sections to accommodate injection, extraction and RF systems. It follows that the bending radius is given by $\rho = 75\,\mathrm{km}/2\pi$. Assuming the length of a bending magnet to be $l_\mathrm{B} = 21\,\mathrm{m}$ the bending angle is $\theta \approx 1.76\,\mathrm{mrad}$.

These considerations lead to a cell length of $L = 50\,\mathrm{m}$. The equilibrium emittance for 175 GeV beam energy according to Eq. (2.4) and Eq. (2.6) is then $\epsilon_x = 1.04\,\mathrm{nm\,rad}$, which was verified with a MAD-X calculation ($\epsilon_x = 1.00\,\mathrm{nm\,rad}$). Taking the factor two margin into account this value is conform to the requirement of $\epsilon_x = 2.00\,\mathrm{nm\,rad}$.

The studies performed in the context of this thesis made use of two different FODO cell designs, which have the same cell length, but differ slightly in the arrangement of the elements.

Asymmetric arc cell: The first design foresees a focusing and a defocusing quadrupole with the length of 1.5 m each, which divide the cell into two parts of equal length. After each quadrupole a sextupole with the length of 0.5 m, a beam position monitor and a small dipole magnet for orbit correction in the respective plane are placed. The space between the quadrupoles is occupied by four dipole magnets with the length of 10.5 m. Their maximum length is the result of careful simulations of the synchrotron light fan and the requirements for the absorber scheme to protect the machine components [39]. The current FCC-ee FODO cell layout already includes space for absorbers, flanges and bellows [40].

Fig. 2.5 shows the lattice functions of this FODO cell layout. The sketch of the lattice elements above the plot illustrates the asymmetric arrangement of the sextupoles with respect to the quadrupole magnets. The beta function of the horizontal plane oscillates between $\hat{\beta}_x = 77.0\,\mathrm{m}$ and $\check{\beta}_x = 16.2\,\mathrm{m}$, where the maximum value is reached in the focussing quadrupole and the minimum value in the defocussing quadrupole. In the vertical plane the beta functions are slightly larger because of the smaller phase advance, as expected from Eq. (2.1). The maximum value is $\hat{\beta}_y = 96.5\,\mathrm{m}$ and the minimum value is $\check{\beta}_x = 26.0\,\mathrm{m}$. As a consequence of the large machine circumference and the large bending radius the maximum value of the horizontal dispersion function is only 12.7 cm. This is one order of magnitude smaller compared to the last high-energy lepton collider LEP, which had a horizontal dispersion in the arcs of 2.2 m [25].

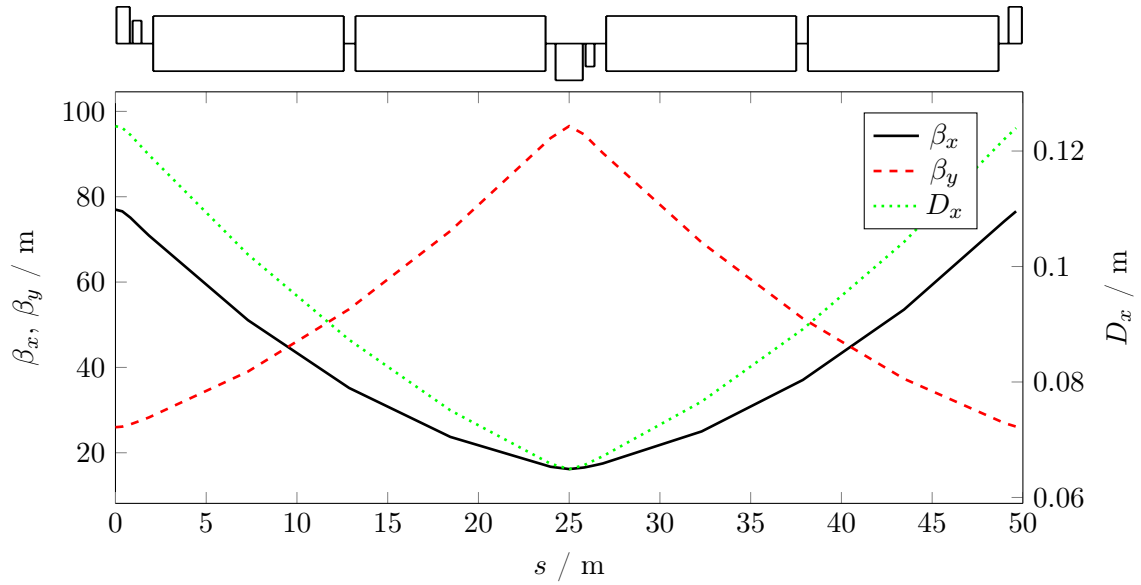

Figure 2.5: Beta functions and horizontal dispersion function in the asymmetric FODO cell designed for highest dipole filling factor in FCC-ee. Above, the elements of the lattice are depicted: the large blocks are the dipole magnets and the rectangles above and below the centre line show the position of the quadrupole magnets. The smaller rectangles next to them are the sextupoles.

This asymmetric cell layout is designed to obtain the highest possible dipole filling factor and was used in all calculations regarding the emittance tuning study.

Symmetric arc cell: During the optimisation of chromaticity correction schemes in the arc sections it became important to design a completely symmetric FODO cell to allow precise adjustment of phase advances and to place the effective correction provided by the sextupoles in the centre of the quadrupoles, which are considered as the source of the chromatic aberrations. Therefore sextupoles were installed at both sides of the quadrupoles. The previous design included only one sextupole per quadrupole. To create space for the additional sextupoles the length of the dipoles was reduced to 10.0 m. Since the chromaticity is much larger in the vertical plane, the second design foresees the defocusing quadrupole at the beginning of the cell. This allows to perfectly adjust the phase advance from the interaction region to the sextupoles correcting the vertical chromaticity.

The optical functions shown in Fig. 2.6 are the same as in the asymmetric layout. The FODO cell parameters of both designs are compared to the ones of LEP in Tab. 2.3.

Dipole filling factor: The design of a high-energy lepton collider ring aims for the highest integrated dipole field in order to minimise the amount of synchrotron radiation power. To compare different layouts the so-called *dipole filling factor* is defined, which describes the

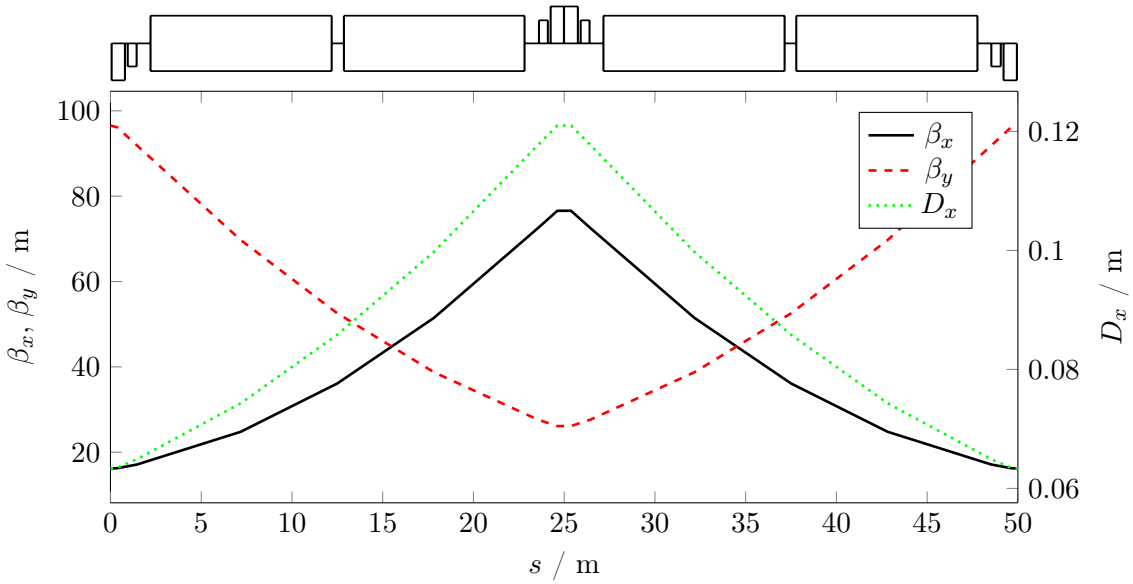

Figure 2.6: Beta functions and horizontal dispersion function in the symmetric FODO cell layout optimised for the chromaticity correction studies.

Table 2.3: Arc FODO cell parameters of both FCC designs compared to the LEP FODO cell according to the LEP Design Report [25].

	Asymmetric FODO 12-fold	Symmetric FODO 12-fold/Racetrack	LEP
Cell length/m	50	50	79.0
Number of dipoles per half-cell	2	2	6
Dipole magnetic length per cell/m	42	40	70.02
Dipole filling factor (FODO cell)	84 %	80 %	89 %
Bending radius in the dipoles/m	10749	10237/10491	3096
Bending angle per half-cell/mrad	1.95373	1.95373/1.90630	11.30640
Horizontal phase advance/2π	0.2500	0.2500	0.1666
Vertical phase advance/2π	0.1666	0.1666	0.1666
Max. hor. beta function/m	76.98	77.00/76.98	135
Max. vert. beta function/m	96.55	96.55/96.55	135
Max. hor. dispersion function/m	0.124	0.124/0.121	2.219

ratio between the integrated dipole length and the length of the design orbit length in the machine. To achieve the theoretical maximum achievable filling factor the straight sections are reduced to a minimum and all space of the FODO cells in the arc, which is not occupied by quadrupoles and sextupoles, is filled with bending magnets. In the case of FCC-ee a dipole filling factor of 94 % could be reached in the arc lattice. However, space for the magnet coils, absorbers, flanges and beam instrumentation must be allocated. For reasons of technical feasibility and maintenance a minimum distance of 15 cm between quadrupoles and sextupoles and 55 cm between quadrupoles and bending magnets is reserved. Between two bending magnets and between the sextupoles and the bending magnets a minimum gap of 65 cm is required [40]. Taking these boundary conditions into account, the dipole filling factor can be optimised as a function of the number of bending magnets per cell and their length. A value as high as 84 % could be achieved for the asymmetric FODO cell. For the symmetric FODO cell the dipole filling factor drops to 80 % because of the shorter bending magnets. In a later stage the quadrupole length and the drift space reserved for beam instrumentation will be optimised again to further increase the dipole filling factor.

FODO cells for the straight sections: The FODO cells in the straight sections follow the design of the FODO cells of the arc lattice. The length is 50 m as well and the quadrupoles are located at the same position. However, since the horizontal dispersion is zero in the straight sections, no sextupoles are installed and the bending magnets are replaced by the RF system. In the 12-fold Layout one single RF cavity with the length of 1 m is installed in the middle of every half-cell. In the Racetrack Layout the cavities were combined to five-cell modules to minimise the length of the RF system. The lattice functions of such a FODO cell are shown in Fig. 2.7. For the straight sections without RF installation FODO cells without RF cavities were designed.

2.2.2 Dispersion suppressor

In the arc lattice the horizontal dispersion function oscillates with the same phase as the horizontal beta function (see Fig. 2.5 and Fig. 2.6). In the straight sections with RF installation, however, the dispersion function has to disappear, because otherwise the RF cavities would create coupling between the transverse planes and the longitudinal plane, which leads to additional resonances in the tune diagram. Moreover, non-vanishing dispersion at the interaction point of a collider storage ring would dilute the luminosity of the machine [36]. Therefore special insertions between regular arc lattice and straight FODO cells have to be installed to suppress dispersion and guarantee a smooth transition of the lattice functions. Depending on the arc layout different arrangements of magnets can be chosen to design such a so-called *dispersion suppressor*. During the studies of the lattice for FCC-ee the following three dispersion suppressor schemes were used.

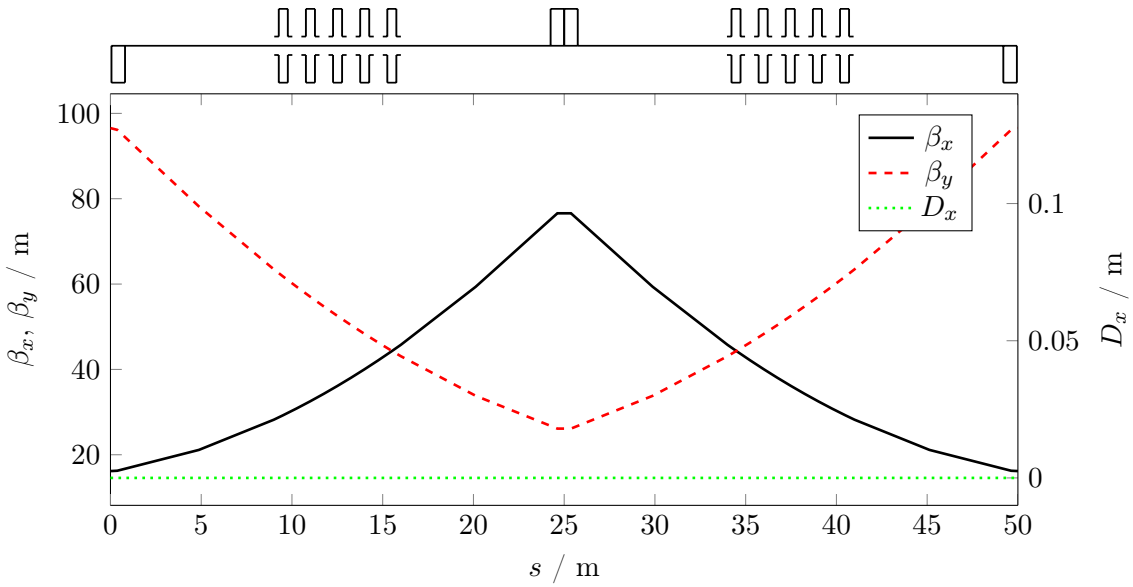

Figure 2.7: Beta functions and horizontal dispersion function of a FODO cell in the straight sections of the Racetrack Layout. The sextupoles were removed and the bending magnets were replaced by a five-cell RF cavity module.

Half-bend dispersion suppressor: An elegant way to match the dispersion to zero is to install a certain number of FODO cells at the end of the arcs, in which the dipoles have half of the bending strength. The value of the dispersion coming out of the arc is then twice of the local matched value. The dispersion function begins to oscillate and reaches zero at half a wavelength. Depending on the horizontal FODO cell phase advance a different number of half-bend cells are needed. If π/φ_x is an integer, π/φ_x half-bend cells are necessary to suppress the dispersion. This means in case of FCC-ee with a phase advance of 90° ($\varphi_x = \pi/2$) such a dispersion suppressor consists of two half-bend cells.

Since the beta functions are not affected by the half-field dipoles[1] the aperture requirements stay the same. Moreover, the optics do not need to be re-matched and no additional power supplies are required for free quadrupoles. However, special dipole magnets with half of the field strength are needed. This has a strong impact on the geometry of the ring, which is why such a concept needs to be included to the design at an early stage [36].

This kind of dispersion suppressors were chosen for the standard FCC-ee lattice for 175 GeV beam energy. The length of each dispersion suppressor is 100 m as two half-bend cells are needed. As shown in Fig. 2.8, the dispersion suppressor provides a smooth transition from the regular arc optics to the optics of the straight section, where the dispersion vanishes.

[1] The weak focussing effect of the dipoles is neglectable because of the large bending radius.

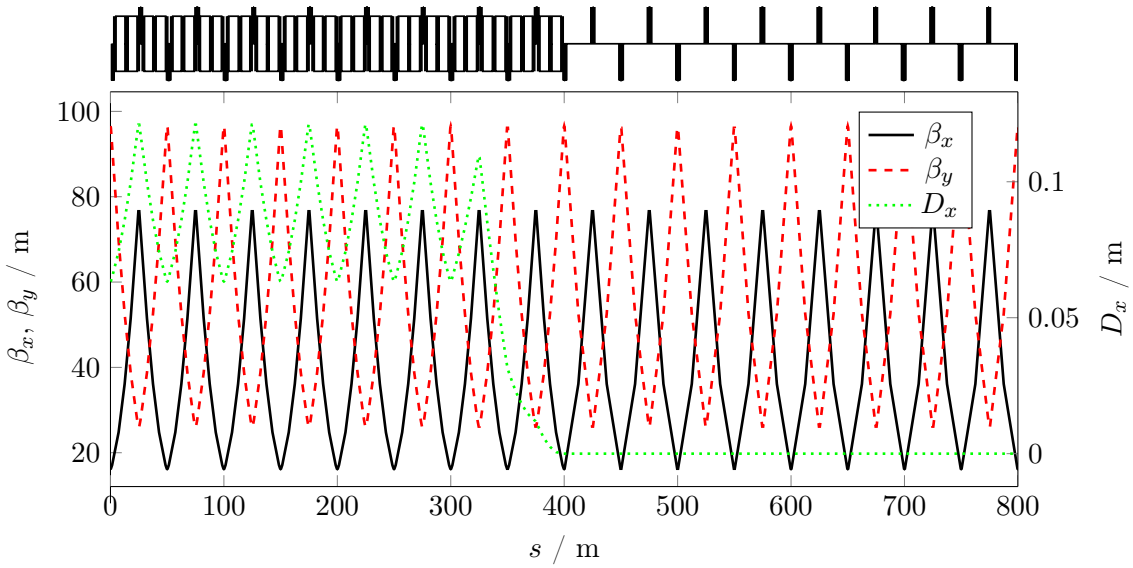

Figure 2.8: Transition of beta functions and horizontal dispersion function from the regular arc optics to the optics of the straight section. The two half-bend cells at the end of the arc suppress the dispersion without affecting the beta functions.

Two-cell dispersion suppressor with diverse dipole fields: The half-bend dispersion suppressor scheme only works for certain values of the phase advance. For calculations of the machine parameters in which the phase advance was modified a different dispersion suppressor scheme was chosen. For any FODO cell phase advance φ_x the dispersion can be suppressed within two cells, if following conditions are fulfilled [26]:

$$\theta_{\mathrm{B},1} = \frac{\theta_{\mathrm{B}}}{4\sin^2(\varphi_x/2)}\ , \quad \theta_{\mathrm{B},2} = \theta_{\mathrm{B}}\left(1 - \frac{1}{4\sin^2(\varphi_x/2)}\right) \tag{2.7}$$

θ_{B} is the nominal bending strength of the regular arc dipoles, $\theta_{\mathrm{B},1}$ is the strength of the dipole in the FODO cell next to the arc cells and $\theta_{\mathrm{B},2}$ is the bending strength of the FODO cell next to the straight section. For $\varphi_x \leq \pi/3$ reversed dipoles are used in one cell of the dispersion suppressor [26].

Again beta functions and phase advance are not affected by this way of dispersion suppression. The change of the bending angles for different phase advances, however, implies a modification of the geometry. For simulations this is not a problem, but for a real machine the change of phase advance would imply major reconstruction work.

Quadrupole based dispersion suppressor: The dispersion can also be suppressed using only quadrupole lenses. Since the suppression of the dispersion and its derivative now affects the optics, the Twiss parameters beta and alpha need to be re-matched. So in total six individually powered quadrupoles are needed.

Quadrupole based dispersion suppressors work for any FODO cell phase advance and leave the geometry unchanged. They also allow different values of the beta function in the arc and in the straight sections. However, the individual strengths of the quadrupoles require separate power supplies, which might be expensive. Also, depending on number and distance of the quadrupoles, the beta function might reach high values that require a modification of the vacuum chamber.

In the context of this thesis the quadrupole based dispersion suppressor scheme was used during the emittance studies, where the length of the FODO cells was modified without changing the geometry.

2.2.3 Matching section

Matching sections consist of regular FODO cells with individually powered quadrupoles that allow to match the optics functions from one section to the other. At the beginning and the end of each straight section in FCC-ee a matching section is installed consisting of four straight FODO cells. Six free quadrupoles provide sufficient degrees of freedom to adapt the optics of the arcs to the straight FODO cells. The matching sections, for example, become important when the phase advance of the straight FODO cells is modified to set the working point. The modified phase advance in the straight sections leads to a different periodic solution and hence different beta functions. Without the matching sections in-between, the modified phase advance in the straight sections would create a beta beat in the whole machine.

2.2.4 Mini-beta insertion

In collider storage rings very small beam sizes are required at the interaction points to obtain a high luminosity for the experiments. Special *mini-beta insertions* are included in the lattice, that on the one hand provide sufficient drift space to house the experiment and on the other hand focus the beta function to very small values in the centimeter or even millimeter range. Apart from the drift space through the detector, mini-beta insertions consist of a final focus quadrupole doublet[2] and a certain number of additional quadrupoles to match the Twiss parameters to the values of the regular lattice.

The interaction point is placed at the beam waist of the drift space through the detector. This means, the Twiss parameter α is zero in both planes and the beta function grows quadratically with the distance s from the interaction point:

$$\beta = \beta^* + \frac{s^2}{\beta^*}, \tag{2.8}$$

[2] For flat beams like in FCC-ee, where $\sigma_x \gg \sigma_y$, a quadrupole doublet is used as a final focus system, while for round beams, like in LHC, a quadrupole triplet is used.

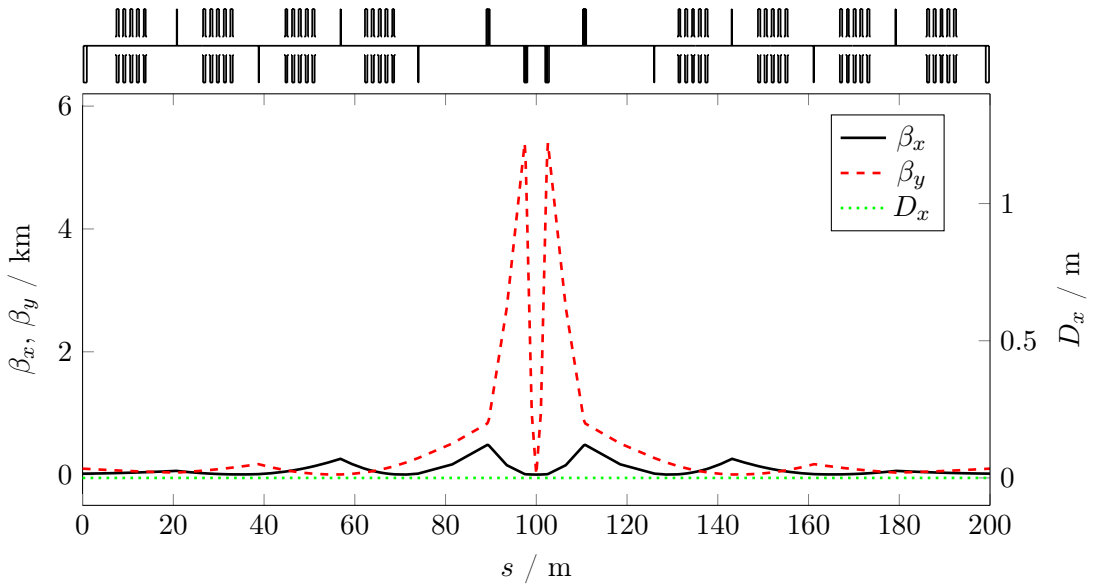

Figure 2.9: Beta functions and horizontal dispersion function of the mini-beta insertion used in the context of this thesis. In the shown case, the vertical beta function at the interaction point is $\beta_y^* = 1\,\text{mm}$.

where β^* refers to the beta function at the interaction point. As a consequence of Liouville's Theorem, the divergence of the beam increases for small values of β^*. The distance from the interaction point to the first quadrupole L^* should therefore be as short as possible to keep reasonable beam sizes. After all, the minimum spot size is limited by the value of L^* and the technical feasibility of the quadrupole gradient for a given aperture. If the aperture cannot be further increased, the beam emittance must be reduced to obtain smaller beam sizes and so push the luminosity to higher values.

As a consequence of the radiation damping, the vertical beam size in lepton storage rings is much smaller than the horizontal beam size. Depending on the level of alignment precision and coupling correction it is the the percent or even per mille range. The first quadrupole in the final doublet therefore focusses the beam in the vertical plane, where the beta functions grow faster. Still, the beam can reach large dimensions, which puts constraints on the field quality and the alignment precision of the final doublet. Furthermore, the large beta function in the final doublet quadrupoles together with the very high quadrupole gradient drive the chromaticity of the lattice to very high values. The strong non-linear fields required for the correction are one of the strongest limitations to the dynamic aperture of the machine.

The design values for the interaction regions of FCC are summarized in Tab. 2.4. Fig. 2.9 shows the optical functions of the mini-beta insertion used in the context of this thesis with an over-all length of 200 m. Besides the final doublet, four quadrupoles on each side are

Table 2.4: Design parameters for the interaction regions of FCC-ee [16,33]. IP stands for interaction point and FD is the abbreviation for final doublet.

Over-all length	L	200 m
Distance between IP and FD	L^*	2 m
Horizontal beta function at IP	β_x^*	1 m
Vertical beta function at IP	β_y^*	1 mm/2 mm
Horizontal beam size (175 GeV)	σ_x^*	36 µm
Vertical beam size (175 GeV)	σ_y^*	70 nm

used to match the optics. In-between the matching section quadrupoles RF cavities are installed. At the interaction point the horizontal beta function reduced to $\beta_x^* = 1\,\text{m}$. The design value for the vertical plane was first $\beta_y^* = 1\,\text{mm}$ [33] before it was increased to 2 mm [16]. Although the distance between interaction point and first quadrupole is only $L^* = 2\,\text{m}$, the beta function in the vertical plane reaches about 5.5 km in the case of $\beta_y^* = 1\,\text{mm}$. For comparison, in the horizontal plane, where the beta function at the interaction point is $\beta_x^* = 1\,\text{m}$, the beta function only rises up to 500 m.

2.3 Alternative arc lattice

The FODO lattice is the standard beam transport system in collider storage rings, because it allows the highest dipole filling factor. In context of this thesis a second arc lattice design with Double Bend Achromat cells was studied for comparison. The Double Bend Achromat (DBA) Lattice, also known as *Chasman Green Lattice*, was designed for third generation low emittance light sources to produce high brilliant synchrotron light from low emittance beams [41]. In order to increase the luminosity such low emittance lattices might be interesting for collider storage rings as well.

As the name "achromat" indicates, the dispersion function is zero at the beginning and the end of each cell, only between the two bending magnets it takes finite values. As a result the value of the synchrotron radiation integral $\mathcal{I}_5$ decreases compared to the previously studied FODO lattice. The theoretical minimum equilibrium beam emittance in a DBA lattice with the size of FCC-ee at 45.5 GeV beam energy would be

$$\epsilon_{\text{DBA}} = \frac{C_\text{q}}{4\sqrt{15}}\gamma^2\theta^3 = 2.8 \times 10^{-5}\,\text{nm rad}. \tag{2.9}$$

The parameter $C_\text{q} = \frac{55}{32\sqrt{3}}\frac{\hbar c}{m_0 c^2} = 3.832\times10^{-13}\,\text{m}$ for electrons. $\gamma = 89041$ is the relativistic Lorentz factor and $\theta = 0.52\,\text{mrad}$ is the deflection angle per bending magnet. The detailed derivation of Eq. (2.9) is given in [37] and [22]. Compared to the FCC-ee baseline parameter

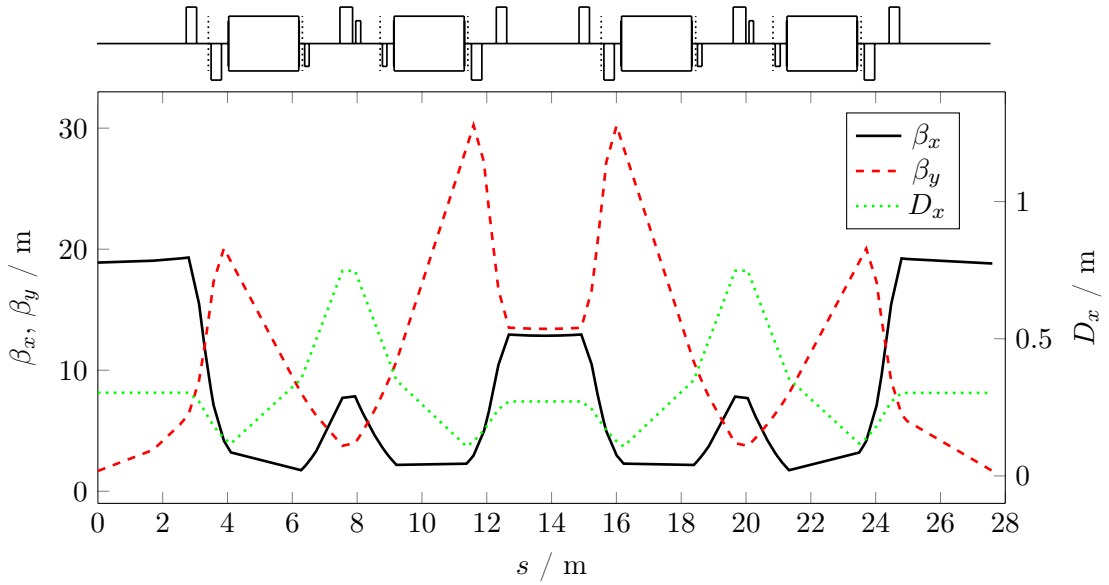

Figure 2.10: Beta functions and horizontal dispersion function in the first sector of the ANKA storage ring. Each sector consists of two DBA cells, a long and a short straight section. For smallest emittance the DBA optics is modified and operated with non-vanishing dispersion in the straight sections.

$\epsilon_x = 2\,\text{nm rad}$ the theoretical minimum emittance of the DBA lattice is three orders of magnitude smaller.

The implementation of an DBA lattice in the arc sections in the MAD-X model of FCC-ee was done to verify this estimation and compare other global machine parameters to those of the lattice based on the FODO cell design.

2.3.1 Arc lattice based on the Double Bend Achromat cells of ANKA

The cell layout used for the DBA version of FCC-ee was based on the lattice of the ANKA storage ring at the Karlsruhe Institute of Technology (KIT). The ANKA lattice has a circumference of 110.4 m and consists of eight non-symmetric DBA cells each containing five quadrupoles, two bending magnets, and three sextupoles. Two straight sections and two DBA cells form a periodic unit, called sector, with the length of 27.6 m. Beta functions and horizontal dispersion of such a sector are shown in Fig. 2.10. The straight sections in the middle of the sector have a length of 2.2 m and are used for RF installation and injection. In the fourth straight section and in the longer straight sections with 5.6 m length insertion devices are installed. The different length and purpose of of the straight sections lead to the non-symmetric optics functions at beginning and end of one DBA cell.

For the study of an alternative arc design for FCC-ee the Racetrack Layout was chosen. The new FCC-ee arcs are defined as a series of ANKA sectors, as they are the smallest

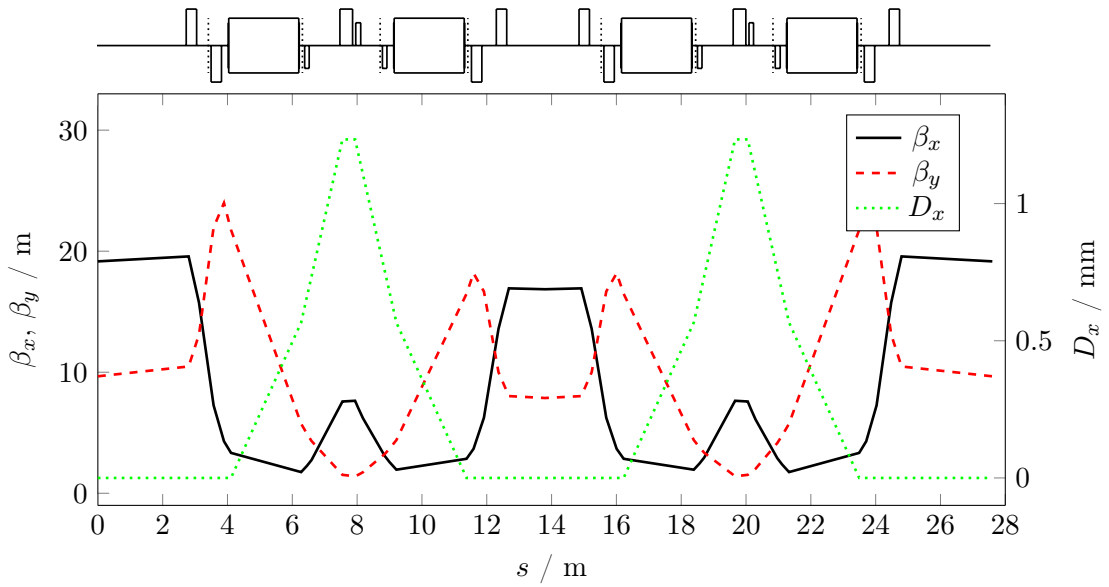

Figure 2.11: Beta functions and horizontal dispersion after re-matching the lattice functions of one ANKA sector for the alternative FCC-ee arc lattice. The dispersion is set to zero at the beginning and the end of each DBA and its maximum dropped to 1.23 mm because of the large bending radius.

periodic unit of the lattice. The SARCs consist of 160 of these twin-DBA cells, which add up to a length of 4.42 km. For the LARCs 590 twin-DBA cells are connected resulting in a length of 16.28 km. The overall circumference of the new lattice is 99.2 km.

As the FCC-ee lattice consists of much more sectors compared to the ANKA storage ring, the bending angle of the dipole magnets had to be adjusted. The total number of bending magnets in the lattice is 12000 leading to a bending angle per dipole of $\theta_B = 2\pi/12000 = 0.5236$ mrad.

To achieve smallest emittances at user operation the ANKA storage ring is operated with non-vanishing dispersion in the straight sections[3] as shown in Fig. 2.10 [42–44]. For the alternative FCC-ee arcs the dispersion function was re-matched to zero at the beginning and the end of each DBA. The lattice functions of one sector as used in FCC-ee are shown in Fig. 2.11. Because of the large circumference the maximum value of the dispersion function shrinks from $D_x = 748.69$ mm to 1.23 mm, which is less than one percent of the value in the FODO cell (127 mm).

The new arcs consisting of the twin-DBA cells were directly connected to the unchanged straight sections. As the dispersion function is zero at the end of the DBA, dispersion suppressors are not needed any more. The length of the first FODO cell in the matching section was reduced to 25 m. The contracted cell was necessary to find stable optics as

[3]The integrated value of the dispersion function can be further decreased, if the dipoles are entered with non-zero dispersion and a negative value of its derivative.

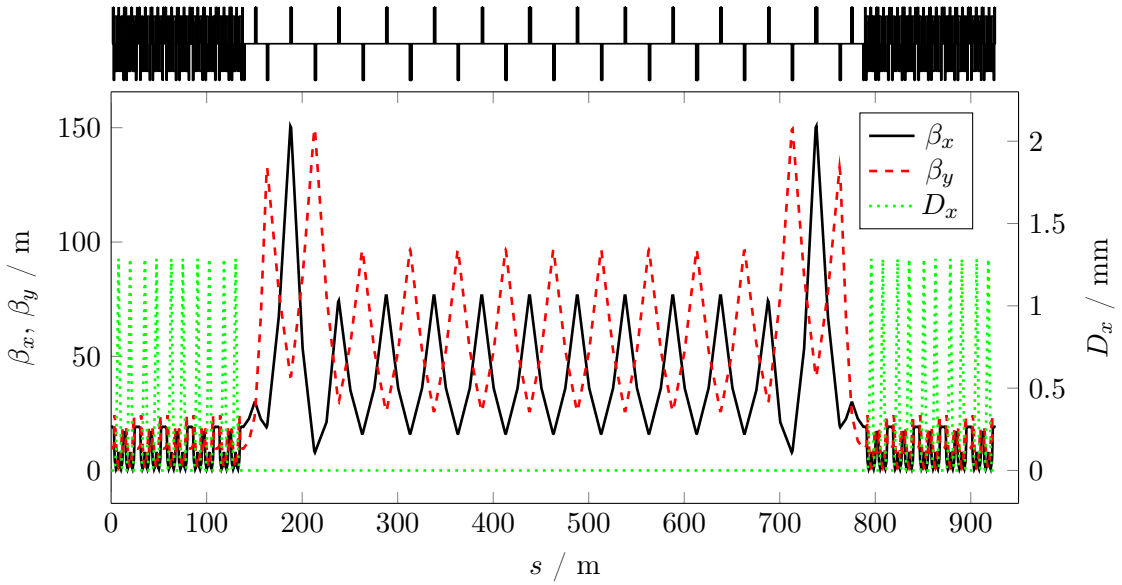

Figure 2.12: Mini straight section used for optics matching. After a short arc section consisting of five twin-DBA cells a four-cell matching section is used to adapt the lattice functions of the DBA lattice to the FODO optics in the straight section.

it provides a link between the DBA cells with very short distances between quadrupoles and the FODO cells with comparably long distance. Fig. 2.12 shows the beta functions and the horizontal dispersion function of a mini straight section to illustrate the transition from the DBA optics in the arcs to the FODO lattice in the straight sections. The beta functions in the matching section reaches large values up to 150 m in both planes. In case the DBA lattice would be chosen to be the baseline lattice the beta functions could be further optimised by varying strength and position of the matching section quadrupoles. Still, the optics is absolutely fine for the comparison of general characteristics of the two lattice designs.

The comparison of the regular FCC-ee lattice using a FODO design in the arc sections and the alternative lattice with DBA cells comprises general parameters of the optics and parameters that depend on the beam energy. However, it turned out that stable optics could only be found for the two lower beam energies of 45.5 GeV and 80 GeV, which will be explained later. The results of the comparison are summarized in Tab. 2.5 and will be discussed in detail in the following paragraphs.

Phase advance, tune and chromaticity: The DBA twin-cell with 27.6 m has about half the length of one FODO cell (50 m), while having a more than six times larger horizontal phase advance of $\varphi_x = 1.7 \times 2\pi$. This consequently results in a tune, which is one order

Table 2.5: Comparison between the FCC-ee lattices based on DBA and FODO cell design. The table summarises parameters of the single periodic structure and the global parameters.

	DBA cell		FODO cell	
Cell length (m)	27.6		50.0	
Dipole filling factor (%)	31.4		80.0	
Dipole bending radius (km)	4.1		10.5	
Max. hor. beta function (m)	19.57		76.98	
Max. vert. beta function (m)	23.98		96.55	
Phase advance per cell	1.701		0.250	
Phase advance per cell	0.740		0.167	
Max. hor. dispersion (mm)	1.2		121.2	
Circumference (km)	99.2		100.0	
Horizontal tune	5189.19		501.08	
Vertical tune	2277.01		335.14	
Linear chromaticity x	-10778.23		-585.74	
Linear chromaticity y	-7710.86		-859.98	
Beam energy (GeV)	45.5	80.0	45.5	80.0
Energy loss per turn (MeV)	91.7	876.7	36.0	343.7
Hor. emittance (pm rad)	0.060	0.185	62.6	193.4
Mom. compaction factor	1.20×10^{-8}	1.20×10^{-8}	5.45×10^{-6}	5.36×10^{-6}
Damping time (s)	0.328	0.060	0.844	0.155

of magnitude larger than the one of the FODO lattice, reaching 5189.19. In the vertical plane the phase advance is smaller ($\varphi_y = 0.7 \times 2\pi$), but still the tune is 2277.01 because of the large number of cells.

A side product of the large tunes are very large values of the linear chromaticities. $Q'_x = -10778.23$ in the horizontal plane and $Q'_y = -7710.86$ in the vertical plane exceed the already remarkable values of the FODO lattice by factors of 18.4 and 9.0 respectively. The sextupole strengths required for the correction of the linear chromaticity would be $k_2^{\mathrm{SF}} = 37001\,\mathrm{m}^{-3}$ in the horizontal plane and $k_2^{\mathrm{SD}} = -32421\,\mathrm{m}^{-3}$ in the vertical plane. These very large values are not only needed because of the increased chromaticity, but also to compensate the smaller beta functions and the tiny dispersion function of only 1.23 mm. It is needless to say, that such sextupole strengths are far beyond technical limits.

Synchrotron radiation power, momentum compaction and emittance: For 45.5 GeV beam energy the energy loss per turn reaches already 91.74 MeV compared to 35.96 MeV. While the FODO lattice is designed to obtain highest possible dipole filling factor and so minimum synchrotron radiation losses, the DBA lattice is optimised to reach minimum values of the beam emittance and provide space for insertion devices. The dipole filling

factor of the ANKA DBA is 31.4 %, while for the FODO design ≥80 % could be achieved. As a consequence of the smaller dipole filling factor the local bending radius must be decreased from $\rho = 10.5\,\mathrm{km}$ to $\rho = 4.1\,\mathrm{km}$. As the synchrotron radiation power depends on the square of the bending radius like

$$P = \frac{e^2 c}{6\pi\epsilon_0}\frac{1}{(m_0 c^2)}\frac{E^4}{\rho^2},$$

the energy loss per turn increases for a given beam energy. The energy loss per turn was also calculated for a beam energy of 80 GeV. In this case the energy loss per turn increases from 343.70 MeV to 876.73 MeV.

As another consequence of the smaller value of the horizontal dispersion the momentum compaction factor

$$\alpha_\mathrm{c} = \frac{1}{L_0}\oint\frac{D(s)}{\rho(s)}ds$$

describing the variation of the orbit length for particles with energy deviation is two orders of magnitude smaller than for the FODO lattice. While it has the value $\alpha_\mathrm{c} = 5.45 \times 10^{-6}$ (5.36×10^{-6}) for the FODO lattice, it now takes $\alpha_\mathrm{c} = 1.20 \times 10^{-8}$ (1.20×10^{-8}) for 45.5 GeV (80 GeV) beam energy. Although the bending radius decreases as well, the very small dispersion creates only minimal orbit offsets and thus very small changes of the orbit length. According to Eq. (1.41) a decrease of the momentum compaction factor by two orders of magnitude results in a bunch length of only 10 % compared to the FODO cell lattice.

Last but not least, the horizontal equilibrium emittance reaches values in the sub-picometer range. The tiny dispersion leads to a reduced effect of the quantum excitation and results in emittances of $\epsilon_x = 0.060\,\mathrm{pm\,rad}$ for 45.5 GeV beam energy and $\epsilon_x = 0.185\,\mathrm{pm\,rad}$ for 80 GeV beam energy. The value of 45.5 GeV is about twice of the theoretical minimum, but still three orders of magnitude smaller than the value obtained in the FODO cell lattice. The reduced effect of the quantum excitation also leads to shorter damping times in the DBA lattice.

Limitation of the beam energy: For the performance comparison between the DBA lattice and the FODO lattice just the beam energies 45.5 GeV and 80.0 GeV could be investigated. For larger beam energies MAD-X could not find stable orbits any more. It turned out, that the calculations were very sensitive to energy deviations. Even for 45.5 GeV beam energy and an energy offset of only plus-minus one per mill, no stable orbit could be found. The reason can be found when reviewing the higher-order chromaticities (see Sec. 4.2):

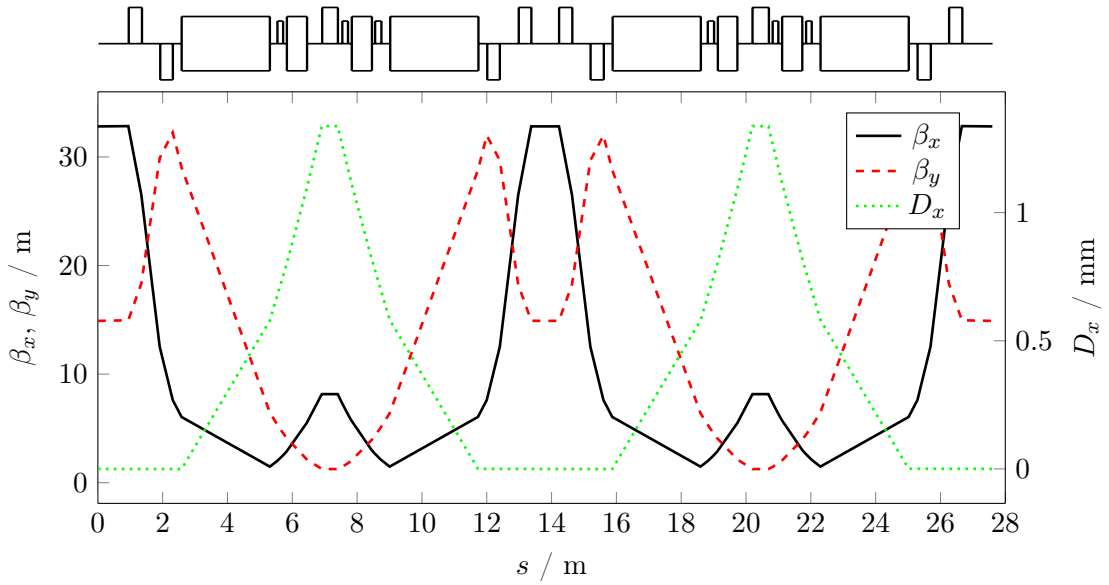

Figure 2.13: Beta functions and horizontal dispersion function in one modified twin-DBA cell. Additional dipoles and shorter drift spaces increase the dipole filling factor to 48.5 %. The maximum beta functions are about 50 % larger than before.

Q'_x	=	1.50×10^{-03}	Q'_y	=	-6.06×10^{-04}
Q''_x	=	$1.92 \times 10^{+05}$	Q''_x	=	$-1.79 \times 10^{+07}$
$Q_x^{(3)}$	=	$-3.27 \times 10^{+07}$	$Q_y^{(3)}$	=	$5.87 \times 10^{+10}$
$Q_x^{(4)}$	=	$9.82 \times 10^{+13}$	$Q_y^{(4)}$	=	$-1.13 \times 10^{+17}$

Although the linear order chromaticity is well-corrected, the higher order terms create large tune shifts that drive the particles to resonances, where they get lost. Since the energy offset generated by synchrotron radiation is considered by MAD-X during the calculation of emittance and energy loss per turn, a careful correction of the higher orders of the chromaticity would be needed to allow larger beam energies with larger energy offsets.

2.3.2 Modified Double Bend Achromat lattice

As a second approach the ANKA Double Bend Achromat was optimised for collider requirements. To increase the dipole filling factor the length of the long drift spaces was reduced by 2.83 m and the length of the short drift spaces in the middle of each twin-DBA cell by 1.55 m. Moreover, two additional short bending magnets were introduced between the already existing dipoles and the centre quadrupole leading to a dipole filling factor of 48.5 %. The cell with all is elements was then re-scaled to the initial length of 27.6 m to allow comparison to the previous case. For investigations concerning the length of the DBA cell a parameter was introduced into the lattice definition, which allows to scale the

length of the cell and each element by a certain factor. All variables and strengths are defined in such a way, that they adapt automatically. The length of the DBA cell was increased by factors of 2, 5 and 10. From the beginning on, the number of cells in the arcs was chosen to allow this modification without changing the machine circumference.

In Fig. 2.13 the optics functions of the new twin-DBA cell with shorter drift spaces and additional bending magnets is shown. The matching of the optics was modified to obtain equal conditions in the middle of a twin-cell and at the beginning. Fig. 2.14 shows the cell scaled to ten times of the initial length. The beta functions in the DBA scale accordingly and the dispersion even increased by a factor of 100. Fig. 2.15 shows the same mini-straight section as previously presented in Fig. 2.12 to illustrate the transition of the arc optics to the optics in the straight sections, but for ten times longer DBA cells. The beta functions of the arcs now exceed the ones in the straight sections by more than a factor of three.

Parameter comparison: The lattice parameters of the modified DBA lattice with 27.6 m cell length and 276.0 m cell length are summarised in Tab. 2.6 and also compared to the values of the lattices using the initial DBA layout and the FODO cells. The value of the beta functions in the 27.6 m cell length increased by 50 %, which results in even larger values of the chromaticity compared to the initial DBA lattice. The momentum compaction factor also increased, because the additional bending magnets are installed very close to the quadrupole in the middle of the DBA cell, where the dispersion peaks. Their contribution to the first synchrotron radiation integral is therefore relatively large. The main difference is, as expected, the reduced synchrotron radiation loss. As a consequence of the larger dipole filling factor the energy loss per turn could be decreased by about 35 % from 91.7 MeV and 876.7 MeV to 59.4 MeV and 567.5 MeV for 45.5 GeV and 80.0 GeV beam energy, respectively.

As a second step the length of the twin-DBA cell was increased by a factor of ten, to reduce the enormous value of the chromaticity and to increase the values of momentum compaction factor and horizontal beam emittance, which are still far below the requirements specified in [16]. The scaling also involved the length of all elements and their strength. As the phase advance per twin-DBA cell stayed the same while the number of cells was reduced by a factor of ten, the tunes dropped to $Q_x = 590.35$ in the horizontal plane and $Q_y = 271.74$ in the vertical plane and are now comparable to the tunes of the FODO cell lattice ($Q_x = 501.08$ and $Q_y = 335.14$). As a consequence, the chromaticity decreased as well by a factor of ten. The momentum compaction factor is now in the same order of magnitude, now just differing by a factor of 2.6. The horizontal emittance equals the one of the FODO lattice exactly.

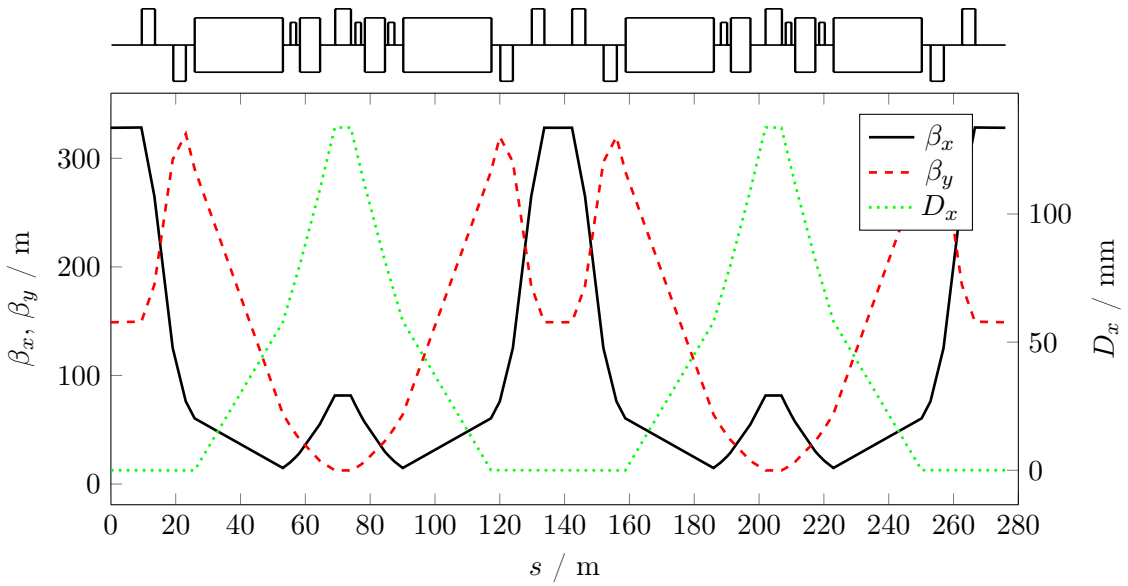

Figure 2.14: Beta functions and horizontal dispersion function for a modified twin-DBA cell scaled to ten times of the initial length. The maximum beta functions increase accordingly, the dispersion function increases with the square of the scaling factor.

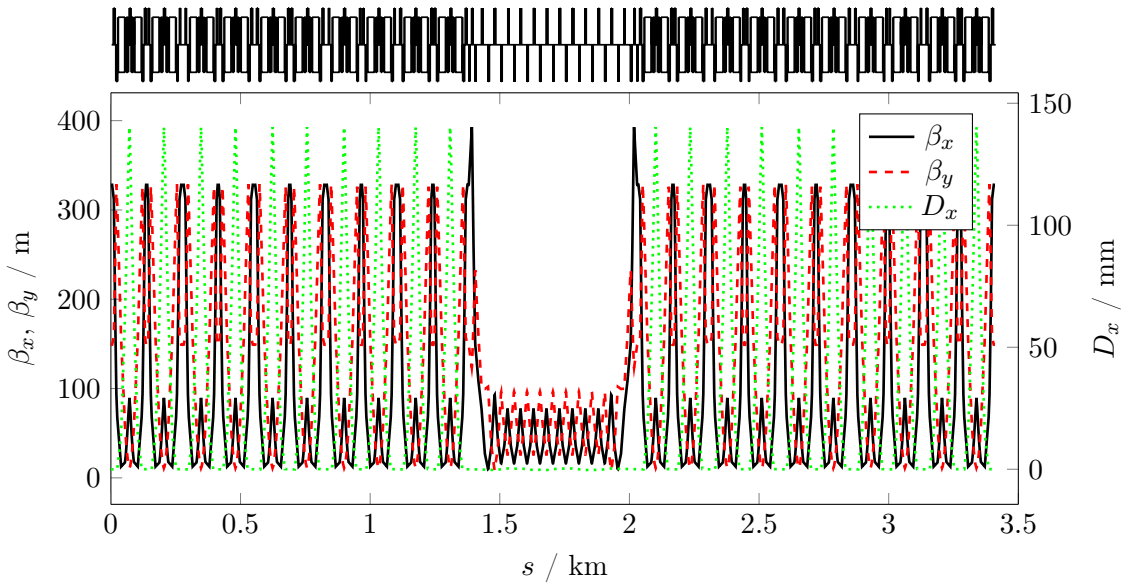

Figure 2.15: Mini straight section used for optics matching. Because of the increased cell length the arc section is now longer compared to Fig. 2.12. In this case the beta functions exceed the ones of the FODO cell.

Table 2.6: Comparison between the lattices with DBA and FODO arc lattice design. The table summarises both the parameters of the single periodic structure and the global parameters.

	DBA cell		Modified DBA cell	
Cell length (m)	27.6		27.6	
Dipole filling factor (%)	31.4		48.5	
Dipole bending radius (km)	4.1		6.4	
Max. hor. beta function (m)	19.57		32.84	
Max. vert. beta function (m)	23.98		32.24	
Phase advance per cell	1.701		1.690	
Phase advance per cell	0.740		0.720	
Max. hor. dispersion (mm)	1.2		1.3	
Circumference (km)	99.2		99.2	
Horizontal tune	5189.19		5153.58	
Vertical tune	2277.01		2216.51	
Linear chromaticity x	-10778.23		-13241.86	
Linear chromaticity y	-7710.86		-9228.83	
Beam energy (GeV)	45.5	80.0	45.5	80.0
Energy loss per turn (MeV)	91.7	876.7	59.4	567.5
Hor. emittance (pm rad)	0.060	0.185	0.063	0.194
Damping time (s)	0.328	0.060	0.507	0.093
Mom. compaction factor	1.20×10^{-8}	1.20×10^{-8}	2.12×10^{-8}	2.12×10^{-8}
	Modified DBA cell (2)		FODO cell	
Cell length (m)	276.0		50.0	
Dipole filling factor (%)	48.5		80.0	
Dipole bending radius (km)	6.4		10.5	
Max. hor. beta function (m)	328.37		76.98	
Max. vert. beta function (m)	322.43		96.55	
Phase advance per cell	1.690		0.250	
Phase advance per cell	0.720		0.167	
Max. hor. dispersion (mm)	133.8		121.2	
Circumference (km)	99.2		100.0	
Horizontal tune	590.35		501.08	
Vertical tune	271.74		335.14	
Linear chromaticity x	-1440.34		-585.74	
Linear chromaticity y	-1349.66		-859.98	
Beam energy (GeV)	45.5	80.0	45.5	80.0
Energy loss per turn (MeV)	59.4	567.5	36.0	343.7
Hor. emittance (pm rad)	62.6	193.6	62.6	193.5
Damping time (s)	0.507	0.093	0.844	0.155
Mom. compaction factor	2.12×10^{-6}	2.10×10^{-6}	5.45×10^{-6}	5.36×10^{-6}

2.3.3 Summary and conclusion

To justify the choice of FODO cells for the arc lattice an alternative design was studied. DBA lattice of the ANKA storage ring at the Karlsruhe Institute of Technology (KIT) was adapted to the circumference of FCC and compared to the lattice based on FODO cells. Because of their high dipole filling factor the FODO cells are the usual choice for collider lattices, while the DBA lattice is designed to obtain low horizontal emittance for a high brilliance in synchrotron light sources. In order to maximise luminosity, such low emittance beams are interesting for collider storage rings as well. As expected, the beam emittance at 45.5 GeV beam energy could be reduced to 0.06 pm rad, which is three orders of magnitude smaller than the value of the FODO cell lattice (63 pm rad).

In order to mitigate the synchrotron radiation losses, the DBA layout was optimised for collider requirements, i.e. the dipole filling factor was increased from 31.4 % to 48.5 % by reducing the length of drift spaces and installing two additional bending magnets in the free space next to the centre quadrupole. The energy loss per turn could be decreased, but it still exceeds the one of the FODO lattice by 65 %.

The most limiting factor of the DBA lattice was its large chromaticity of up to 13000 units in the horizontal plane. The sextupole strengths required for their corrections are proportional to the reciprocal of the dispersion function and the beta function

$$k_2 \propto \frac{1}{D_x}\frac{1}{\beta}.$$

As a consequence of the tiny value of the dispersion function of $D_x = 1.23\,\mathrm{mm}$ and the small beta functions compared to the FODO cell lattice, sextupole strengths are needed with values of $k_2^{\mathrm{SF}} = 2.15 \times 10^{+4}\,\mathrm{m}^{-3}$ and $k_2^{\mathrm{SD}} = -1.51 \times 10^{+4}\,\mathrm{m}^{-3}$. These strengths are not only far beyond technical capability, but also limit the dynamic aperture so far, that a closed orbit could only be found for the two lower beam energies 45.5 GeV and 80 GeV.

In order to reduce the chromaticity of the DBA lattice the unit cell was scaled to 276 m, which is ten times the initial length. Element lengths and magnet strengths were scaled accordingly. As a consequence, the phase advance in the arcs is ten times smaller resulting in lower tunes and chromaticities. The now required sextupole strengths, $k_2^{\mathrm{SF}} = 3.2\,\mathrm{m}^{-3}$ and $k_2^{\mathrm{SD}} = -3.1\,\mathrm{m}^{-3}$, are in the same order of magnitude compared to the sextupole strengths in the FODO lattice. However, the horizontal emittance increased so much, that it now has exactly the same value as in the FODO cell lattice.

In summary, the studies of the alternative DBA design have shown, that a reduction of the emittance can only be achieved with the side-effect of a large increase of chromatic aberrations. In combination with the already challenging effects of the interaction regions just solutions for the low energies could be found.

Since the large circumference of FCC-ee already leads to small emittances, a further reduction is not compulsory. Therefore, it was decided to keep the FODO cell lattice in the arc sections, because it features 40 % less synchrotron radiation power. For synchrotron radiation facilities, where the beam energy is in the order of a few GeV, this is not a severe limitation. As the synchrotron radiation power increases with the fourth power of the beam energy, in high-energy storage rings this becomes a matter of cost and technical feasibility in terms of shielding requirements. Moreover, the requested momentum acceptance of ± 2 % energy deviation needs a sophisticated chromaticity correction with a multi-family sextupole scheme. Because of the dedicated phase advance such a scheme is easier to set up for FODO cells.

2.4 Design constraints from synchrotron radiation

In high-energy lepton storage rings the emitted synchrotron radiation is an undesired side product. Both the energy loss of the beam and the energy deposition in the machine components demand careful treatment during the design phase. For FCC-ee the over-all synchrotron radiation power was set to 50 MW [33]. Since the emitted radiation power is proportional to the fourth power of the beam energy, this allows to increase the maximum beam current for lower energies to reach higher luminosity. In addition, the high energies lead to very small opening angles from $\theta = 2/\gamma = 0.022$ mrad at 45.5 GeV beam energy to $\theta = 0.006$ mrad at 175 GeV beam energy. The large radiation power in combination with the punctual energy deposit requires a sophisticated absorber layout to protect the machine.

At LEP the aluminum vacuum chamber was water cooled to prevent heat-up and coated with a 3-8 mm thick lead shielding for radiation protection [25]. This option would be very expensive for a 100 km machine. Instead the CERN vacuum group works on a design using discrete water-cooled absorbers [39]. Taking these boundary conditions into account the general cell layout of the arc lattice was optimised to avoid direct photon hits from the bending magnets on the vacuum chamber. One consequence is a serious limit on the maximal allowed dipole length [39]. The results of this optimisation are already included in the previously presented FODO cell designs.

Beyond the general limits of P_γ the lattice has to be optimised to keep the critical energy well below the pair production threshold. In the arc section this requirement is fulfilled. The critical energy is $E_{\text{crit}} = 755$ keV.

2.4.1 Sawtooth orbit for different RF schemes

The emission of synchrotron light photons results in a decreasing beam energy in the arc sections. The particles follow dispersion orbits with smaller and smaller bending radii,

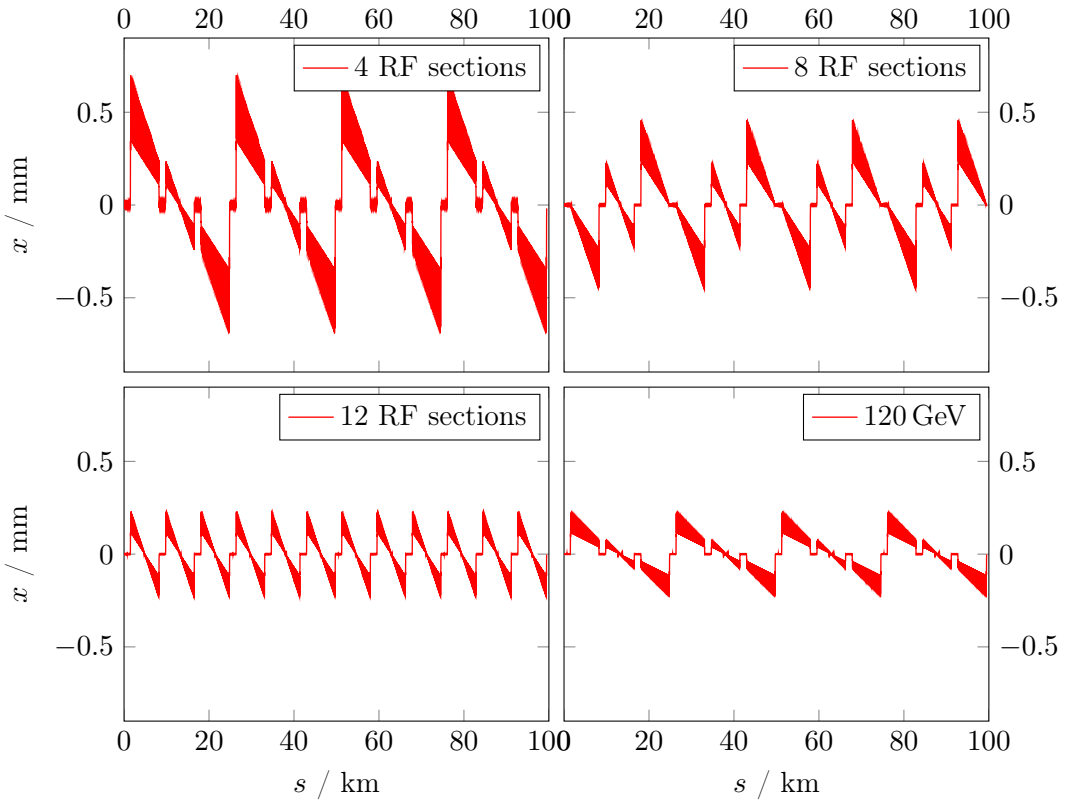

Figure 2.16: Sawtooth orbits in the lattice with 12-fold Layout at 175 GeV beam energy for different numbers of RF sections. For comparison the sawtooth orbit for 120 GeV beam energy and four RF sections is presented in addition.

which causes them to drift to the inside of the ring as they propagate through the arc lattice. In the RF sections between two arcs they regain energy. As soon as they enter the next arc section the particles now follow a dispersion orbit for positive energy offset and again start to drift to the inside as they travel through the arc lattice. The constant energy loss in the arcs in combination with the re-acceleration in the straight RF sections creates a particular pattern for the horizontal beam position, which is known as the *sawtooth orbit*.

Fig. 2.16 shows the sawtooth orbit at 175 GeV beam energy for four, eight and twelve RF sections. Each particle looses approximately 7.8 GeV per turn, which corresponds to 4.5 % of their total energy. The amplitude of the orbit offsets is directly correlated to the number of RF sections. In the lattice with twelve RF stations the maximum sawtooth amplitude is only one third compared to the scheme with four RF stations. Nevertheless, the maximum orbit offset still is $x_\delta = 227\,\mu\text{m}$, which compared to the beam size of $\sigma_x \approx 300\,\mu\text{m}$ is a considerable effect. As the radiation losses decrease for smaller energies, the sawtooth effect becomes smaller as well. For 120 GeV beam energy the maximum amplitude with four RF sections is comparable with the one in the twelve RF section scheme at 175 GeV.

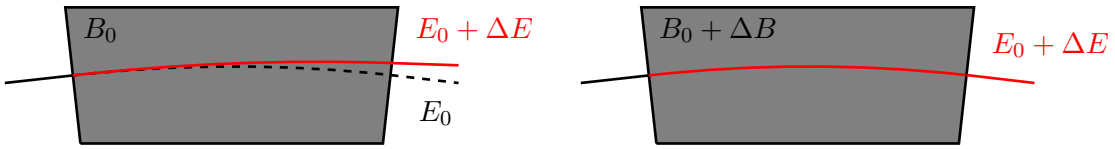

(a) Without tapering **(b)** With tapering

Figure 2.17: Illustration of the tapering method. In order to restore the ideal bending angle the magnetic field of the dipoles is adjusted to the local beam energy.

Assuming the chromatic aberrations are well-corrected, the energy loss along the arcs does not perturb the beam optics. However, since the sawtooth orbit does not traverse the sextupoles in their centre, the feed-down of the sextupoles creates an additional focussing term, which does perturb the optics. Therefore, a maximum of equally distributed RF systems is desirable to limit the sawtooth amplitude. Additional dispersion free sections are needed in the lattice to provide space for the installation of the RF cavities. These dispersion free sections, however, will significantly reduce the dipole filling factor of the machine and so increase the overall synchrotron radiation losses. In addition, space will be needed to suppress the dispersion either in missing bend or half-bend dispersion suppressor schemes. If a quadrupole-based scheme is chosen instead, additional independent quadrupole lenses are required. The lattice design therefore needs a careful optimisation between the tolerable sawtooth amplitude, the overall synchrotron light losses and the RF distribution needs, which are directly correlated to the dipole filling factor and functional aspects. Several optics have been studied and at present the most preferable is a two RF system in combination with a sophisticated compensation of the sawtooth effect in the arc section.

2.4.2 Tapering options for the dipoles in the arc sections

In the last section it has been motivated that a large number of RF sections is desired to keep the radial orbit excursions small. Considering the large size of FCC it nevertheless is aimed to restrict the RF system to two sections in order to lower cost and simplify maintenance. To compensate the lack of RF distribution shimming methods were studied, in which the bending angle of the dipoles was readjusted to the current particle energy in the arc [45, 46]. The concept of tapering the dipole strength is illustrated in Fig. 2.17. When the particles enter the arc, they have an energy larger than the design energy E_0. Its bending angle therefore is smaller than for a particle with design energy and they exit the dipole with an orbit offset as shown in Fig. 2.17 (a). The idea of the tapering is to adjust the dipole field to the local beam energy $E_0 + \Delta E$ in order to restore the ideal bending angle. In MAD-X tapering can be realised in two ways: additional orbit corrector

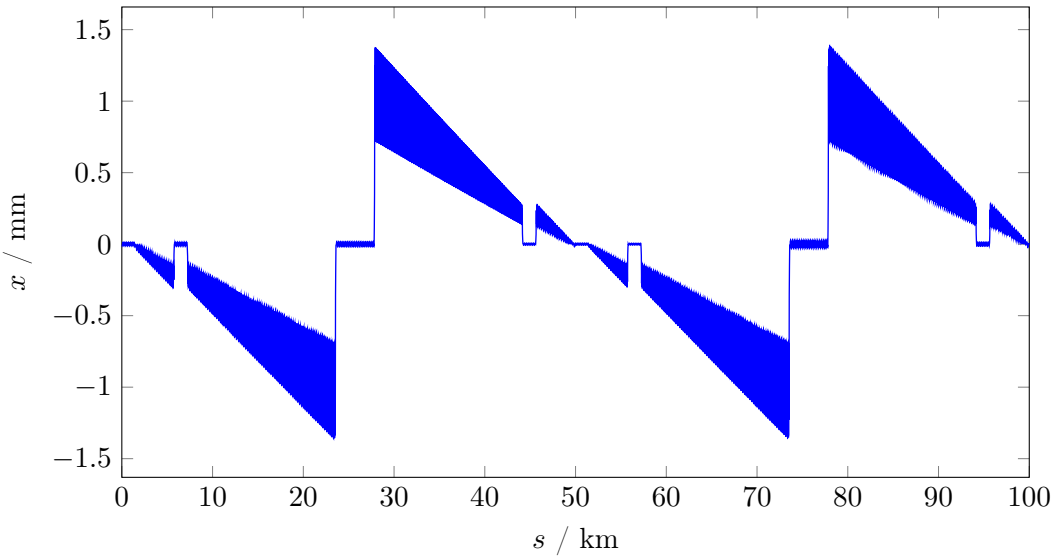

Figure 2.18: Sawtooth orbit in the lattice with Racetrack Layout with two RF sections in the Extended Straight Sections.

magnets can be installed after each dipole to provide an additional bending angle or errors of the bending field can be introduced. The nominal value of the bending strength cannot be modified, since this would have effects on the geometry of the whole machine. In a real machine the dipole strength will most probably be adjusted with back-leg windings connected to individual power supplies.

To obtain full compensation of the energy variation along the lattice the strength of each and every element needs to be adjusted to the local beam energy. This, however, would require individual power supplies for every magnet, which, considering the size of FCC-ee, would be tremendously expensive. Therefore, the tapering studies are focussed on the compensation of the sawtooth effect by adjusting only the dipole fields. If necessary, the tapering of quadrupoles still can be included on top.

The tapering was investigated for both layouts and different numbers of RF sections [45]. In the context of this thesis only the options for the Baseline Layout, the Racetrack Lattice with two RF stations, will be presented for the most critical beam energy of 175 GeV.

The orbit without adjusted dipole strengths is shown in Fig. 2.18. In the first Long Straight Section (LSS) with interaction region the beam energy has design value. In the subsequent arcs it constantly decreases until the first Extended Straight Section (ESS) is reached. At the end of the first Long Arc (LARC) the maximum orbit offset is about $x_\delta = -1.4\,\text{mm}$. The RF cavities in the ESS increase the beam energy by 3.9 GeV, which is half the energy loss per turn. In the second LARC the orbit offset now is $x_\delta = 1.4\,\text{mm}$ before it decreases until it reaches design value again in the LSS with the second interaction region at $s = 50\,\text{km}$.

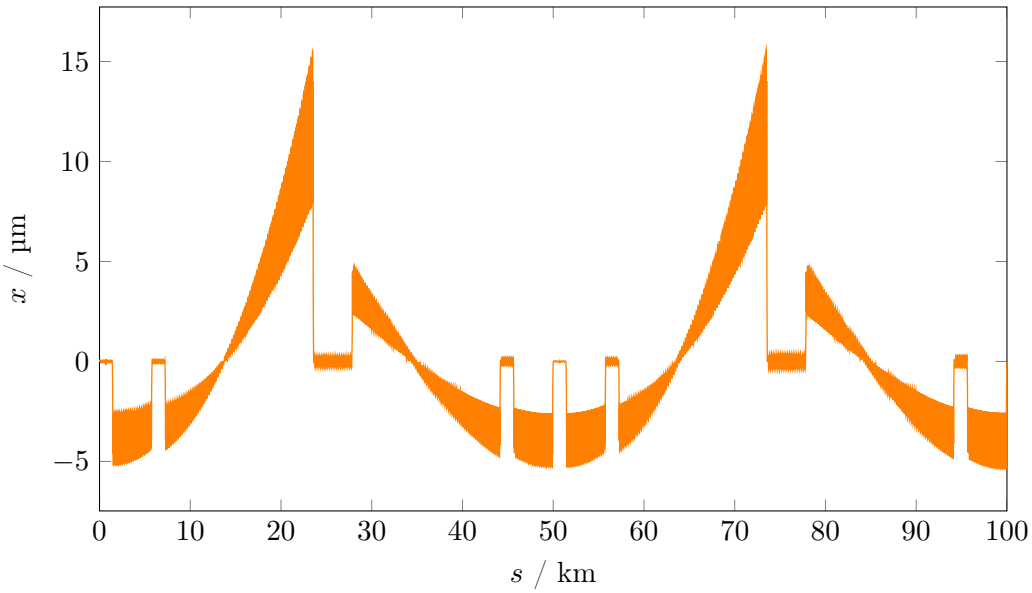

Figure 2.19: Horizontal orbit in the Racetrack Lattice with two RF sections after adjusting the strength of every dipole individually to the local beam energy.

In the remaining part of this section two scenarios of tapering will be presented: in the first scheme every single bending magnet was tapered individually and in the second approach the bending magnets in-between two RF sections were grouped into six blocks with equal bending strength in order to save costs for power supplies and increases the reliability because of the lower number of components.

Individually adjusted dipole strengths: The first tapering option is to equip every single dipole with its own correction mechanism. The local beam energy was both calculated analytically and with MAD-X to determine the required correction of the bending angle using the equation

$$\theta(E + \Delta E) = \theta_0 \left(1 - \frac{\Delta E}{E_0}\right). \tag{2.10}$$

The maximum modification is $\Delta\theta = 1.1 \times 10^{-2}\,\text{mrad}$, which corresponds to about 1.2 % of the nominal bending angle $\theta_0 = 9.53 \times 10^{-4}\,\text{mrad}$.

After assigning the strengths based on the energy calculations of MAD-X the sawtooth amplitude could be reduced to a maximum value of $x_\delta = 17\,\mu\text{m}$. This corresponds to a correction of the sawtooth amplitude of 98.8 %. The horizontal orbit with tapered dipole strengths is shown in Fig. 2.19. It still shows some excursions. Especially in front of the RF section the correction of the bending angles was too strong and the beam is now shifted to a positive orbit offset. As the radiated synchrotron radiation power depends on both the particle energy and the bending dipole field, the energy loss along the lattice is

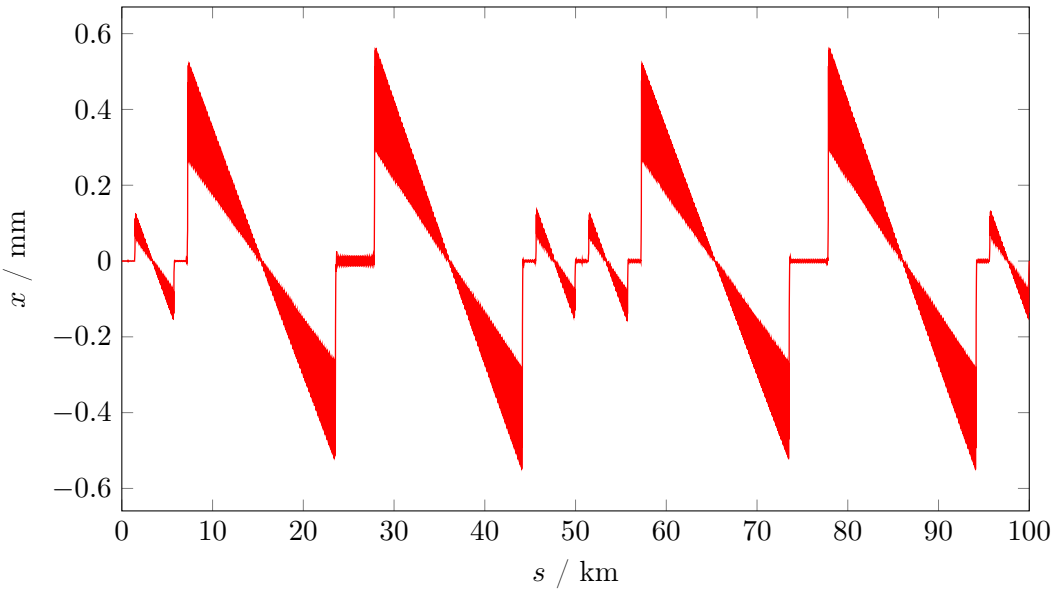

Figure 2.20: Sawtooth orbit of the Racetrack Lattice with two RF sections after arc-wise adjustment of the bending strength of the dipoles.

slightly changed after the modification of the bending angles. The sawtooth amplitude could probably be further decreased with another iteration of local energy calculation. However, the results suffice for a qualitative discussion and since the accouterment of each dipole with its own power supply still is an expensive task, it was decided investigate a more global tapering option instead.

Sector-wise tapered dipole strengths: Depending on the tolerance limits of the resulting sawtooth amplitude the dipoles do not necessarily need to be tapered individually. Instead, sectors of dipoles can be defined that have the same strength determined by the average beam energy in the sector. As a first step the dipole strengths were tapered arc-wise. All dipoles of a certain arc had the same strength leading to eight families of dipoles. The resulting orbit is shown in Fig. 2.20. The maximum amplitude could already be reduced from $x_\delta = 1.4\,\text{mm}$ to $x_\delta = 0.52\,\text{mm}$. The pattern of this orbit could also be created by a lattice with RF stations in every straight section. To obtain symmetric orbit offsets the cavities of the respective straight section must compensate the energy loss in the last half of the previous and the first half of the subsequent arc.

A further sub-division of the dipole chain in the long arcs could improve the reduction of the sawtooth effect: in Fig. 2.21 the orbit is shown for the FCC-ee dipole chain divided into twelve sectors. In the middle of the LARCs, where the dipole strength switches, a matching section of four FODO cells with individually powered quadrupoles is needed to provide a smooth transition of the lattice functions. This creates the unique orbit

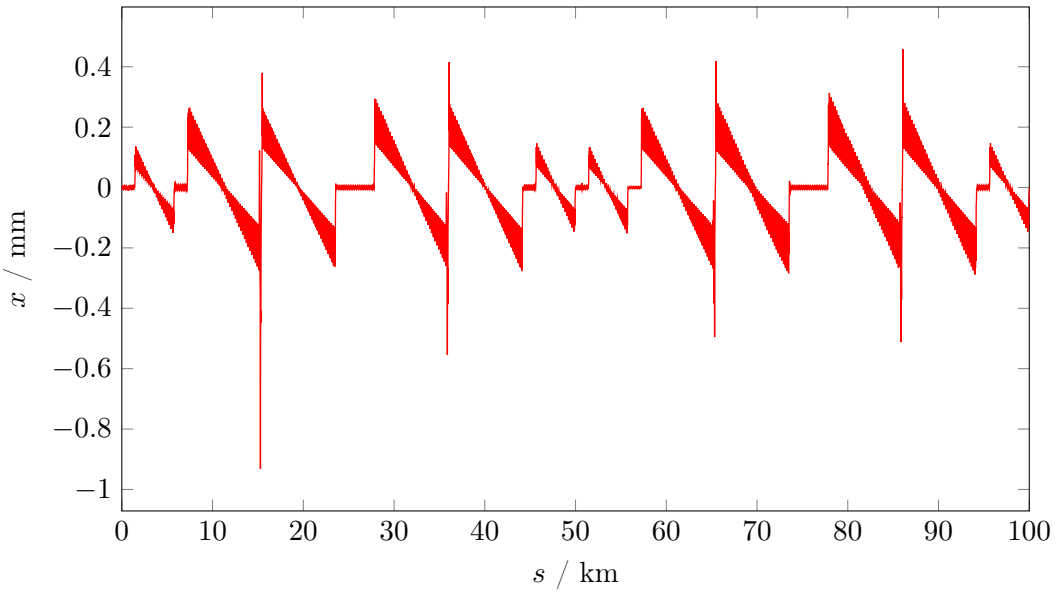

Figure 2.21: Sawtooth orbit of the Racetrack Lattice with two RF sections where the dipole chain is divided into twelve sectors. The excursions in the middle of the LARCs are created by the matching sections required to provide a smooth transition between the two sectors within the arc.

excursions that can be observed in Fig. 2.21. Apart from these exceptions the residual sawtooth amplitude is approximately 0.3 mm for the maximum design energy of 175 GeV. Since this orbit variations are in the same order of magnitude compared to the 12-fold RF scheme studied before, the remaining sawtooth amplitude is so far considered to be tolerable for FCC-ee. Fig. 2.22 shows a comparison of the obtained orbits without modified bending angles, with sector-wise tapering and with individual tapering.

Studies of alignment tolerances and coupling correction will investigate, whether the design emittance ratio of one per mille can be reached or if the sawtooth effect has to be corrected by either more sectors or individual tapering.

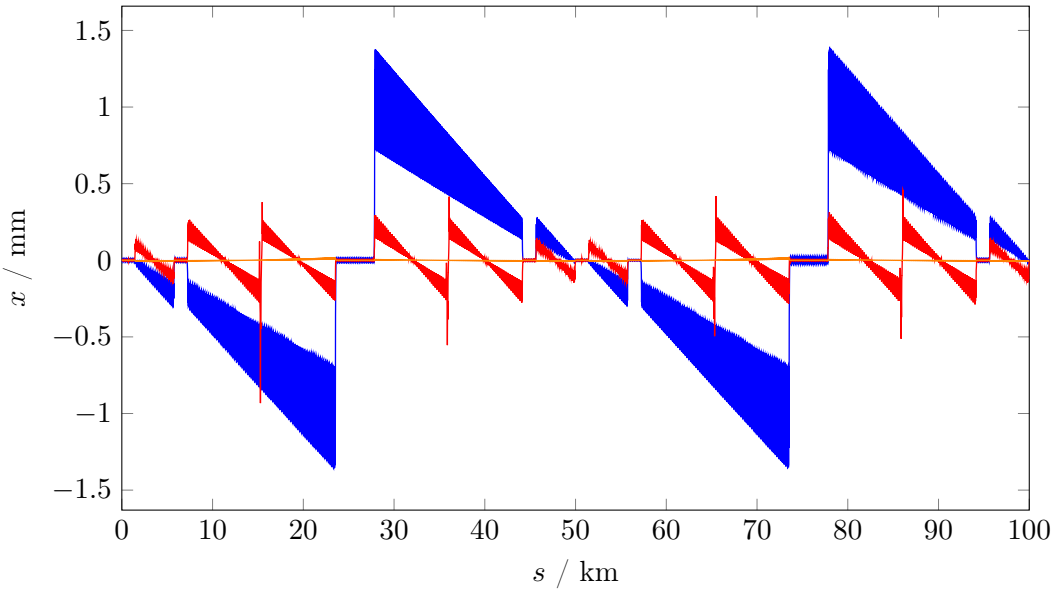

Figure 2.22: Orbits in the lattice with Racetrack Layout and two RF sections in comparison. While the orbit without corrected bending angles shows the largest orbit excursions, they nearly vanish, if the dipole strengths are individually adjusted to the local beam energy. The case with the twelve sectors compromises between orbit correction and a reasonable number of power supplies.

CHAPTER 3

Emittance tuning

The beam emittance describes the particle density of the beam in phase space. Therefore, it is one of the most important parameters in beam dynamics and influences both single particle and collective effects. In lepton storage rings the emittance determines the size of the source point of the synchrotron radiation. Modern synchrotron light sources therefore aim for lowest emittance to obtain radiation with high brilliance. In colliders a small beam size is required during the collision of the bunches to gain highest luminosity. One of the limits to the minimum beta function at the interaction point is the aperture of the final doublet quadrupoles. A smaller emittance therefore not only decreases the beam size at the interaction point, but also allows larger beta functions in the final focus quadrupoles for a given beam size. This on the other hand allows to reduce the value of β^* and focus the beam even stronger.

In lepton storage rings the emittance can be controlled during operation in a certain range, but it mainly depends on the machine geometry, the lattice and the beam energy. This means the emittance is already defined during the design phase of the machine. This chapter presents the considerations taken into account for the design of the linear lattice, in order to obtain the required design values. For the calculations the 80 km version of the lattice with 12-fold Layout was used. Since the equilibrium emittance is determined by the parts of the lattice with non-vanishing dispersion, the mini-beta insertions were replaced by regular straight FODO cells to facilitate the constraints for the calculations.

3.1 Horizontal emittance

In hadron machines, where the effect of energy loss by synchrotron radiation can usually be neglected, the emittance is given by the Maxwell-Boltzmann statistics of the particle source through the temperature of the ensemble [47]. If only conservative forces are present, it

will remain a constant of motion. In lepton machines, on the contrary, the horizontal beam emittance depends on two equally important effects that both result from the emission of synchrotron light: quantum excitation and radiation damping. When both effects reach an equilibrium, the horizontal beam emittance results in

$$\epsilon_x = C_\mathrm{q} \frac{\gamma^2}{J_x} \frac{\mathcal{I}_{5x}}{\mathcal{I}_2}, \tag{3.1}$$

which for a given beam energy is defined by the value of the synchrotron radiation integrals and thus the lattice design. As discussed in Sec. 2.2.1, the basic cell layout of FCC-ee lattice was designed to obtain the design emittance value for 175 GeV beam energy. At this energy the highest radiation losses occur, which requires best performance of the lattice. Using the same lattice and geometry at lower beam energies will produce a smaller beam emittance, because according to Eq. (3.1) the emittance also depends on the square of the Lorentz factor γ and thus on the beam energy. The expected decline was calculated using Eq. (2.4), which was given by

$$\epsilon_x = \frac{C_\mathrm{q}}{J_x} \gamma^2 \theta^3 F \tag{3.2}$$

with the lattice form factor

$$F_\mathrm{FODO} = \frac{1}{2 \sin \varphi} \frac{5 + 3 \cos \varphi}{1 - \cos \varphi} \frac{L}{2 l_\mathrm{B}}. \tag{3.3}$$

Although Eq. (3.2) is an approximation and $F = 2.98$ simplifies the situation, the comparison with an exact calculation shows a remarkably good agreement. In Tab. 3.1 the values according to Eq. (3.2) and the respective MAD-X results are summarised for the four design energies of FCC-ee. It has to be emphasised that due to quadratic dependence on γ the emittance shrinks from $\epsilon_x = 1.0\,\mathrm{nm\,rad}$ to $0.2\,\mathrm{nm\,rad}$ for 80 GeV beam energy and for 45.5 GeV even to 0.07 nmrad. Such a small value of the emittance in combination with the bunch population in the order of 10^{11} particles leads to high charge densities within the bunches. It still has to be proven whether such parameters are feasible, especially in terms of the beam-beam tune shift. The beam-beam parameter introduced in Sec. 1.5.2 is proportional to the reciprocal of the beam energy and the beam emittance:

$$\xi_u \propto \frac{1}{\gamma} \frac{\beta_u}{\sigma_u^2} \tag{3.4}$$

Therefore the effect becomes more important at lower energies and can be compensated by larger emittance values. A second set of parameters with an increased beam emittance for 45.5 GeV and 80 GeV was therefore proposed [33]. The alternative design values are included in Tab. 3.1. The value $\epsilon_x = 0.47\,\mathrm{nm\,rad}$ for 120 GeV is consistent with the natural emittance decrease.

Table 3.1: Lorentz factor and equilibrium beam emittances for all design energies. Both the analytically calculated emittance values from Eq.(2.4) and the results of the MAD-X calculation were compared to the alternative design parameters of [33] with increased emittance for 45.5 GeV and 80 GeV. Following the discussions in Sec. 2.2.1 the designed values leave a factor of two margin to the baseline values for emittance increase due to lattice imperfections.

	Z	W	H	tt
Beam energy (GeV)	45.5	80	120	175
Lorentz factor γ	89041	156556	234834	342466
Horizontal emittance ϵ_x (nm rad)				
- Analytical calculation	0.071	0.218	0.491	1.04
- MAD-X calculation	0.068	0.209	0.488	1.00
- Alternative design parameter	14.60	1.65	0.47	1.00

In the context of this thesis several possibilities were studied to increase the horizontal beam emittance and meet the required design values. Following the discussion in Sec. 2.2.1, the key parameter to define the beam emittance is the horizontal dispersion function. Via the $\mathcal{H}$ function

$$\mathcal{H}_u(s) = \beta_u D_u'^2 + 2\alpha_u D_u D_u' + \gamma_u D_u^2 \tag{3.5}$$

in the fifth synchrotron radiation integral, it determines the strength of the quantum excitation and thus modifies the equilibrium state. The minimum and maximum value of the dispersion function in a FODO cell are given by

$$\hat{D} = \frac{L^2}{\rho}\frac{\left(1+\frac{1}{2}\sin\left(\varphi/2\right)\right)}{4\sin^2\left(\varphi/2\right)} \quad \text{and} \quad \check{D} = \frac{L^2}{\rho}\frac{\left(1-\frac{1}{2}\sin\left(\varphi/2\right)\right)}{4\sin^2\left(\varphi/2\right)} \tag{3.6}$$

and they depend on the bending radius ρ, the length L of the FODO cell and the phase advance φ. The bending radius obviously needs to stay the same, because the new lattice must fit the same geometry. This leaves cell length and phase advance for modification. Both options were studied in detail towards their capabilities and limitations. The boundary conditions for the modification and the resulting lattices will be presented in the following sections.

3.1.1 Modification of the cell length

For a constant phase advance per cell the length of the FODO cell has been modified and the obtained minimum and maximum value of the horizontal dispersion function according to Eq. (3.6) are presented in Fig. 3.1. For the calculation the parameters of FCC were used, i.e. a bending radius of $\rho = 11.7\,\text{km}$ was used and a phase advance per cell of $\varphi = 90°$. For given

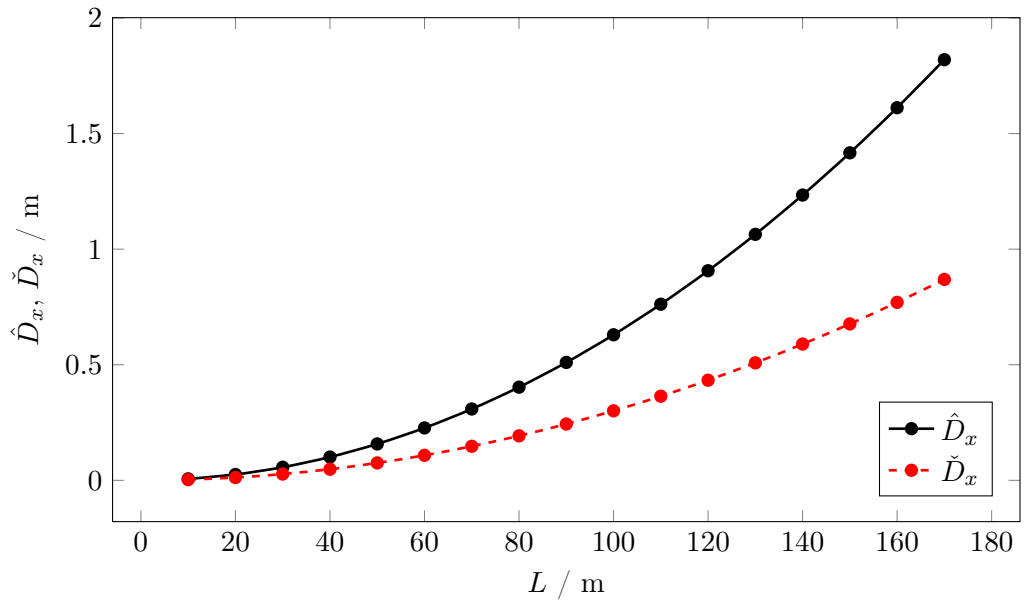

Figure 3.1: Minimum and maximum value of the horizontal dispersion depending on the FODO cell length. The values are results of Eq. (3.6) with using the FCC bending radius of $\rho = 11.7\,\text{km}$ and $\varphi = 90°$ phase advance per cell. The line connecting the single marks was added to guide the eye.

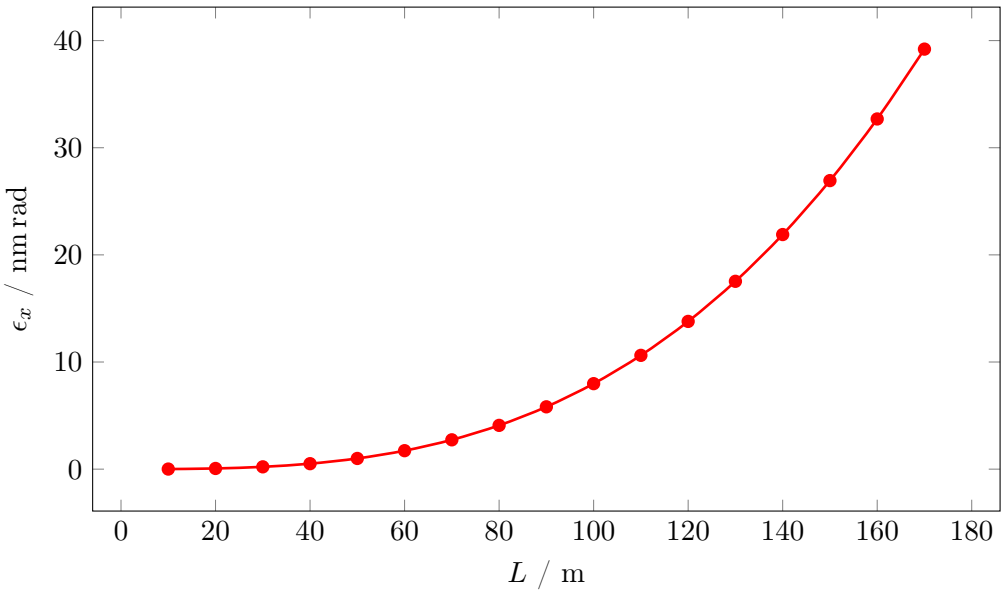

Figure 3.2: Horizontal equilibrium emittance for different length of the arc FODO cells. The values were calculated with Eq. (3.2) for a phase advance of $\varphi = 90°$ and 175 GeV beam energy. Bending angle θ and length of the bending magnets l_B were adapted to keep the bending radius constant.

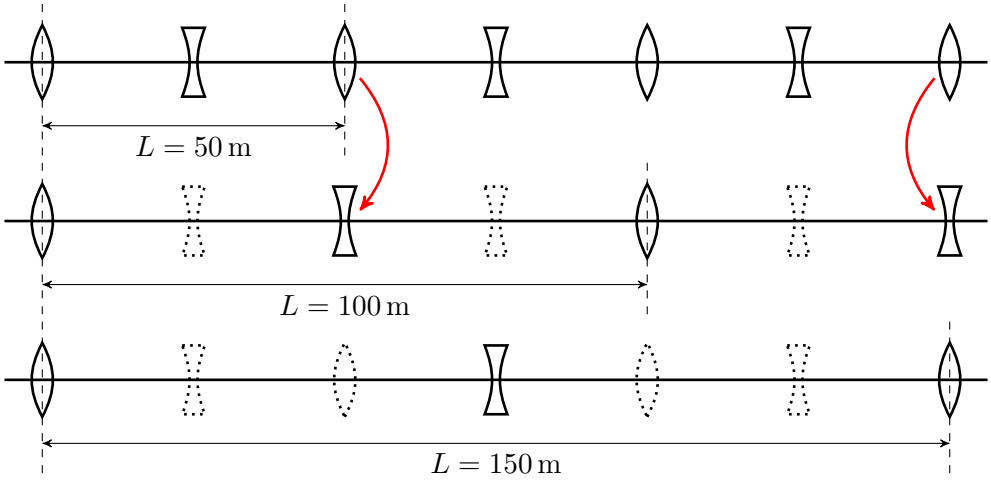

Figure 3.3: Proposed method to increase the FODO cell length. By switching off all the defocussing quadrupoles and reversing the polarity of every second remaining quadrupole the cell length can be increased from $L = 50\,\mathrm{m}$ (top) to $100\,\mathrm{m}$ (middle). $L = 150\,\mathrm{m}$ is obtained by keeping just every third quadrupole of the regular lattice (bottom).

phase advance and bending radius the values show a quadratic increase for larger FODO cells as expected from Eq. (3.6). As mentioned before, the dispersion function affects the horizontal emittance via the $\mathcal{H}$ function in the fifth synchrotron radiation integral. Since the $\mathcal{H}$ function contains the square of the dispersion, the increase of the beam emittance is even larger for longer cells. The values presented in Fig. 3.2 were calculated with Eq. (3.2) for a phase advance of $\varphi = 90^\circ$ and 175 GeV beam energy. The bending angle θ and length of the bending magnets l_B were adapted such that the bending radius stayed constant. Fig. 3.2 illustrates what a powerful lever the cell length is for the modification of the emittance. It is an obvious boundary condition that a modification of the effective length of the arc cells has to be based on the same hardware installed in the lattice. Re-positioning or exchanging lattice elements would lead to intolerably long technical interruptions in the machine operation. For carefully chosen FODO cell parameters however, i.e. mainly the phase advance per cell, a very elegant solution is proposed: the cell length can be increased by switching off a certain number of quadrupoles and changing the polarity of others. The method is illustrated in Fig. 3.3, where the symbols of lenses depict the quadrupole magnets. The schematic on the top shows the regular lattice for 175 GeV beam energy with 50 m cell length. In the second row all defocussing quadrupoles have been switched off (dotted elements) and the polarity of every second focussing quadrupole has been reversed as indicated by the red arrows. The effective cell length is now $L = 100\,\mathrm{m}$, which is twice as long as before in the regular lattice. If more quadrupoles are switched off, even longer cell lengths can be arranged as for example $L = 150\,\mathrm{m}$, which is presented in the third

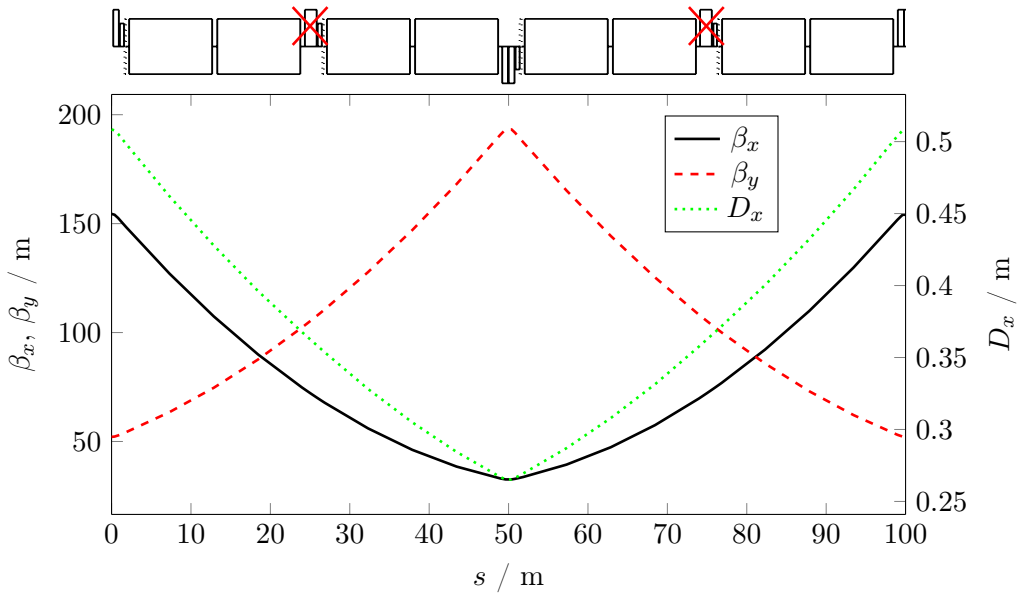

Figure 3.4: Beta functions and horizontal dispersion function in the modified FODO cell with a length of 100 m. The quadrupoles at $s = 25$ m and $s = 75$ m were switched off. The polarity of the quadrupole at $s = 50$ m was reversed, it is now used as a defocussing quadrupole. The beta functions increased by a factor of two according to Eq. (2.1), the dispersion by a factor of four, since it depends on the square of the cell length.

schematic. To guarantee smooth operation, it is foreseen to equip the relevant quadrupoles with switches, that should be included in the technical design from the beginning. A similar concept had been realised for the sextupoles at the HERA storage ring [48]. Beyond the context of this thesis a sophisticated powering scheme should be addressed.

Eq. (3.2) allows to estimate the required cell lengths to obtain the baseline values presented in Tab. 3.1. Taking the corresponding Lorentz factor into account and assuming the same phase advance of $\varphi = 90°$, a cell length of $L = 100$ m creates an emittance of $\epsilon_x = 1.74$ nm rad, which complies with the baseline value within 5.5 %. For 45.5 GeV beam energy the cell length needs to be increased to $L = 300$ m. The obtained emittance is then $\epsilon_x = 15.24$ nm rad, only 4.4 % larger than the baseline of 14.60 nm rad.

3.1.2 Lattice for 80 GeV beam energy with 100 m cell length

In order to fulfill the requirements for the horizontal emittance at 80 GeV beam energy the FODO cells in the arc lattice were increased to a length of $L = 100$ m as described in the previous section. The phase advance of $\varphi_x = 90°$ and $\varphi_y = 60°$ per cell was not modified. The beta functions and the horizontal dispersion function of the new FODO cell are presented in Fig. 3.4. The maximum and the minimum values of the beta functions

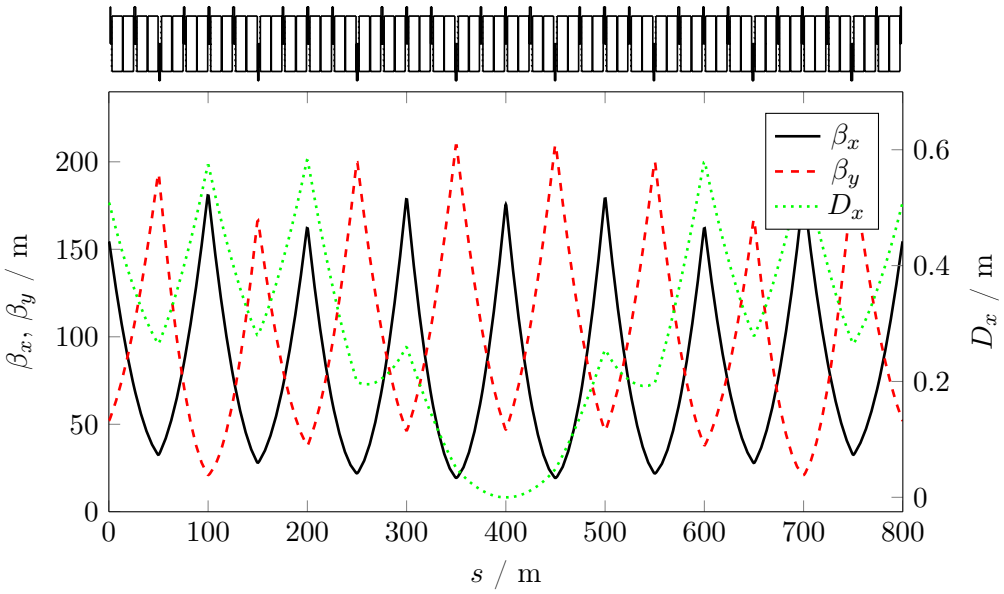

Figure 3.5: Optics of the dispersion suppressor in the lattice with 100 m cell length in the arcs. Eight free quadrupoles are used to suppress the dispersion.

increased by a factor of two as expected from Eq. (2.1). According to Eq. (2.2) and the previous discussions, the dispersion function increased by a factor of four.

The different optics functions correspond to a different periodic solution of the particle trajectory. As a consequence the matching sections and dispersion suppressors between arcs and straight sections need to be readjusted. For the lattice with 50 m cell length a half-bend dispersion suppressor was installed. This scheme does not work any more for the 100 m FODO cells, because the two half-bend cells correspond to one cell in the 100 m case and a second cell would be required to match the dispersion to zero. Instead, free quadrupoles are used to suppress the dispersion. A minimum of six degrees of freedom is required to match the dispersion, its derivative and Twiss parameters β and α. Since this dispersion suppressor scheme affects the optics, eight quadrupoles were used for this lattice of FCC-ee to re-optimise the Twiss parameters and avoid large values of the beta functions. Fig. 3.5 shows two dispersion suppressor sections next to each other. In-between, the dispersion functions is vanishing as required.

The lattice in the straight sections was not modified in order to preserve the same optics conditions for the injection scheme, interaction regions etc. As no dipole magnets are installed in these parts of the lattice the synchrotron radiation integral $\mathcal{I}_5$ is vanishing and the optics of the straight sections does not affect the equilibrium emittance. It can be optimised in a wide range following other boundary conditions. The radiation effects defining the equilibrium beam emittance are thus small compared to the ones in the arc sections. The matching sections at the beginning and at the end of the straight sections

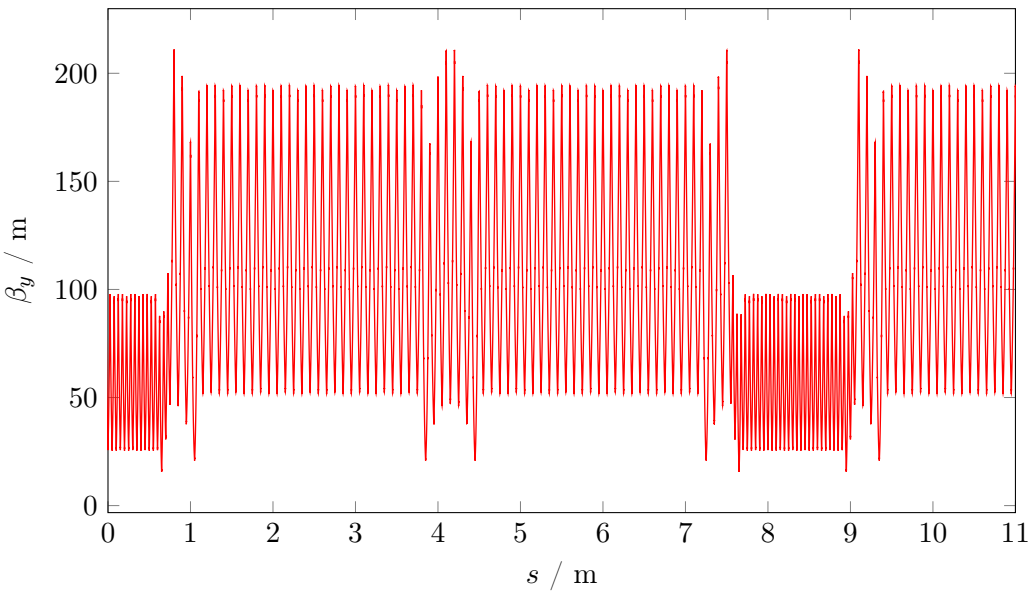

(a) Vertical beta function

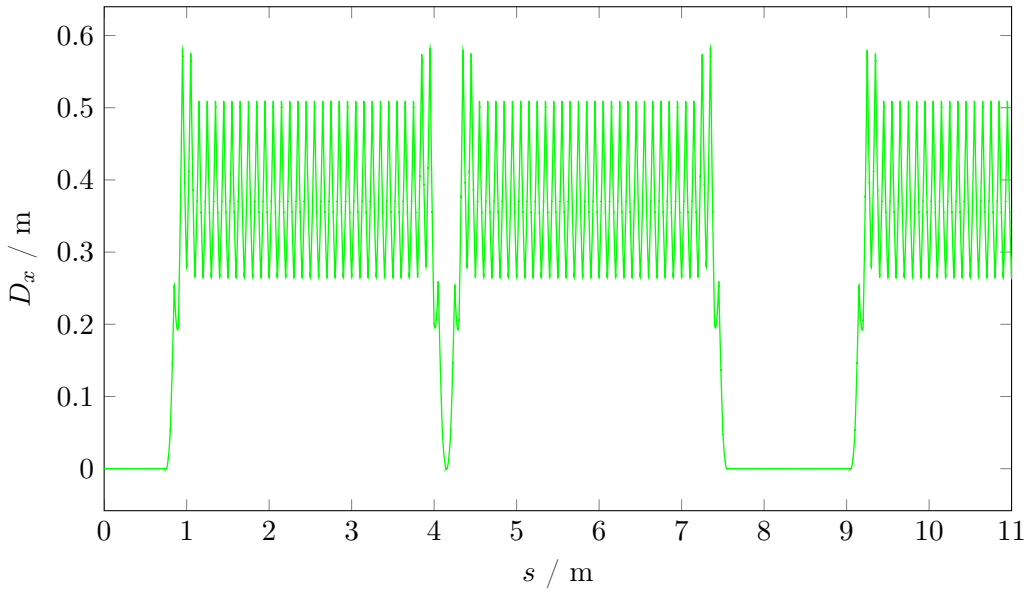

(b) Horizontal dispersion function

Figure 3.6: Vertical beta function and horizontal dispersion function in the first 11 km of the 80 km version of the lattice with 12-fold Layout and 100 m FODO cell length in the arcs. The beta functions increase, as expected, by a factor of two in the arc sections. To allow a clear view only the beta function of one plane is presented. The dispersion increases even by a factor of four, which results in the aimed emittance increase. The dispersion suppressors in the middle of the arc were included to allow additional RF sections, if required.

were used to provide a smooth transition between the two different periodic solutions of the beta functions. Fig. 3.6 presents the matched optics in the first 11 km of the 80 km-12-fold lattice. The vertical beta function in Fig. 3.6 (a) nicely shows the different period length of the betatron oscillation and the increase of the beta functions arising from the different length of the FODO cells. The irregularity of the beta function in the middle of the arc is created by the dispersion suppressor, which were installed in the beginning to allow installation of additional RF section if required. As shown in Fig. 3.6 (b) the dispersion reaches zero in the middle of the arc.

The change of the beta functions inevitably results in a modification of the tune, which according to Eq. (1.12) was defined as the integral of $1/\beta$. The beta functions increase because the focusing of the quadrupoles in the arc sections is weaker. As a consequence, the tune decreases from $Q_x = 495.05$ to 296.68 in the horizontal plane and from $Q_y = 329.45$ to 204.75 in the vertical plane.

The horizontal beam emittance calculated by MAD-X for the lattice with 100 m cell length is $\epsilon_x = 1.70\,\text{nm rad}$. Including a factor of two margin for emittance increase due to alignment errors, this value is even closer to the baseline value of $\epsilon_x = 1.65\,\text{nm rad}$ than the previously estimated value using Eq. (3.2) (1.74 nm rad).

3.1.3 Modification of the phase advance

A second possibility to modify the dispersion function without repositioning or even recabling elements is to change the phase advance per FODO cell by modifying the gradients of the quadrupoles. To demonstrate the effect of the phase advance on the dispersion function and thus the beam emittance, the optics of the FCC-ee FODO cell was matched to different values of the phase advance in the range from $\varphi = 20°$ to 130°. While the phase advance of the regular FCC-ee FODO cell is set to 90° in the horizontal and 60° in the vertical plane, for this scan the same phase advance in both planes was chosen for stability reasons. This also allows to compare the MAD-X results with the analytical values expected from Eq. (3.6), which was derived under exactly this assumption. Fig. 3.7 shows the resulting maximum and minimum values of the dispersion function calculated by MAD-X and the functions of Eq. (3.6). Both minimum and maximum values of the dispersion function increase quickly for phase advances below $\varphi = 40°$, because the denominator in Eq. (3.6) $\sin^2(\varphi/2) \to 0$ for $\varphi \to 0$. Even though the analytical formula assumes thin lenses, the agreement of the values is very good. Only for phase advances below 60° the MAD-X results deviate slightly. In order to obtain a considerable increase of the dispersion function and thus the emittance, the phase advance must be decreased to values in the range of $\varphi = 20°$ to 40°.

The largest emittance increase from $\epsilon_x = 0.07\,\text{nm rad}$ to 14.60 nm rad has to be achieved for 45.5 GeV, which is why it was decided to investigate the correlation of phase advance

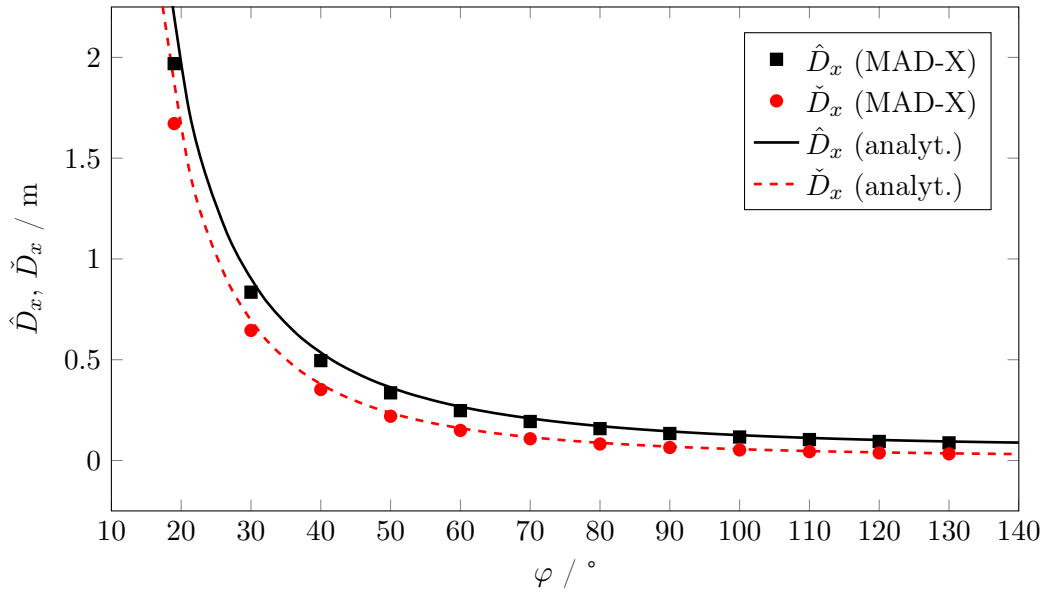

Figure 3.7: Maximum and minimum horizontal dispersion of an FCC-ee FODO cell for different FODO cell phase advance.

and emittance at this beam energy. In addition to the analytical calculations, the emittance of the FCC-ee lattice was calculated for the FCC-ee model in MAD-X. Since the emittance calculation in MAD-X takes both synchrotron radiation and re-acceleration of the particles into account, the straight sections with the RF installation has to be included in the lattice. Therefore the modification of the phase advance in the arc FODO cells requires for each step considered a careful re-matching of the dispersion suppressors in order to sustain a valid periodic optics. As the phase advance varies in a wide range, a quadrupole-based dispersion suppressor is not capable of providing a stable solution in all cases. Instead, the two-cell dispersion suppressor described in Sec.2.2.2 had to be implemented in addition. The hereby resulting geometric modifications of the layout were neglected in this very case.

The scan of the FODO cell phase advance reached from $\varphi = 19°$ to 136°. For smaller or larger values the matching of the FODO cell did not converge successfully. The resulting horizontal emittances as a function of the phase advance are shown in Fig. 3.8. To allow a detailed view only the values from $\varphi = 19°$ to 90° are presented. For phase advances below 30° the emittance increases rapidly. The analytically calculated values of Eq. (3.2) are shown as the dotted line for comparison and indicate a more moderate emittance growth. However, Eq. (3.2) is an approximation, which does not include effects for extreme situations. For example, as a side-effect at small values of the phase advance, the energy loss per turn U_0 seems to be correlated to the increase of the dispersion and emittance as well. For a better understanding of this behaviour, the optics at the upper and lower limit of the phase advance were studied in detail.

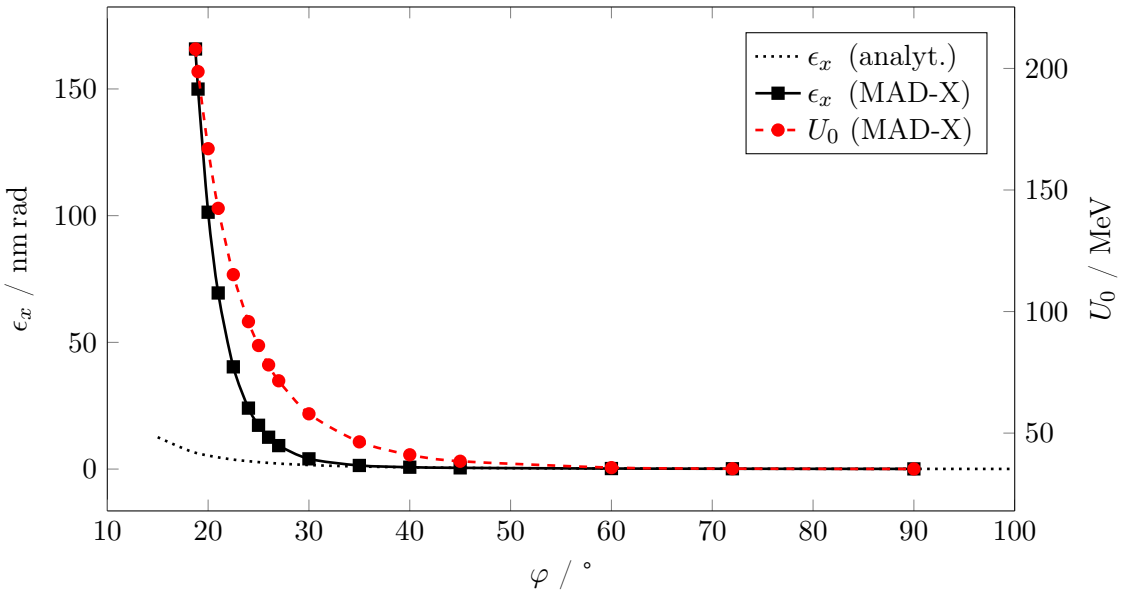

Figure 3.8: Horizontal emittance of the 80 km 12-fold Lattice at 45.5 GeV beam energy and energy loss per turn for different phase advances. The values calculated by MAD-X were connected to guide the eye. The values expected from Eq. (3.6) are given by the dotted line for comparison.

Upper phase advance limit: A large phase advance is created by strong focussing of the beam in the quadrupoles, which corresponds to a short focal length. The minimum acceptable focal length for stable particle motion depends on the length of the FODO cell. To provide a periodic solution of the equation of motion the lattice needs to fulfill the so-called *stability criterion*: the trace of the transport matrix $\mathbf{M}$ describing the lattice must be smaller than two:

$$\mathrm{tr}(\mathbf{M}) < 2 \tag{3.7}$$

The transport matrix of a FODO cell can be obtained by the multiplication of the matrices describing focusing quadrupole - drift - defocusing quadrupole - drift [36]. The trace of this matrix is in thin lens approximation given by

$$\mathrm{tr}(\mathbf{M}_{FODO}) = 2 + \frac{L^2}{f_1 f_2} - 2L\left(\frac{1}{f_1} + \frac{1}{f_2}\right), \tag{3.8}$$

where f_1 is the focal length of the first quadrupole, f_2 is the focal length of the second quadrupole and L is the cell length. Since in this case the quadrupoles have the same gradients ($f_1 = f_2 = f$) Eq.(3.7) and Eq.(3.8) lead to following requirement as a limit for particle stability in FCC-ee:

$$f > \frac{L}{4} = 12.5\,\mathrm{m} \quad \text{or} \quad k_1 < 0.053\,\frac{1}{\mathrm{m}^2} \tag{3.9}$$

Although the calculations of the FCC-ee lattice include elements of finite length and non-linear contributions from sextupole magnets, the agreement with the expectations from the linear approximation is very accurate: the normalised quadrupole strengths in the lattices with the largest stable phase advances are

$$k_1(\varphi = 120^\circ) = 0.047\,\frac{1}{\mathrm{m}^2},$$
$$k_1(\varphi = 130^\circ) = 0.049\,\frac{1}{\mathrm{m}^2},$$
$$k_1(\varphi = 136^\circ) = 0.050\,\frac{1}{\mathrm{m}^2}.$$

The required quadrupole strengths for a FODO cell phase advance of $\varphi = 140^\circ$ are already too close to the upper limit and the lattice is not stable any more. Therefore, a maximum phase advance of $\varphi = 135^\circ$ per FODO cell is considered as a feasible limit for FCC-ee.

Lower phase advance limit: As mentioned before, the dispersion function increases rapidly for values of the phase advance below $\varphi = 40^\circ$. For $\varphi = 19^\circ$ phase advance per cell the dispersion function reaches a maximum value of $D_{x,\mathrm{max}} = 2.00\,\mathrm{m}$ while it was only $D_{x,\mathrm{max}} = 0.13\,\mathrm{m}$ in the case of 90° phase advance per cell. It has to be emphasised that as a consequence of this considerable increase the sawtooth amplitude for a given beam energy becomes more than ten times larger than for $\varphi = 90^\circ$ phase advance. As the magnetic field in the quadrupoles increases linearly with the distance from the centre, particles with larger orbit offset experience stronger fields. The consequence is a considerable increase of the energy loss due to synchrotron radiation, as presented in Fig. 3.8, because of the larger deflection. The additional energy loss modifies the local particle energy and increases the sawtooth amplitude even further.

The sawtooth orbits for different FODO cell phase advances are compared in Fig. 3.9 and Fig. 3.10. Fig. 3.9 shows the orbit in the lattice with $\varphi = 90^\circ$ phase advance per cell, where the amplitude of the sawtooth is about $\pm 4\,\mu\mathrm{m}$. As shown in Fig. 3.10 the sawtooth amplitude reaches 25 µm for 35° phase advance and 50 µm for 30°. For a phase advance of 20° the orbit excursions become larger than 200 µm. In addition to the larger energy loss such sawtooth amplitudes bring a second complication: the feed-down of the sextupole fields, which are used to correct the linear chromaticity, creates an additional quadrupole field and results in a perturbation of the optics. The orbits presented in Fig. 3.10 show an increasing distortion for reduced phase advance and larger sawtooth amplitudes. In order to prevent a negative influence on the optics a minimum phase advance in the range of $\varphi = 35^\circ$ to 40° is considered as a reasonable limit.

As discussed before, the dispersion function was increased to obtain a larger emittance. This results in a larger beam size, which according to Eq. (1.9) reaches values of up to

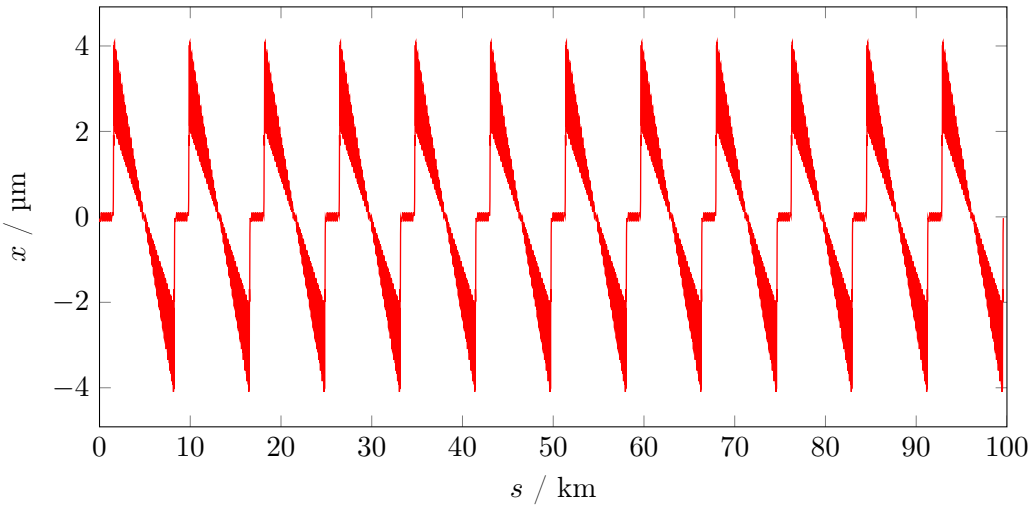

Figure 3.9: Horizontal orbit for 45 GeV beam energy in the FCC-ee lattice with 12-fold Layout without interaction regions and 90° FODO cell phase advance.

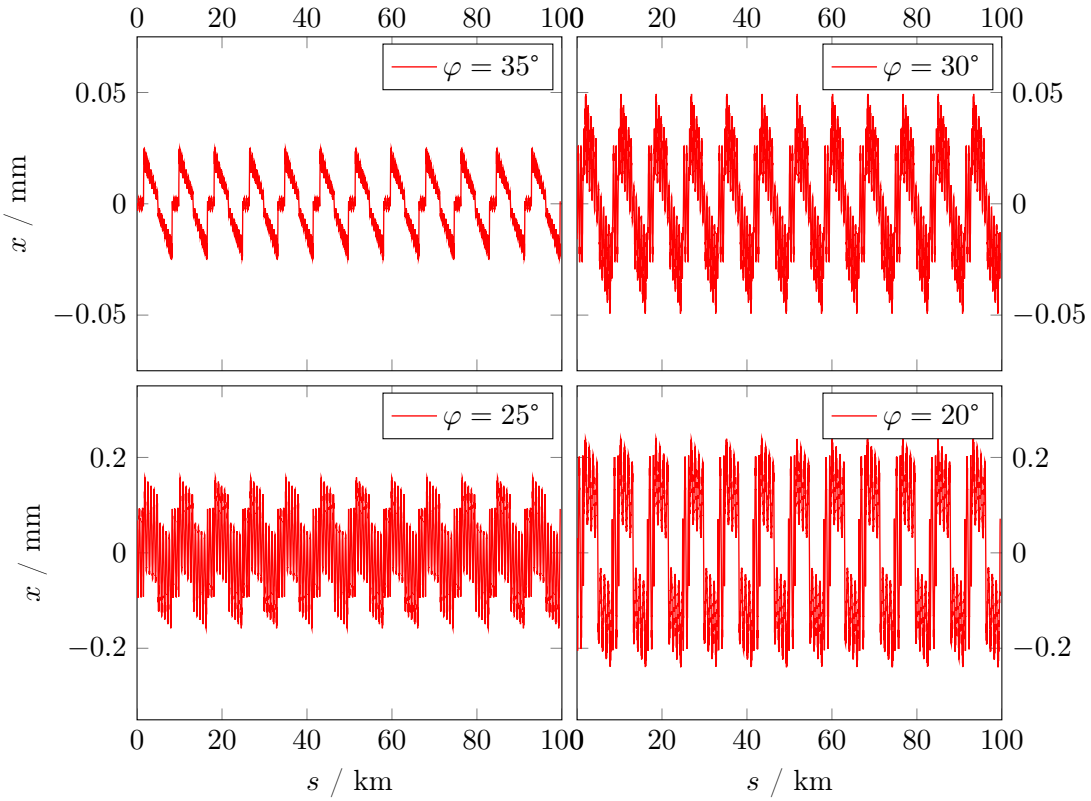

Figure 3.10: Horizontal orbit for 45 GeV beam energy in the FCC-ee lattice with 12-fold Layout without interaction regions for different FODO cell phase advances close to the lower limit.

$\sigma_x = 5.18\,\text{mm}$ for $\varphi = 19°$ phase advance compared to the beam size $\sigma_x = 0.07\,\text{mm}$ in the case of 90° phase advance of the standard cell. However, in lepton storage rings the emission of synchrotron radiation photons creates a considerable energy spread of the beam. Eq. (1.9) therefore needs to be expanded by a term, which takes the energy spread of the beam and the resulting blow-up into account:

$$\sigma_x = \sqrt{\epsilon_x \beta_x + \left(\frac{\Delta p}{p} D_x\right)^2} \tag{3.10}$$

For FCC-ee with 45.5 GeV beam energy synchrotron radiation and beamstrahlung lead to an estimated energy spread of $\Delta p/p \approx 0.1\,\%$ [16], which increases the beam size by 60 µm to $\sigma_x = 5.24\,\text{mm}$. While the increase of the beam size is small, such a large beam size in general would require an unreasonably large magnet aperture and therefore seems not to be feasible.

In addition to the previously discussed reasons, it was decided to choose a phase advance larger than 40° because of considerations for beam stability in terms of lattice imperfections. At operation below that value the beam emittance becomes very sensitive to tune shifts. Already small variations of the phase advance have a large impact on the emittance at 45.5 GeV beam energy:

$$\begin{aligned} \varphi = 24° = 0.067 \times 2\pi: &\qquad \epsilon_x = 24.05\,\text{nm rad} \\ \varphi = 25° = 0.069 \times 2\pi: &\qquad \epsilon_x = 17.28\,\text{nm rad} \\ \varphi = 26° = 0.072 \times 2\pi: &\qquad \epsilon_x = 12.57\,\text{nm rad} \end{aligned}$$

However, since the arc optics should allow a multi-family sextupole scheme for higher-order chromaticity correction it is mandatory to keep certain phase advance relations between the sextupoles. Therefore the phase advance per cell cannot be chosen freely. Values that allow sextupole schemes with $\varphi = n \times \pi$ phase advance between two sextupoles of one family are for example $\varphi = 90°$, 45°, 72° or 60°.

3.1.4 Lattice for 80 GeV beam energy with 45° phase advance per cell

For operation at 80 GeV beam energy the horizontal emittance needs to be increased from $\epsilon_x = 0.21\,\text{nm rad}$ to 1.65 nm rad. A first lattice with an increased length of the FODO cells in the arc sections has already been proposed earlier in this section. However, an alternative configuration with modified phase advance per FODO cell was studied in addition. To obtain the required emittance value, estimations with Eq. (3.2) suggest to decrease the FODO cell phase advance from $\varphi = 90°$ to 45° in both planes. The estimated emittance would then be $\epsilon_x = 1.50\,\text{nm rad}$. The phase advance is still above the recommended limit and allows to install a multi-family sextupole scheme.

To set up a valid lattice the geometry must be compatible to the regular lattice for 175 GeV. The regular dispersion suppressor based on two half-bend cells therefore needs to replaced by a quadrupole-based dispersion suppressor scheme. As mentioned earlier, a minimum of six quadrupoles is required to connect the optical functions of the new arc lattice with the optics based on the 50 m FODO cells in the straight sections. The resulting optics in the dispersion suppressors is shown in Fig. 3.11 (a). For this optics solution the polarity of two quadrupoles had to be reversed and the beta functions reach values of about 350 m in both planes. In order to obtain a more regular quadrupole configuration and lower beta functions a second scheme was implemented: an additional FODO cell was assigned to the dispersion suppressor, which increases the number of quadrupoles and thus degrees of freedom to eight. The optics of this second approach is shown in Fig. 3.11 (b). The two additional quadrupoles allowed to considerably decrease the maximum value of the beta functions to 140 m. Fig. 3.12 shows the optics in the first 11 km of the whole lattice. Fig. 3.12 (a) presents the vertical beta function and (b) the horizontal dispersion function.

The decrease of the phase advance in the arc cells affects of course the transverse tunes. In the horizontal plane it reduced from $Q_x = 495.05$ to 294.25, which is basically the same value as in the lattice with 100 m cell length for obvious reasons. In the vertical plane the tune reduced from $Q_x = 329.45$ to 260.25, which is 55 units larger than in the alternative lattice. In both planes a fine-tuning will have to be applied for exact matching of the non-integer part of the tune. The horizontal beam emittance calculated by MAD-X is $\epsilon_x = 1.47\,\text{nm rad}$, in nice agreement with the analytical value of 1.50 nm rad.

3.1.5 Lattices for 45.5 GeV beam energy

For the lowest beam energy of 45.5 GeV the beam emittance has to be increased to $\epsilon_x = 14.60\,\text{nm rad}$ to limit the beam-beam tune shift. A FODO cell phase advance of 25° would produce an emittance value of $\epsilon_x = 17.28\,\text{nm rad}$, however, following the previous discussions this phase advance is below the recommended minimum. Therefore the emittance increase has to be accomplished by a modification of the cell length or a combination of increased cell length and smaller phase advance. In any case, the cell length must be a multiple of 50 m and the phase advance must allow the installation of sextupole families. Three lattice arrangements were studied, that fulfill those requirements:

1. $L = 200\,\text{m}$ and $\varphi_{x,y} = 60°$
2. $L = 250\,\text{m}$ and $\varphi_{x,y} = 72°$
3. $L = 300\,\text{m}$ and $\varphi_x = 90°$ and $\varphi_y = 60°$

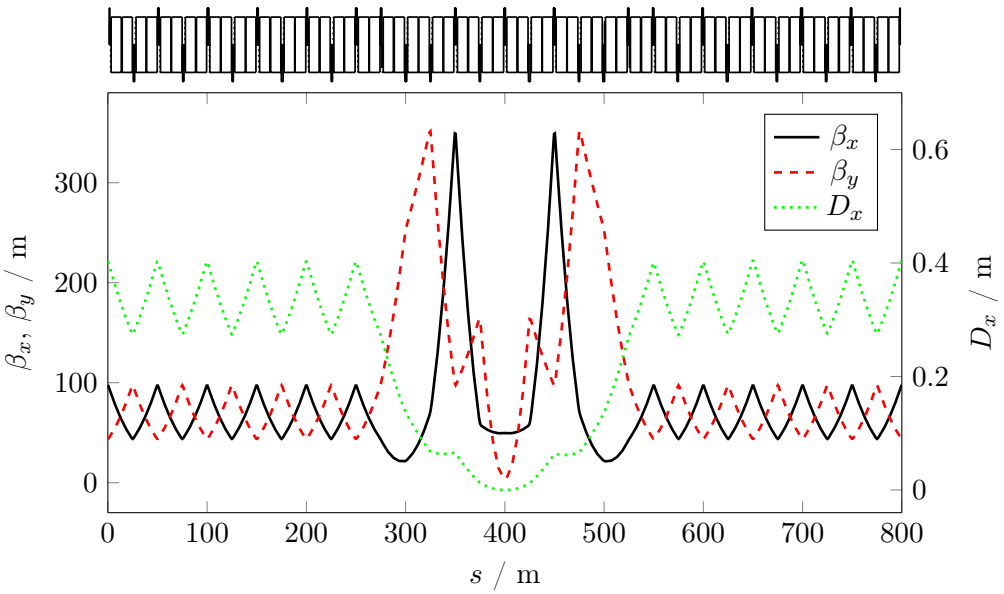

(a) Quadrupole-based dispersion suppressor scheme consisting of six quadrupoles

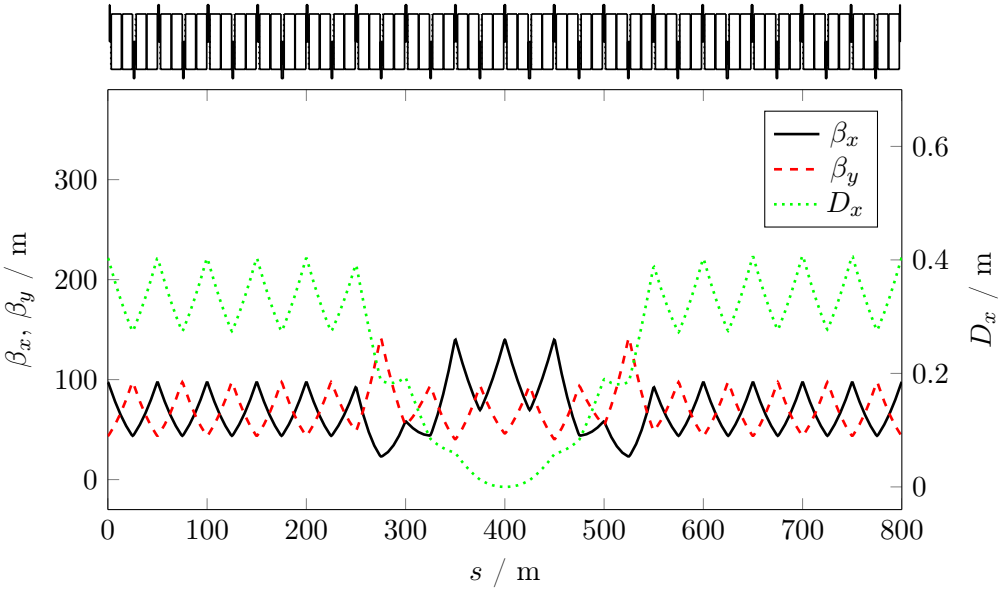

(b) Quadrupole-based dispersion suppressor scheme consisting of eight quadrupoles

Figure 3.11: Beam optics of different quadrupole-based dispersion suppressor schemes for $\varphi = 45°$ phase advance in the arc FODO cells. A minimum of six free quadrupoles is needed to provide sufficient degrees of freedom. The according optics are shown in (a). Two additional quadrupoles per dispersion suppressor allow to reduce the maximum value of the beta functions as shown in (b).

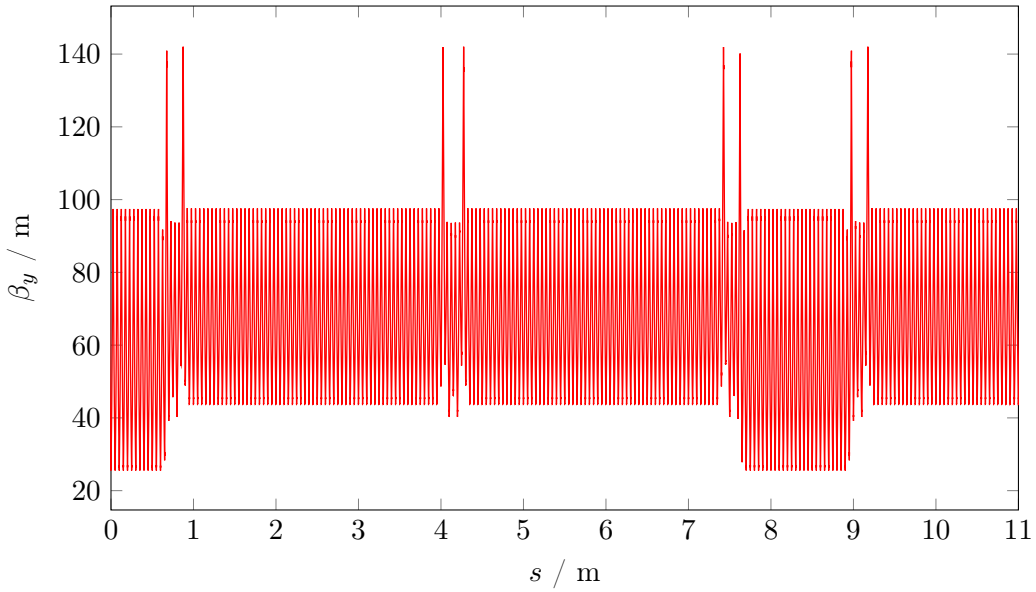

(a) Vertical beta function

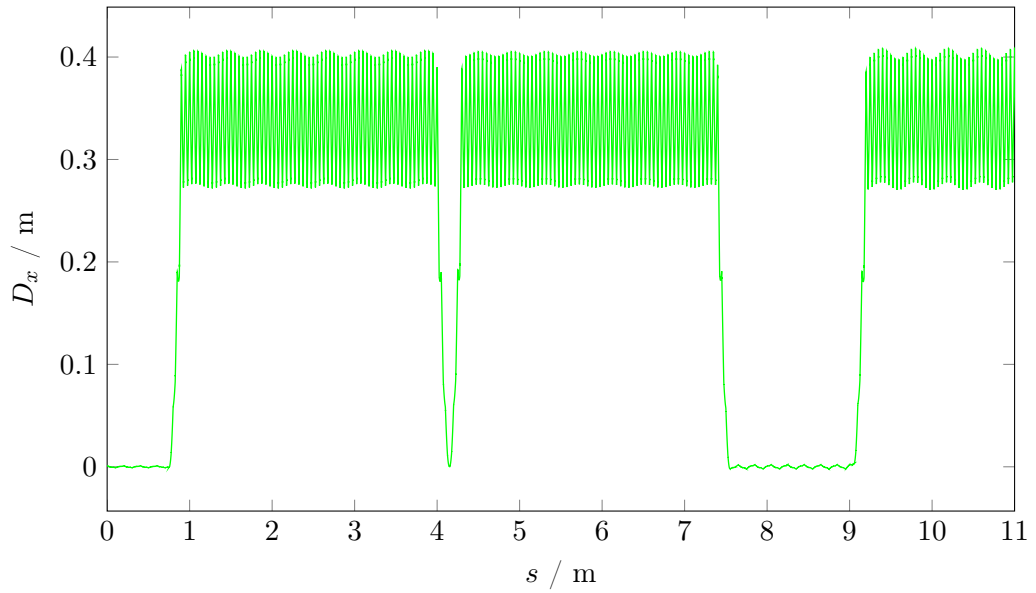

(b) Horizontal dispersion function

Figure 3.12: Optics of the first 11 km of the 12-fold lattice. (a) shows the vertical beta function and (b) the horizontal dispersion function.

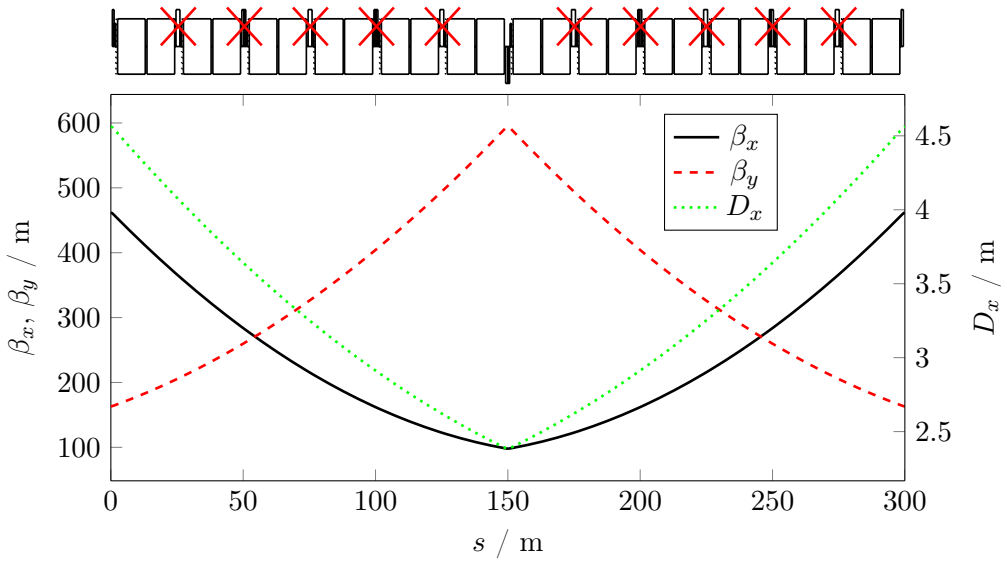

Figure 3.13: Beta functions and horizontal dispersion function in the modified FODO cell with a length of 300 m and the regular phase advance of 90° in the horizontal plane and 60° in the vertical plane. The red crosses mark the quadrupoles, which are switched off. The beta functions increased by a factor of six according to Eq. (2.1), the dispersion by a factor of about 35.5, since it depends on the square of the cell length.

The last option was chosen to be discussed in detail, because in this case the emittance increase was achieved only by a modification of the cell length and the phase advances can stay the same. The beta functions and the horizontal dispersion function for the 300 m FODO cell are presented in Fig. 3.13. The vertical beta function reaches a maximum value of 594 m, the dispersion function 4.6 m. According to Eq. (2.1) the beta functions increased by a factor of six compared to the 50 m long FODO cell, the dispersion even by a factor of about 35.5, since it depends on the square of the cell length (see Eq. (2.2)).

As in the previously discussed lattices for 80 GeV beam energy, the dispersion suppressors need to be modified and re-optimised for each case. Six free quadrupoles were sufficient to match the optics, thus no additional degrees of freedom were required. In order to fit the available number of FODO cells, two of the dispersion suppressor cells have a length of 200 m and for the third one 250 m cell length has been chosen. The optics of the first 11 km of the 80 km-12-fold lattice are presented in Fig. 3.14. The arcs now only consist of 2×7 regular FODO cells. As a direct consequence the tunes are reduced and values of $Q_x = 158.9$ in the horizontal plane and $Q_y = 101.1$ in the vertical plane are obtained.

The emittance calculation with MAD-X yields $\epsilon_x = 14.2\,\text{nm rad}$, which is even closer to the design value of 14.6 nm rad than the analytically estimated value of 15.2 nm rad.

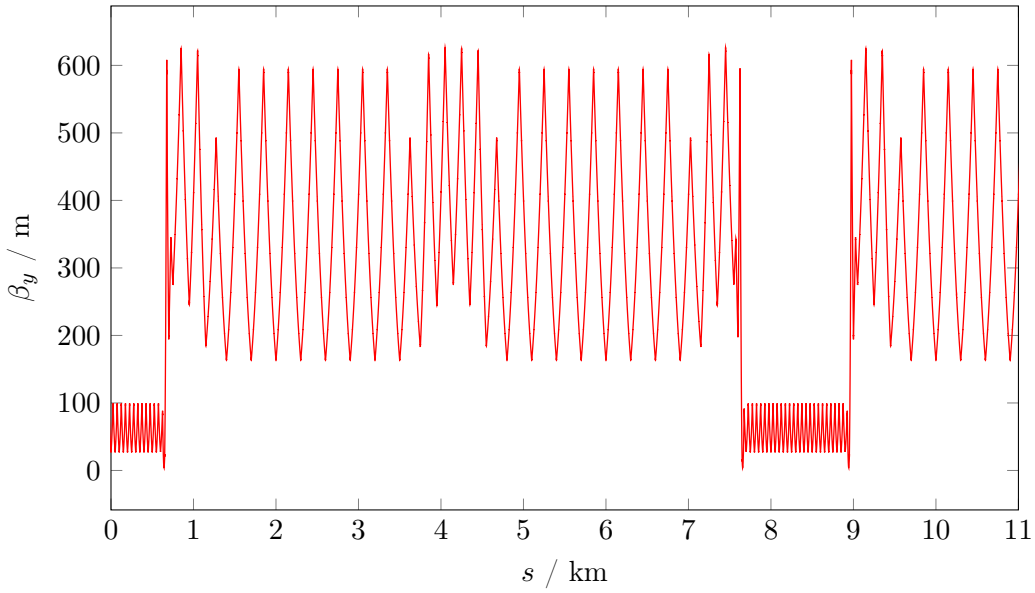

(a) Vertical beta function

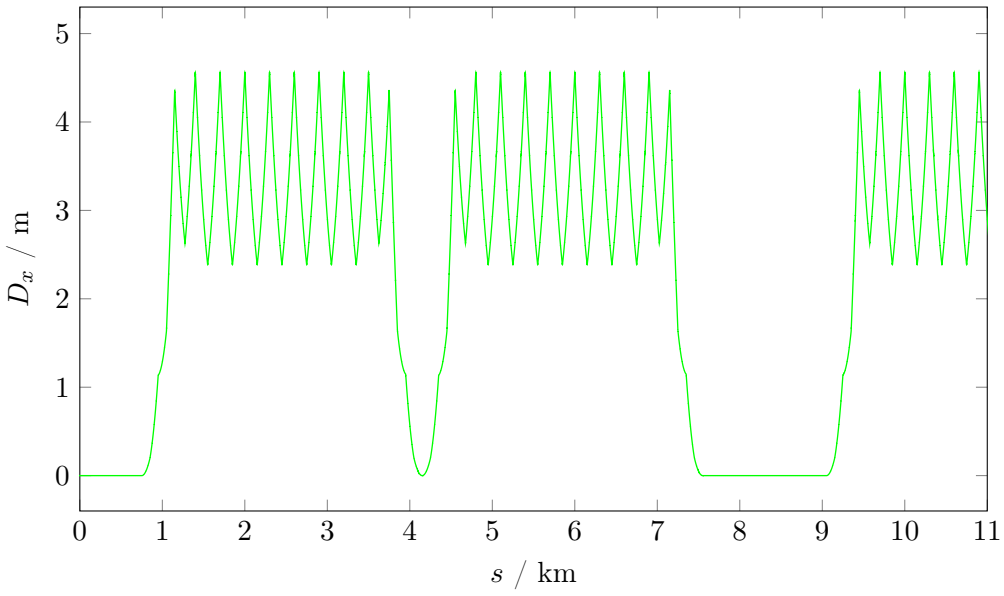

(b) Horizontal dispersion function

Figure 3.14: Optics in the first 11 km of the 12-fold Lattice with 300 m cell length in the arcs. (a) shows the vertical beta function and (b) the horizontal dispersion function.

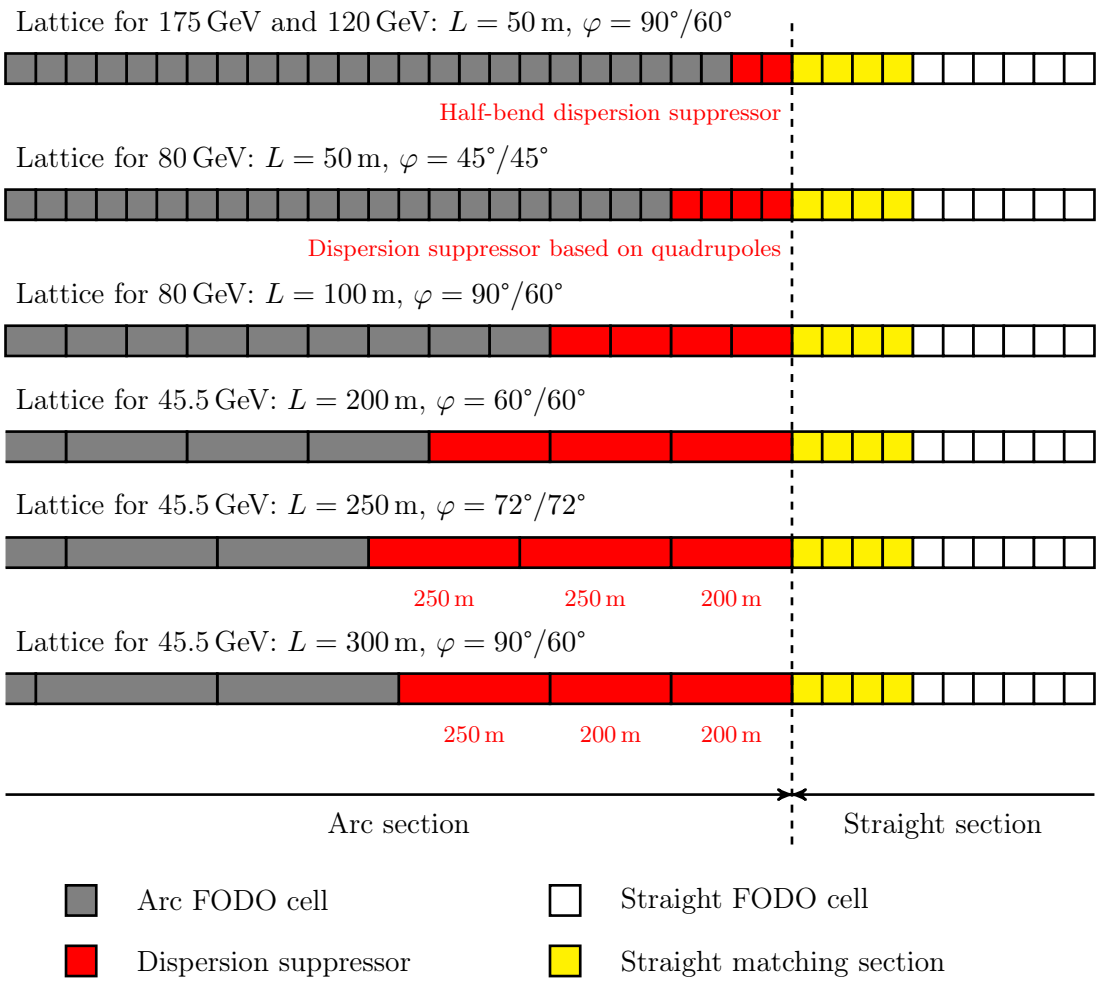

Figure 3.15: Illustration of the lattices proposed for the different beam energies of FCC-ee. Every box symbolises a FODO cell. Starting from the lattice with 50 m cell length designed for the highest beam energies of 175 GeV and 120 GeV the cell length in the arcs is increased in order to increase the beam emittance. The cell length in the straight section is kept constant.

3.1.6 Summary of lattice modification options for FCC-ee

For both 80 GeV beam energy and 45.5 GeV beam energy several options of lattice modifications were studied in order to compensate for the natural shrinking of the emittance with the beam energy and thus to increase the beam emittance to limit the beam-beam tune shift. For 80 GeV two optics are proposed, one with an increased FODO cell length of 100 m and one with half the phase advance per FODO cell. For 45.5 GeV beam energy it is not recommended to increase the beam emittance only by reducing the FODO cell phase advance. Values as small as only 25° would have been needed, which would increase the energy loss, lead to optics distortions and a high sensitivity to tune variations due to lattice imperfections. Therefore lattices with increased cell lengths in the range from 200 m to 300 m are proposed instead. The lattices with 200 m and 250 m cell length in addition require a modification of the phase advance.

Summarising the situation, all five lattices are compared in Fig. 3.15 and Tab. 3.2. Fig. 3.3 illustrates the increase of the cell lengths. The gray boxes symbolise the FODO cells in the arcs, the white boxes the FODO cells in the straight sections. The dispersion suppressor regions are marked in red and the matching sections in the straight section in yellow. While the cell lengths in the straight sections stay the same, the length of the FODO cells is increased for the low energy lattices in order to increase the beam emittance. In the case of 250 m and 300 m length of the regular arc cells, the lengths of the dispersion suppressor cells had to be adapted in order to fit the number of available cells in the arc.

3.2 Vertical emittance

In an ideal circular storage ring the dispersion function and its derivative are zero in the vertical plane. Lepton beams therefore do not experience quantum excitation, which has the result that the vertical equilibrium beam emittance is dominated by radiation damping. By the nature of this effect lepton storage rings therefore feature flat beams. The ultimate minimum of ϵ_y is determined by the so-called *quantum limit*, which means the only vertical momentum of the particles is created by the emission of the synchrotron radiation photons in an opening angle given by $1/\gamma$ [26], where γ is the Lorentz factor. However, in a real machine other effects play a role and the vertical emittance e.g. is increased as a result of alignment errors of the lattice elements. Transverse misalignments of quadrupoles create extra dipole kicks, which create a non-zero vertical dispersion. According to Eq. (1.38) the value of the fifth synchrotron radiation integral increases, which immediately results in a larger equilibrium emittance. The second effect, that leads to vertical emittance growth, is coupling between the transverse planes. If the particle motion is coupled, momentum is transferred from one plane to the other. The consequence is a decreased particle density in phase space and thus a larger beam emittance. The main sources of coupling in the

Table 3.2: Comparison of the parameters of the lattices based on different FODO cell layouts and the design parameters. The listed parameters are the cell length L, the phase advances per cell φ_x and φ_y, the equilibrium emittance ϵ_x, the energy loss per turn U_0, the momentum compaction factor α_c, the maximum values of horizontal and vertical beta functions $\hat{\beta}_x$ and $\hat{\beta}_x$ as well as the maximum horizontal dispersion $\hat{D}_x$ and the maximum horizontal beam size $\hat{\sigma}_x$.

	80 GeV		
L (m)	100	50	
φ_x, φ_y (°)	90, 60		
ϵ_x (nm rad)	1.70	1.47	
U_0 (MeV/turn)	337.03	337.03	
α_c (10^{-5})	2.22	1.99	
$\hat{\beta}_x$ (m)	181.54	141.47	
$\hat{\beta}_y$ (m)	211.05	141.68	
$\hat{D}_x$ (m)	0.58	0.41	
$\hat{\sigma}_x$ (mm)	0.56	0.46	
	45.5 GeV		
L (m)	200	250	300
φ_x, φ_y (°)	60, 60	72, 72	90, 60
ϵ_x (nm rad)	12.5	14.5	14.2
U_0 (MeV/turn)	35.3	35.3	35.3
α_c (10^{-5})	1.69	1.86	1.81
$\hat{\beta}_x$ (m)	366.5	465.71	554.0
$\hat{\beta}_y$ (m)	407.92	477.70	626.43
$\hat{D}_x$ (m)	4.02	4.87	4.56
$\hat{\sigma}_x$ (µm)	2.14	2.60	2.98

case FCC-ee are vertical orbit offsets in the sextupole magnets and errors in the angular alignment of the quadrupoles. In case of collider rings other large sources of coupling are the solenoid fields in the experiments, which are required for the momentum measurements of the created particles inside the detector. Usually these solenoid fields are quire strong and therefore have to be compensated.

In order to maximise luminosity, the design of FCC-ee aims for the very ambitious emittance ratio of

$$\frac{\epsilon_y}{\epsilon_x} = 0.001$$

requiring a vertical emittance of 2 pm rad. Such a small value is comparable with state-of-the-art synchrotron radiation light sources such as ESRF [19] or the Australian Light Source [18]. While light sources are compact machines with circumferences in the order of some hundred meters, which allows to use special girders to pre-align the lattice elements, FCC-ee has a circumference of 80-100 km. Therefore, in the context of this thesis a very first study of the effect of misalignments was undertaken to evaluate, if the desired emittance ratio is feasible assuming today's alignment and correction techniques. The effect of quadrupole misalignments on the vertical emittance was investigated for both the 80 km and the 100 km 12-fold lattice at 175 GeV beam energy. In order to follow a realistic approach, transverse alignment errors are introduced in the lattice and the orbit is corrected in several iterations.

The dipolar field created through the feed-down of a misaligned quadrupole with length L_Q leads to a modification of the angular coordinate

$$\Delta x' = k_1 \, \Delta x L_\mathrm{Q}. \tag{3.11}$$

The orbit distortion created by a single quadrupole is then given by [49]

$$x_\mathrm{c}(s) = \frac{\sqrt{\beta(s)}}{2 \sin Q\pi} \Delta x' \sqrt{\beta(s_0)} \cos\Big[\psi(s) - \psi(s_0) - Q\pi\Big] \tag{3.12}$$

and depends on the square root of both the local beta function $\sqrt{\beta(s)}$ at the observation point and the beta function at the place of the misaligned element $\sqrt{\beta(s_0)}$. As the beta function reaches maximum values in the final focus quadrupoles, they not only amplify the orbit distortions created in the rest of the lattice, but also require best alignment precision. As a first step, only the effect of misalignments in the arc lattice was studied and the mini-beta insertions were replaced by regular straight FODO cells.

Although alignment techniques will hopefully improve over the next 20 years, a worst case scenario using today's alignment precision was done. For LHC the relative rms tolerance of transversal alignment is 0.15 mm and the angular precision is 0.1 mrad [50]. Gaussian-distributed transverse misalignments with a maximum of three σ were introduced to all quadrupoles in both planes. After each quadrupole a beam position monitor and a small

dipole magnet for orbit corrections was installed. The number of orbit correctors thus foreseen in FCC-ee is 1620 per plane.

Starting from an uncorrected orbit, the amplification factor of the misaligned quadrupoles on the orbit amplitudes are so big that a possible solution for the orbit, a so-called *closed orbit*, cannot be determined. Therefore a step-by-step procedure has been used: in a first step the orbit without periodic boundary conditions is calculated as presented in the top picture of Fig. 3.16 for the horizontal plane. Starting on the ideal orbit the transverse offset increases and reaches amplitudes of more than 20 mm. After three iterations of orbit corrections a closed orbit was found and periodic calculations became possible. A fourth iteration could reduce the transverse orbit displacement to about 0.3 mm. The resulting orbit shown in the middle picture of Fig. 3.16 allows now to correct the linear chromaticity with the sextupoles. The final step is to include the RF cavities and the energy loss due to synchrotron radiation, which are required for the EMIT module in MAD-X, that calculates the equilibrium beam parameters. The resulting sawtooth orbit, that has been discussed in the previous section for the ideal lattice, is presented in the bottom picture of Fig. 3.16.

For the 80 km lattice the emittances calculated by MAD-X for the presented error seed are $\epsilon_x = 1.23\,\text{nm rad}$ in the horizontal plane and $\epsilon_y = 1.05\,\text{pm rad}$ in the vertical plane. Compared to the ideal machine the horizontal emittance increased by 0.23 nm rad. The obtained emittance ratio, however, is

$$\frac{\epsilon_y}{\epsilon_x} = 0.00085, \tag{3.13}$$

and thus even below the target value. In the 100 km case the emittances are smaller because of the larger bending radius. The resulting horizontal beam emittance is $\epsilon_x = 0.97\,\text{nm rad}$ and the vertical emittance $\epsilon_y = 0.84\,\text{pm rad}$ leading to the comparable ratio of

$$\frac{\epsilon_y}{\epsilon_x} = 0.00087. \tag{3.14}$$

These very first calculations of the vertical emittance lead to the conclusion, that the aimed emittance ratio of one per mille is achievable with todays's alignment precision. However, to allow an final evaluation the mini-beta quadrupoles need to be taken into account as well. The large beta functions at their location are a challenge for the orbit correction procedure, because they create large contributions to the vertical dispersion function. The impact becomes clear in Fig. 3.17, which shows the vertical orbit in the lattice with mini-beta insertions reaching an amplitude of $y = 1\,\text{m}$. In addition, the effect of angular misalignment and the precision of the coupling correction needs to be further investigated. A more comprehensive study of alignment tolerances is still under investigation. First results were presented in reference [51].

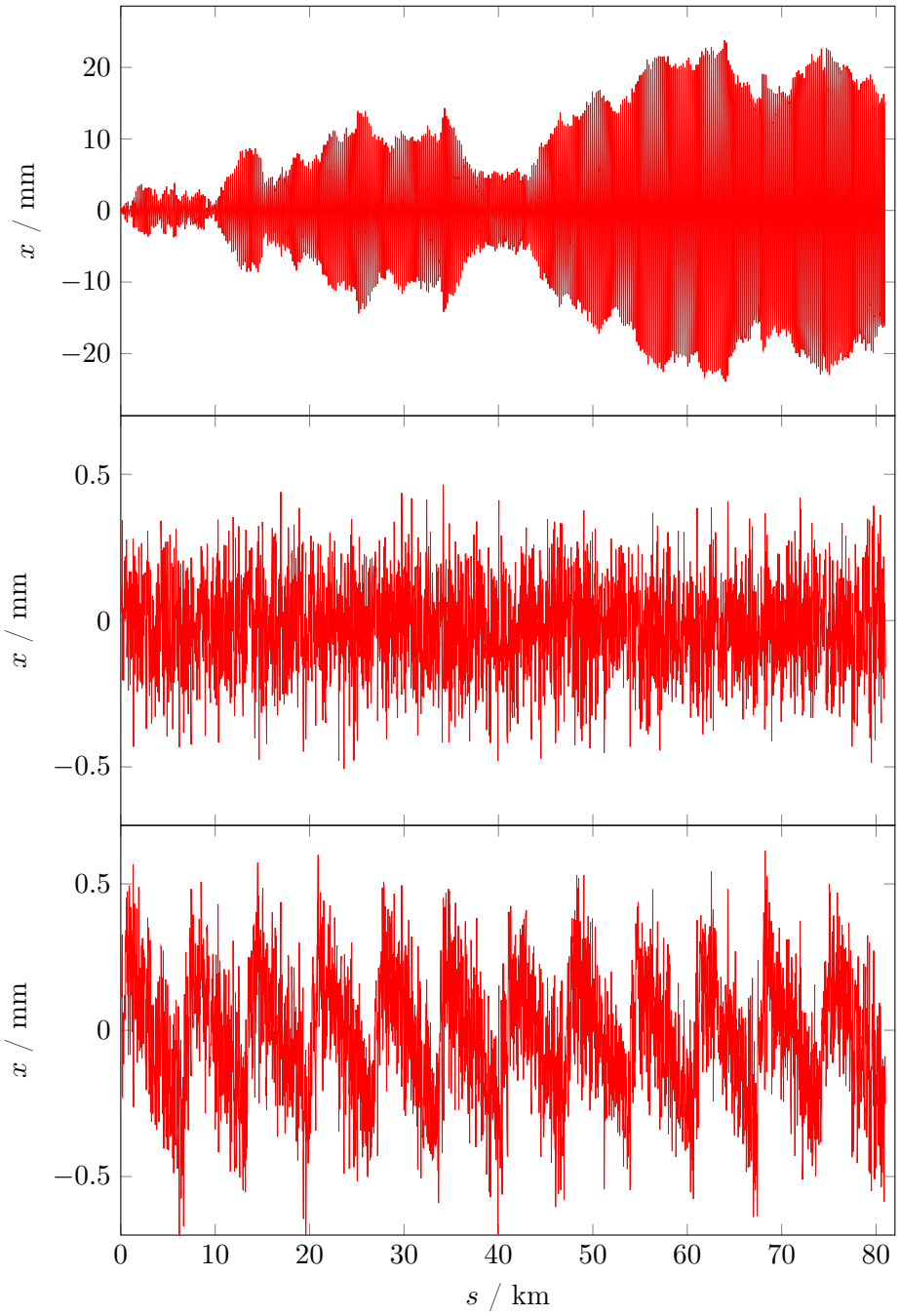

Figure 3.16: Horizontal orbits during with transverse misalignments of the quadrupoles. The top picture shows the uncorrected orbit calculated without periodic boundary conditions. The orbit after four iterations of orbit correction is shown in the middle picture. This stage allowed to correct the linear chromaticity and switch on the radiation effects. The bottom picture presents the resulting sawtooth orbit.

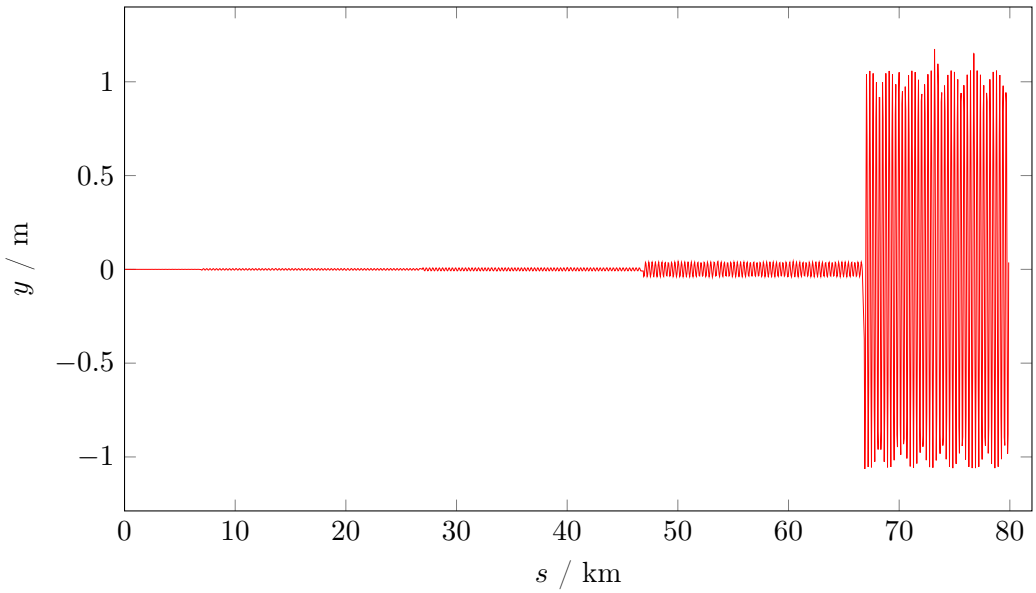

Figure 3.17: Vertical orbit for 175 GeV beam energy in the FCC-ee 12-fold layout. Gaussian distributed, transverse alignment errors with 0.15 mm standard deviation were introduced to the quadrupoles. The orbit was calculated without periodic boundary conditions and shows the increase of the vertical dispersion created by the final focus quadrupoles.

3.3 Emittance fine tuning with wigglers

To allow the precise adjustment of the beam emittance, wigglers were installed in the FCC-ee lattice [45]. If located in dispersion-free sections, they enhance the radiation damping and thus decrease the equilibrium emittance. In this case they are referred to as *damping wigglers*. If they are installed in regions with non-vanishing dispersion, they boost the effect of quantum excitation and are then called *excitation wigglers*. Both types were studied with the aim to vary the horizontal emittance of the lattice with Racetrack Layout by a factor of two.

3.3.1 Installation of damping wigglers

LEP damping wiggler design: As a first approach a wiggler concept based on LEP design was investigated. The wiggler has an overall length of $L = 2.99\,\mathrm{m}$ and consists of three poles as illustrated in Fig. 3.18. The end poles are 0.925 m long while the centre pole has a length of 0.74 m. A maximum field of 1.0 T is foreseen for the centre pole and 0.4 T for the end poles [25].

Assuming the wiggler does neither affect the beta functions nor the dispersion function

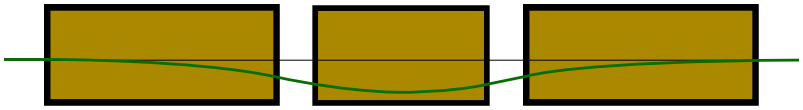

Figure 3.18: Schematic of the damping wiggler with three poles designed for LEP [52].

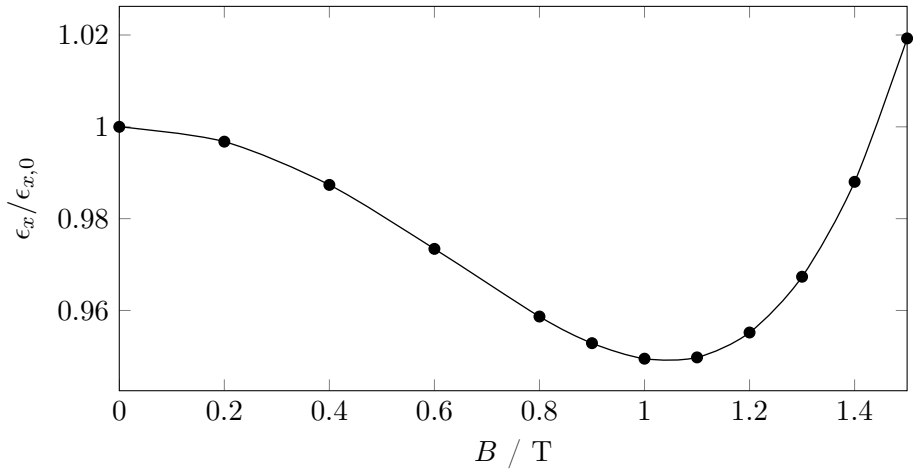

Figure 3.19: Horizontal emittance of the FCC-ee lattice with sixteen LEP-type wigglers for different magnetic fields of the centre pole. The line connects the marks of the discrete calculations.

the effect of the wiggler on the beam emittance can calculated analytically:

$$\epsilon_x = \frac{C_\mathrm{q}\gamma^2}{J_x}\,\frac{I_5}{I_2} = \frac{C_\mathrm{q}\gamma^2}{J_x}\,\frac{I_{5,\mathrm{ring}} + I_{5,\mathrm{wiggler}}}{I_{2,\mathrm{ring}} + I_{2,\mathrm{wiggler}}} \tag{3.15}$$

According to calculations in MATLAB, 200 of these damping wigglers would be required to reduce the emittance by a factor of two, while only 10 excitation wigglers are sufficient to double the emittance [45].

As a next step the effect of the wigglers was calculated with MAD-X. Sixteen wigglers were installed in the dispersion-free straight sections of FCC-ee to study the damping performance. The reduced number of damping wigglers requires stronger dipole fields to achieve the same effect as before. Different magnet strengths of the centre pole were investigated up to $B = 1.5\,\mathrm{T}$. Stronger fields were not considered in order to comply with conventional non-superconducting magnet technology. The strengths of the end poles were adjusted in such way that the total bending angles remained zero. The resulting emittance depending on the field strength of the centre pole is presented in Fig. 3.19.

A minimum emittance of $0.93 \times \epsilon_{x,0}$ can be achieved for the design strengths of the wiggler poles. However, contrary to the expectations, the emittance increases again, if stronger fields are used. This behaviour can be explained by analysing the dispersion function inside the wiggler, which is shown in Fig. 3.22. For a magnetic field of $B = 1\,\mathrm{T}$

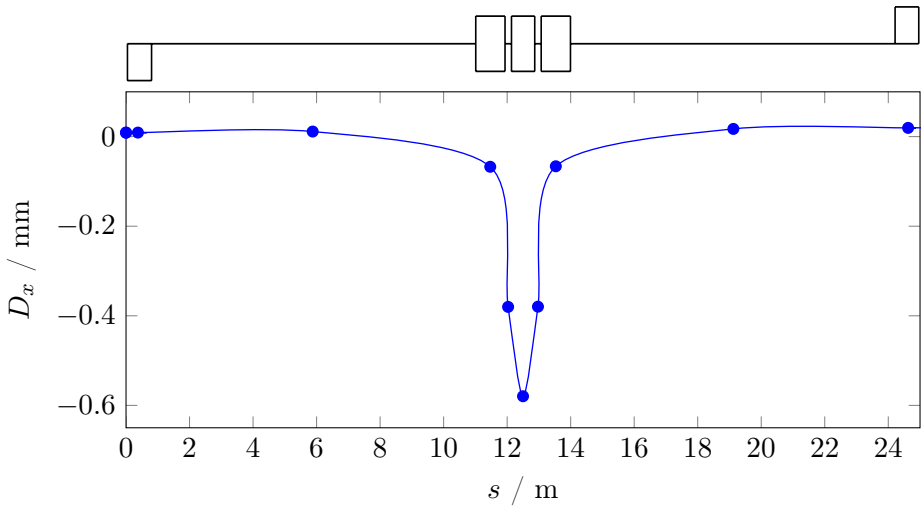

Figure 3.20: Horizontal dispersion function in the first half of a straight FODO cell equipped with a wiggler of LEP design. In the centre pole a maximum value of $D_x \approx 0.6\,\text{mm}$ is reached. For magnetic fields above $B = 1.1\,\text{T}$ the dispersion inside the wiggler results in an undesired quantum excitation effect and an overall emittance increase (see Fig. 3.19).

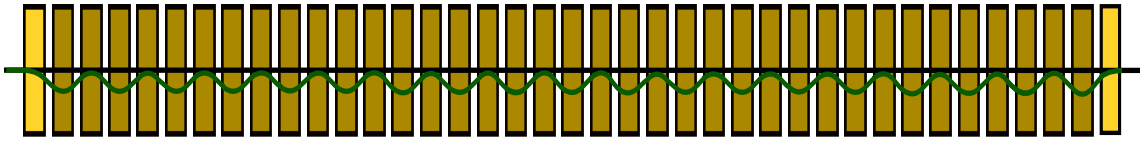

Figure 3.21: Schematic view of the damping wiggler design with 39 poles. The edge poles have only half of the bending field [52].

the dispersion function already reaches a maximum value of $D_x \approx 0.6\,\text{mm}$ in the centre pole. For larger fields this considerable value increases even more and in the end leads to an excitation effect inside the wiggler, that becomes larger than the damping effect.

Wiggler design with 39 poles: To allow larger magnetic fields without increasing the integrated dispersion, the wiggler was optimised towards a larger number of poles. The new design foresees 39 poles with a length of 10 cm and a separation of 2.5 cm leading to a period length of $\lambda = 25\,\text{cm}$. The edge poles have half the strength of the regular poles. The overall length of the insertion device is 4.78 m. A schematic of the design is presented in Fig. 3.21.

Sixteen of those wigglers were installed in the lattice, four in each of the Long Straight Sections without interaction region. The bending field of the wiggler was increased and an emittance reduction of up to $0.53 \times \epsilon_{x,0}$ can be achieved for a pole tip field of 1.75 T. Details of the required optics adjustments are discussed in [45]. The emittance ratio with

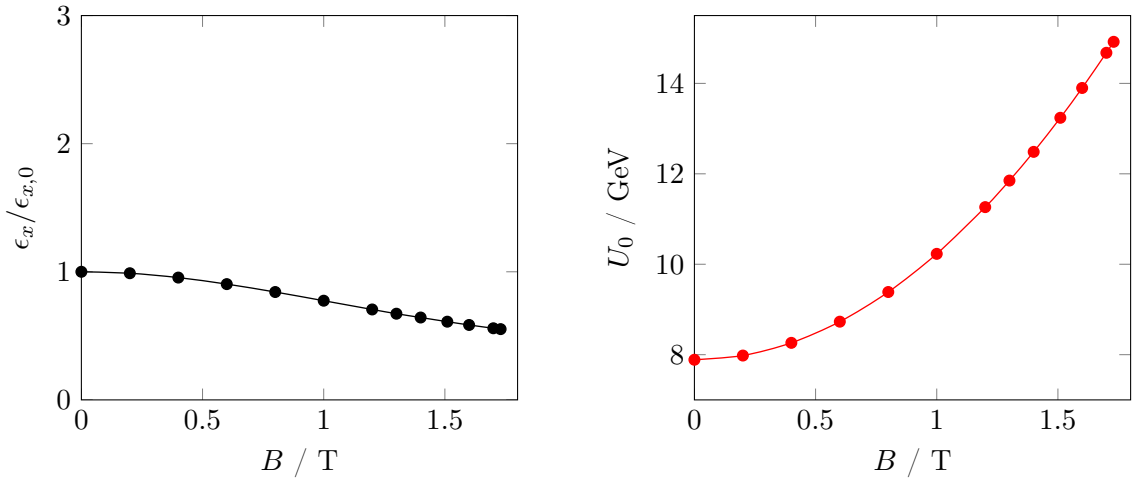

(a) Relative emittance decrease

(b) Energy loss per turn

Figure 3.22: Horizontal beam emittance and energy loss per turn of the FCC-ee lattice with sixteen wigglers of the 39-pole design. (a) shows the beam emittance normalised to the value without wigglers for different magnetic fields. (b) presents the corresponding energy loss per turn.

and without wigglers is shown in Fig. 3.22 (a). It should be mentioned, however, that the decrease of emittance must be paid with additional radiation losses in the wigglers as presented in Fig. 3.22 (b). For the maximum pole field $B = 1.75\,\mathrm{T}$ considered here the energy loss per turn increased from $U_0 = 7.9\,\mathrm{GeV}$ by about an factor of two to $14.9\,\mathrm{GeV}$. Such an increase in energy loss is not feasible as it drives the operation costs beyond budget and puts severe constraints on the absorber design. Assuming, however, an additional energy loss of $10\,\%$ as a reasonable limit, the emittance could be reduced to $0.9 \times \epsilon_{x,0}$, which is considered to be enough for fine-tuning purposes.

3.3.2 Installation of excitation wigglers

In a second step the wiggler design with 39 poles was also investigated as an excitation wiggler. Two wigglers were installed in Long Straight Sections without interaction region at symmetric positions in the lattice. Since a finite value of the dispersion function is required for quantum excitation, the dispersion suppressors of these straight sections were modified to allow for a dispersion beat [45].

As for the previous damping wiggler case, the emittance was calculated depending on the bending field of the regular wiggler poles. The result of the scan is presented in Fig. 3.23 (a). For a bending field of $B = 1.2\,\mathrm{T}$ an emittance increase by a factor of two is obtained. Again, the wiggler produces additional synchrotron radiation, but because of the smaller number of wigglers the increase of the energy loss per turn presented in

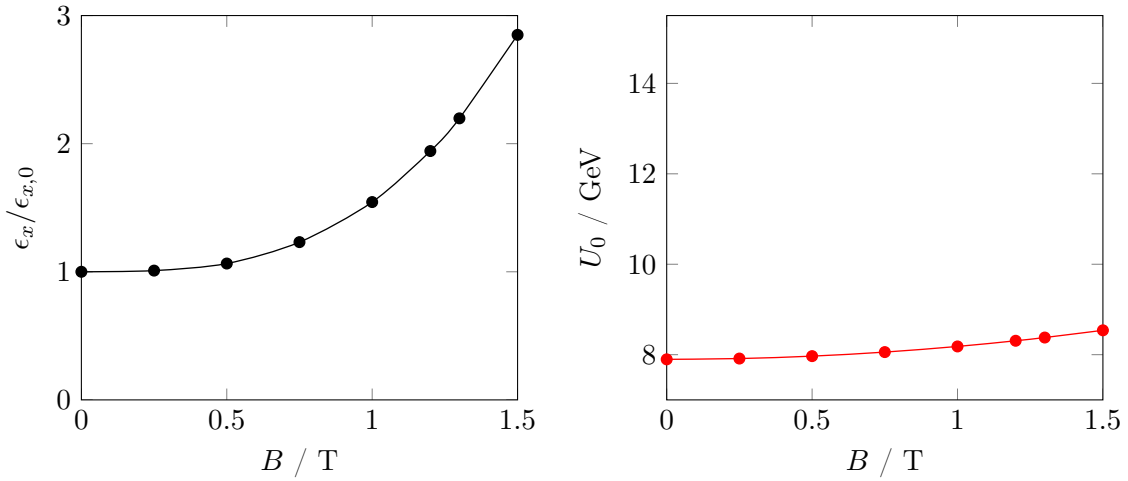

(a) Relative emittance increase

(b) Energy loss per turn

Figure 3.23: Horizontal beam emittance and energy loss per turn of the FCC-ee lattice with two excitation wigglers of 39-pole design. (a) shows the beam emittance normalised to the value without wigglers for different magnetic fields. (b) presents the corresponding energy loss per turn.

Fig. 3.23 (b) is eight times smaller. For +10 % fine-tuning of the emittance only 1.3 % additional energy loss are created.

To summarise this section, wigglers have been installed in the FCC-ee lattice in order to allow both to increase and to decrease the horizontal beam emittance. It was shown, that a fine-tuning within ±10 % can be achieved with reasonable amount of additional synchrotron radiation losses of maximum 10 %. For increasing the emittance less wigglers with lower magnetic field were required, which resulted in considerably less amount of additional energy loss. The basic design of the lattice therefore aims for a lower value of emittance instead of a larger one.

CHAPTER 4

Systematic Optimisation of Chromaticity Compensation Schemes in the Arcs

Particles with momentum deviation experience different focusing strengths in the quadrupole magnets than particles with design momentum. As described in Chapter 1, this leads to a tune shift depending on the momentum offset, which is called the chromaticity of the machine. The large number of quadrupoles and especially the very demanding requirements of the interaction region with beta functions of $\beta_y^* = 1$ or 2 mm at the interaction point drive the linear chromaticity of FCC-ee to absolute values of more than 2000 units in the vertical plane. Without compensation, the resulting tune shift would drive off-momentum particles to resonances where they get lost. The required correction depends on the maximum energy deviation in the machine. In the case of FCC-ee with 175 GeV beam energy the non-colliding particles lose up to two percent of their total energy due to beamstrahlung. As a consequence, the required momentum acceptance of FCC-ee must be $\pm 2\,\%$ in order to prevent losing those particles. It might be emphasised that such an energy range is extremely large. Considering the large chromaticity of FCC-ee $\pm 2\,\%$ momentum acceptance is a very challenging goal. The compensation of the linear chromaticity alone is therefore not sufficient. Higher-order terms must be corrected as well.

In the context of this thesis chromaticity correction schemes in the arc lattice were systematically studied including non-linear orders. Known techniques and methods were implemented and benchmarked towards their capabilities to correct chromaticity of such extraordinary magnitude. In addition, tools were developed to optimise configuration and strength of the sextupoles to improve the momentum acceptance as far as possible.

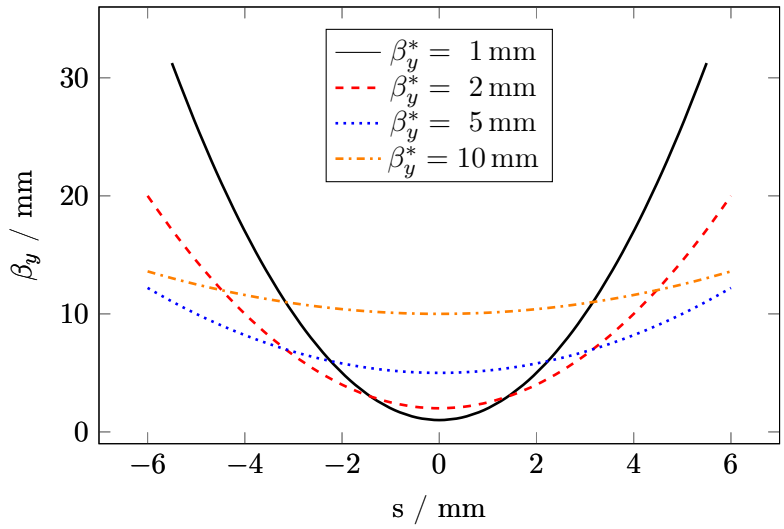

Figure 4.1: The beta function around the interaction point at $s = 0$ for different values of β^*. The beta function increases quadratically with distance s according to Eq. (4.2). The smaller the value of β^*, the higher is the beam divergence.

4.1 Linear chromaticity correction

As a very first step the effects of linear chromaticity were studied. As discussed in Sec. 1.3.4 the chromatic effects created by the quadrupoles in the lattice lead to a tune shift, which is in first order proportional to

$$Q' = \frac{\mathrm{d}Q}{\mathrm{d}\delta} = -\frac{1}{4\pi}\int \beta(s)k_1(s)\ \mathrm{d}s. \tag{4.1}$$

With Eq. (4.1) it can easily be verified, that in high-energy storage ring colliders the final doublet quadrupoles in the interaction regions create the largest contribution to the chromaticity. In order to obtain maximum luminosity, the beam is focused strongly to beam sizes as small as possible. Since the phase space occupied by the beam stays constant, because of the Liouville theorem, the small beam size leads to a large divergence of the beam. For a symmetric beam waist with $\alpha = 0$ and β^* being the beta function at the interaction point the beta function increases quadratically with distance Δs from the interaction point:

$$\beta(\Delta s) = \beta^* + \frac{\Delta s^2}{\beta^*}. \tag{4.2}$$

The divergence of the beam depends on the value of β^*, which increases for small choices of β^* as illustrated in Fig. 4.1.

In the case of FCC-ee the first quadrupole is placed at a distance of $L^* = 2\,\mathrm{m}$ to the interaction point and as a consequence the beta function reaches several kilometers in

Table 4.1: Maximum value of the vertical beta function $\beta_{y,\max}$ in the final doublet and linear chromaticity Q'_y of three different layouts for different values of β^*_y. While the 12-fold Layout was studied for both two and four interaction points, the Racetrack Layout only foresees two interaction points (IPs).

β^*_y (mm)	$\beta_{y,\max}$ (m)	Q'_y 12-fold, 4 IPs	Q'_y 12-fold, 2 IPs	Q'_y Racetrack
1	5397.9	-2048.9	-1253.9	-1154.5
2	2698.9	-1257.9	-858.4	-791.5
5	1079.5	-780.9	-619.9	-573.3
10	539.9	-620.8	-539.9	-500.4
20	270.1	-541.1	-500.0	-464.8
50	198.8	-494.0	-476.5	-443.3

the first quadrupole lenses for values of β^* in the millimeter range. Tab. 4.1 presents the maximum beta functions $\beta_{y,\max}$ in the interaction region introduced in Sec. 2.2.4 for different values of β^*. The table also lists the corresponding vertical chromaticity of the lattices with 12-fold layout both for two interaction points and four interaction points as well as the lattice with Racetrack Layout. For values of β^*_y smaller then 10 mm the final focus quadrupoles become the major contributors to the chromaticity. The very strong quadrupole strengths k_1 in combination with the large beta functions in the final focus quadrupoles dominate the chromatic effects. As a consequence the number of interaction points determines the chromaticity of the lattice, which is confirmed by the comparison between the chromaticities of the 12-fold Layout with two and four interaction points in Tab. 4.1. Fig. 4.2 shows the vertical chromaticity as a function of β^*_y for both cases. The value of the chromaticity without any interaction region, $Q'_y = -458.94$, is indicated by the dotted line.

As already discussed in Sec. 1.3.4, the linear chromaticity can be compensated by installing sextupole magnets in dispersive regions the lattice, preferably next to the quadrupoles. In thin lens approximation, where the elements are treated as a single kick, quadrupole and sextupole form an achromatic doublet when the strength of the sextupole equals

$$k_2 = k_1 \frac{1}{D_x} \frac{\beta(s_\mathrm{Q})}{\beta(s_\mathrm{S})} \frac{L_\mathrm{Q}}{L_\mathrm{S}}. \tag{4.3}$$

The linear chromaticity is then zero. However, this correction is only applicable in the dispersive arc section, where $D_x \neq 0$. The chromaticity created in the dispersion-free straight sections must be compensated by the sextupoles in the arcs as well. If the lattice includes straight sections or even mini-beta insertions the sextupole strengths must be increased accordingly in order to compensate the complete chromaticity of the lattice.

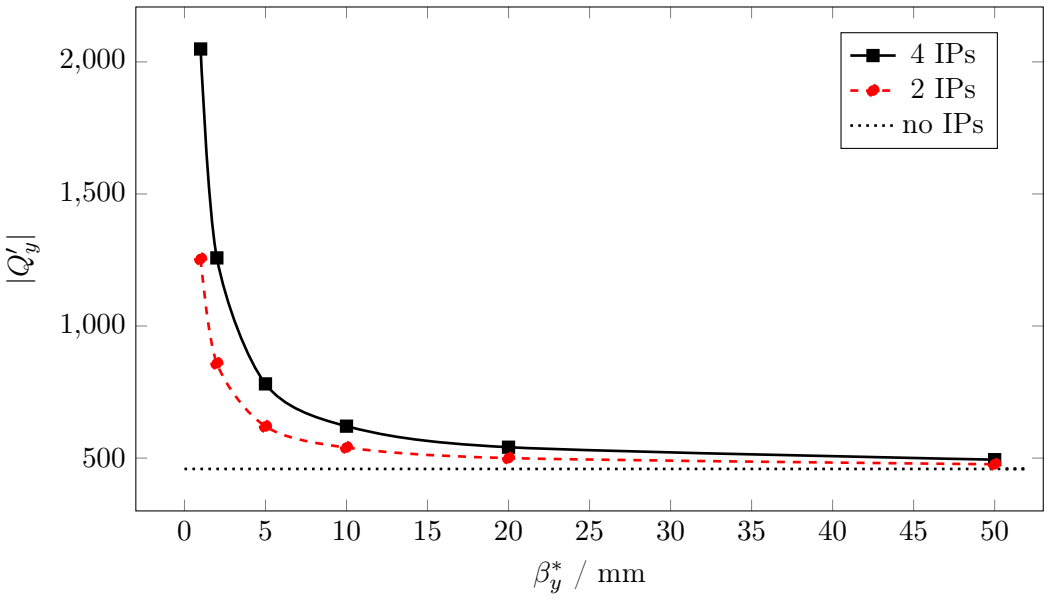

Figure 4.2: Chromaticity of the lattice with 12-fold Layout for different values of β^*_y. For both two and four interaction points the chromaticity increases strongly for β^*_y in the millimeter range and confirms the large contribution of the final doublet quadrupoles depending on the number of interaction points (IPs). The dotted line indicates the chromaticity without any interaction regions.

For the study of chromaticity correction schemes for FCC-ee the lattice with symmetric FODO cells was chosen. This cell layout foresees sextupoles on each side of every quadrupole in the arc sections. The length of of the sextupoles was set to 50 cm as a starting point. This design offers the highest possible symmetry within the cell and provides twice the integrated sextupole length. This means, the sextupole strengths reduce by a factor of two compared to the asymmetric cell layout where only one sextupole next to each quadrupole is foreseen.

Tab. 4.2 summarises the values of chromaticity and the sextupole strengths after correction of the linear chromaticity. For comparison, the sextupole strengths in LEP according

Table 4.2: Number of sextupole magnets and their strengths in one FODO cell and the 12-fold Layout for different numbers of interaction points.

	FODO cell	12-fold, 0 IPs	12-fold, 2 IPs		12-fold, 4 IPs	
β^*_y			1 mm	2 mm	1 mm	2 mm
# of sextupoles	2	6336	6336		6528	
k2SF	0.48	0.60	0.77	0.70	0.94	0.80
k2SD	-0.73	-0.91	-2.02	-1.47	-3.13	-2.04

Table 4.3: First four orders of chromaticity and their corresponding tune shifts for a particle with $\delta = 0.1\,\%$ momentum deviation. The values were calculated using the 12-fold Layout with two and four interaction points (IPs).

	2 IPs		4 IPs		4 IPs	
	$\beta_y^* = 1\,\mathrm{mm}$	ΔQ	$\beta_y^* = 1\,\mathrm{mm}$	ΔQ	$\beta_y^* = 2\,\mathrm{mm}$	ΔQ
Q'_x	-5.86×10^2	-0.59	-6.19×10^2	-0.62	-6.18×10^2	-0.62
Q''_x	1.02×10^4	0.01	1.87×10^4	0.01	1.84×10^4	0.01
$Q_x^{(3)}$	-1.16×10^8	-0.02	-1.20×10^8	-0.02	-1.19×10^8	-0.02
$Q_x^{(4)}$	2.35×10^{12}	0.10	1.28×10^{12}	0.05	1.28×10^{12}	0.05
Q'_y	-1.25×10^3	-1.25	-2.05×10^3	-2.05	-1.28×10^3	-1.26
Q''_y	4.50×10^6	2.25	8.92×10^6	4.46	1.26×10^6	0.63
$Q_y^{(3)}$	-1.38×10^{11}	-23.05	-2.17×10^{11}	-36.11	-1.26×10^{10}	-2.11
$Q_y^{(4)}$	5.62×10^{15}	234.03	7.50×10^{15}	312.52	1.52×10^{14}	6.32

to the design report [25], were in the range from $k_2 = 0.05\,\mathrm{m}^{-3}$ to $0.12\,\mathrm{m}^{-3}$ for the focussing quadrupoles and $k_2 = 0.03\,\mathrm{m}^{-3}$ to $0.10\,\mathrm{m}^{-3}$, which is about one order of magnitude smaller than in the FCC-ee lattice.

4.2 Higher-order chromaticity and the Montague formalism

In order to achieve the required momentum acceptance of $\delta = \pm 2\,\%$, which is needed due to the severe energy loss by beamstrahlung during the interaction process, it is not sufficient to apply a simple correction of the linear chromaticity. Higher-order derivatives of the tune need to be compensated as well. For a description of the higher-order terms the tune function is expanded into a Taylor series

$$\begin{aligned} Q(\delta) &= Q_0 + \frac{\mathrm{d}Q}{\mathrm{d}\delta}\delta + \frac{1}{2}\frac{\mathrm{d}^2Q}{\mathrm{d}\delta^2}\delta^2 + \frac{1}{6}\frac{\mathrm{d}^3Q}{\mathrm{d}\delta^3}\delta^3 + \dots \\ &= Q_0 + Q'\delta + \frac{1}{2}Q''\delta^2 + \frac{1}{6}Q^{(3)}\delta^3 + \dots \end{aligned} \tag{4.4}$$

where δ refers to the relative energy deviation $\Delta p/p$. The higher-order derivatives of the tune are not calculated directly by MAD-X. The values presented in this thesis are based on a macro provided by A. Bogomyagkov [53]. The macro uses five calculations of the tune, one for design momentum and four with $\delta = \pm 0.01$ % and ± 0.02 % momentum offset, to calculate the derivatives from difference quotients. Details about the macro are explained in the Appendix C. For a given energy offset the contribution to the tune shifts of each term can be calculated individually using Eq. (4.4). The chromaticities of the 12-fold lattice and their respective tune shifts calculated with that macro are listed in Tab. 4.3.

The values of both planes are presented up to the fourth order for $\beta_y^* = 1\,\mathrm{mm}$ and $2\,\mathrm{mm}$. As expected, the largest tune shifts of more than one unit are created in the vertical plane, where the beam is focused more strongly than in the horizontal plane.

One of the key aspects of this thesis is the development of a multi-family sextupole scheme in the arc lattice, which is capable of correcting these higher-order terms. The different sextupole schemes will be evaluated according to the momentum acceptance, which is obtained by an energy scan. In the end, six dimensional particle tracking will determine the real dynamic aperture.

4.2.1 The Montague formalism

In [54] B. Montague introduced a very descriptive theory to extend chromaticity correction beyond linear order. A detailed explanation of the theory can also be found in [35]. Instead of correcting the derivatives of the tune the perturbation of the optics due to energy deviation is analysed. The theory applies for both planes, so the indices will be omitted in the following. Instead, the index 0 will refer to the parameters for design energy and the index 1 will refer to the perturbed optics due to energy offset. Two chromatic variables are introduced

$$a = \lim_{\delta \to 0} \frac{1}{\delta} \frac{(\alpha_1 \beta_0 - \alpha_0 \beta_1)}{(\beta_0 \beta_1)^{1/2}} \tag{4.5a}$$

$$b = \lim_{\delta \to 0} \frac{1}{\delta} \frac{(\beta_1 - \beta_0)}{(\beta_0 \beta_1)^{1/2}} \tag{4.5b}$$

which describe the mismatch of the off-momentum beam envelope for an energy deviation $\delta = \Delta p/p_0$. In an achromatic region the difference in focusing strength $\Delta k_n = \lim_{\delta \to 0} \left(\frac{1}{\delta}(-K_1 + K_0)\right) = 0$ und a und b fulfill the equations

$$\frac{\mathrm{d}^2 a}{\mathrm{d}\mu^2} + 4a = 0 \quad \text{and} \quad \frac{\mathrm{d}^2 b}{\mathrm{d}\mu^2} + 4b = 0, \tag{4.6}$$

which means they oscillate with twice the betatron phase μ.

The variables a and b can be represented by vectors in the complex plane. It is also useful to define the so-called *W vector* as

$$\mathbf{W} = b + ia. \tag{4.7}$$

In achromatic regions its magnitude is an invariant, since it can be shown [35], that

$$a^2 + b^2 = \text{constant}. \tag{4.8}$$

The W vector with constant absolute value will therefore rotate in the (b,a) space with

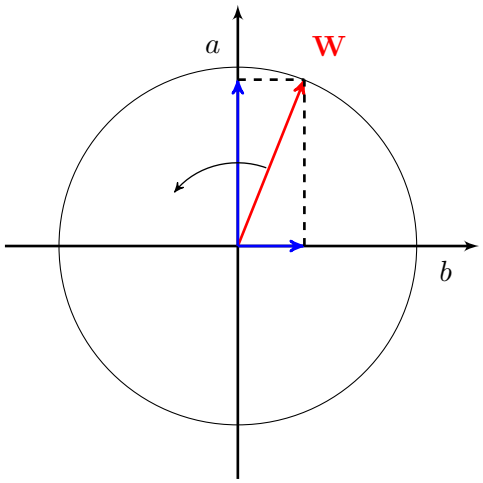

Figure 4.3: In an achromatic region the W is the sum of the chromatic variable a and b and rotates in the (b,a) space.

twice the betratron phase as illustrated in Fig. 4.3. The absolute value of the W vector

$$|\mathbf{W}| = \sqrt{a^2 + b^2} \tag{4.9}$$

is also referred to as the *W function*. It is used as a measure of the strength of the chromatic perturbations and an invariant in achromatic regions.

The W vector is a very useful tool to design chromaticity compensation schemes. In achromatic regions it has a constant absolute value, only when passing a quadrupole or a sextupole magnet its amplitude is modified. In thin lens approximation $\Delta b = 0$, since the beta functions stay the same before and after the kick created the respective element. In this case only Δa is modified in following way [35]:

$$\Delta a = -(\beta_0\beta_1)^{1/2}\Delta k_n \Delta s \simeq \beta_0 k_1 L_\mathrm{q} \qquad \text{for quadrupole} \tag{4.10a}$$

$$\Delta a = -(\beta_0\beta_1)^{1/2}\Delta k_n \Delta s \simeq -\beta_0 D_x k_2 L_\mathrm{s} \qquad \text{for sextupole} \tag{4.10b}$$

Strictly speaking, Eq. (4.10a) and Eq. (4.10b) only apply in the approximation of thin lenses. Exact expressions, taking the finite length of the elements into account, are for example given in [35]. The theory is also implemented in the MAD-X programme. The W functions are calculated when the option "chrom" is used in the Twiss command.

As the Montague formalism describes the perturbations of the optics, the effect of the higher-orders of the chromaticity are already taken into account.

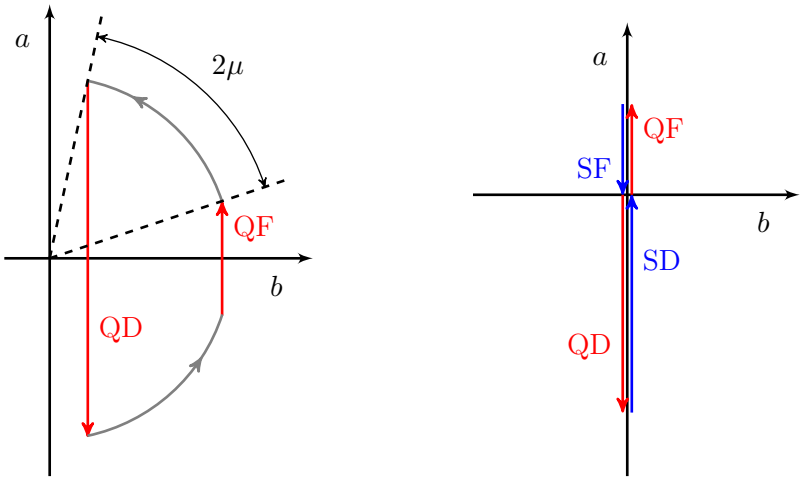

(a) **(b)**

Figure 4.4: The periodic evolution of the vertical W vector in a FODO cell lattice. The phase advance per cell is $\varphi_x = \varphi_y = 60°$, focusing and defocusing quadrupoles have same strength $k_{1,f} = k_{1,d}$ and equal separation. So the phase advance between two quadrupoles is $\mu = 30°$ in both planes. (a) shows the uncompensated case and (b) shows the compensated case starting without chromatic aberrations according to [35].

The *W* vector in a FODO lattice

The regular FODO cells in the arcs have periodic lattice functions. Consequently the W functions are periodic as well and form a closed curve in the (b,a) space. As described in the previous section, the W vector rotates with twice the phase advance in the achromatic sections, like drift spaces, and performs jumps due to the effect of quadrupoles and sextupoles. Fig. 4.4 shows the W vector of the vertical plane in the (b,a) space. The FODO cell phase advance in this case is $\varphi = 60°$ in both planes and focusing and defocusing quadrupoles have same strength $k_1 = k_{1,f} = k_{1,d}$, same length L_Q and equal distance. Fig. 4.4 (a) shows the uncompensated case. At the focusing quadrupole the chromatic variable a is modified by $\Delta a \simeq \beta_\mathrm{QF} k_1 L_\mathrm{Q}$ with positive absolute value. In the subsequent drift the W vector rotates by $2 \times (0.5\,\varphi) = 60°$ before it experiences another jump at the defocusing quadrupole. This time the absolute value of Δa is negative and larger than before, because of the different value of the beta function. The second rotation of 60° brings the W vector back to its starting point. Fig. 4.4 (b) shows the case of a lattice consisting only of FODO cells, in which the chromatic aberrations are corrected by a sextupole that is located immediately after the quadrupole. This picture gives a nice visualisation how the source and corrections of the chromatic perturbations act together.

4.2.2 Non-linear chromaticity expressed with Montague functions

As a further benefit, the Montague formalism also allows very descriptive expressions for the non-linear terms of the chromaticity derived by A. Bogomyagkov [55]. In addition to the two chromatic variables a and b, which in future will be referred to as a_1 and b_1, second order chromatic derivatives of the Twiss parameters are introduced. In A. Bogomyagkov's notation the first order terms, which are used for the definition of the W vector, are given by

$$b_1 = \frac{1}{\beta}\frac{\partial\beta}{\partial\delta} \qquad \text{and} \qquad a_1 = \frac{\partial\alpha}{\partial\delta} - \frac{\alpha}{\beta}\frac{\partial\beta}{\partial\delta} \tag{4.11}$$

and the second order terms by

$$b_2 = \frac{1}{\beta}\frac{\partial^2\beta}{\partial\delta^2} \qquad \text{and} \qquad a_2 = \frac{\partial^2\alpha}{\partial\delta^2} - \frac{\alpha}{\beta}\frac{\partial^2\beta}{\partial\delta^2}. \tag{4.12}$$

The horizontal dispersion function D_x is expanded until the third order. Assuming a flat machine, where the vertical dispersion is zero, the index can be omitted, which yields following equations for dispersion and orbit offset:

$$x = D_0\delta + D_1\delta^2 + D_2\delta^3 \tag{4.13a}$$

$$D_x = D_0 + D_1\delta + D_2\delta^2 \tag{4.13b}$$

The formulae for the higher-order terms of chromaticity are derived using the canonical perturbation method as described by M. Takao in [56]. However, the expressions derived in this paper contain many-fold integrals up to third order. The same equations can be represented in a much easier way using the higher-order chromatic derivatives:

$$\frac{\partial Q_y}{\partial\delta} = \frac{1}{4\pi}\oint \beta_y(k_1 - k_2D_0)\,\mathrm{d}s \tag{4.14a}$$

$$\frac{\partial^2 Q_y}{\partial\delta^2} = -2\frac{\partial Q_y}{\partial\delta} - \frac{1}{2\pi}\oint \beta_y\left(k_2D_1 + k_3\frac{D_0^2}{2}\right)\mathrm{d}s + \frac{1}{4\pi}\oint \beta_y b_{1y}(k_1 - k_2D_0)\,\mathrm{d}s \tag{4.14b}$$

$$\begin{aligned}\frac{\partial^3 Q_y}{\partial\delta^3} = 6\frac{\partial Q_y}{\partial\delta} &- \frac{1}{2\pi}\oint \beta_y(k_1 - k_2D_0)(a_{1y}^2 + b_{1y}^2)\,\mathrm{d}s \\ &+ \frac{3}{2\pi}\oint \beta_y\left(k_2D_1 + k_3\frac{D_0^2}{2} - k_2D_2 - k_3D_0D_1\right)\mathrm{d}s \\ &+ \frac{3}{4\pi}\oint \beta_y b_{2y}(k_1 - k_2D_0)\,\mathrm{d}s\end{aligned} \tag{4.14c}$$

These equations allow direct conclusions about how the different orders are created and how they can be controlled. For example, the second term in the third-order formula contains $(a_{1,y}^2 + b_{1,y}^2)$, which is the square of the W function. This means the integral of the W function around the ring must be minimised to reduce the third-order chromaticity.

4.3 Planning the chromaticity correction scheme for FCC-ee

For the arrangement of the sextupoles several issues were considered, which will be discussed in the this section.

FODO cell layout: As already mentioned before, the chromaticity in the vertical plane is much larger than in the horizontal plane because of the smaller beta function at the interaction point. The first sextupole of the arc lattice, which is the closest to the final focus quadrupoles, should therefore be a defocussing one, which corrects the chromaticity in the vertical plane. The basic cell layout presented in Sec. 2.2 was designed accordingly: the first quadrupole is a defocussing quadrupole, not a focussing as in the standard FODO cell. This FODO cell layout was already . In order to obtain the highest possible symmetry of the layout, sextupoles are installed at each side of a quadrupole. The chromatic error is thereby corrected partly before and partly after the quadrupole. Also the integrated length of the sextupoles is longer compared to the asymmetric cell layout, which helps to decrease their required strength.

A FODO cell layout with split quadrupoles and a sextupole magnet in the centre was studied as well. Such a design would allow to adjust the phase relations between the sextupoles perfectly, since they define the symmetry point of the cell. However, this layout was not further investigated, since no difference to the regular lattice was observed.

$-I$ transformation and geometric aberrations: While the sextupole magnets are used to correct chromatic aberrations for off-momentum particles, which arise from the modified focusing properties, they introduce so-called *geometric aberrations*, which become significant for any particle with large betatron oscillation amplitude. To overcome the effect of the geometric aberrations, as many sextupoles as possible are installed in the lattice to minimise the strength of the non-linear fields. If the stability still suffers from geometric aberrations, a more sophisticated sextupoles scheme is required: the geometric effects of the sextupoles can be canceled, if they are installed in pairs with equal strength and the separating transfer matrix for x, x', y and y' is a negative unity transformation:

$$-I = \begin{pmatrix} -1 & 0 & 0 & 0 \\ 0 & -1 & 0 & 0 \\ 0 & 0 & -1 & 0 \\ 0 & 0 & 0 & -1 \end{pmatrix} \tag{4.15}$$

Since the chromatic perturbations oscillate with twice the phase advance, the chromatic correction of the sextupoles still adds up while the geometric aberrations are canceled for all oscillation amplitudes.

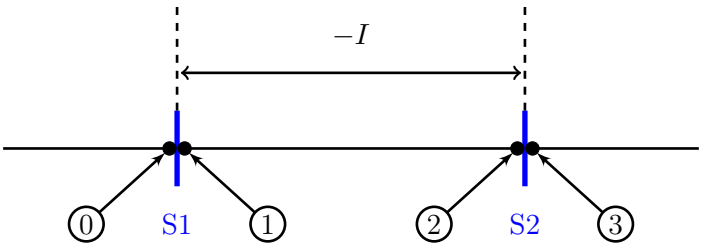

Figure 4.5: Sextupole layout used to prove the cancellation of geometric aberrations. The sextupoles are considered as thin lenses separated by a $-I$ transformation.

In thin lens approximation where the sextupoles create single kicks the cancellation of geometric aberrations can be calculated quickly. Assuming a layout as illustrated in Fig. 4.5 the particle arrives at the sextupole S1 at the coordinates (x_0,y_0). Its direction of motion is given by (x_0',y_0'). The kicks induced by the sextupoles are then

$$\Delta x' = \frac{1}{2}\,(k_2 L_\mathrm{S})\,(x^2 - y^2) \tag{4.16a}$$

$$\Delta y' = (k_2 L_\mathrm{S})\,x\,y. \tag{4.16b}$$

So after traversing the sextupole the particle motion is defined by

$$x_1 = x_0 \qquad\qquad y_1 = y_0$$

$$x_1' = x_0' - \frac{k_2 L_\mathrm{S}}{2}\,(x_0^2 - y_0^2) \qquad\qquad y_1' = y_0' - k_2 L_\mathrm{S}\,x_0\,y_0$$

After the $-I$ transformation the particle arrives at the second sextupole with

$$x_2 = -x_1 = -x_0 \qquad\qquad y_2 = -y_1 = -y_0$$

$$x_2' = -x_0' = -x_0' + \frac{k_2 L_\mathrm{S}}{2}\,(x_0^2 - y_0^2) \qquad\qquad y_2' = -y_1' = -y_0' + k_2 L_\mathrm{S}\,x_0\,y_0$$

Because of $x_2 = -x_0$ and $y_2 = -y_0$ the second sextupole applies a kick of equal strength, which cancels the additional transverse momentum created by the first one:

$$x_3 = x_2 = -x_0 \qquad\qquad y_3 = y_2 = -y_0$$

$$x_3' = x_2' - \frac{k_2 L_\mathrm{S}}{2}\,(x_2^2 - y_2^2) = -x_0' \qquad\qquad y_3' = y_2' - k_2 L_\mathrm{S}\,x_2\,y_2 = -y_0'$$

In summary, to cancel the geometric aberrations sextupoles should be installed in pairs separated by a $-I$ transformation, which corresponds to a phase advance of $\mu = \pi$ or 180°. As a matter of fact, it can be shown in a similar calculation that geometric aberrations are also canceled for a $+I$ transformation in the vertical plane as long there still is a $-I$

transformation in the horizontal. As a direct consequence, a sophisticated chromaticity correction scheme comprises an even number of sextupoles and phase advance errors should be kept on a minimum level, since they reduce the effectiveness of the cancellation [22].

In strict sense the above described compensation of geometric effects only applies for thin lenses. The finite length of the sextupoles introduces higher-order terms [57], which are not canceled by the $-I$ transfer map. Still the cancellation of geometric aberrations of first order can be reduced significantly.

Sextupole families: So far the sextupoles have been grouped into focusing and defocussing types, each dedicated to adjust the linear chromaticity of one transverse plane. This setup is not capable of correction of the W function. Fig. 4.6 shows the W vector for the vertical plane and its absolute value, the W function, in eight cells of the first FCC-ee arc after linear chromaticity correction. The phase advance per FODO cell is $\varphi_y = 60°$. The effect of the sextupoles Δa_1 is the same for every sextupole, but as the W rotates by $2\,\varphi_y = 120°$ in-between two sextupoles their effect on the W vector is different as shown in Fig. 4.6 (a). While the sextupoles S2 and S3 reduce the absolute value of the W vector, S1 increases it, which leads to the oscillation of the absolute value presented in Fig. 4.6 (b). After three FODO cells, corresponding to 180° phase advance, the W reaches again its starting point. It is therefore reasonable to group the sextupoles in families, where the phase advance separation between two members of each families equals π. This arrangement not only cancels the geometric aberrations introduced to the lattice, but also allows to modify the W vector effectively. As the sextupoles of a certain family affect the W vector always at the same chromatic phase, such a scheme allows to iteratively reduce the W functions in the lattice and thus the chromatic perturbance of the lattice function. However, it also puts constraints on the FODO cell phase advance, as already discussed in the emittance tuning chapter. In order to obtain a $-I$ transformation from one family member to the next, the phase advance must be an odd integer of π. Possible phase advances and their corresponding number of sextupole families are listed in Tab. 4.4. Different arrangements of the families will be discussed in Sec. 4.3.1.

Phase advance between final doublet and sextupoles: The orientation of the W vector must not only be considered within the arc itself, especially its orientation at the beginning of the arc must be adjusted carefully. Assuming no chromatic aberrations at the interaction point the quadrupoles of the final doublet create the largest contribution to the W vector. Since the interaction region with the mini-beta insertion is located in a straight section the chromatic perturbations cannot be corrected locally due to the missing dispersion and are therefore carried through the lattice until the next arc section with finite dispersion, where they finally can be corrected. Special dispersive insertions for chromaticity correction are

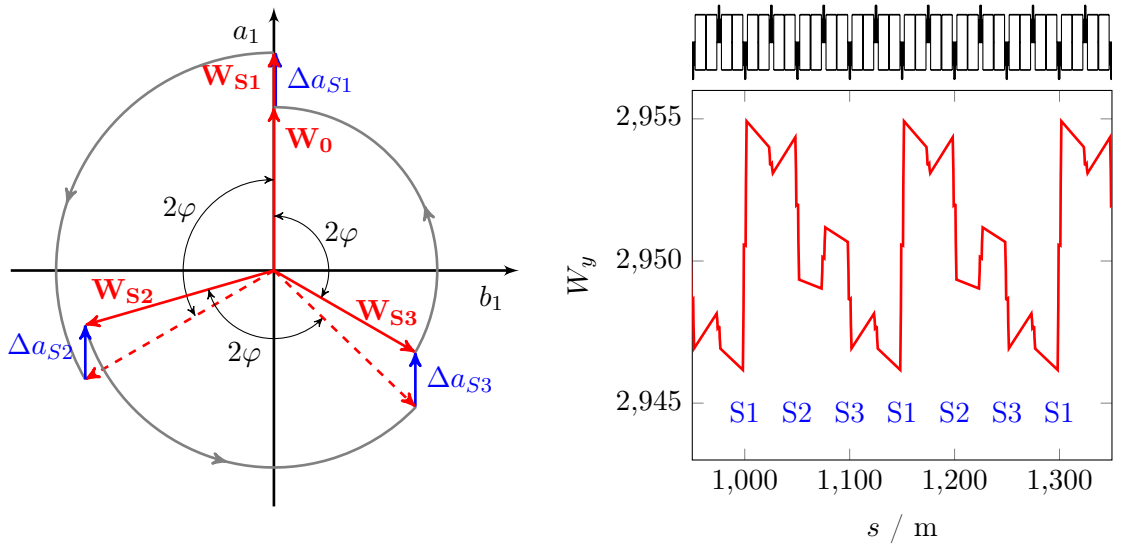

(a) **(b)**

Figure 4.6: The W vector and its absolute value in a $\varphi = 60°$ FODO cell lattice after linear chromaticity correction. (a) shows how the sextupoles modify the W vector during passage of three FODO cells. (b) shows the corresponding absolute value of the W vector in eight cells of the first arc in the FCC-ee Racetrack lattice.

Table 4.4: Possible FODO cell phase advances to establish a multi-family sextupole scheme in the arc and the corresponding number of sextupole families. More exotic arrangements are for example presented in [58] and [54].

Phase advance		# of families
$\pi/4$	45°	4
$\pi/3$	60°	3
$\pi/2$	90°	2
$3\pi/5$	108°	5
$3\pi/4$	135°	4

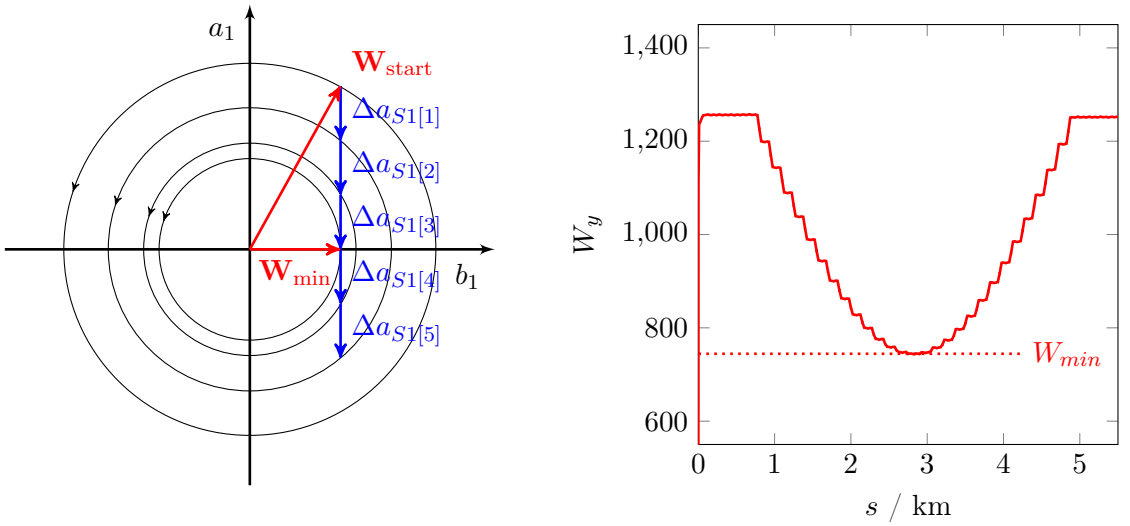

(a) **(b)**

Figure 4.7: Modification of the W vector by sextupoles with $\mu = \pi$ phase advance separation. The square brackets denote the occurrence of the sextupole of the family. (a) shows the orientation of the W vector in the (b_1,a_1) space. Since the phase advance between final doublet and first sextupole is not adjusted properly, the absolute value, shown in (b) only reaches a minimum and increases again.

under investigation [59,60] but not considered in the context of this thesis. The contribution of the FODO cell quadrupoles in the straight section is small compared to the effect of the final doublet, because beta function and quadrupole strength are both by an order of magnitude smaller. Therefore, the W vector rotates with twice the phase advance. Since the sextupoles just affect the chromatic parameter a_1, the correction of the W vector is most effective, when $b_1(s) = 0$ and the W vector points in the direction of a_1 in the (b_1,a_1) space. This means the phase advance between final doublet quadrupole and respective correcting sextupole has to be an integer of π to fulfill a full rotation in the (b_1,a_1) space.

Fig. 4.7 illustrates the situation for a phase advance mismatch of $\Delta\mu_y = 0.05 \times 2\pi$. Fig. 4.7 (a) shows the orientation of the W vector in the (b_1,a_1) space and its iterative modification by sextupoles of the family S1. The phase advance separation between two members of the family is $\mu = \pi$, the number in the square brackets denotes the number of the sextupole in the lattice. The absolute value of the W vector is first decreased, but as the phase advance is not adjusted properly, it does not reach zero and the chromatic perturbance cannot be corrected completely.

The same is shown in Fig. 4.8. However, this time the phase advance between final doublet and first sextupole S1 is adjusted correctly. For a given number of sextupoles a certain strength can be found to achieve full compensation of the chromatic aberrations.

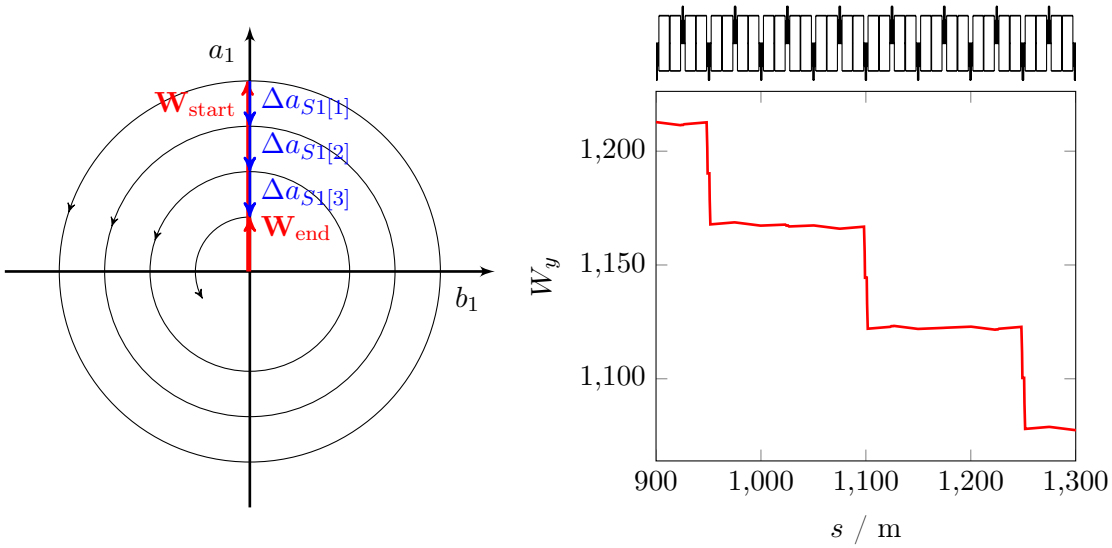

(a) **(b)**

Figure 4.8: Correction of the W vector by sextupoles with $\mu = \pi$ phase advance separation. The square brackets denote the number of the sextupole within the family. (a) shows the orientation of the W vector in the (b_1,a_1) space. The sextupoles iteratively decrease the absolute value of W as shown in (b).

4.3.1 Interleaved and non-interleaved sextupole schemes

The arrangement of sextupoles in families is the key aspect in designing the chromaticity compensation scheme and should be given careful thought. The number of families defines the degrees of freedom for chromaticity correction and depends on the characteristics of the lattice. In general there are two different ways to arrange sextupole families among each other in the lattice: interleaved schemes and non-interleaved schemes. Both have advantages and disadvantages, which will be highlighted in the following discussion.

Non-interleaved sextupole schemes: In order to obtain the best cancellation of geometric effects every sextupole should have a partner separated by a $-I$ transfer map. In the ideal case only linear elements are installed between the two sextupoles. Other sextupoles might disturb the phase relation and the cancellation of the geometric effects is hindered. When no other sextupoles are installed in-between a pair of sextupoles with a phase shift of $\mu = \pi$ in-between, the sextupole scheme is called a *non-interleaved* scheme.

Fig. 4.9 shows an illustration of such a non-interleaved scheme for the FCC-ee arcs, where the FODO cell phase advance is $\varphi_x = 90°$ in the horizontal plane and $\varphi_y = 60°$ in the vertical plane. The grid represents the FODO cells, the long vertical lines stand for the defocussing quadrupoles and the short lines for the focussing quadrupoles. The sextupoles

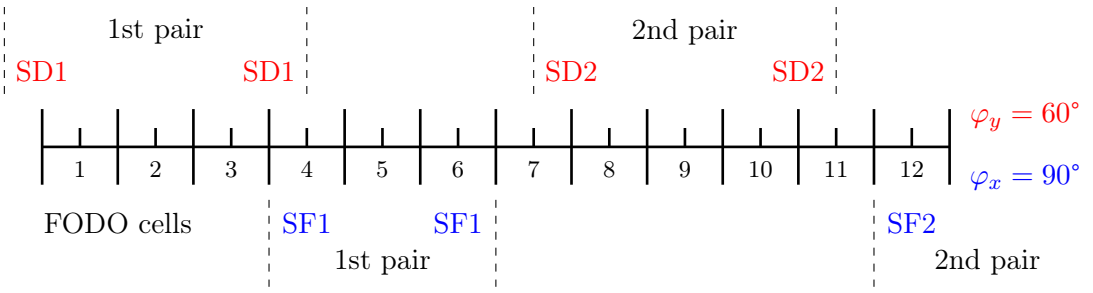

Figure 4.9: Completely non-interleaved sextupole scheme for the FCC-ee FODO cell lattice with $\varphi_x = 90°$ phase advance in the horizontal plane and $\varphi = 60°$ in the vertical plane. Only linear elements are installed between two sextupoles forming a pair.

installed at each side of one quadrupole form a doublet, which is considered as one member of a family. As the phase advance is 60° in the vertical plane, two sextupoles forming a pair are separated by three FODO cells. In the horizontal plane, where the phase advance is 90°, the separation corresponds to two cells. The scheme starts with a pair of defocussing sextupoles located at the beginning of the cells 1 and 4. Since the sextupole pairs are completely non-interleaved the first focusing sextupole pair is installed in the middle of the cells 4 and 6. Although the next defocusing sextupole could be placed at the beginning of cell 7, it is installed at the beginning of cell 8. Otherwise the phase advance to the previous pair would be $\mu = \pi$ and the sextupoles would belong to the same family as the first pair.

A non-interleaved sextupole scheme with completely non-interleaved sextupole pairs requires many FODO cells. In the example shown in Fig. 4.9 only seven sextupoles are installed in twelve cells. The low number of sextupoles requires large strengths, which in the end might have a bad effect on the dynamic aperture. In order to save space and increase the number of sextupoles most studied and applied non-interleaved schemes interlace the sextupole pairs of the horizontal plane and the vertical plane, but not the sextupole pairs within the same plane. If the difference of the beta functions is large enough, the effect of the sextupoles on the other plane is small and the resulting distortion is tolerable. Such a scheme is illustrated in Fig. 4.10. The twelve FODO cells now accommodate fifteen sextupoles instead of seven in the completely non-interleaved scheme.

Interleaved scheme: The highest amount of sextupoles in the lattice can be achieved, if every quadrupole is paired with sextupoles. Since the FODO cell phase advance is smaller than π this requires to interleave the sextupole pairs of the families forming groups of the first elements of each family, second elements of each family etc. Depending on the FODO cell phase advance a different number of families can be established. The main advantage of this arrangement is the high number of sextupoles, which allows to decrease the sextupole strengths.

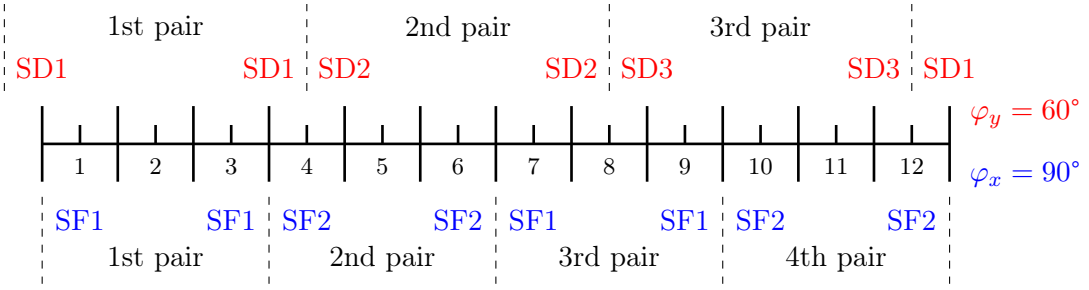

Figure 4.10: Sextupole scheme with interleaved focusing and defocussing sextupoles. Within one plane the sextupole pairs are non-interleaved. The number of sextupoles can be increased significantly.

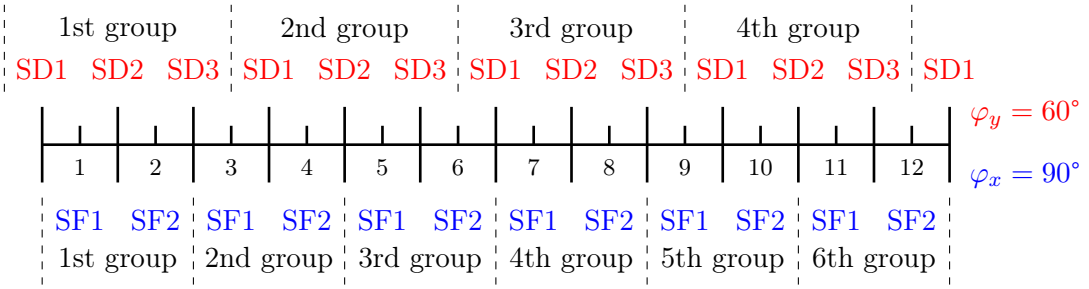

Figure 4.11: Interleaved sextupole scheme with two families in the horizontal and three families in the vertical plane as installed in the FCC-ee lattice.

A non-interleaved sextupole scheme for FCC-ee is studied by K. Oide [60]. Nearly 600 independent sextupole pairs (300 per half-ring) are varied in strength in order to optimise the dynamic aperture. The required strengths are moderate since the scheme includes a local chromaticity correction section in a special insertion close to the interaction point. The study of chromaticity correction schemes in the context of this thesis focus on schemes based only on the arc lattice like it was realised for LEP or LHC [4,25] and the investigation of their capabilities and limitations. Because of the large value of the chromaticity it was decided to use an interleaved scheme to reduce the sextupole strength. According to the FODO cell phase advance of $\varphi_x = 90°$ and $\varphi_y = 60°$ the scheme consists of two families in the horizontal plane and three families in the vertical plane as illustrated in Fig. 4.11.

4.4 Correction of the W functions in the arc lattice

After the correction of the linear chromaticity the momentum acceptance obtained for the FCC-ee lattice is limited to $\pm 0.04\,\%$. In order to reach the design goal for luminosity stable operation must be guaranteed for $\pm 2\,\%$ momentum acceptance. Therefore, as a next step the sextupoles of the arcs are grouped into interleaved sextupole families as described

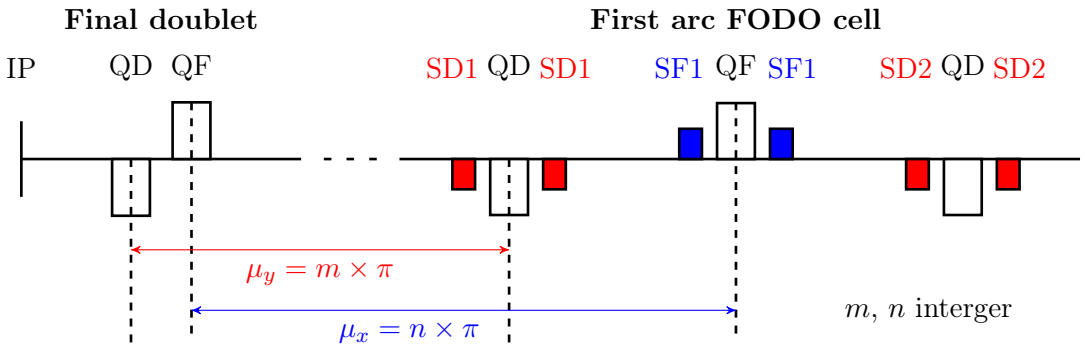

Figure 4.12: Matching of the phase advance between final doublet and the first quadrupoles in the regular arc lattice. The phase advance must be an integer number of π to allow effective correction of the W vector with a multi-family sextupole scheme.

above. Each arc has independent families. Such a multi-family sextupole scheme allows in addition to the linear chromaticity compensation to correct the W functions, the absolute value of the W vector. This correction involves following steps in exactly this order:

1. Adjusting the phase advance between the final doublet and the first arc cell
2. Rematching the betatron tunes
3. Correcting the W functions in the arcs next to the interaction regions
4. Matching the linear chromaticity with the sextupoles of the arcs in-between

Adjusting the phase advance between final doublet and arc lattice: As mentioned before, the W vector rotates in the (b_1,a_1) while propagating through the lattice with twice the average phase advance. For most efficient manipulation, the b_1 component should be zero at the place of the sextupole, since only the a_1 component is modified. Therefore the phase advance between the source of the chromatic perturbation, where the W vector is created, and the correcting element must be an integer number of π. Since sextupoles are installed at both sides of the quadrupoles in the arc lattice, the phase advance was adjusted in reference to the first quadrupole in the respective plane as illustrated in Fig. 4.12.

Before adjusting the linear optics, the phase advance between the defocussing quadrupole of the final doublet to the beginning of the first defocussing quadrupole in the regular arc lattice is $\mu_y = 3.05$. In the horizontal plane the phase advance from the corresponding final doublet quadrupole to the first focusing quadrupole in the middle of the first arc FODO cell is $\mu_x = 4.89$. The modification of the phase advance should be as small as possible to keep the effect on the beta functions on a feasible level. This basically leaves two alternatives in this case: $\mu_x = 4.5$, $\mu_y = 3.0$ and $\mu_x = 5.0$, $\mu_y = 3.0$. The beta functions for both options as well as for the initial optics are shown in Fig. 4.13. In the first case the horizontal beta function reaches a large peak of $\beta_x \approx 130\,\mathrm{m}$ at the third matching quadrupole of the

matching section between dispersion suppressor and the regular straight FODO cells. This high value could be prevented by adding further constraints to the optimisation, but this would require more free quadrupoles. As the difference between initial phase advance and final phase advance is smaller in the second case also the effect on the optics is smaller.

Phase advance fine-tuning: The phase relations discussed earlier once again just apply in the thin lens approximation. Because of their finite length the beta function varies within the quadrupole and the actual phase advance therefore slightly deviates from the thin lens case. In order to obtain highest possible efficiency of the sextupole families, the phase advance was varied until the best correction of the W functions was achieved.

For the variation of the phase advance a so-called *phasor* was used. A phasor is a symplectic matrix, which modifies the phase functions within the range of $\pm\pi$ but leaves the other lattice functions unchanged. Additional information to the matrix and the used MAD-X macro is given in Appendix B. For optimisations a phasor is a useful tool, because it is quickly installed and removed, while actual re-matching of the optics for each step would require a considerable amount of time. The phase advance was optimised in such a way, that the W functions reached a minimum value at the end of the arc. Once the optimum phase was found, the phasor was removed and the phase advance was matched with the quadrupoles.

In the FCC-ee Racetrack Layout the optimum phase advance was found smaller than the theoretical value. The difference was $\Delta\mu_x = -4.18 \times 10^{-3}$ in the horizontal plane and $\Delta\mu_y = -4.07 \times 10^{-4}$ in the vertical plane, which corresponds to $\Delta\mu_x = -0.24°$ and $\Delta\mu_y = -0.02°$ and shows that the thin lens approximation applied in Fig. 4.13 already leads to quite accurate results.

Rematching the tunes: Calculations of the beam-beam tune shift suggest fractional parts of the tunes of $Q_x = .54$ and $Q_y = .57$[1] [61]. After the presented adjustments of the phase advances the ideal tune values need to be restored by modifying the phase advance in other sections. For a large number of FODO cells in the arcs the flexibility of the phase advance per cell gets more and more restricted. In long arcs deviations from the nominal phase advance quickly add up to values, where the effect of the sextupoles become counterproductive. To fully exploit the potential of sextupole families the phase advance in the arcs should be kept constant and the tune should be adjusted in specific insertions without sextupoles [62]. In the FCC-ee lattices the FODO cells of straight sections were used to set the tunes. The matching sections were adjusted simultaneously in order to prevent the beta functions from beating. An example of the optics is shown in Fig. 4.14.

[1] The optimisation of the tune with respect to the beam-beam tune shift are still ongoing and the recommended values as well. For consistency all the calculations in context of this thesis were performed with the above mentioned working point.

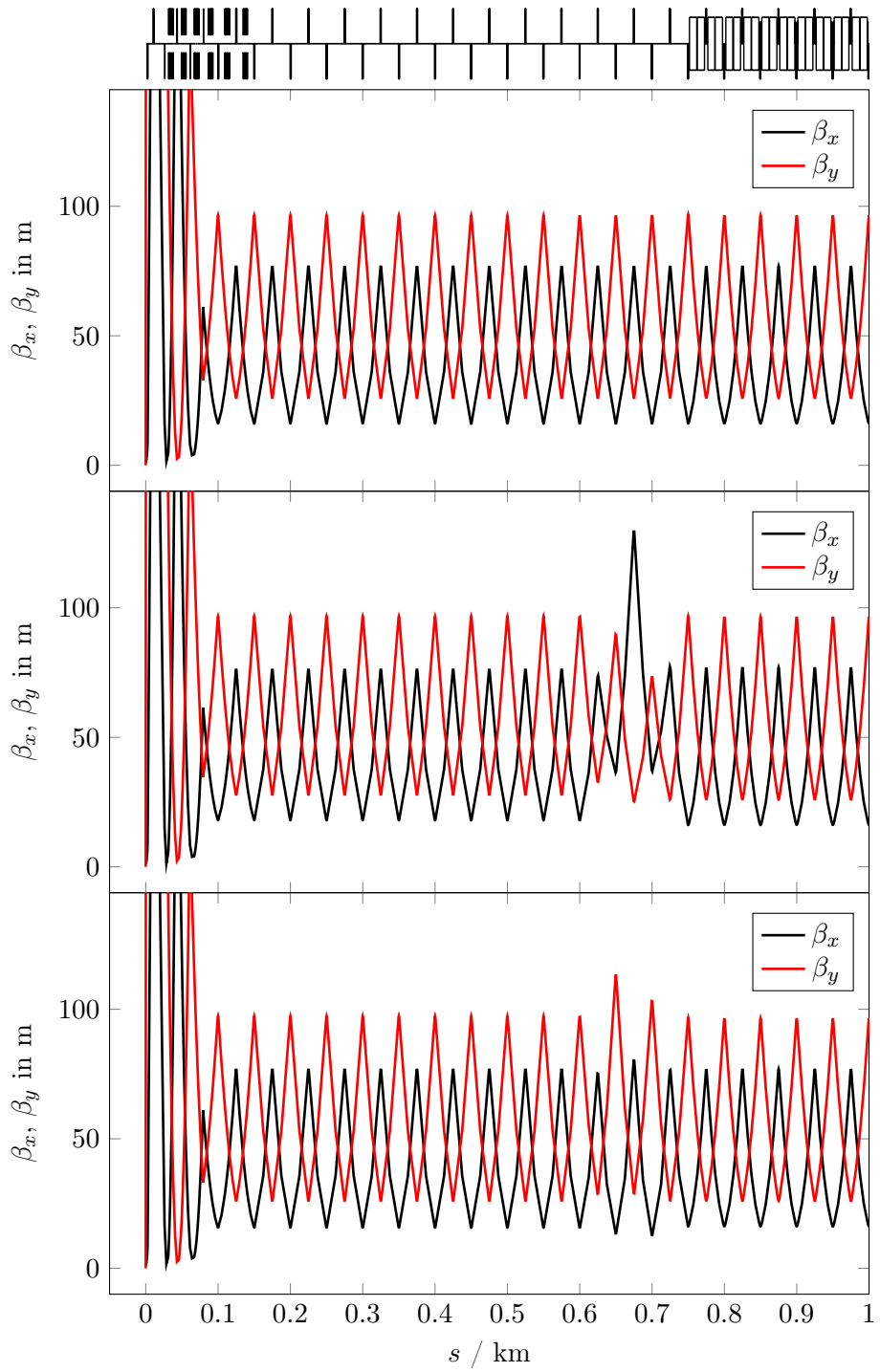

Figure 4.13: Beta function before and after matching the phase advance between final doublet and arc. The interaction point is located at $s = 0$. The phase advance was adjusted using the quadrupoles of the FODO cells in the straight section and the matching section towards the arc. The picture on the top shows the initial state. In the middle the optics for the phase advances $\mu_x = 4.5$, $\mu_y = 3.0$ are shown and below the optics for $\mu_x = 5.0$, $\mu_y = 3.0$.

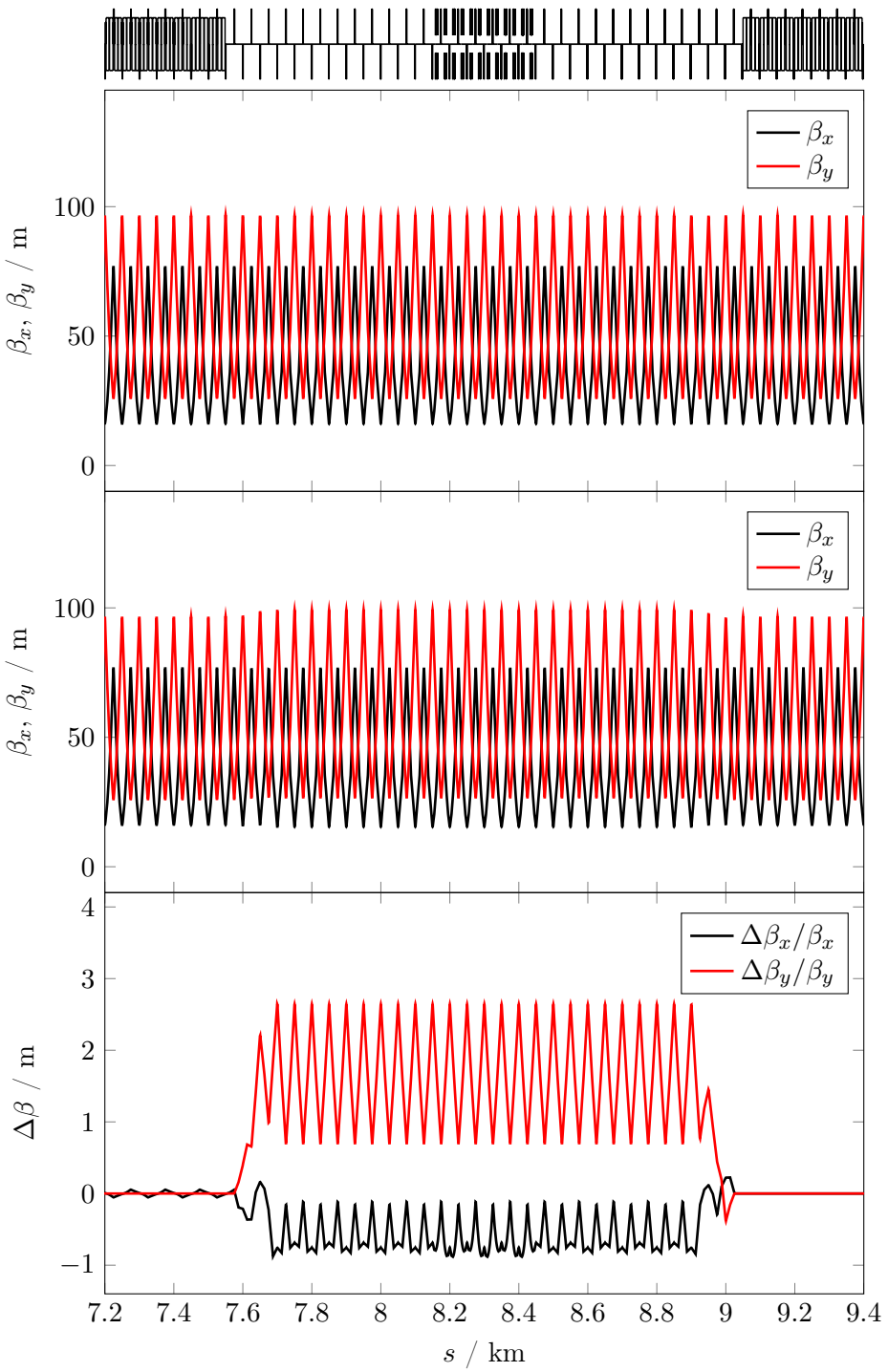

Figure 4.14: Beta functions in the straight section used to adjust the tunes. The plot on the top presents the initial optics, the one below the optics after matching. The plot on the bottom shows the difference between the beta functions.

Matching of the W functions: After the preparation of the linear lattice, described in the previous paragraphs, the correction of the W functions and the linear chromaticity was performed. This involves certain steps, which depend on the lattice, the actual beam optics and the sextupole scheme. Sometimes several iterations were necessary to achieve all the constraints. The following procedure was most effective and mainly used:

1. The W functions created by the final doublet are corrected iteratively by the sextupoles of the first family in each plane without periodic boundary conditions. Using the Matching Module of MAD-X the sextupole strengths are adjusted in such a way, that the W functions reach minimum values at the end of the arc.
2. The obtained sextupole strengths are also assigned to the last sextupole family of the arc in front of the next interaction region to increase the W functions again.
3. The sextupoles of the arcs in-between are used to compensate the remaining linear chromaticity. It is corrected to be zero.
4. The last step is an optimisation with periodic boundary conditions and all constraints. Additional families can be used for fine-tuning.

After the matching of the W functions the momentum acceptance was measured to evaluate the performance of the sextupole scheme. The dynamic aperture needs to be determined with six-dimensional particle tracking, which is very time-consuming. Therefore, a series of optics calculations with different energy deviations was done instead to get a first estimate.

The correction of the W functions was first applied to the 12-fold Layout described in Sec. 2.1.1. This layout allows to study lattices with different numbers of interaction points, which, as discussed in Sec. 4.1, has a major impact on the chromaticity budget. For FCC-ee two designs were proposed: an option with four interaction regions and an alternative option with only two interaction regions. Both were investigated.

4.4.1 12-fold Layout with four interaction points

As a first step the option with four interaction points was investigated. The minimum beta functions at the interaction points were $\beta_x^* = 1\,\text{m}$ and $\beta_y^* = 1\,\text{mm}$. Fig. 4.15 shows the W functions for one quarter of the ring after correction according to above described method. A detailed view of the first 11 km of the lattice is presented in Fig. 4.16. Starting from $W_x = W_y = 0$ at the first interaction point at $s = 0$ the W functions reach values of about $W_x = 105$ in the horizontal plane and $W_y = 2500$ in the vertical plane due to the strong field and the large beta functions in the mini-beta quadrupoles. After the final doublet they are not modified considerably before they reach the first arc. Here, mainly the sextupoles of the first family are used. As shown in Tab. 4.5, the strengths of the second and third sextupole family are by orders of magnitude smaller as they are just used for fine-tuning of the chromatic phase. As a result the W functions get iteratively decreased

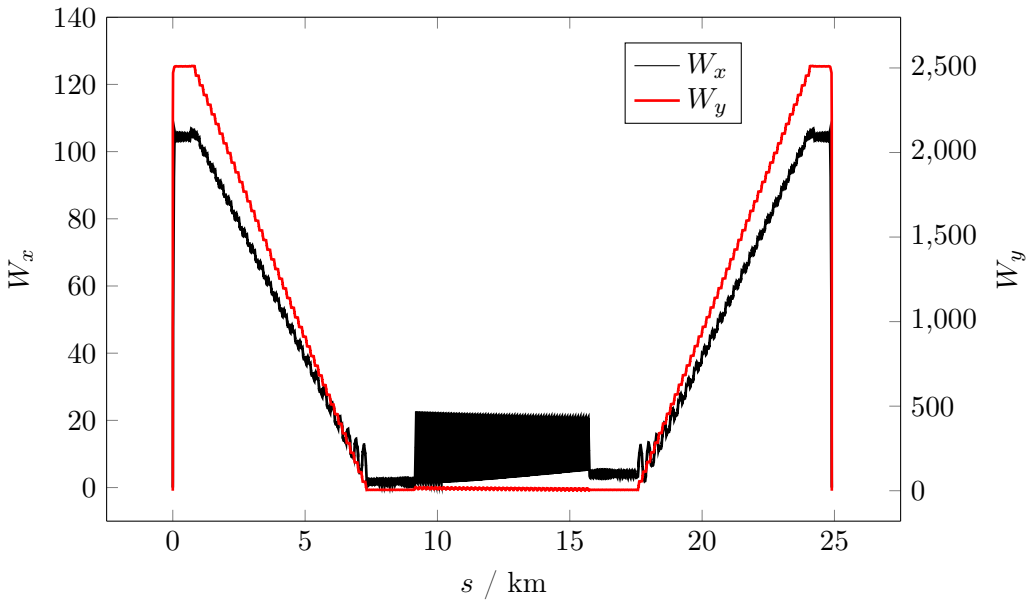

Figure 4.15: W functions of both transverse planes in-between two interaction points after correction. Starting from zero the W functions are created in the final doublet quadrupoles. They are iteratively decreased using one sextupole family in the first arc. The sextupoles of the second arc are used with equal strength for linear chromaticity correction. In the third arc one sextupole family per plane is used to increase the W again in order to compensate the left side of the next final focus system.

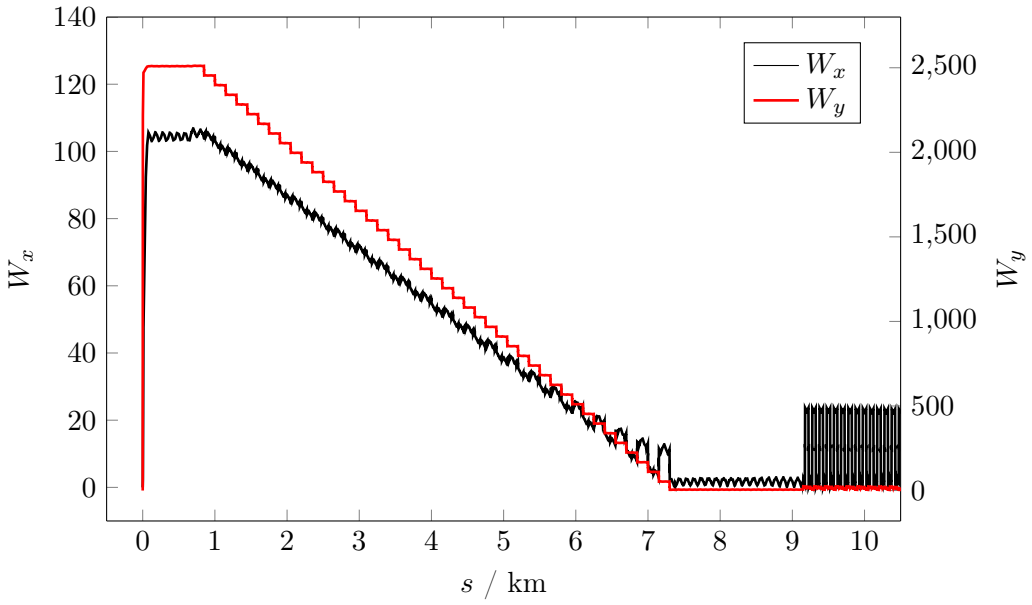

Figure 4.16: Detailed view of the W functions shown in Fig. 4.15. At the end of the arc, where the W functions are small, a considerable effect of the defocusing sextupoles in the horizontal plane is observed.

Table 4.5: Sextupole strengths of the 12-fold lattice with four interaction points after correction of W functions and linear chromaticity.

	Sextupole strengths in $1/m^3$	
	Horizontal plane	Vertical plane
Arc 1	k2sf1.1 = 0.18	k2sd1.1 = -9.29
	k2sf1.2 = 1.92×10^{-9}	k2sd1.2 = 1.25×10^{-3}
		k2sd1.3 = -9.18×10^{-3}
Arc 2	k2sf2.1 = 2.64	k2sd2.1 = -3.24
	k2sf2.2 = 2.64	k2sd2.2 = -3.28
		k2sd2.3 = -3.27
Arc 3	k2sf3.1 = -1.89×10^{-3}	k2sd3.1 = -9.29
	k2sf3.2 = 0.18	k2sd3.2 = -9.83×10^{-3}
		k2sd3.3 = -7.78×10^{-3}

until they reach values below 10 at the end of the arc. When the W functions are small, a considerable effect of the defocusing sextupoles in the horizontal plane is observed.

In the second arc all sextupoles are used with roughly the same strength. The W functions oscillate as earlier illustrated in Fig. 4.6. Because of the different scales of the axes, the oscillation is mainly observable in the horizontal plane, where the sextupoles increase the amplitude of the oscillation considerably compared to the straight section before. The variation of amplitude and the different values of W_x in the straight section between arc 2 and arc 3 is created, because the lattice is not completely symmetric. The request to arrange the sextupoles in pairs to cancel geometric aberrations requires to remove the sextupoles next to the last defocusing quadrupole of the second arc. As a consequence the phase relations from first interaction point to first arc and from the third arc to the second interaction point are slightly different. The sextupole families in the second arc therefore cannot have exactly the same strength. They were optimised to be slightly different in order to compensate the difference in phase advance.

In the third arc the W functions are built up again in order to compensate the chromatic effect of the left final doublet of the second interaction region. Again, the strengths of the second and third family are slightly different compared to the first arc, because the sextupoles are not distributed completely symmetrically.

The effect of the correction on the optics is illustrated in Fig. 4.17. The picture on top shows the beta functions – after correction – for design energy and for relative energy deviations of $\delta = \pm 0.06\,\%$. The picture below shows the same for the vertical plane. Especially in the vertical plane the beta beat is very strong. The beta function reaches more than 700 m, which is seven times its nominal value. As the W function is iteratively decreased also this chromatic beta-beat becomes smaller.

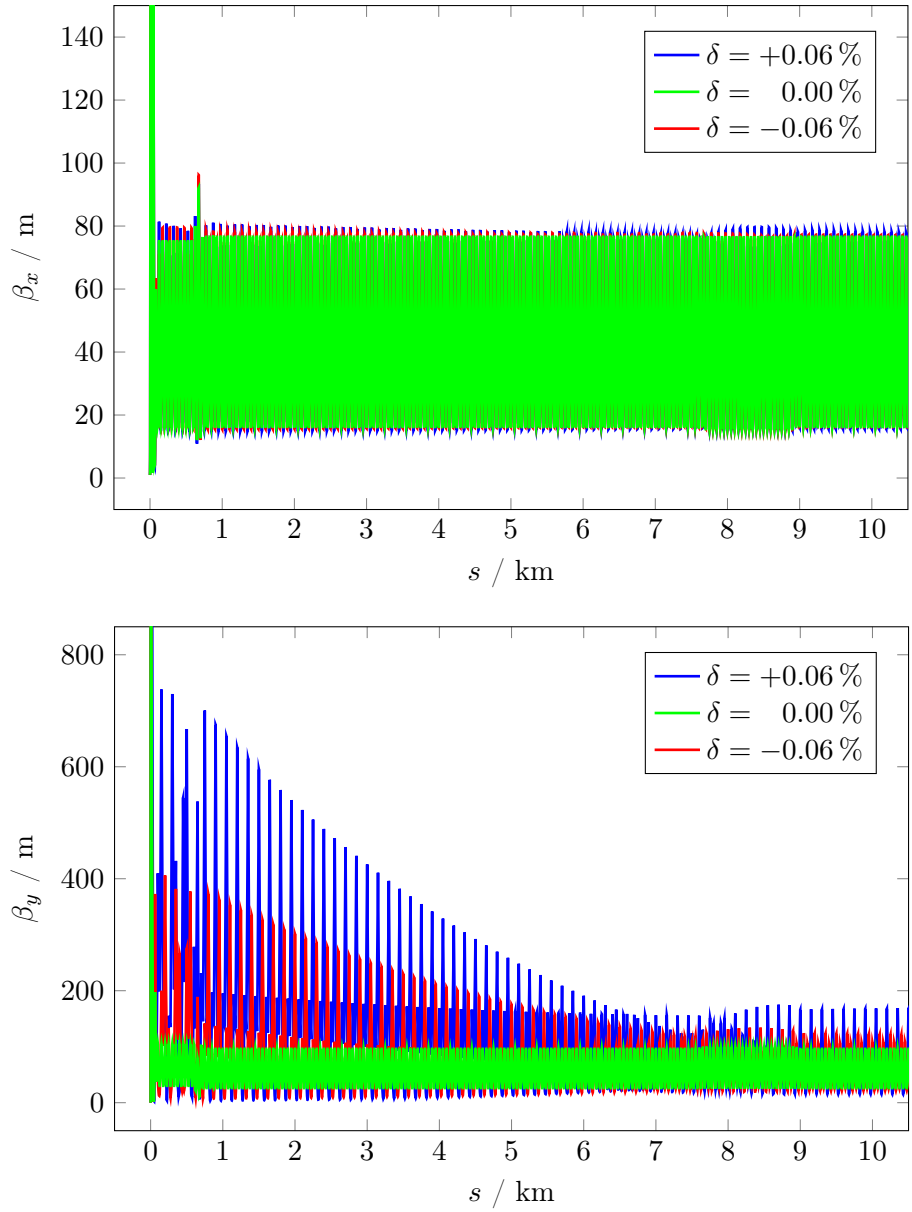

Figure 4.17: Beta functions after chromaticity correction. The top picture compares the horizontal beta functions for ideal energy and $\pm 0.06\,\%$ energy offset. The plot below shows the same for the vertical plane. As the W function is iteratively decreased the chromatic beta-beat becomes smaller. Still, even for an optimised W function a considerable chromatic distortion of the beta functions remains especially in the vertical plane.

Table 4.6: First four orders of chromaticities and their respective tune shifts in the 12-fold Layout before and after correction of W functions and linear chromaticity. The tune shift correspond to a relative energy offset of $\delta = 0.1\,\%$.

	Uncorrected	ΔQ (0.1 %)	Corrected	ΔQ (0.1 %)
Q'_x	-6.19×10^{2}	-6.19×10^{-1}	8.07×10^{-6}	8.07×10^{-9}
Q''_x	1.87×10^{4}	9.33×10^{-3}	-2.72×10^{3}	-1.36×10^{-3}
$Q_x^{(3)}$	-1.20×10^{8}	-2.00×10^{-2}	-7.46×10^{6}	-1.24×10^{-3}
$Q_x^{(4)}$	1.28×10^{12}	5.33×10^{-2}	-2.18×10^{10}	-9.09×10^{-4}
Q'_y	-2.05×10^{3}	-2.05×10^{0}	-6.25×10^{-6}	-6.25×10^{-9}
Q''_y	8.92×10^{6}	4.46×10^{0}	9.11×10^{3}	4.56×10^{-3}
$Q_y^{(3)}$	-2.17×10^{11}	-3.61×10^{1}	-2.21×10^{9}	-3.68×10^{-1}
$Q_y^{(4)}$	7.50×10^{15}	3.13×10^{2}	-2.60×10^{11}	-1.08×10^{-2}

Chromaticity: The values of the different orders of chromaticity before and after correction are compared in Tab. 4.6. In the horizontal plane the second order could be reduced by one order of magnitude, the third and fourth even by two orders. In the vertical plane the correction of the third order was relatively poor. While the second order was reduced by three orders of magnitude and the fourth order even by four, the decrease of the third order chromaticity was only two orders of magnitude. Comparing the tune shifts created by each order of chromaticity, the correction resulted in considerably smaller tune shifts. The largest tune shift is created by the third order chromaticity in the vertical plane.

Momentum acceptance: The strong effect of the third order chromaticity in the vertical plane is well visible in Fig. 4.18, which shows the tunes as a function of the energy offset $\delta = \Delta p/p$. As calculated, the tune mainly follows a negative third order polynomial.

MAD-X was able to calculate stable optics in a range from $\delta = -0.21\,\%$ to $\delta = +0.7\,\%$. However, the vertical tune function for negative energy deviation crosses both an integer and even before a half-integer resonance. The momentum acceptance corresponding to this chromaticity correction scheme is therefore restricted to the range from $\delta = -0.08\,\%$ to $\delta = +0.07\,\%$. This is already considerably larger compared to the simple linear chromaticity correction, where the momentum acceptance was $\delta < \pm 0.04\,\%$, but at the same time still more than one order of magnitude below the requirement of $\pm 2\%$.

In addition to the tune functions calculated by MAD-X Fig. 4.19 shows the functions calculated from the chromaticity values of the macro. In the range of $\delta = \pm 0.05\,\%$ both calculations agree very well, for larger energy offsets the values deviate, but still show good agreement within the accepted momentum range. This means the higher-order terms calculated with the macro suffice for a first evaluation of the sextupole scheme.

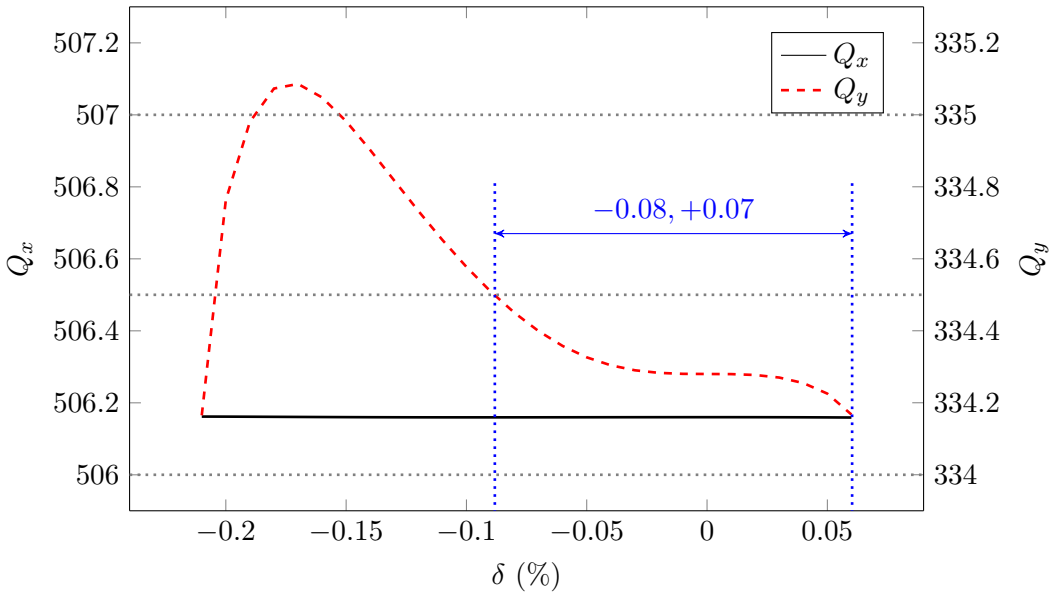

Figure 4.18: Tune functions and omentum acceptance of the lattice with 12-fold Layout and four interaction points after the correction of W functions and linear chromaticity.

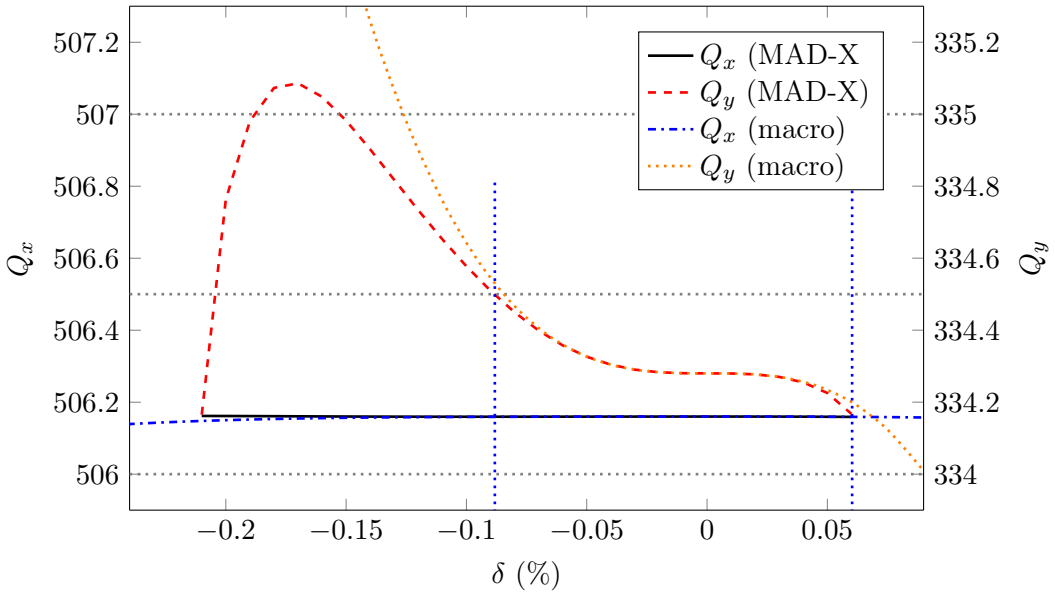

Figure 4.19: Comparison of the tune functions obtained with optics calculations in MAD-X and the with the macro used to evaluate the chromaticity. In the range of $\delta = \pm 0.05\,\%$ the agreements is very good. The deviations for larger momentum offsets are still small enough within the accepted energy range to allow a first evaluation of the sextupole scheme.

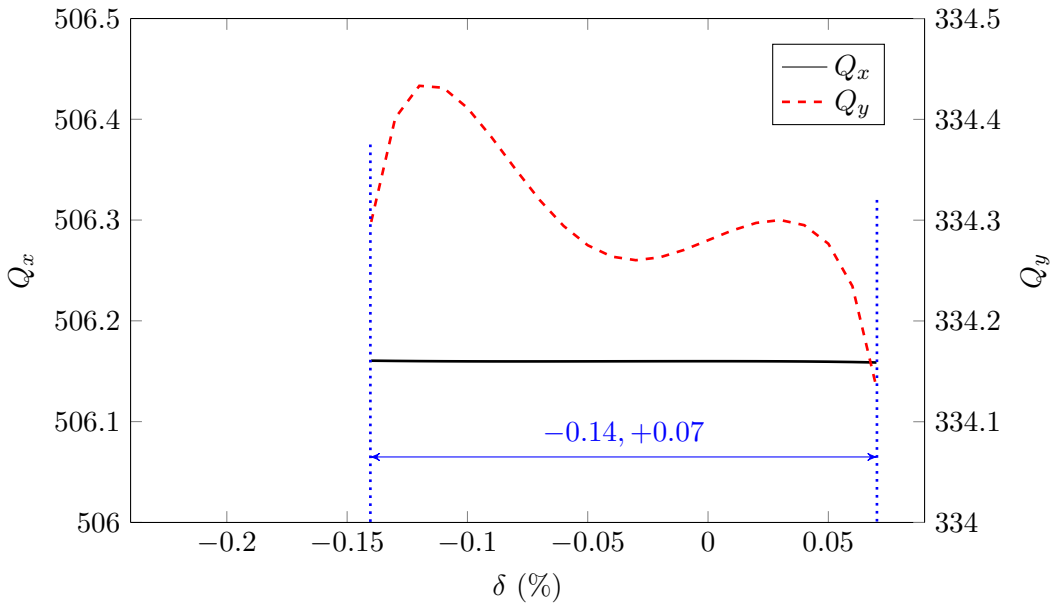

Figure 4.20: Tune functions and momentum acceptance of the lattice with 12-fold Layout and four interactions points. The W functions were matched as before, but in this case the vertical linear chromaticity of the lattice is set to $Q'_y = +25$.

Positive linear chromaticity: The momentum acceptance obtained after matching the W functions and compensation of the linear chromaticity is limited by the integer resonance $Q_y = 334$ for positive energy offset and the half integer resonance $Q_y = 334.5$ for particles with negative energy offset. In order to further increase the momentum acceptance, the vertical tune must be decreased for particles with negative momentum deviation and increased for particles with positive energy deviation. Such energy dependent tune shifts can be provided by a larger linear chromaticity. Instead of matching the linear chromaticity of the vertical plane to zero, as in the previous case, it is now set to a positive value. Fig. 4.20 shows the resulting tune functions for an increased vertical linear chromaticity of $Q'_y = +25$. The additional linear contribution is visible in the slope of the vertical tune function at $\delta = 0$. With this simple modification the momentum acceptance could be increased by another 40 % and reaches now values between $\delta = -0.14\,\%$ to $\delta = +0.07\,\%$.

4.4.2 12-fold Layout with two interaction points

As a next step the design option with two interaction regions was studied. Following the same procedure, explained above, the W functions were iteratively decreased by the first sextupole family in Arc 1 and increased again in Arc 6 as shown in Fig. 4.21. The four remaining arcs in-between were used for linear chromaticity correction, while for symmetry reasons the families of Arc 2 and Arc 3 had the same strength and the families in Arc 4

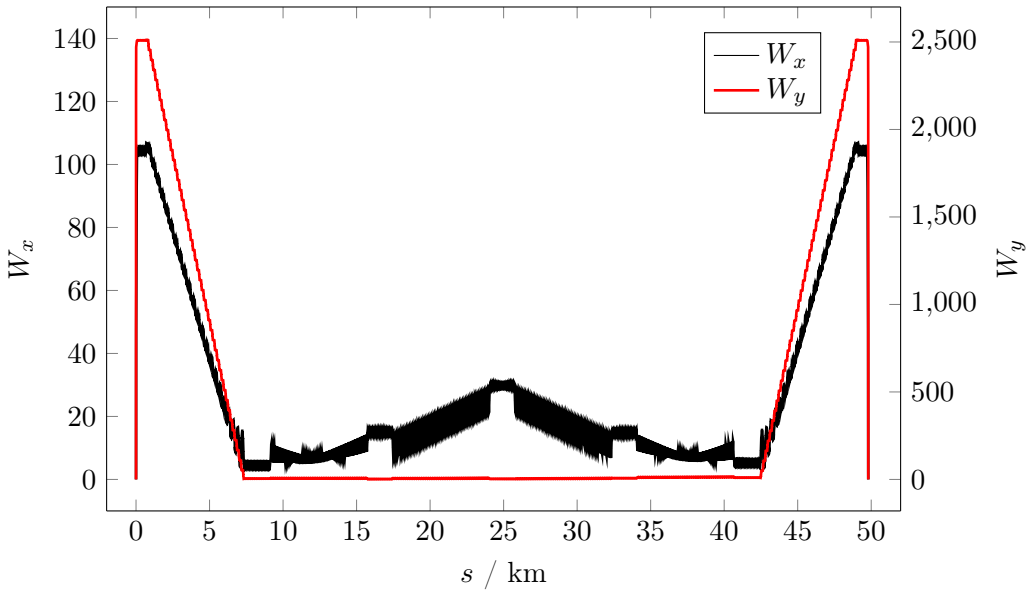

Figure 4.21: Matched W functions in the 12-fold Layout with two interaction points. The plot shows the lattice between two interaction points, which corresponds to half of the ring.

and Arc 5. The increase of the W function in the horizontal plane is remarkable. In the straight section at $s = 25\,\text{km}$ it reaches a value of about $W_x = 30$.

The corresponding sextupole strengths after correction are listed in Tab. 4.7. The families used for correction of the W functions have similar strength compared to the lattice with four interaction regions. The sextupole families used for linear chromaticity correction, have less than half the strength compared to the lattice with four interaction regions. As discussed earlier in Sec. 4.1, the linear chromaticity created by the final doublet quadrupoles decreases from $Q'_y = -2048.9$ to $Q'_y = -1253.9$ for two interaction points. In addition, the sextupole magnets of four arcs are now used for the correction instead of only one as in the case of four interaction points. While in the vertical plane all sextupoles families in the Arcs 2, 3, 4 and 5 have the same strength, a considerable difference is observed in the horizontal plane leading to the previously mentioned increase of the W function.

The smaller number of interaction points also leads to a decrease of the higher-order terms of the natural chromaticity, which were presented in Tab. 4.3. The values after correction should therefore be smaller compared to the case with four interaction points, resulting in smaller tune shifts and a larger momentum acceptance. Tab. 4.8 compares the chromaticities of both cases after correction of W functions and linear chromaticity. Except the linear chromaticity and the second order in the horizontal plane, the higher order terms have indeed roughly half the value than in the four interaction point lattice.

Table 4.7: Sextupole strength of the 12-fold Layout with two interaction points after correction of W functions and linear chromaticity.

	Sextupole strengths in $1/m^3$	
	Horizontal plane	Vertical plane
Arc 1	k2sf1.1 = 0.19	k2sd1.1 = -9.30
	k2sf1.2 = 0.00	k2sd1.2 = -0.01
		k2sd1.3 = -0.03
Arc 2, 3	k2sf2.1 = 1.10	k2sd2.1 = -1.54
	k2sf2.2 = 1.13	k2sd2.2 = -1.54
		k2sd2.3 = -1.53
Arc 4, 5	k2sf4.1 = 1.12	k2sd4.1 = -1.53
	k2sf4.2 = 1.11	k2sd4.2 = -1.53
		k2sd4.3 = -1.55
Arc 6	k2sf6.1 = -0.01	k2sd6.1 = -9.31
	k2sf6.2 = 0.17	k2sd6.2 = -0.02
		k2sd6.3 = -0.09

Table 4.8: Chromaticities and tune shifts of the 12-fold Layout compared for four and for two interaction points (IPs). The tune shifts correspond to an energy deviation of $\delta = 0.1\,\%$.

	Four IPs	ΔQ (0.1 %)	Two IPs	ΔQ (0.1 %)
Q'_x	8.07×10^{-6}	8.07×10^{-9}	-3.56×10^{-5}	-3.56×10^{-8}
Q''_x	-2.72×10^{3}	-1.36×10^{-3}	-4.63×10^{2}	-2.31×10^{-4}
$Q^{(3)}_x$	-7.46×10^{6}	-1.24×10^{-3}	-3.88×10^{6}	-6.47×10^{-4}
$Q^{(4)}_x$	-2.18×10^{10}	-9.09×10^{-4}	-1.35×10^{10}	-5.63×10^{-4}
Q'_y	-6.25×10^{-6}	-6.25×10^{-9}	-1.45×10^{-4}	-1.45×10^{-7}
Q''_y	9.11×10^{3}	4.56×10^{-3}	4.92×10^{3}	2.46×10^{-3}
$Q^{(3)}_y$	-2.21×10^{9}	-3.68×10^{-1}	-1.11×10^{9}	-1.85×10^{-1}
$Q^{(4)}_y$	-2.60×10^{11}	-1.08×10^{-2}	-1.33×10^{11}	-5.54×10^{-3}

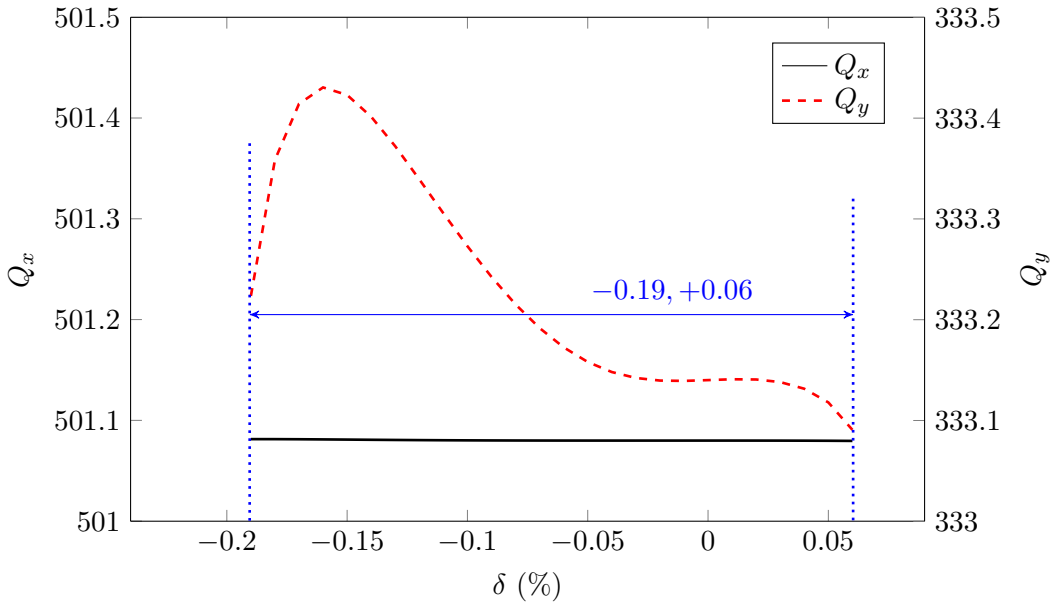

(a)

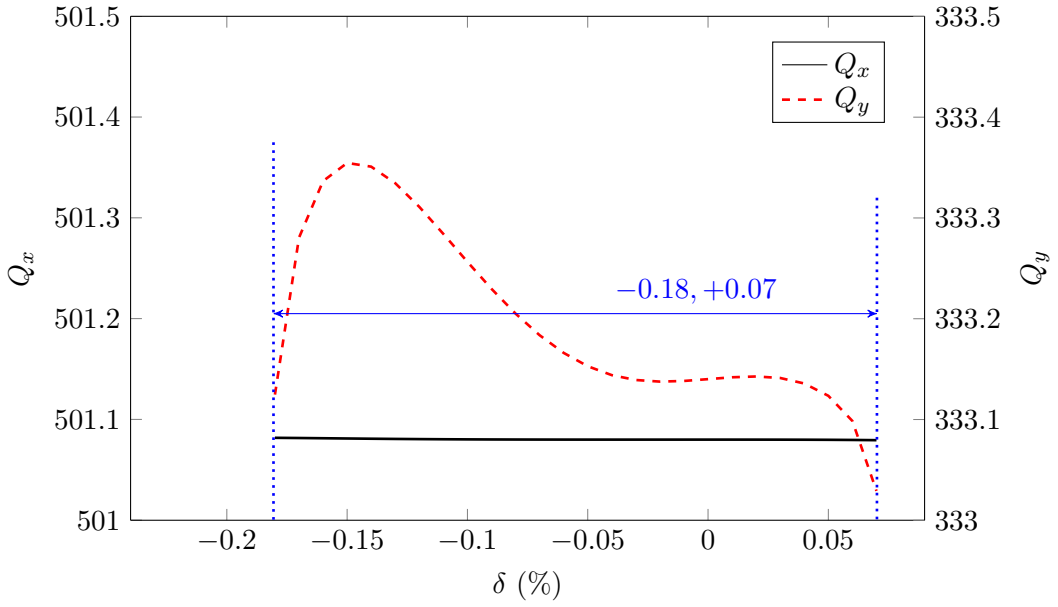

(b)

Figure 4.22: Tune functions and momentum acceptance of the 12-fold lattice with two interactions points after matching the W functions. In case (a) the linear vertical chromaticity is set to $Q'_y = +5$ to prevent crossing the half-integer resonance. If the the linear chromaticity is further increased to $Q'_y = +10$ the tune function gets flatter and the momentum acceptance slightly shifts to positive values of δ.

The largest tune shifts are still created in the vertical plane, especially by the third-order chromaticity.

Fig. 4.22 (a) shows the result of the momentum scan after matching the W function. The vertical tune function is still determined by the third order, but since the tune shifts are smaller it was sufficient to set the linear chromaticity to $Q'_y = +5$ to avoid crossing the half-integer resonance $Q_y = 334.5$ instead of $Q'_y = +25$. The obtained momentum acceptance reaches from $\delta = -0.19\%$ to $+0.06\%$. If the linear chromaticity is increased to $Q'_y = +10$ the stable energy range shifts to $\delta = -0.18\,\%$ to $+0.07\,\%$, which is slightly more symmetrical around $\delta = 0$, as illustrated in Fig. 4.22 (b).

4.5 *W* functions of the FCC-ee Racetrack Layout

The first corrections of the W functions in the FCC-ee 12-fold lattice helped to understand the applied correction method. It once again became clear how important the number of interaction points is for the chromaticity budget and thus the momentum acceptance. As a next step the same method was applied to the FCC-ee lattice with Racetrack Layout introduced in Sec. 2.1.2. This layout is compatible with the requirements of the FCC hadron collider and the site-specific constraints of the Geneva basin. For an optimised correction of the W functions the lattice is designed to offer highest possible symmetry of both linear lattice and the sextupole distribution. In addition, the arcs next to the straight sections with interaction regions have a length of 4.4 km instead of 6.8 km in the 12-fold Layout, which means the W functions are corrected in a shorter distance. According to Eq. (4.14c) this will reduce the third order chromaticity. The formula consists of four terms

$$\begin{aligned}\frac{\partial^3 Q_y}{\partial \delta^3} = \; & 6\frac{\partial Q_y}{\partial \delta} - \frac{1}{2\pi}\oint \beta_y (k_1 - k_2 D_0)(a_{1y}^2 + b_{1y}^2)\,\mathrm{d}s \\ & + \frac{3}{2\pi}\oint \beta_y \left(k_2 D_1 + k_3 \frac{D_0^2}{2} - k_2 D_2 - k_3 D_0 D_1\right)\mathrm{d}s \\ & + \frac{3}{4\pi}\oint \beta_y b_{2y}(k_1 - k_2 D_0)\,\mathrm{d}s\end{aligned}$$

The first one is determined by the linear chromaticity, which is considered to be compensated. The third term describes the effect of octupole fields to the lattice, represented by the normalised octupole strength k_3. Since no octupoles are installed in the lattice, these factors vanish. It also describes the effect of sextupoles at places with finite higher-order dispersion D_1 and D_2. The contribution of these factors has been evaluated and proved to be negligible [63], since the D_1 and D_2 are small. The last term includes the second-order chromatic derivative of the beta function b_2, which is determined by the FODO lattice and cannot be modified. The second term, however, is the integral over the square of the W

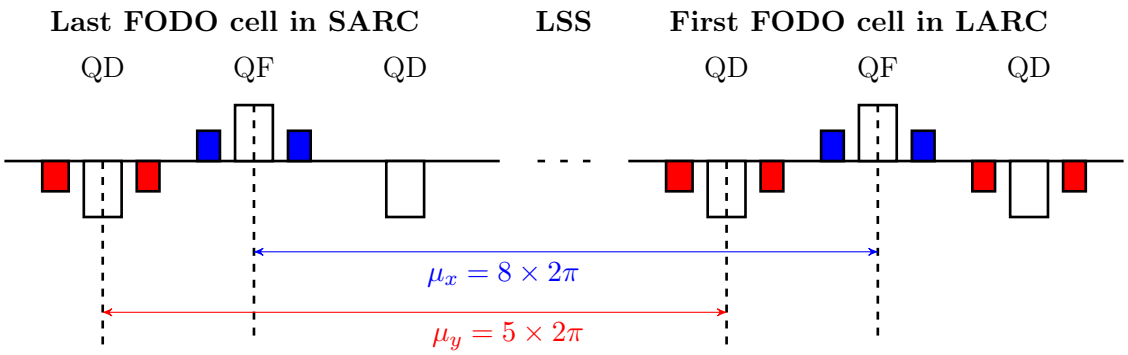

Figure 4.23: Phase advance between the LSS straight sections in the Racetrack Layout. The phase advance was adjusted to be $\mu_x = 8 \times 2\pi$ and $\mu_y = 5 \times 2\pi$. The $+I$ transformation makes the straight section invisible for the chromaticity correction scheme.

function and depends on the actual sextupole correction scheme:

$$-\frac{1}{2\pi} \oint \beta_y (k_1 - k_2 D_0) \underbrace{(a_{1y}^2 + b_{1y}^2)}_{W^2} \, \mathrm{d}s \tag{4.17}$$

Therefore, when the W function is corrected in shorter arcs, the integral decreases and so should the third-order chromaticity.

In the end, the FCC-ee Racetrack Layout not only corresponds to the machine baseline of the design study since it is compatible with the requirements of the FCC hadron collider, but also features better conditions for the design of the chromaticity correction scheme.

4.5.1 Comparison of 12-fold and Racetrack Layout for $\beta_y^* = 1\,\mathrm{mm}$

The Racetrack Layout includes two interaction regions. For the comparison to the corresponding 12-fold layout the same beta functions at the interaction point $\beta_x^* = 1\,\mathrm{m}$ and $\beta_y^* = 1\,\mathrm{mm}$ were established. The W functions, starting from zero at the interaction point, consequently reach the same values as in the 12-fold Layout and are then iteratively corrected by the first sextupole family of the SARC. The phase advance of the subsequent LSS straight section between short arcs and long arcs are adjusted as illustrated in Fig. 4.23. The phase advance from the sextupoles in the first arc to the sextupoles of the second arc is $\mu_x = 8 \times 2\pi$ in the horizontal plane and $\mu_y = 5 \times 2\pi$ in the vertical one. The $+I$ transformation makes the straight section transparent for the chromaticity correction scheme. In the LARCs the symmetric sextupole distribution allows to group all sextupoles in only one family per plane, which is then used to compensate the linear chromaticity. In the SARC before the second interaction region the W functions are built up again to compensate the effect of the left final doublet.

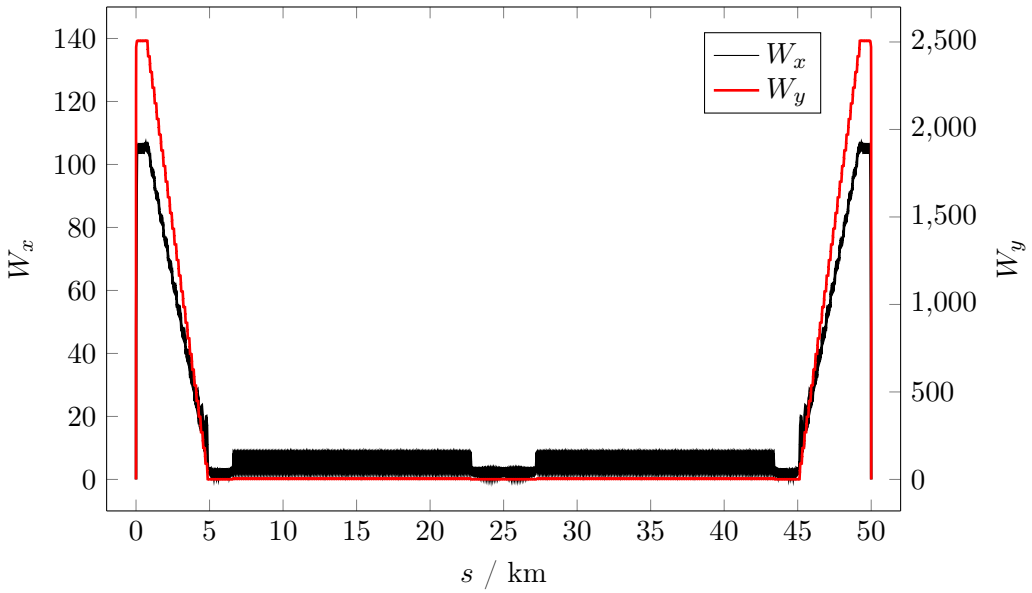

Figure 4.24: W functions in the first half of the Racetrack Layout after chromaticity correction.

The W functions for the first half of the lattice are shown in Fig. 4.24. The second half is identical. As in the cases before, the W functions are zero at the interaction point at $s = 0$. However, because of the shorter length, the W functions are corrected already after 5 km instead of approximately 7.5 km in the 12-fold Layout. Different to the previous cases presented in Fig. 4.15 and Fig. 4.21 the oscillation of the W function in the arcs used for the correction of the linear chromaticity is regular and has the same amplitude in the whole arc.

Sextupole strengths: The sextupole strengths applied for the correction of the W function in the Racetrack Layout are listed in Tab. 4.9. Compared to the sextupole strengths of the two interaction point 12-fold Layout (Tab. 4.7) the strength of the first defocussing family in Arc 1 increased by a factor of +0.53, which corresponds to the lower number of sextupoles. While in the 12-fold Layout 88 sextupoles were used to correct the W function, only 54 are available in the Racetrack Layout. In the horizontal plane the second family of the first arc counteracts the compensation of the W function, probably because of a phase mismatch. Taking this extra increase for the first family into account the increase compared to the value of the 12-fold Layout is also equal to +0.53. For the same reason the strength of the sextupoles for the linear chromaticity correction on the other side becomes smaller. On the one hand more sextupoles are available in the LARCs, on the other hand the absolute value of the natural linear chromaticity is about 100 units smaller in the Racetrack Layout (compare Tab. 4.1).

Table 4.9: Sextupole strengths in the Racetrack lattice after correction of the W function and linear chromaticity compensation. The vertical beta function at the interaction point was $\beta_y^* = 1\,\text{mm}$.

	Sextupole strengths in m^{-3}	
	Horizontal plane	Vertical plane
Arc 1,4	k2sf1.1 = 0.37	k2sd1.1 = -14.91
	k2sf1.2 = 0.08	k2sd1.2 = 7.57×10^{-4}
		k2sd1.3 = -4.81×10^{-3}
Arc 2,3	k2sf = 0.91	k2sd = -1.26

Table 4.10: Comparison of the chromaticities and respective tune shifts ΔQ of the 12-fold Layout with two interaction points (IPs) and the Racetrack Layout.

	12-fold (2 IPs)	ΔQ (0.1 %)	Racetrack (2 IPs)	ΔQ (0.1 %)
Q'_x	-3.56×10^{-5}	-3.56×10^{-8}	5.76×10^{-2}	5.76×10^{-5}
Q''_x	-4.63×10^{2}	-2.31×10^{-4}	6.86×10^{2}	3.43×10^{-4}
$Q_x^{(3)}$	-3.88×10^{6}	-6.47×10^{-4}	-3.19×10^{6}	-5.32×10^{-4}
$Q_x^{(4)}$	-1.35×10^{10}	-5.63×10^{-4}	-1.03×10^{10}	-4.27×10^{-4}
Q'_y	-1.45×10^{-4}	-1.45×10^{-7}	3.76×10^{-2}	3.76×10^{-5}
Q''_y	4.92×10^{3}	2.46×10^{-3}	6.33×10^{2}	3.16×10^{-4}
$Q_y^{(3)}$	-1.11×10^{9}	-1.85×10^{-1}	-8.44×10^{8}	-1.40×10^{-1}
$Q_y^{(4)}$	-1.33×10^{11}	-5.54×10^{-3}	-6.50×10^{10}	-2.70×10^{-3}

Chromaticity and momentum acceptance: As the correction of the W functions is obtained in a shorter distance a smaller third-order chromaticity contribution is expected. Tab. 4.10 compares the chromaticity of the two interaction point version of the 12-fold lattice to the Racetrack Layout. In the horizontal plane the third-order chromaticity reduced about 18 % from $Q_x^{(3)} = -3.88 \times 10^6$ to $Q_x^{(3)} = -3.19 \times 10^6$. In the vertical plane the effect is even larger: the third order-term decreased about 34 % from $Q_y^{(3)} = -1.11 \times 10^9$ to $Q_y^{(3)} = -8.44 \times 10^8$. The linear vertical chromaticity was increased to $Q'_y = 15$ to avoid the half-integer resonance. In the 12-fold Layout a linear chromaticity of just $Q'_y = 5$ was necessary. The tune shift for negative energy deviation created by the forth order decreased as well. This could be the reason, why a larger linear chromaticity is required.

The momentum acceptance of the Racetrack Layout obtained by an energy scan in MAD-X is presented in Fig. 4.25. Compared to the 12-fold Layout the momentum acceptance could be increased by another 14 % to a range from $\delta = -0.22\,\%$ to $\delta = +0.07\,\%$. The more efficient correction of the W functions in the Racetrack Layout results, as expected, in a larger momentum acceptance than in the 12-fold Layout for the same conditions.

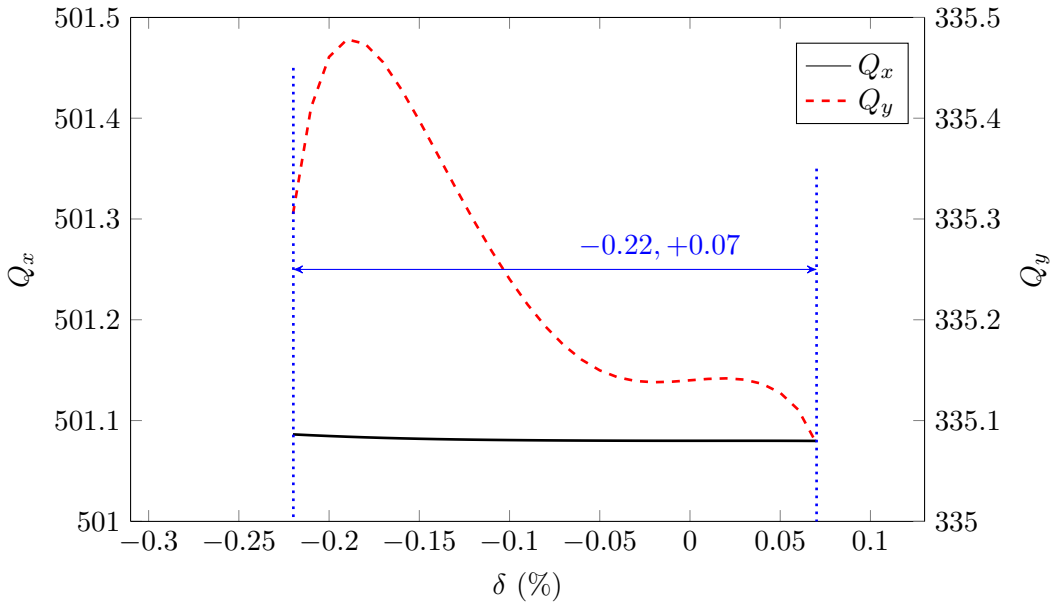

Figure 4.25: Tune functions and momentum acceptance of the Racetrack Layout with $\beta_y^* = 1\,\text{mm}$. The linear chromaticity of the vertical plane was set to $Q'_y = 15$ to avoid crossing the half-integer resonance.

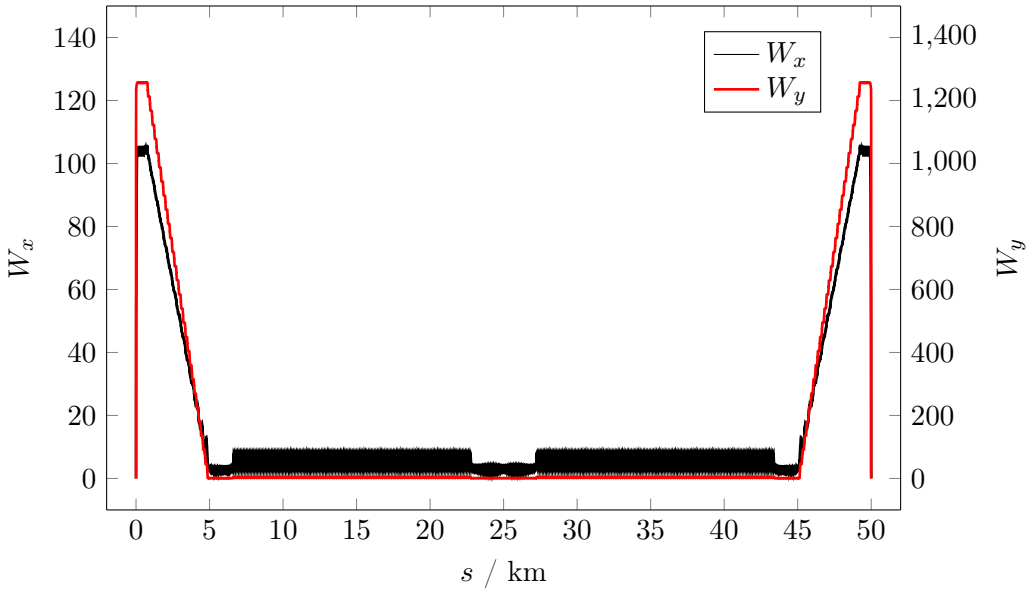

Figure 4.26: W functions in the first half of the Racetrack Layout with $\beta_y^* = 2\,\text{mm}$ after chromaticity correction.

4.5.2 Racetrack Layout with $\beta_y^* = 2\,\mathrm{mm}$

The committee of the FCC-ee Review in October 2015 recommended a set of new baseline parameters, which are summarized in [16]. The main outcome for the chromaticity compensation scheme was the increase of the vertical beta function at the interaction points from $\beta_y^* = 1\,\mathrm{mm}$ to $2\,\mathrm{mm}$ in order to reduce the chromaticity budget of the machine and so to achieve higher momentum acceptance of the lattice. This development was highly appreciated, because it relaxes the requirements for the chromaticity correction scheme. The discussions in Sec. 4.1 showed, that the linear chromaticity strongly depends on the value of β^*. It is no surprise that this also applies for the higher-order terms (see Tab. 4.3).

The W functions after their correction are shown in Fig. 4.26. The only difference to the $\beta_y^* = 1\,\mathrm{mm}$ case (Fig. 4.24) is the maximum value of the vertical W function in the straight sections with the interaction regions. The focussing of the final focus quadrupole is less strong and consequently creates less chromatic aberrations. The maximum value is therefore $W_y = 1256$ instead of 2500. This means, by doubling β^* the maximum W function decreases as expected by a factor two.

The sextupole strengths after correction are listed in Tab. 4.11. The smaller value of the W function consequently leads to reduced sextupole strengths in the vertical plane. In the horizontal plane the non-zero strength of the second family in the first arc indicates a phase mismatch between final doublet and arc sextupoles, which is compensated by the strength of the second sextupole family.

Tab. 4.12 compares the chromaticities of the Racetrack lattices after correction: in the case of the higher $\beta_y^* = 2\,\mathrm{mm}$ all values could be decreased. The main tune shift is still created by the third order in the vertical plane, but for the first time it is in the order of 10^{-2}. This improvement can of course also be recognized in the momentum acceptance. This lattice offers the largest momentum acceptance so far, which spans a range from $\delta = -0.29\,\%$ to $\delta = 0.11\,\%$. The tune functions are shown in Fig. 4.27. This time no linear chromaticity contribution was required to avoid the half-integer resonance.

Table 4.11: Sextupole strengths of the Racetrack Layout with $\beta_y^* = 2\,\mathrm{mm}$ after chromaticity correction with two families in the horizontal plane and three families in the vertical plane.

	Sextupole strengths in m^{-3}	
	Horizontal plane	Vertical plane
Arc 1, 4	k2sf1.1 = 0.47	k2sd1.1 = -7.47
	k2sf1.2 = -0.19	k2sd1.2 = 0.01
		k2sd1.3 = 0.00
Arc 2, 3	k2sf = 0.79	k2sd = -1.21

Table 4.12: Chromaticities and tune shifts for 0.1 % energy deviation of the Racetrack Layout for $\beta_y^* = 1\,\text{mm}$ and 2 mm.

	$\beta_y^* = 1\,\text{mm}$	ΔQ (0.1 %)	$\beta_y^* = 2\,\text{mm}$	ΔQ (0.1 %)
Q'_x	5.76×10^{-2}	5.76×10^{-5}	-3.99×10^{-3}	-3.99×10^{-6}
Q''_x	6.86×10^{2}	3.43×10^{-4}	3.56×10^{2}	1.78×10^{-4}
$Q_x^{(3)}$	-3.19×10^{6}	-5.32×10^{-4}	-1.89×10^{6}	-3.15×10^{-4}
$Q_x^{(4)}$	-1.03×10^{10}	-4.27×10^{-4}	-3.02×10^{9}	-1.26×10^{-4}
Q'_y	3.76×10^{-2}	3.76×10^{-5}	7.81×10^{-3}	7.81×10^{-6}
Q''_y	6.33×10^{2}	3.16×10^{-4}	2.36×10^{3}	1.18×10^{-3}
$Q_y^{(3)}$	-8.44×10^{8}	-1.40×10^{-1}	-2.29×10^{8}	-3.82×10^{-2}
$Q_y^{(4)}$	-6.50×10^{10}	-2.70×10^{-3}	1.64×10^{9}	6.85×10^{-5}

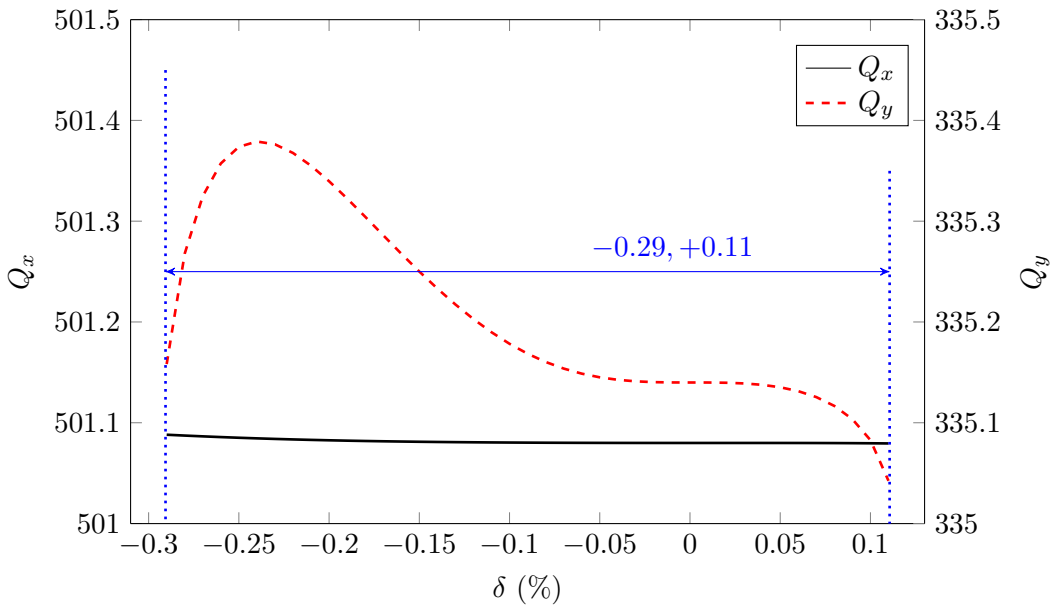

Figure 4.27: Tune functions and momentum acceptance of the Racetrack Lattice with $\beta_y^* = 2\,\text{mm}$ after correction of W functions and linear chromaticity.

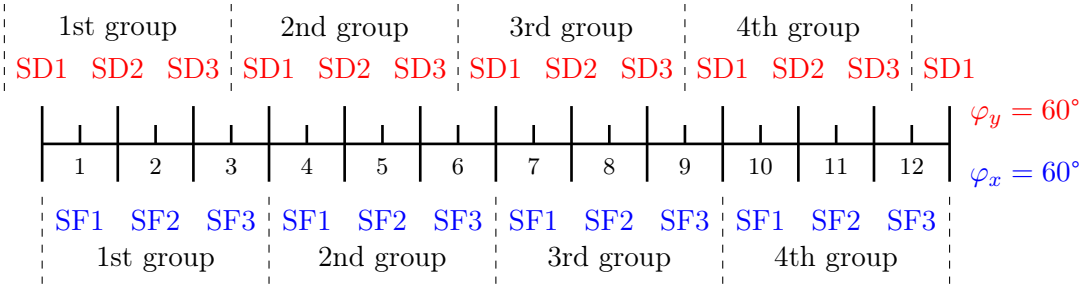

Figure 4.28: Sextupole scheme for the the 60°/60° optics with three interleaved sextupole families per plane.

4.5.3 Three sextupole families per plane in a 60°/60° optics

To complete the study of sextupole schemes for the correction of the W functions the efficiency of this method was benchmarked for a different phase advance per cell. It was decided to investigate an optics with $\varphi_{x,y} = 60°$ FODO cell phase advance in both planes, which was the phase advance chosen for LEP during the design phase of the machine [25]. The corresponding sextupole scheme now comprises three interleaved families per plane as illustrated in Fig. 4.28, which during the investigations of the 90°/60° optics proved to be more flexible than a two-family scheme.

Linear optics: For completeness it might be mentioned, that beyond the fact that the allocation of the sextupoles magnets had to follow the new phase advance, a modification of the dispersion suppressors was required. A third half-bend cell was installed in order to create a smooth transition of the dispersion function from the arc lattice to the straight cells. The phase advance between final focus quadrupoles and first quadrupoles in the regular arc lattice was set to $\mu_x = 3.5 \times 2\pi$ and $\mu_y = 2.5 \times 2\pi$ and the phase advance of the LSS to $\mu = 5.5 \times 2\pi$ in both planes. The tunes of the 60°/60° optics are $Q_x = 337.08$ and $Q_y = 335.14$. The natural linear chromaticity is $Q'_x = -336.93$ in the horizontal plane and $Q'_y = -635.92$ in the vertical plane.

W functions and sextupole strengths: The W functions in the 60°/60° case were corrected as described before. Fig. 4.29 shows the W functions after their correction and the compensation of the linear chromaticity with the sextupoles of the LARCs. At first sight they look the same as for the 90°/60° optics, but a closer look in Fig. 4.30 reveals an oscillation of the horizontal W with a large amplitude in the first arc, where the W functions are corrected. This oscillation can easily be explained: since the phase advance is the same in both planes, the families of one plane have now an additive effect in the other plane as well, which has to be compensated in addition. The details of this effect

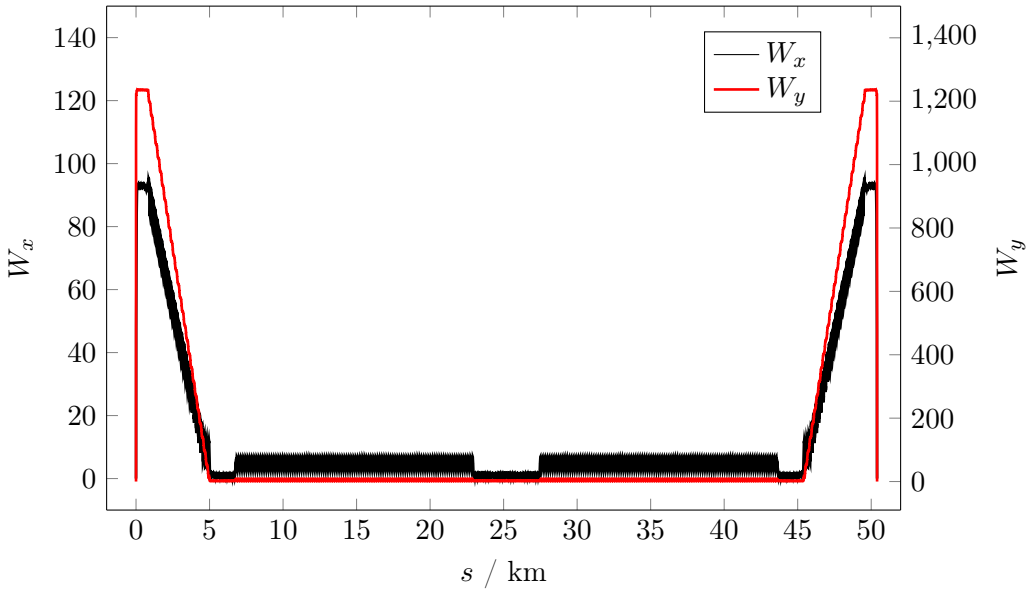

Figure 4.29: W functions in the first 50 km of the Racetrack lattice with 60°/60° optics after chromaticity correction with three sextupole families per plane.

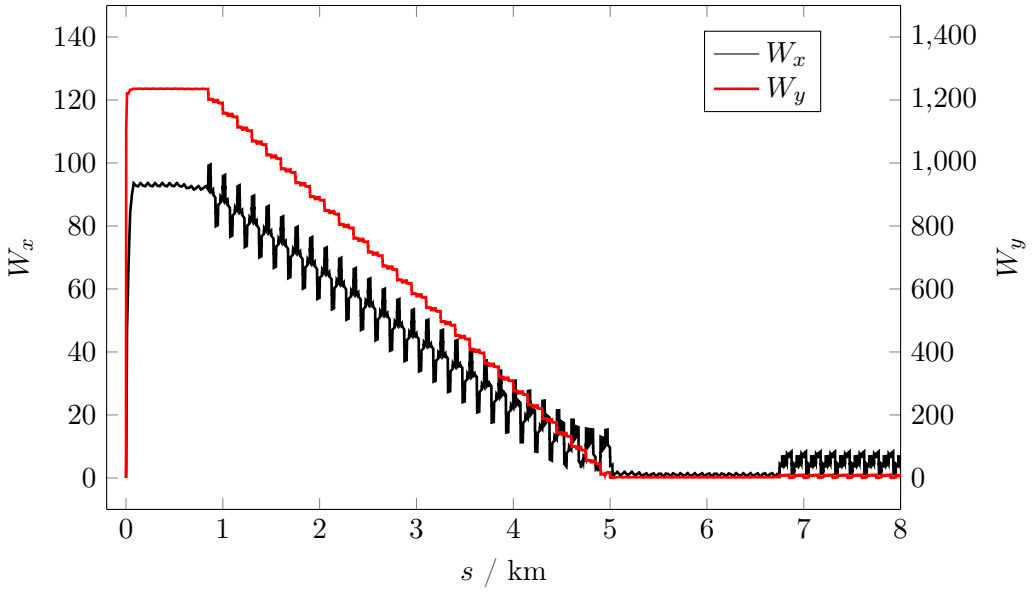

Figure 4.30: Detailed view of the W functions shown in Fig. 4.29. The strong oscillation of the W function in the horizontal plane is created by the defocussing sextupoles. Because of the 60°/60° optics the defocussing sextupoles have an additive effect in the horizontal plane as well.

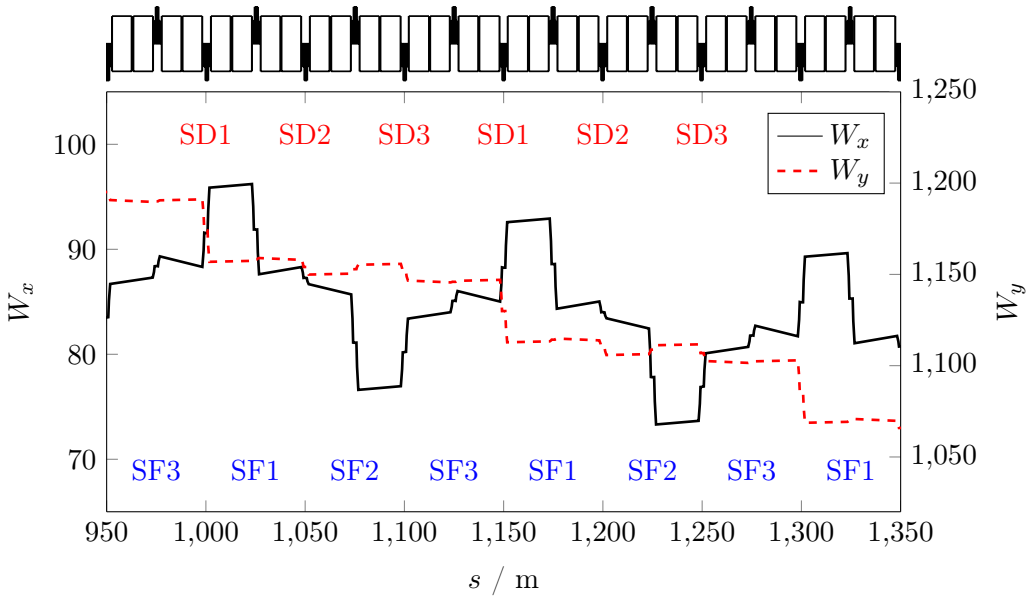

Figure 4.31: W functions in eight cells of the first arc. While having a correcting effect in one plane, the sextupoles increase the W functions of the other.

Table 4.13: Sextupole strengths in the Racetrack Layout with 60°/60° optics after correction of the W function and linear chromaticity compensation.

	Sextupole strengths in m^{-3}	
	Horizontal plane	Vertical plane
Arc 1, 4	k2sf1.1 = 0.45	k2sd1.1 = -2.81
	k2sf1.2 = -0.68	k2sd1.2 = 1.34
	k2sf1.3 = 0.26	k2sd1.3 = 1.47
Arc 2, 3	k2sf = 0.38	k2sd = -0.83

are presented in Fig. 4.31, which shows the W functions and the position of the sextupole magnets in eight FODO cells of the first arc. The effect of the families SD1.1 and SD1.3 in the horizontal plane is comparable to the one of the focussing families.

In the 90°/60° optics only the first sextupole family was used to correct the W functions. The others were just required for fine-tuning and had small strengths compared to the first family. As shown in Tab. 4.13 the strengths of the sextupole families in the 60°/60° optics are distributed in a completely different way. The second and third family now have considerable values in the same order of magnitude than the first family. In the horizontal plane the second family is even stronger. It is also remarkable, that three of the families switched their sign to obtain a convenient W-matching. This change of sign can be explained by locating the effect of the sextupole families in the (b_1,a_1) space.

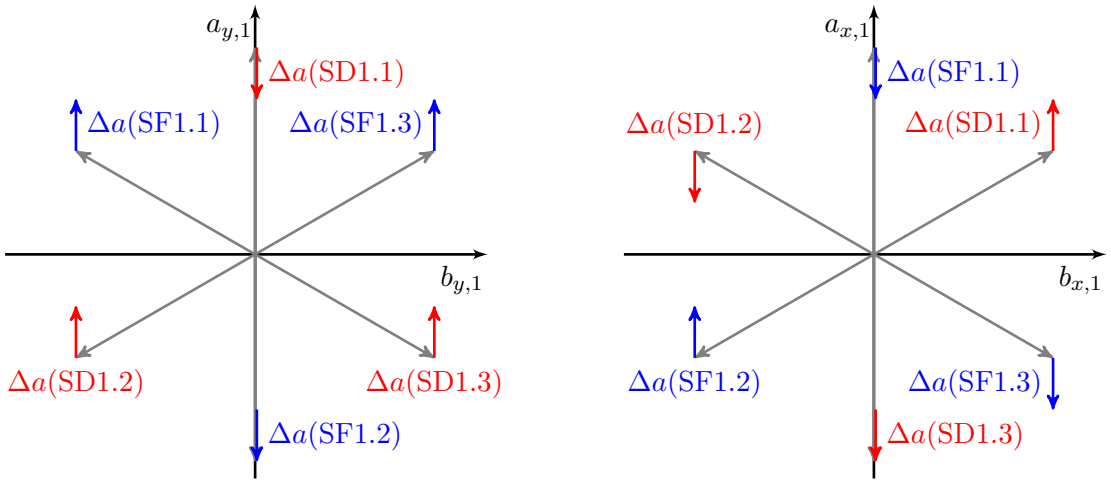

(a) Vertical plane **(b)** Horizontal plane

Figure 4.32: Schematic illustration of the orientation of the W vector at the location of each sextupole family in the first arc. The arrows indicate, the positive or negative modification of a_1 under the influence of the sextupole fields. The estimated values of the modification are given in Tab. 4.14.

Table 4.14: Effect of sextupoles in the first arc on the variable a_1 according to Eq. (4.10b).

family	k_2/m^3	$\Delta a_{1,x}$	$\Delta a_{1,y}$	family	k_2/m^3	$\Delta a_{1,x}$	$\Delta a_{1,y}$
SF1.1	0.45	-4.59	1.62	SD1.1	-2.81	5.90	-16.71
SF1.2	-0.68	6.94	-2.45	SD1.2	1.34	-2.81	7.97
SF1.3	0.26	-2.65	0.94	SD1.3	1.47	-3.09	8.75

Fig. 4.32 shows a schematic illustrating the orientation of the W vector at the position of the respective sextupole family. The direction of the arrows indicate, whether the sextupole family induces a positive or negative change of the variable a_1. The absolute value of the change can be estimated with Eq. (4.10b), which was given by

$$\Delta a_1 \simeq -\beta_0 D_x k_2 L_\mathrm{s}.$$

They are summarised in Tab. 4.14. The effect of a certain sextupole family is not equally strong in both planes, because of the different values of the beta functions. Also, a negative change of the variable a_1 does not necessarily result in a decrease of the W vector. Referencing Fig. 4.32 (a) it becomes clear, that the families SD1.2 and SD1.3 need to switch their sign in order to have a decreasing effect. Still, because of the orientation of the W vector their contribution is less effective than the one of the first family SD1.1.

Table 4.15: Comparison of the chromaticities of the Racetrack Layout for the 90°/60°optics and the 60°/60°optics. The tune shifts correspond to a relative energy deviation of $\delta = 0.1\,\%$.

	90°/60°optics	ΔQ (0.1 %)	60°/60°optics	ΔQ (0.1 %)
Q'_x	-3.99×10^{-3}	-3.99×10^{-6}	1.10×10^{-5}	1.10×10^{-8}
Q''_x	3.56×10^{2}	1.78×10^{-4}	3.53×10^{3}	1.76×10^{-3}
$Q_x^{(3)}$	-1.89×10^{6}	-3.15×10^{-4}	-9.68×10^{5}	-1.61×10^{-4}
$Q_x^{(4)}$	-3.02×10^{9}	-1.26×10^{-4}	-2.12×10^{9}	-8.83×10^{-5}
Q'_y	7.81×10^{-3}	7.81×10^{-6}	2.39×10^{-6}	2.39×10^{-9}
Q''_y	2.36×10^{3}	1.18×10^{-3}	-3.90×10^{3}	-1.95×10^{-3}
$Q_y^{(3)}$	-2.29×10^{8}	-3.82×10^{-2}	-7.50×10^{8}	-1.25×10^{-1}
$Q_y^{(4)}$	1.64×10^{9}	6.85×10^{-5}	-2.82×10^{11}	-1.17×10^{-2}

Chromaticity and momentum acceptance: The different orders of chromaticity for the 90°/60° optics and the 60°/60° optics after correction of the W function is presented in Tab. 4.15. Comparing the results of both optics the most remarkable differences are the values of the even higher-order terms. In the horizontal plane the second order increased by a factor of 10 and creates the largest tune shift now. The reason for this increase can be explained by analysing the equation of the second-order chromaticity in the horizontal plane, which is given by Eq. (4.14b)

$$\frac{\partial^2 Q_x}{\partial \delta^2} = -2\frac{\partial Q_x}{\partial \delta} + \frac{1}{2\pi}\oint \beta_x \left(k_2 D_1 + k_3 \frac{D_0^2}{2}\right) \mathrm{d}s - \frac{1}{4\pi}\oint \beta_x b_{1x} \left(k_1 - k_2 D_0\right) \mathrm{d}s.$$

Without octupole magnets and assuming the higher-order dispersion term D_1 to be small [63], the second order chromaticity is mainly driven by the third term,

$$-\frac{1}{4\pi}\oint \beta_x b_{1,x} \left(k_1 - k_2 D_0\right) \mathrm{d}s,$$

which is the integral over βb_1. The evolution of this product along the lattice is shown in Fig. 4.33 for eight FODO cells in the first arc. Not only the amplitude is larger for the 60°/60° optics, but also the oscillation is less symmetric, which creates a non-vanishing contribution to the integral and thus leads to the increase of the second order chromaticity.

Despite of the large increase of the second-order term in the horizontal plane, the induced tune shift of $\Delta Q_x = 1.76 \times 10^{-3}$ is still by two orders of magnitude smaller than the largest tune shift in the vertical plane $\Delta Q_y = -1.25 \times 10^{-1}$. The pattern of the vertical tune function is still determined by the third-order chromaticity. However, the second- and fourth-order terms not only increased their value but also changed their sign. The con-

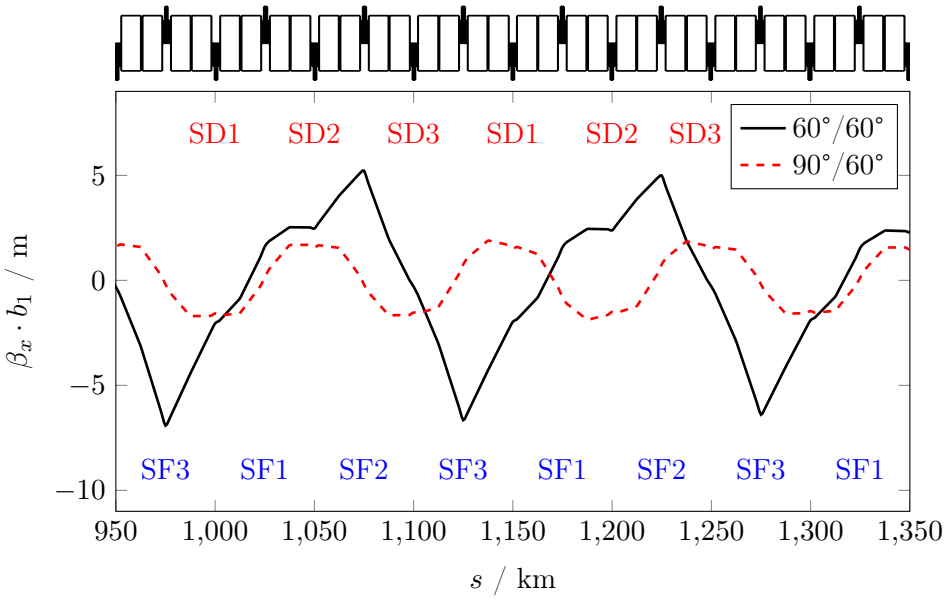

Figure 4.33: Product of beta function β_x times chromatic variable $b_{1,x}$, which drives the second order chromaticity.

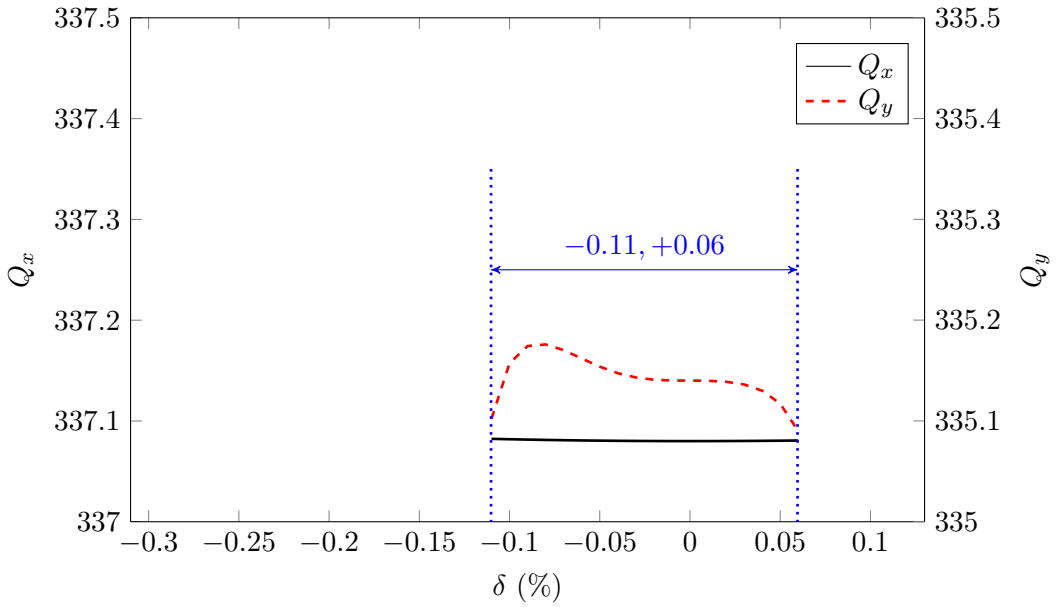

Figure 4.34: Tune functions and momentum acceptance of the Racetrack lattice with 60°/60° optics. Compared to the 90°/60° optics the momentum acceptance is 58 % smaller.

sequences are large negative tune shifts, which limit the momentum acceptance to a range between $\delta = -0.11\,\%$ and $+0.06\,\%$ as shown in Fig. 4.34. Compared to the 90°/60° optics the momentum acceptance is 58 % smaller. This result agrees with the experience of LEP, where the 90°/60° optics also had a better performace then the 60°/60° optics [38].

4.6 Further studies with additional tools

So far, the largest momentum acceptance was obtained for the Racetrack Lattice with 90°/60° optics after correcting the W functions with two sextupole families per arc in the horizontal plane and three families per arc in the vertical plane and reaches from $\delta = -0.29\,\%$ to $+0.11\,\%$. Compared to the $\pm 0.04\,\%$ momentum acceptance obtained after linear chromaticity correction this is already a considerable success, but the required $\pm 2\,\%$ are by far not achieved. For further improvement both the sextupole scheme and the correction method are changed. This section presents the studies, that were undertaken in addition to or instead of the correction of the W function.

4.6.1 Sextupole scheme with six families per plane

The SARCs, where the W function is corrected, have a length of 4.4 km and consist of 84 regular FODO cells. In the horizontal plane there are 42 sextupoles per family and in the vertical plane 28. That the tolerances on the phase advance per cell gets smaller with increasing number of sextupoles per family [62]. To allow a little bit more flexibility in the sextupole strength, a scheme with six interleaved families per plane was investigated. The scheme is illustrated in the top picture of Fig. 4.35. Although the phase advance per cell is different, the first order geometric aberrations should cancel, because two sextupoles of each family are separated by a $-I$ transfer map in the horizontal plane and by a $+I$ transformation in the vertical plane (see bottom schematic of Fig. 4.35).

As the phase advance in the linear arc lattice was not modified, the six families should basically behave similarly to the previous scheme with two and three families per plane. The sextupole strengths after correction of the W functions confirm this hypothesis as shown in Tab. 4.16. Still, deviations can be observed like the increased strength of the families SF4.5 and SD4.6 in Arc 4. Although they seem very small, the momentum acceptance obtained with the same correction method can be increased compared to the 2/3 family scheme by 10 % to a range from $\delta = -0.33\,\%$ to $+0.11\,\%$. Unfortunately only the range for negative energy deviation could be improved. The shape of the tune functions are still determined by the third order chromaticity in the vertical plane, as shown in Fig. 4.36, and is limited by the integer resonance $Q_y = 337$. Since now the range is three times larger for negative momentum offset than for positive, the main emphasis of further corrections must be placed to obtain a symmetric tune function.

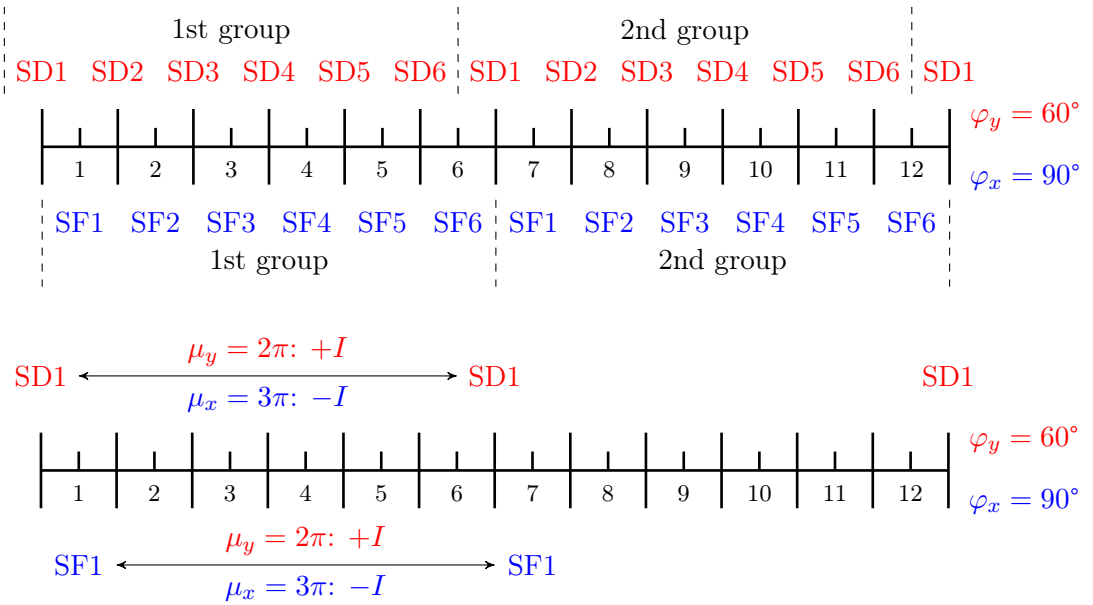

Figure 4.35: Sextupole scheme with six families per plane for $\varphi_x = 90°$ and $\varphi_y = 60°$ phase advance of per FODO cell. In the horizontal plane two members of a family are separated by a $-I$ transformation, in the vertical plane by a $+I$ transformation to cancel geometric aberrations as discussed in Sec. 4.3.

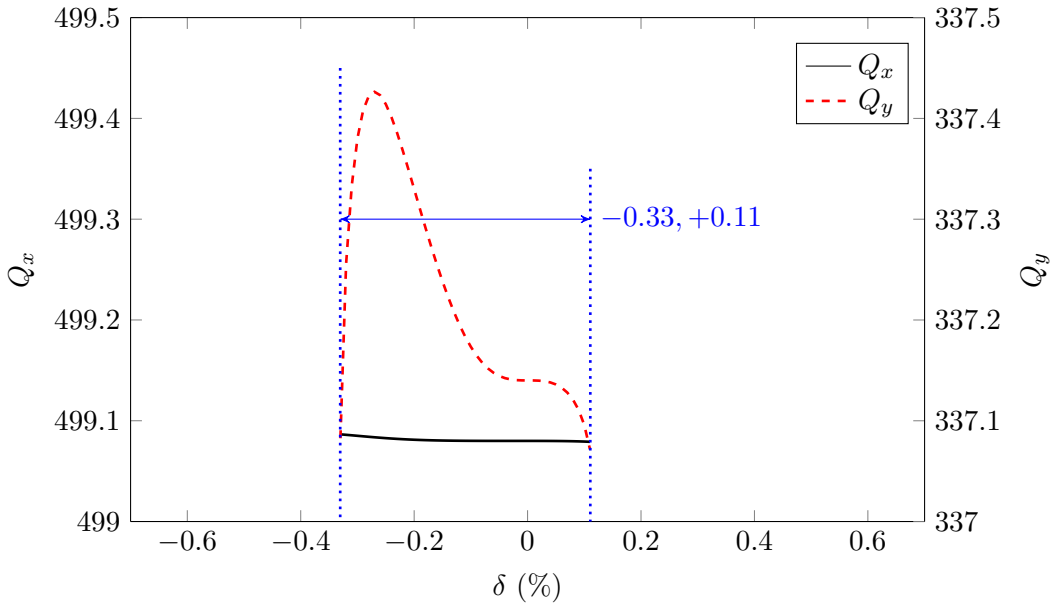

Figure 4.36: Momentum acceptance of the Racetrack Lattice after correction of W functions and linear chromaticity with six sextupole families per plane.

Table 4.16: Sextupole strengths in the Racetrack lattice with 90°/60° optics after the correction of W functions and linear chromaticity with six sextupole families per plane.

	Sextupole strengths in m^{-3}			
	Horizontal plane		Vertical plane	
Arc 1	k2sf1.1	= 0.228	k2sd1.1	= -7.429
	k2sf1.2	= 0.000	k2sd1.2	= 0.000
	k2sf1.3	= 0.228	k2sd1.3	= 0.000
	k2sf1.4	= 0.000	k2sd1.4	= -7.429
	k2sf1.5	= 0.228	k2sd1.5	= 0.000
	k2sf1.6	= 0.000	k2sd1.6	= 0.000
Arc 4	k2sf4.1	= 0.228	k2sd4.1	= -7.425
	k2sf4.2	= 0.000	k2sd4.2	= 0.068
	k2sf4.3	= 0.228	k2sd4.3	= -0.012
	k2sf4.4	= 0.001	k2sd4.4	= -7.425
	k2sf4.5	= -0.228	k2sd4.5	= 0.069
	k2sf4.6	= 0.000	k2sd4.6	= -0.012
Arc 2	k2sf2.1	= 0.841	k2sd2.1	= -1.209
	k2sf2.2	= 0.841	k2sd2.2	= -1.209
	k2sf2.3	= 0.841	k2sd2.3	= -1.209
	k2sf2.4	= 0.841	k2sd2.4	= -1.209
	k2sf2.5	= 0.841	k2sd2.5	= -1.209
	k2sf2.6	= 0.841	k2sd2.6	= -1.209
Arc 3	k2sf3.1	= 0.841	k2sd3.1	= -1.203
	k2sf3.2	= 0.841	k2sd3.2	= -1.209
	k2sf3.3	= 0.841	k2sd3.3	= -1.209
	k2sf3.4	= 0.841	k2sd3.4	= -1.204
	k2sf3.5	= 0.841	k2sd3.5	= -1.209
	k2sf3.6	= 0.841	k2sd3.6	= -1.209

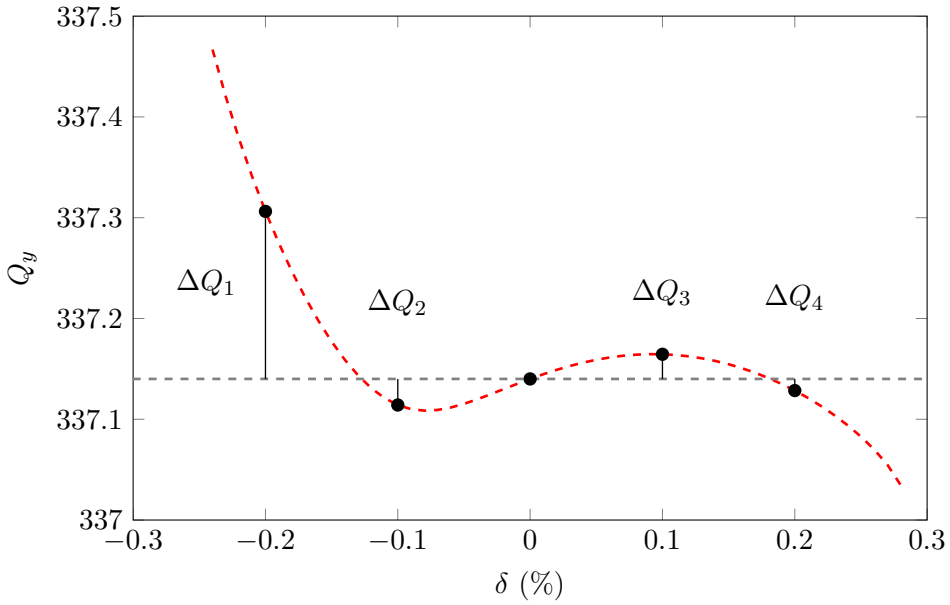

Figure 4.37: Illustration of the functionality of the macro used to flatten the tune functions. The tune is calculated for different momentum offsets and the squared difference to the nominal tune for $\delta = 0$ is then minimised by optimising the available sextupole strengths.

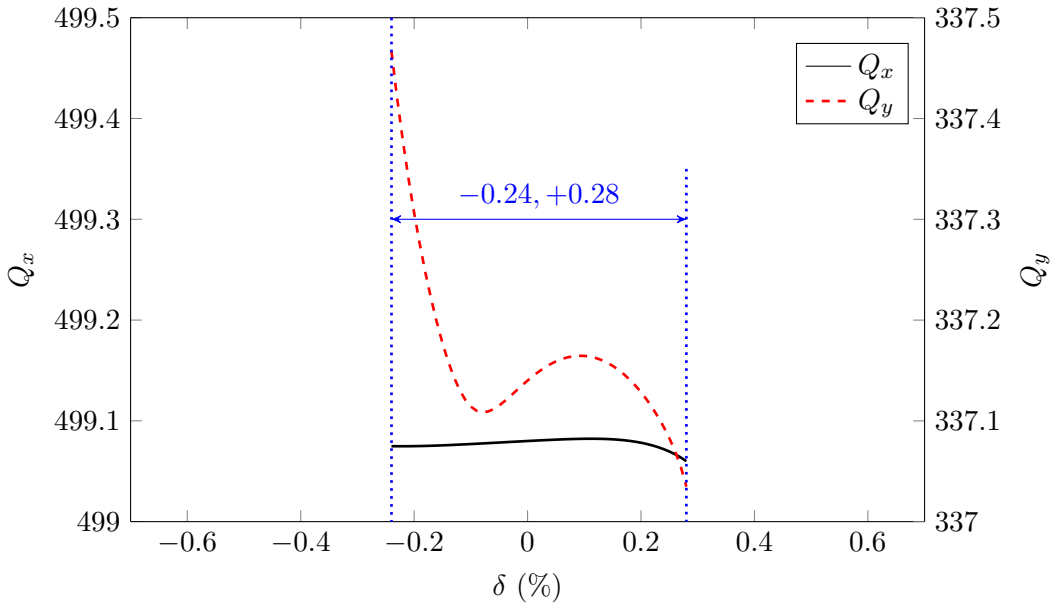

Figure 4.38: Tunes depending on the energy deviation δ after the optimisation with the macro to flatten the tune function. A significant improvement of the symmetry of the acceptance could be achieved.

Table 4.17: First four orders of the chromaticity after correction of the W function and linear chromaticity compared to the case after optimising the bandwidth in addition. The tune shifts correspond to a relative energy deviation of $\delta = 0.1\,\%$.

	W corrected	ΔQ (0.1 %)	Optimised bandwidth	ΔQ (0.1 %)
Q'_x	-2.87×10^{-2}	-2.87×10^{-5}	2.96×10^{0}	2.96×10^{-3}
Q''_x	-2.98×10^{2}	-1.49×10^{-4}	-4.72×10^{2}	-2.36×10^{-4}
$Q_x^{(3)}$	-1.64×10^{6}	-2.73×10^{-4}	-1.67×10^{6}	-2.79×10^{-4}
$Q_x^{(4)}$	-3.46×10^{9}	-1.44×10^{-4}	-3.90×10^{9}	-1.62×10^{-4}
Q'_y	-3.00×10^{-2}	-3.00×10^{-5}	4.84×10^{1}	4.84×10^{-2}
Q''_y	2.38×10^{3}	1.19×10^{-3}	-2.94×10^{4}	-1.47×10^{-2}
$Q_y^{(3)}$	-1.96×10^{8}	-3.27×10^{-2}	-1.03×10^{8}	-1.72×10^{-2}
$Q_y^{(4)}$	1.45×10^{9}	4.78×10^{-5}	3.08×10^{11}	1.29×10^{-2}

4.6.2 Optimisation tool to flatten the tune function

For positive energy offset very strong negative tune shifts occur, that limit the acceptance by crossing the integer resonance. As a first step to a more symmetrical acceptance range the nominal tunes were increased from $Q_x = 499.54$ to 499.56 and from $Q_y = 337.57$ to 337.59. This increases the allowed an additional tune shift of $\Delta Q = -0.02$. In a second step the third-order chromaticity in the vertical plane must finally be corrected as it still determines the limit for positive energy deviation. To correct even higher orders of the chromaticity, that might limit the momentum acceptance, a macro was written to flatten the tune function in the allowed bandwidth. The functionality of the macro is illustrated in Fig. 4.37. The tune is calculated by MAD-X for a user-defined number of steps within the acceptable range of energy deviation. The squared difference to the nominal tune for $\delta = 0$ is then minimised by optimising the available sextupole strengths using the matching routines in MAD-X. The MAD-X code of this macro is given in Appendix D.

Fig. 4.38 shows the tune functions after two iterations of the optimisation. The momentum acceptance reaches from $\delta = -0.24\,\%$ to $+0.28\,\%$. It is not only 18 % larger compared to the previous case, also the symmetry of the acceptance range could be improved significantly. While the acceptance for negative energy offsets was three times of the acceptance for positive energy deviation before, the range in both directions is similar now. However, the resulting vertical tune function includes a very strong positive linear component for on-momentum particles. The analysis of the chromaticity summarised in Tab. 4.17 yields a vertical linear chromaticity of $Q'_y \approx 50$. The third order indeed reduced by nearly 50 %, but the absolute values of the second- and fourth-order terms increased by orders of magnitude. Since the function is still dominated by an odd polynomial, the

Table 4.18: Sextupole strengths in the Racetrack Layout with six sextupole families per plane after optimisation with the macro to flatten the tune function.

	Sextupole strengths in m^{-3}			
	Horizontal plane		Vertical plane	
Arc 1	k2sf1.1	= 0.231	k2sd1.1	= -7.537
	k2sf1.2	= 0.011	k2sd1.2	= -0.682
	k2sf1.3	= 0.231	k2sd1.3	= -0.284
	k2sf1.4	= 0.006	k2sd1.4	= -7.534
	k2sf1.5	= 0.231	k2sd1.5	= -0.635
	k2sf1.6	= 0.004	k2sd1.6	= -0.263
Arc 4	k2sf4.1	= 0.232	k2sd4.1	= -7.533
	k2sf4.2	= 0.004	k2sd4.2	= -0.671
	k2sf4.3	= 0.232	k2sd4.3	= -0.289
	k2sf4.4	= 0.003	k2sd4.4	= -7.530
	k2sf4.5	= -0.231	k2sd4.5	= -0.619
	k2sf4.6	= 0.004	k2sd4.6	= -0.266
Arc 2	k2sf2.1	= 0.853	k2sd2.1	= -1.532
	k2sf2.2	= 0.854	k2sd2.2	= -1.184
	k2sf2.3	= 0.852	k2sd2.3	= -0.902
	k2sf2.4	= 0.855	k2sd2.4	= -1.533
	k2sf2.5	= 0.852	k2sd2.5	= -1.185
	k2sf2.6	= 0.855	k2sd2.6	= -0.893
Arc 3	k2sf3.1	= 0.853	k2sd3.1	= -1.524
	k2sf3.2	= 0.854	k2sd3.2	= -1.188
	k2sf3.3	= 0.853	k2sd3.3	= -0.905
	k2sf3.4	= 0.854	k2sd3.4	= -1.525
	k2sf3.5	= 0.853	k2sd3.5	= -1.189
	k2sf3.6	= 0.854	k2sd3.6	= -0.896

fifth order increased probably as well. It is interesting, that the tune shifts for a relative energy deviation of $\delta = 0.1\,\%$ created by the vertical terms of the chromaticity are all in the same order of magnitude now. This means at the same time, that the effect of the higher-orders increase for larger momentum offsets. In the horizontal plane the linear chromaticity increased as well, which also can be recognised by the slope of the tune function around $\delta = 0$. At the upper limit of the acceptance range, the influence of the even terms is visible, which increased as well.

The sextupole strengths after the optimisation of the tune function are listed in Tab. 4.18. The correction now benefits from the flexibility of the additional sextupole families. Especially in Arc 1 and Arc 4, where the W functions were matched, the secondary sextupole families in the vertical plane deviate from the three family symmetry. The strength of the families 2 and 5 are different as well as the strengths of the families 3 and 6.

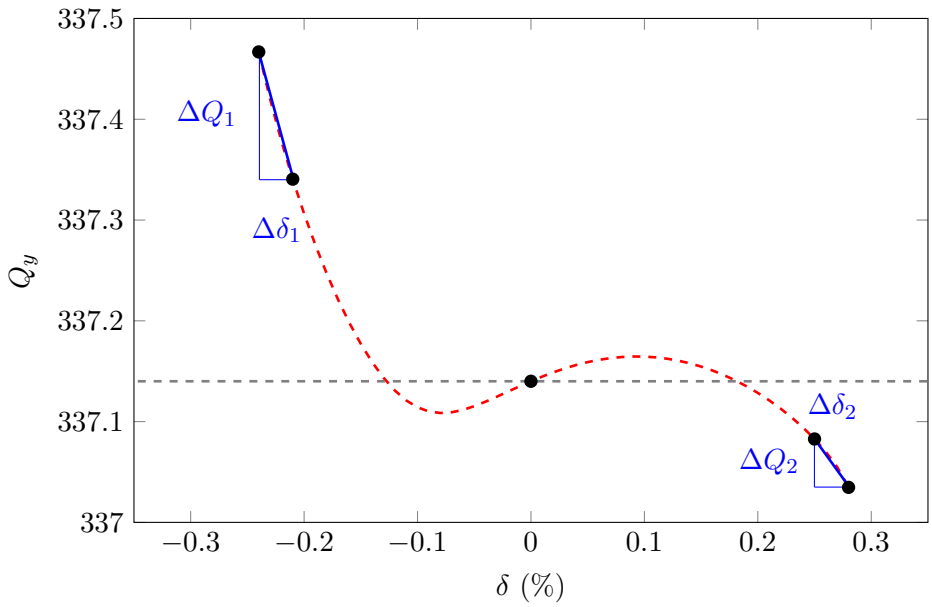

Figure 4.39: Illustration of the functionality of the tool used to minimise the slopes of the tune functions at the edge of the acceptance range. Two optics calculations for different energy offset determine the tunes close the edge. The difference between the tunes is minimised by optimising the strengths of the individually powered sextupole pairs next to the straight sections with interaction regions.

4.6.3 Individual sextupole pairs at the beginning of the arc sections

As a next step the first six sextupole pairs in both planes in Arc 1 and the last six sextupole pairs of Arc 4 were powered individually. Hence, the sextupole scheme consists of six families per arc per plane and 24 individually powered sextupole pairs next to the straight sections including mini-beta insertions. Assuming the two superperiods have the same sextupole scheme, the number of degrees of freedom is now $4 \times 6 + 2 \times 6 = 36$. It turned out, however, that the best results are obtained, when the main sextupole families of the arcs are kept constant and the additional sextupole pairs are optimised on top.

In order to enlarge the energy acceptance, the very steep slopes of the tune functions at the edge of the acceptance range need to be flattened. Therefore an second optimisation tool was implemented, which calculates the tunes of particles with two different energy deviations close to the edge and minimises their difference. The user can define, whether both sides should be optimised or just one. The momentum acceptance can be increased iteratively until the current configuration does not allow any further progress. The functionality of this tool is illustrated in Fig. 4.39. The MAD-X code can be found in Appendix E.

Table 4.19: Optimised sextupole strengths of the individual sextupole pairs, that were installed in addition to the sextupole families in the arcs.

	Sextupole strengths in m^{-3}	
	Horizontal plane	Vertical plane
Arc 1	k2sf.p1 = 0.449	k2sd.p1 = -7.489
	k2sf.p2 = 0.052	k2sd.p2 = -0.838
	k2sf.p3 = 0.437	k2sd.p3 = -0.563
	k2sf.p4 = 0.085	k2sd.p4 = -7.488
	k2sf.p5 = 0.373	k2sd.p5 = -0.726
	k2sf.p6 = 0.069	k2sd.p6 = -0.571
Arc 6	k2sf.p1 = 0.456	k2sd.p1 = -7.488
	k2sf.p2 = 0.045	k2sd.p2 = -0.956
	k2sf.p3 = 0.444	k2sd.p3 = -0.757
	k2sf.p4 = 0.081	k2sd.p4 = -7.488
	k2sf.p5 = 0.379	k2sd.p5 = -0.828
	k2sf.p6 = 0.067	k2sd.p6 = -0.754

Starting from the sextupole configuration of Tab. 4.18 the slopes of the tune functions were optimised in several iterations. The obtained tune functions are shown in Fig. 4.40 for a selection of six steps. The initial tune functions are shown in the top left plot. The one right to it shows the functions after an iteration of optimising the vertical tune function for negative energy deviation. The optimisation of both sides of the horizontal tune yields the functions shown in the left plot in the middle. It followed two iterations of optimisation of the vertical tune function for negative energy offset, before the optimisation of the horizontal tune was repeated. A final optimisation of both sides of the vertical tune functions result in the tune functions displayed in Fig. 4.41. The strengths of the individual sextupole pairs are summarised in Tab. 4.19. The acceptance could be increased for energy offsets up to $\delta = -0.49\,\%$ and $+0.69\,\%$. This range for the first time approximates the percent range, which having the challenging conditions in mind can be considered as a large success.

Characteristics of the tune functions: The shape of the tune functions already indicates very strong higher-order terms of the chromaticity. The values calculated with the macro in MAD-X are given in Tab. 4.20. The energy offset used for the calculation of the difference quotients was increased from $\delta = 0.01\,\%$ to $\delta = 0.1\,\%$ to follow the larger of the momentum acceptance. Compared to the values before optimising the strength of the additional sextupole pairs (Tab. 4.17) the absolute value of the third order could be further decreased in both planes. Also the linear order increased in both planes in order to counteract the very strong negative tune shifts for positive energy offsets. In the vertical

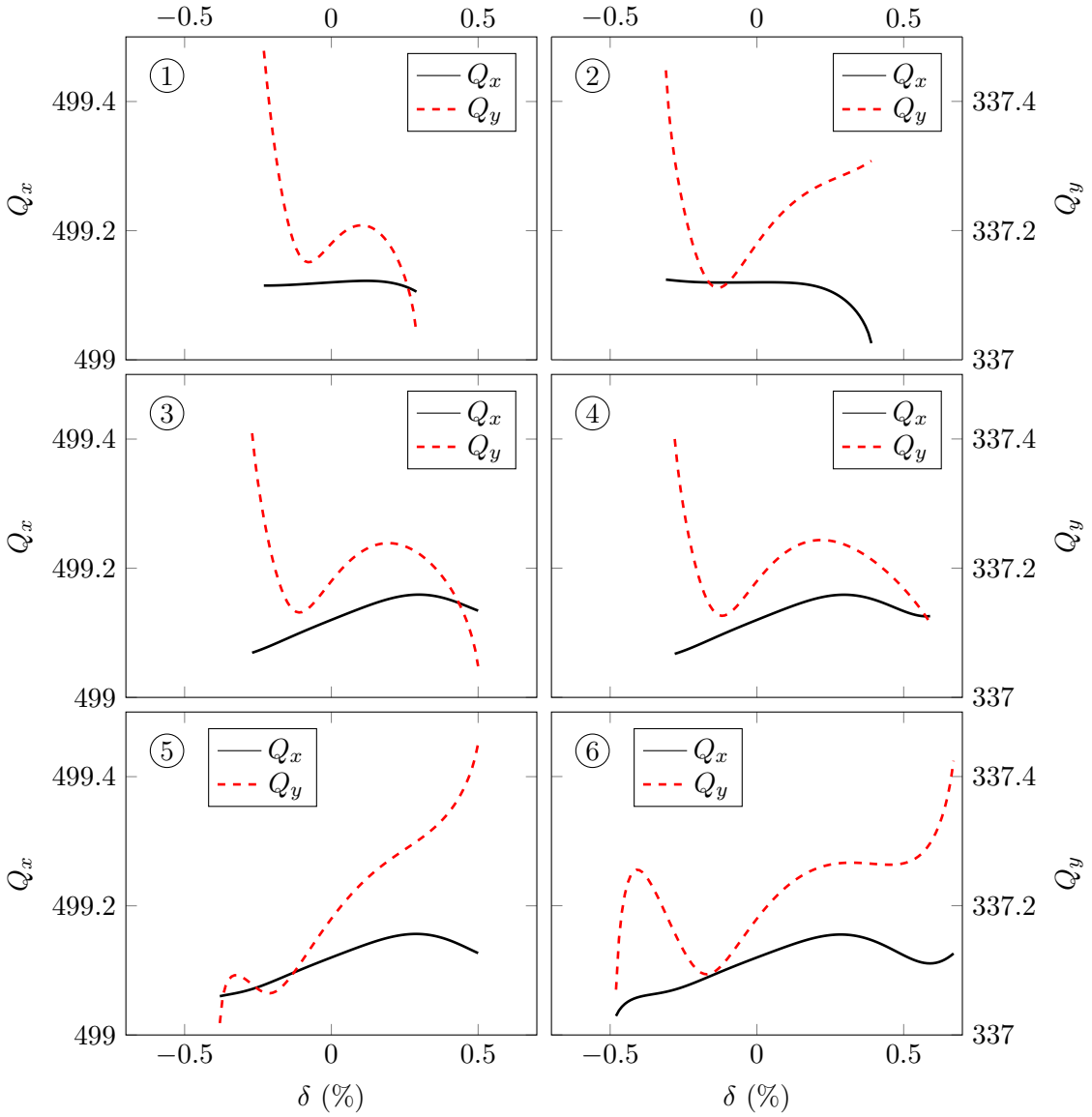

Figure 4.40: In order to further increase the momentum acceptance additional free parameters in the chromaticity control are taken into account: on top of the correction of the W functions the first six sextupole pairs in the mini-arcs next to the interaction regions were powered individually. In several iterations the momentum acceptance has been increased varying the strengths of the additional free sextupole pairs.

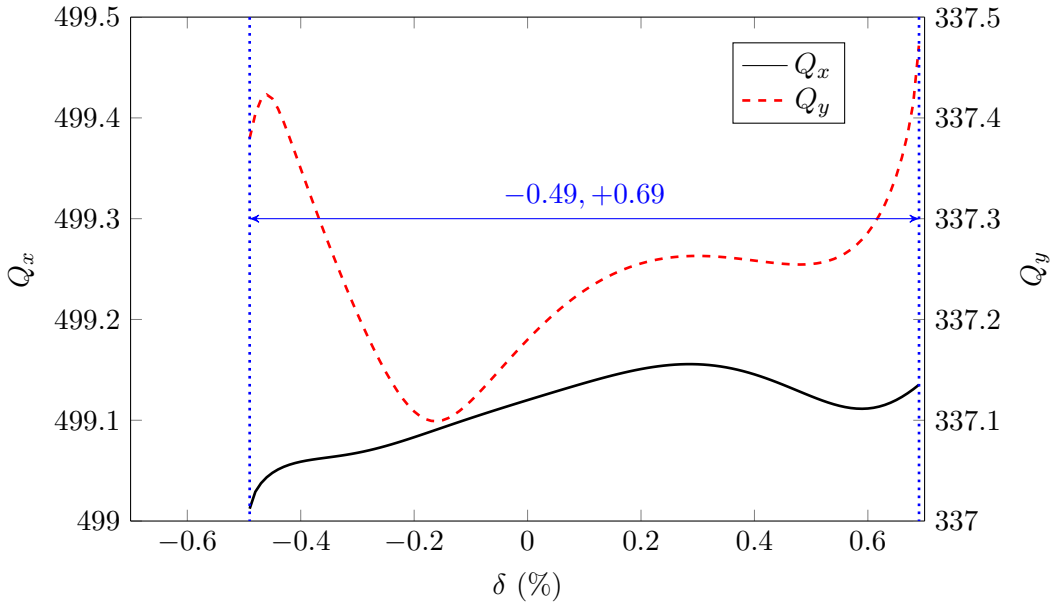

Figure 4.41: Energy acceptance of the Racetrack Layout after optimisation of the strengths of the individual sextupole pairs in addition to the regular arc families.

Table 4.20: Chromaticitiy including higher-order terms and tune shifts for different energy deviations after optimising the bandwidth using individually powered sextupole pairs at the beginning of the arcs adjacent to the mini-beta insertions.

	Chromaticity	$\Delta Q(-0.4\,\%)$	$\Delta Q(-0.1\,\%)$	$\Delta Q(0.1\,\%)$	$\Delta Q(0.4\,\%)$
Q'_x	1.73×10^{1}	-6.90×10^{-2}	-1.73×10^{-2}	1.73×10^{-2}	6.90×10^{-2}
Q''_x	-9.57×10^{2}	-7.66×10^{-3}	-4.79×10^{-4}	-4.79×10^{-4}	-7.66×10^{-3}
$Q^{(3)}_x$	-8.64×10^{5}	9.22×10^{-3}	1.44×10^{-4}	-1.44×10^{-4}	-9.22×10^{-3}
$Q^{(4)}_x$	-2.20×10^{9}	-2.34×10^{-2}	-9.15×10^{-5}	-9.15×10^{-5}	-2.34×10^{-2}
Q'_y	5.83×10^{1}	-2.92×10^{-1}	-5.83×10^{-2}	5.83×10^{-2}	2.92×10^{-1}
Q''_y	-1.21×10^{4}	-9.71×10^{-2}	-6.07×10^{-3}	-6.07×10^{-3}	-9.71×10^{-2}
$Q^{(3)}_y$	-3.61×10^{7}	3.85×10^{-1}	6.02×10^{-3}	-6.02×10^{-3}	-3.85×10^{-1}
$Q^{(4)}_y$	5.29×10^{10}	5.64×10^{-1}	2.20×10^{-3}	2.20×10^{-3}	5.64×10^{-1}

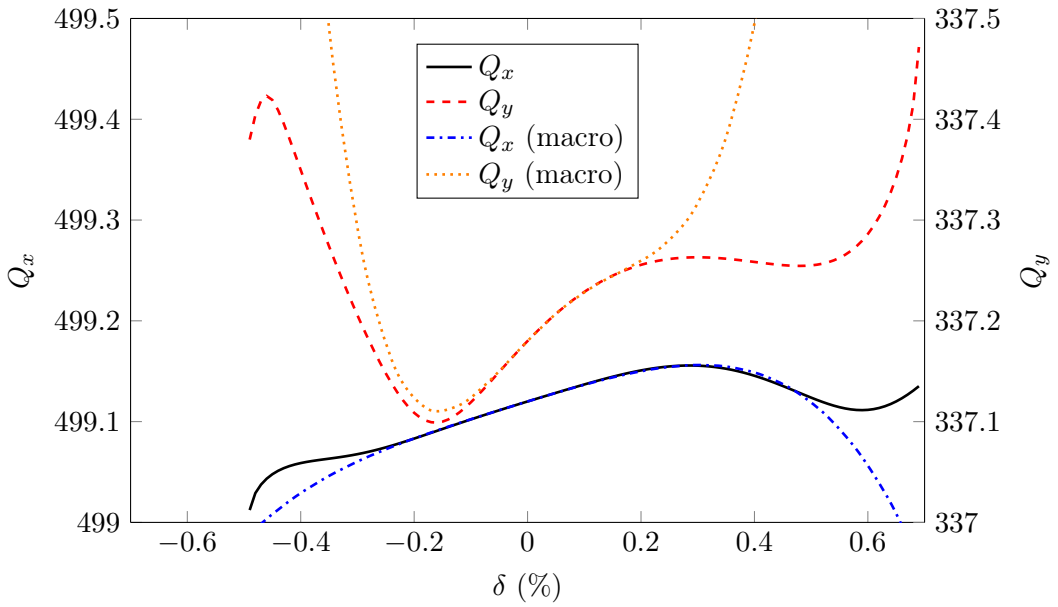

Figure 4.42: Comparison of the tune functions calculated consisting of the first four orders and the tunes calculated by MAD-X.

plane the linear chromaticity has now a value of $Q'_y = 58$. In the horizontal plane all orders create negative tune shits for $\delta < 0$. At $\delta = -0.5\,\%$ this causes the horizontal tune function to cross the integer resonance and thus defines the lower limit of the momentum acceptance.

Tab. 4.20 also shows the tune shifts for $\delta = \pm 0.1\,\%$ and $\delta = \pm 0.4\,\%$. For $\delta = 0.1\,\%$ adding the tunes using Eq. (4.4) yields $Q_y^{\mathrm{c}} = 337.2285$, which is in very good agreement to the value of MAD-X, which is $Q_y = 337.2287$. For $\delta = 0.4\,\%$, on the contrary, the value $Q_y^{\mathrm{c}} = 337.4948$ obtained by the macro exceeds the value of MAD-X $Q_y = 337.2584$ by a quarter unit. Also, considering the irregular shape of the functions, it is questionable, if the calculated orders are sufficient to represent the behaviour of the tunes for momentum offset. To investigate the accuracy of the first four orders, the function consisting of the calculated polynomials was plotted together with the tunes obtained by MAD-X in Fig. 4.42. While the calculated tunes agree well for energy deviation smaller than $\pm 0.2\,\%$, large deviations arise above those values. Especially in the vertical plane the plateau of relatively constant tune values between $\delta = 0.2\,\%$ and $\delta = 0.5\,\%$ is not dissolved. In the horizontal plane, the slope becomes positive again for tune shifts larger than $\delta = 0.6\,\%$, which is not represented by the first four orders. Before continuing this optimisation method additional orders should be included to the macro or a different way to evaluate the higher-order chromaticities should to be chosen. One possibility would be to switch to the Polymorphic Tracking Code (PTC), which is included in MAD-X. PTC was not used so far, because it is very slow for machines as large as FCC-ee.

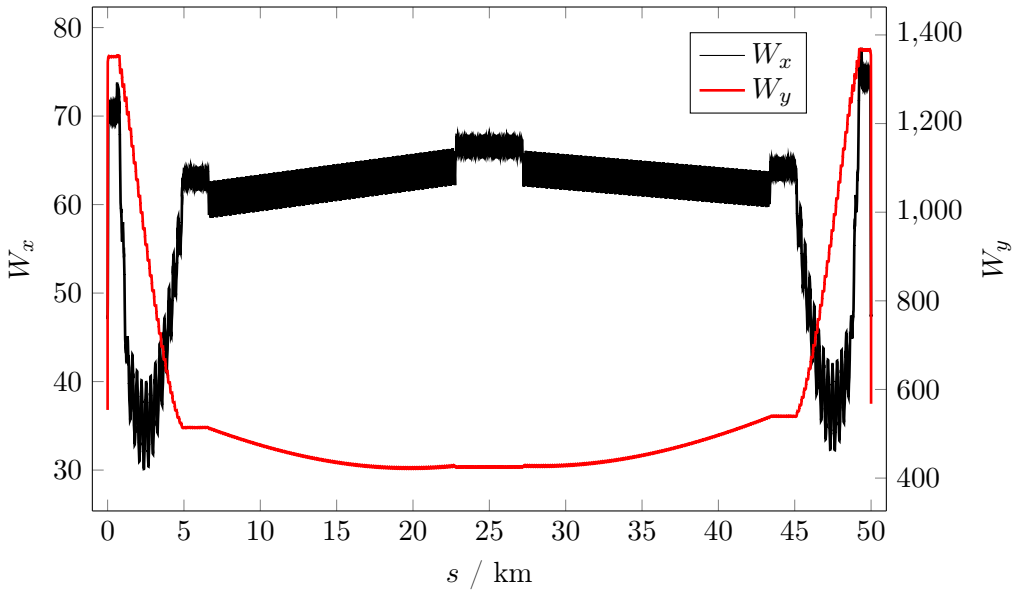

Figure 4.43: W functions after optimising the bandwidth with additional free sextupole pairs next to the straight sections with mini-beta insertions.

The optimisations described in the last two sections were performed on top of the previously corrected W functions. The modification of the sextupole strengths during the flattening process of the tune functions and especially the introduction of the individual sextupole pairs in the SARCs caused a perturbation of the carefully matched situation. For completeness the mismatched W functions are shown in Fig. 4.43.

To summarise the optimisations undertaken in addition to the correction of the W functions, the individual sextupole pairs proved to be a powerful tool. The stable energy range could be more than doubled. The studies of such a sextupole scheme could be continued with a more reliable method to calculate the higher-order terms of the chromaticity. After the optimisation to flatten the bandwidth a considerable contribution of the linear chromaticity was introduced. Based on these results a set of sextupole strengths without linear contribution is proposed as a starting point for the next step. Also different optimisation algorithms outside MAD-X might have a better performance. However, six dimensional tracking calculations need to examine, whether an optics with tune functions such as the ones presented in Fig. 4.42 provides sufficient dynamic aperture. For $\delta = -0.15\,\%$ the functions for the horizontal and the vertical tune get very close. The difference of the fractional parts is just $\Delta Q = 0.1000 - 0.0927 = 0.0073$, which is very close to the coupling resonance. In further optimisations, this difference should be increased for example by choosing a slightly larger tune in the vertical plane. For optimisations on this level of precision the effect of the beam-beam tune shift has to be taken into account as well.

4.6.4 Optimisation with the Downhill-Simplex-Algorithm

All previous optimisations of the momentum acceptance were done with analytical approximations and built-in tools of MAD-X. The optimisation of the individual sextupole pairs with the matching module brought an increase of the momentum acceptance by a significant amount, but the matching module was not able to find any solutions, if all the sextupoles including the nominal families were included to the optimisation. Indeed, the matching module in MAD-X is not meant to perform a global optimisation of a large parameter space with initial values far away from the solution [64].

For completeness and comparison a numerical approach outside the MAD-X programme was studied in this thesis. In order to keep track of the optimisation process and to gain full comprehension of the algorithm it was decided to set up an own tool instead of relying on available libraries. The *Downhill-Simplex-Algorithm* [65] was implemented [45], which is a standard optimisation algorithm. $N+1$ data sets consisting of different values of the N variables, which are being optimised, are modified during the execution of the algorithm and are evaluated using a penalty function. In this case the variables are the sextupole strengths and the penalty function consisted of the tune shifts created by the first four orders of both vertical and horizontal chromaticity:

$$\begin{aligned} P = {} & Q'_x\delta + \frac{1}{2}Q''_x\delta^2 + \frac{1}{6}Q_x^{(3)}\delta^3 + \frac{1}{24}Q_x^{(4)}\delta^4 \\ & + Q'_y\delta + \frac{1}{2}Q''_y\delta^2 + \frac{1}{6}Q_y^{(3)}\delta^3 + \frac{1}{24}Q_y^{(4)}\delta^4 \end{aligned} \tag{4.18}$$

The algorithm was started independently from MAD-X in a Fortran programme, which created the data sets and managed their modifications. MAD-X is only used to evaluate the penalty function.

Several sextupole schemes with different numbers of families were studied: 6 interleaved families per plane, 12 and 54 families per plane. In contrast to the previous schemes the same strengths are used for the families in all arcs. The number of degrees of freedom is thus reduced by a factor of four. The largest momentum acceptance was obtained for the scheme with six families per plane reaching from $\delta = -0.38\,\%$ to $+0.54\,\%$ as shown in Fig. 4.44. Within $\delta = \pm 0.2$ % the tunes stay constant in both planes. Beyond this range the vertical tune is defined by an odd polynomial, which limits the momentum acceptance by crossing the integer resonance at $Q_y = 335$ and the half-integer resonance at $Q_y = 335.5$ for negative and positive energy offset respectively. In the horizontal plane an even polynomial creates the main tune shift.

To understand the results and evaluate the performance of the algorithm the first four orders of the chromaticity were calculated as usual. The energy offsets used in the macro were increased from $\delta = \pm 0.01\,\%$ to $\pm 0.15\,\%$, following the increasing acceptance. The

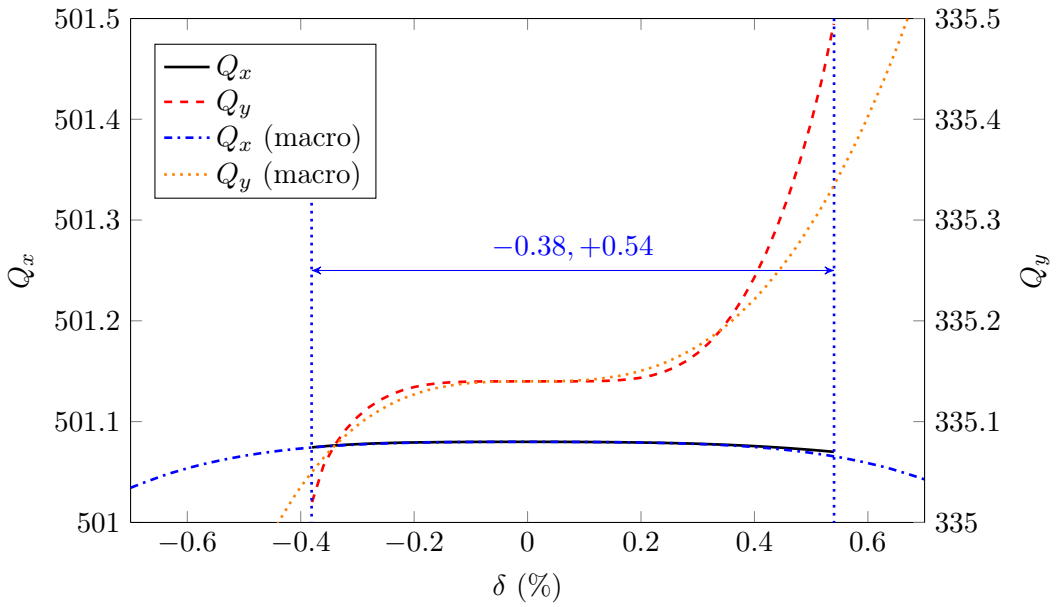

Figure 4.44: Tune functions and momentum acceptance of the Racetrack Layout with six families per plane after optimising the sextupole strengths

absolute value of all higher-order terms could be decreased (see Tab. 4.21). The third-order term was reduced by two orders of magnitude in both planes. In the vertical plane it still has the largest contribution to the tune shift and it changes its sign compared to the case of corrected W functions, which explains the pattern of the tune function. In the horizontal plane the largest tune shift is created by the second-order chromaticity, which agrees with the expectations from above.

Compared to the previously studied cases, the required sextupole strengths are relatively small. The very strong sextupole fields required for the W correction are not needed as shown in Tab. 4.22. It is interesting to see, that this scheme with less degrees of freedom can be optimised to a better performance than the case with corrected W functions. With only six degrees of freedom an acceptance range close to the one with independent sextupole pairs (36 degrees of freedom) could be achieved. Also the pattern of the tune functions is much more regular. The stability of the numerically optimised scheme will be verified including field error studies.

The optimisation outside of the MAD-X frame proved to be very efficient and can most likely be further extended. At present it seems the main limitation still comes from the third order chromaticity in the vertical plane, but the fifth and sixth order could be taken into account as well. For an optimisation on top of the presented results the energy deviation used for the calculation of the higher-order chromaticity should be further increased to follow the larger acceptance range. As a further step it is proposed to define further sextupole families and thereby increase the number of variables.

Table 4.21: Chromaticities of the Racetrack Layout with Downhill-Simplex-optimised sextupole strengths compared to the case with corrected W functions. The tune shifts correspond to a relative energy deviation of $\delta = 0.1\,\%$.

	90°/60°optics	ΔQ (0.1 %)	Simplex	ΔQ (0.1 %)
Q'_x	-3.99×10^{-3}	-3.99×10^{-6}	-1.98×10^{-2}	-1.98×10^{-5}
Q''_x	3.56×10^{2}	1.78×10^{-4}	-2.72×10^{2}	-1.36×10^{-4}
$Q^{(3)}_x$	-1.89×10^{6}	-3.15×10^{-4}	7.55×10^{4}	1.26×10^{-5}
$Q^{(4)}_x$	-3.02×10^{9}	-1.26×10^{-4}	-3.48×10^{8}	-1.45×10^{-5}
Q'_y	7.81×10^{-3}	7.81×10^{-6}	6.42×10^{-3}	6.42×10^{-6}
Q''_y	2.36×10^{3}	1.18×10^{-3}	-3.19×10^{2}	-1.59×10^{-4}
$Q^{(3)}_y$	-2.29×10^{8}	-3.82×10^{-2}	8.73×10^{6}	1.45×10^{-3}
$Q^{(4)}_y$	1.64×10^{9}	6.85×10^{-5}	-8.53×10^{8}	-3.55×10^{-5}

Table 4.22: Sextupole strengths after the optimisation with the Downhill-Simplex-Algorithm. All arcs use the same strengths.

Sextupole strengths in m^{-3}					
Horizontal plane			Vertical plane		
k2sf1	=	0.179	k2sd1	=	-0.678
k2sf2	=	0.221	k2sd2	=	-0.285
k2sf3	=	0.100	k2sd3	=	-0.244
k2sf4	=	0.198	k2sd4	=	-0.514
k2sf5	=	0.209	k2sd5	=	-0.257
k2sf6	=	0.140	k2sd6	=	-0.237

Summary

The Future Circular Collider (FCC) Study investigates the potential of 100 km circular colliders for future high-energy physics research in the post-LHC era. In this thesis the electron-positron collider version FCC-ee was studied with emphasis on the lattice design, the beam optics and mainly the optimisation of the chromaticity compensation scheme.

Two models of the machine were implemented with the optics code MAD-X: a lattice with 12-fold symmetry for generic studies and a racetrack-shaped lattice considering technological aspects and geological factors of the Geneva basin. The layout of the basic cell is of FODO design, which provides the highest dipole filling factor and thus produces 40 % less synchrotron radiation power than the Double-Bend-Achromat lattice investigated for comparison. To guarantee a smooth transition of the lattice functions between arc and straight sections, half-bend dispersion suppressors and matching sections with individually powered quadrupoles were installed. Up to four mini-beta insertions were included for the experiments. Considering the large size of FCC only two RF sections are foreseen. Still, simulations presented in this thesis showed, that the amplitude of the sawtooth orbit can be kept on a reasonable level by adjusting the dipole strength to the local beam energy. Both individual and sector-wise approaches were proposed. The final choice will be determined by the available alignment tolerances and their impact on the vertical emittance.

The large circumference of FCC-ee allows operation in the range of 90 to 350 GeV centre-of-mass energy with acceptable amount of synchrotron radiation power. Not only the properties of the Z and W bosons can be measured with unprecedented precision, also first precise measurements of the Higgs particle and the top quark are possible for the first time. In order to obtain highest luminosity, different beam parameters are required for each beam energies. To reduce the beam-beam tune shift the horizontal beam emittance might have to be increased towards the lower beam energies of 45.5 GeV and 80 GeV. Possible lattice arrangements with longer cells and/or smaller phase advance were studied and implemented including re-matching of the whole optics. The proposed lattices, based on the same hardware as the regular lattice, allow for the installation of a multi-family sextupole scheme. An emittance fine-tuning in the range of 10 % could be achieved with tolerable increase of synchrotron radiation power using damping and excitation wigglers.

The main subject investigated in the context of this thesis was the optimisation of the chromaticity correction scheme in the arc sections. Unprecedented values of the chromaticities require a correction including higher-order terms to obtain the very ambitious momentum acceptance of $\Delta p/p = \pm 2\,\%$, which is required because of the severe energy loss due to beamstrahlung. As a first step towards this goal this thesis includes a systematic study of multi-family sextupole schemes in the arc sections evaluated according to the obtained momentum acceptance. A scheme of two interleaved families in the horizontal plane and three families in the vertical plane allowed to correct the Montague W functions for different numbers of interaction points and different values of the vertical beta function at the interaction point β_y^*. With this method the momentum acceptance could be increased from $\Delta p/p = \pm 0.04\,\%$ to a range from $-0.3\,\%$ to $+0.1\,\%$ for two interaction points with $\beta_y^* = 2\,\mathrm{mm}$. In order to increase the degrees of freedom and allow more flexibility of the correction, the number of families was increased to six per arc per plane and the first twelve sextupole pairs in the arcs next to the interaction regions were powered individually. Several optimisation tools were implemented and used successfully to maximise the acceptance range from $\Delta p/p = -0.5\,\%$ to $+0.7\,\%$. For completeness and comparison the Downhill-Simplex-Algorithm was implemented to study a numerical optimisation independent from the built-in tools of MAD-X. Considering the challenging values of the chromaticity this already is a remarkable success.

In summary the work presented in this thesis highlights the benefit of a state-of-the-art chromatic correction scheme in the arc sections of a particle collider. To obtain highest possible momentum acceptance in a storage ring that aims for new and un-precedented luminosities and on four different beam energies, a flexible lattice layout had to be established, the cell parameters had to be optimised following the synchrotron radiation integrals and so the resulting emittance, and the chromatic effects had to be studied and compensated up to fourth order. The proposed lattice layout provides the option to have a direct influence on the beam emittance to control and limit the beam-beam effect via a tunable equilibrium emittance at all foreseen collision energies. Fine-tuning methods are available using wiggler sequences that were included in the lattice. The proposed sextupole scheme provides an efficient method to optimise the momentum acceptance of the lattice arcs. Combined with a local chromaticity correction scheme in the interaction regions, the design values for dynamic aperture and momentum acceptance are within reach.

In continuation of the work presented in this thesis the powering scheme for the lattice modifications could be addressed. The synchrotron radiation power could be further decreased by investigating a combined but separately powered quadrupole-sextupole design. Dynamic aperture studies and the combination of the multi-family sextupole scheme in the arcs with a local chromaticity correction section would be the next step towards the realisation of a new electron positron collider for future high-energy physics research.

Appendix

A FCC-ee Design Parameter Sets

The specifications for the FCC Lepton Collider were first published in February 2014 and summarised in [33]. The document includes a list of the design parameters for all four beam energies, which are compared to the values of the last high-energy lepton collider LEP. A selection of these design parameters were already presented in the introduction chapter, the full table according to [33] is given in Tab. A1.

The machine specifications were revised after the FCC-ee Design Review in October 2015 and then published in [16]. The new set of baseline parameters is presented in Tab. A2. As a main difference, the crab-waist crossing scheme [66] was included into the design of the interaction region to increase the luminosity for 45.5 GeV and 80 GeV. This interaction scheme not only increases the luminosity but also allows larger beam-beam tune shifts. While in the first parameter set the horizontal emittance had to be increased for the lower beam energies, in theory this is not necessary any more. Still, if the low emittances lead to instabilities, methods to increase it again were presented in Sec. 3.1. In order to relax the requirements for the chromaticity correction scheme the vertical beta function at the interaction point was increased from $\beta_y^* = 1\,\text{mm}$ to 2 mm. An ultimate set of parameters with $\beta_y^* = 1\,\text{mm}$ for 45.5 GeV beam energy is given in addition.

Table A1: The full FCC-ee Baseline Parameter Set, published in February 2014 [33].

	LEP1	LEP2	Z	W	H	tt
Circumference C (km)	26.7	26.7	100	100	100	100
Bending radius ρ (km)	3.1	3.1	11	11	11	11
Beam energy E (GeV)	45.4	104	45.5	80	120	175
Beam current (mA)	2.6	3.04	1450	152	30	6.6
Bunches/beam	12	4	16700	4490	1360	98
Bunch population (10^{11})	1.8	4.2	1.8	0.7	0.46	1.4
Transverse emittance ϵ						
- Horizontal (nm)	20	22	29.2	3.3	0.94	2
- Vertical (pm)	400	250	60	7	1.9	2
Momentum comp. (10^{-5})	18.6	14.0	18.0	2.0	0.5	0.5
Betatron function at IP						
- Horizontal β^* (m)	2.0	1.2	0.5	0.5	0.5	1.0
- Vertical β^* (mm)	50	50	1	1	1	1
Beam size at IP σ^* (µm)						
- Horizontal	224	182	121	41	22	45
- Vertical	4.5	3.2	0.25	0.084	0.044	0.045
Energy spread (%)						
- Synchrotron radiation	0.07	0.16	0.04	0.07	0.1	0.14
- Total (including beamstrahlung)	0.07	0.16	0.06	0.09	0.14	0.19
Bunch length (mm)						
- Synchrotron radiation	8.6	11.5	1.64	1.01	0.81	1.16
- Total (including beamstrahlung)	8.6	11.5	2.56	1.49	1.17	1.49
Energy loss/turn (GeV)	0.12	3.34	0.03	0.33	1.67	7.55
SR power/beam (MW)	0.3	11	50	50	50	50
Total RF voltage (GV)	0.24	3.5	2.5	4.0	5.5	11.0
RF frequency (MHz)	352	352	800	800	800	800
Longitudinal damping time t_{E} (turns)	371	31	1320	243	72	23
Energy acceptance RF (%)	1.7	0.8	2.7	7.2	11.2	7.1
Synchrotron tune Q_{s}	0.065	0.083	0.65	0.21	0.096	0.1
Polarization time t_{p} (min)	252	4	11200	672	89	13
Hourglass factor H	1.00	1.00	0.64	0.77	0.83	0.78
Luminosity $\mathcal{L}$/IP ($10^{34}\,\mathrm{cm}^{-2}\mathrm{s}^{-1}$)	0.002	0.012	28	12	6	1.8
Beam-beam parameter ξ						
- Horizontal	0.044	0.040	0.031	0.060	0.093	0.092
- Vertical	0.044	0.060	0.030	0.059	0.093	0.092
Luminosity lifetime (min)	1750	434	298	73	29	21
Beamstrahlung critical	No	No	No	No	Yes	Yes

Table A2: Updated set of baseline parameters for FCC-ee published in January 2016 [16].

	Z	Z	W	H	tt
Circumference C (km)	100	100	100	100	100
Bending radius ρ (km)	11	11	11	11	11
Beam energy E (GeV)	45.5	45.5	80	120	175
Beam current (mA)	1450	1450	152	30	6.6
Bunches/beam	30180	91500	5260	780	81
Bunch spacing (ns)	7.5	2.5	50	400	4000
Bunch population (10^{11})	1.0	0.33	0.6	0.8	1.7
Horizontal emittance ϵ (nm)	0.2	0.09	0.26	0.61	1.3
Vertical emittance ϵ (pm)	1.0	1.0	1.0	1.2	2.5
Momentum comp. (10^{-5})	0.7	0.7	0.7	0.7	0.7
Betatron function at IP					
- Horizontal β^* (m)	0.5	1	1	1	1
- Vertical β^* (mm)	1	2	2	2	2
Horizontal beam size at IP σ^* (µm)	10	9.5	16	25	36
Vertical beam size at IP σ^* (nm)	32	45	45	49	70
Crossing angle at IP (mrad)	30	30	30	30	30
Energy spread (%)					
- Synchrotron radiation	0.04	0.04	0.07	0.10	0.14
- Total (including beamstrahlung)	0.22	0.09	0.10	0.12	0.17
Bunch length (mm)					
- Synchrotron radiation	1.2	1.6	2.0	2.0	2.1
- Total (including beamstrahlung)	6.7	3.8	3.1	2.4	2.5
Energy loss/turn (GeV)	0.03	0.03	0.33	1.67	7.55
SR power/beam (MW)	50	50	50	50	50
Total RF voltage (GV)	0.4	0.2	0.8	3.0	10.0
RF frequency (MHz)	400	400	400	400	400
Longitudinal damping time (turns)	1320	1320	243	72	23
Energy acceptance RF (%)	7.2	4.7	5.5	7.0	6.7
Synchrotron tune Q_s	0.036	0.025	0.037	0.056	0.075
Polarization time t_p (min)	11200	11200	672	89	13
Interaction region length L_i (mm)	0.66	0.62	1.02	1.35	1.74
Hourglass factor $H(L_i)$	0.92	0.98	0.95	0.92	0.88
Luminosity $\mathcal{L}$/IP for 2 IPs ($10^{34}\,\mathrm{cm^{-2}s^{-1}}$)	207	90	19.1	5.1	1.3
Beam-beam parameter ξ					
- Horizontal	0.025	0.05	0.07	0.08	0.08
- Vertical	0.16	0.13	0.16	0.14	0.12
Luminosity lifetime (min)	94	185	90	67	57
Beamstrahlung critical	No/Yes	No	No	No	Yes

B Phasor

The correction of the W functions in Chapter 4 requires careful adjustment of the phase advance between final focus quadrupoles and the first sextupoles in the arc lattice. As the matching of the optics is time-consuming, a so-called *phasor* was used to speed up the optimisation process. A phasor is a symplectic transfer matrix $\mathbf{R}(\Delta\mu_x, \Delta\mu_y)$, which modifies the betatron phase functions and thus the phase advances μ_x and μ_y within a range of $\pm\pi$ while leaving the the optical functions unchanged. Following [67], the matrix for phase advance modification without coupling and vertical dispersion is represented by:

$$\mathbf{R}(\Delta\mu_x, \Delta\mu_y) = \begin{pmatrix} R_{11} & R_{12} & 0 & 0 & 0 & R_{16} \\ R_{21} & R_{22} & 0 & 0 & 0 & R_{26} \\ 0 & 0 & R_{33} & R_{34} & 0 & 0 \\ 0 & 0 & R_{43} & R_{44} & 0 & 0 \\ R_{51} & R_{52} & 0 & 0 & 1 & 0 \\ 0 & 0 & 0 & 0 & 0 & 1 \end{pmatrix} \quad \text{with} \tag{B.1}$$

$$\begin{aligned} R_{11} &= \cos(\Delta\mu_x) + \alpha_x \sin(\Delta\mu_x) & R_{33} &= \cos(\Delta\mu_y) + \alpha_y \sin(\Delta\mu_y) \\ R_{12} &= \beta_x \sin(\Delta\mu_x) & R_{34} &= \beta_y \sin(\Delta\mu_y) \\ R_{21} &= -\gamma_x \sin(\Delta\mu_x) & R_{43} &= -\gamma_y \sin(\Delta\mu_y) \\ R_{22} &= \cos(\Delta\mu_x) - \alpha_x \sin(\Delta\mu_x) & R_{44} &= \cos(\Delta\mu_y) - \alpha_y \sin(\Delta\mu_y) \\ R_{16} &= D_x(1 - R_{11}) - D'_x R_{12} & R_{51} &= D'_x(1 - R_{11}) + D_x R_{21} \\ R_{26} &= D'_x(1 - R_{22}) - D'_x R_{21} & R_{52} &= D_x(R_{22} - 1) - D'_x R_{12} \end{aligned}$$

$\beta_{x/y}$, $\alpha_{x/y}$ and $\gamma_{x/y}$ denote the Twiss parameters. D_x is the horizontal dispersion and D'_x its derivative.

Such a phasor is not provided by MAD-X, but can be defined. A macro to calculate the matrix elements for given phase shifts and to install the phasor at a certain position was provided by A. Bogomyagkov [53]. The MAD-X code used in the context of this thesis is:

```
PHASESHIFT(seqname,LOC,FROMRK,dphix,dphiy) :  macro = {

    markLOC: marker;

    seqedit,sequence=seqname;
    remove, element=MATLOC;
    remove, element=markLOC;
    endedit;

    seqedit,sequence=seqname;
    install,element=markLOC,at=LOC,from=FROMRK;
    endedit;
```

```
    MATLOC : MATRIX,   RM11:=R11LOC,RM12:=R12LOC,RM21:=R21LOC,RM22:=R22LOC,
                       RM16:=R16LOC,RM26:=R26LOC,RM51:=R51LOC,RM52:=R52LOC,
                       RM33:=R33LOC,RM34:=R34LOC,RM43:=R43LOC,RM44:=R44LOC,
                       RM55:=1.,RM66:=1.;
    use,sequence=seqname;
    twiss;
    betxLOC  =table(twiss,markLOC,betx);
    betyLOC  =table(twiss,markLOC,bety);
    alfxLOC  =table(twiss,markLOC,alfx);
    alfyLOC  =table(twiss,markLOC,alfy);
    dispxLOC =table(twiss,markLOC,dx);
    disppxLOC=table(twiss,markLOC,dpx);

    R11LOC:= cos(twopidphix)+alfxLOCsin(twopidphix);
    R12LOC:= betxLOCsin(twopidphix);
    R22LOC:= cos(twopidphix)-alfxLOCsin(twopidphix);
    R21LOC:=-sin(twopidphix)(1+alfxLOC^2)/betxLOC;
    R33LOC:= cos(twopidphiy)+alfyLOCsin(twopidphiy);
    R34LOC:= betyLOCsin(twopidphiy);
    R44LOC:= cos(twopidphiy)-alfyLOCsin(twopidphiy);
    R43LOC:=-sin(twopidphiy)(1+alfyLOC^2)/betyLOC;
    R16LOC:= dispxLOC(1-R11LOC)-R12LOCdisppxLOC;
    R26LOC:= disppxLOC(1-R22LOC)-R21LOCdispxLOC;
    R51LOC:= R21LOCR16LOC-R11LOCR26LOC;
    R52LOC:= R22LOCR16LOC-R12LOCR26LOC;

    seqedit,sequence=seqname;
    install, element=MATLOC,at=0.0,from=markLOC;
    endedit;

    use, sequence=seqname;

};
```

C Macro for the calculation of higher-order chromaticity

The tune as a function of the momentum deviation $\delta = \Delta p/p$ can be expanded to a Taylor series:

$$Q(\delta) = Q_0 + \frac{\mathrm{d}Q}{\mathrm{d}\delta}\delta + \frac{1}{2}\frac{\mathrm{d}^2Q}{\mathrm{d}\delta^2}\delta^2 + \frac{1}{6}\frac{\mathrm{d}^3Q}{\mathrm{d}\delta^3}\delta^3 + \dots$$

In the case of FCC-ee the large chromatic perturbations created due to the aggressive design values of the beta functions at the interaction point require a chromaticity compensation beyond the linear order to obtain a momentum acceptance of $\delta = \pm 2\,\%$. The higher-order derivatives of the tune function are not calculated directly by MAD-X. A macro with calculations based of difference quotients was provided by A. Bogomyagkov [53]. For the calculation of the linear and the second-order term three Twiss calculations are required: one with design energy and two for $\pm\delta$ momentum deviation. The tune of the calculation with design energy will be denoted with Q_0, the one for the particles with energy deviation

with $Q_{+\delta}$ and $Q_{-\delta}$. The linear chromaticity is then given by

$$\frac{\mathrm{d}Q}{\mathrm{d}\delta} = \frac{1}{2\delta}(Q_{+\delta} - Q_{-\delta}). \tag{C.1}$$

To calculate the second-order derivative the slope of the tune function is evaluated separately for positive and negative momentum deviation. A second difference quotient gives the second order derivative:

$$\begin{aligned}\frac{\mathrm{d}^2Q}{\mathrm{d}\delta^2} &= \frac{1}{\delta}\left[\frac{(Q_{+\delta} - Q_0)}{\delta} - \frac{(Q_0 - Q_{-\delta})}{\delta}\right] \\ &= \frac{1}{\delta^2}(Q_{+\delta} + Q_{-\delta} - 2Q_0)\end{aligned} \tag{C.2}$$

For the calculation of third- and forth-order terms two additional Twiss calculations with $\pm 2\delta$ are needed to allow a third and fourth iteration of calculating the difference quotients. After simplifying the equations the third- and fourth-order terms are given by

$$\frac{\mathrm{d}^3Q}{\mathrm{d}\delta^3} = \frac{1}{2\delta^3}(Q_{+2\delta} - Q_{-2\delta} - 2Q_{+\delta} + 2Q_{-\delta}) \qquad \text{and} \tag{C.3}$$

$$\frac{\mathrm{d}^4Q}{\mathrm{d}\delta^4} = \frac{1}{\delta^4}(Q_{+2\delta} + Q_{-2\delta} - 4Q_{+\delta} - 4Q_{-\delta} + 6Q_0). \tag{C.4}$$

Different values of δ were used in the context of this thesis. The value was adapted to the range of the momentum acceptance in order to obtain a good agreement with the tunes calculated by MAD-X.

```
check_chromaticity(aux_seq):  macro = {
print, text = "check_chromaticity...";
!*********************************************
print, text = "1st order...";

    use,sequence=aux_seq;!, range=IP2R/IP1L;
    deltap=1e-4;

    dpp=deltap*0;
    TWISS,DELTAP=dpp,chrom;
    dq1_0=table(summ,q1); dq2_0=table(summ,q2);
    dq1_1=table(summ,dq1); dq2_1=table(summ,dq2);


!*********************************************
print, text = "2nd order...";

    dpp=deltap;
    TWISS,DELTAP=dpp,chrom;
    qxp1=table(summ,q1); qyp1=table(summ,q2);
    TWISS,DELTAP=-dpp,chrom;
    qxn1=table(summ,q1); qyn1=table(summ,q2);
```

```
    !  qx1=(qxp1-qxn1)/(2deltap);
    !  qy1=(qyp1-qyn1)/(2deltap);

    dq1_2=(qxp1+qxn1-2dq1_0)/deltap^2;
    dq2_2=(qyp1+qyn1-2dq2_0)/deltap^2;


!*********************************************
print, text = "3rd and 4th order...";

    dpp=deltap*2;
    TWISS,DELTAP=dpp,chrom;
    qxp2=table(summ,q1); qyp2=table(summ,q2);
    TWISS,DELTAP=-dpp,chrom; qxn2=table(summ,q1); qyn2=table(summ,q2);

    dq1_3=0.5*(qxp2-qxn2-2qxp1+2qxn1)/deltap^3;
    dq2_3=0.5*(qyp2-qyn2-2qyp1+2qyn1)/deltap^3;

    dq1_4=(qxp2+qxn2-4qxp1-4qxn1+6dq1_0)/deltap^4;
    dq2_4=(qyp2+qyn2-4qyp1-4qyn1+6dq2_0)/deltap^4;


!*********************************************


value,dq1_0,dq2_0,dq1_1,dq2_1,dq1_2,dq2_2,dq1_3,dq2_3,dq1_4,dq2_4;
};
```

D Optimisation tool to flatten the tune function

This section presents the MAD-X code of the tool for the optimisation of the tune function used in Sec. 4.6.2. The macro calculates the tune for a user-defined number of steps within the acceptable range of energy deviation. The squared difference to the nominal tune for $\delta = 0$ is then minimised by optimising the available sextupole strengths using the matching routines in MAD-X.

```
penalty_x = 0;
penalty_y = 0;
penalty := penalty_x + penalty_x;

counter = 0;
optimise_bandwidth :  macro = {
    value, counter;
    counter = counter + 1;

    delete, table=mytab;
    create, table=mytab, column=dp, tune_x, tune_y, penalty_x, penalty_y;
    tune_x:=table(summ,q1);
    tune_y:=table(summ,q2);
    dp:=deltap_min;

    penalty_x = 0;
```

```
    penalty_y = 0;

    deltap_max = 0.0025;
    deltap_min =-0.0025;
    deltap_int = 0.001;

    twiss;
    q1ref = table(summ,q1);
    q2ref = table(summ,q2);
    !value, q1ref, q2ref;

    while (deltap_min<=deltap_max) {
        value, deltap_min;
        twiss, deltap=deltap_min;

        if (tune_x>0) {
             penalty_x = penalty_x + (table(summ,q1)-q1ref)^2;
        }
        if (tune_y>0) {
             penalty_y = penalty_y + (table(summ,q2)-q2ref)^2;
        }

        fill, table=mytab;

        deltap_min = deltap_min + deltap_int;
    }

    value, penalty;
    !write,table=mytab;
}
```

E Optimisation tool to decrease the slope of the tune function at the edge

This section presents the MAD-X code of the tool for the minimisation of the slopes of the tune function at the edge of the momentum acceptance used in Sec. 4.6.3. The tunes of particles with two different energy deviations close to the edge of the accepted energy range are calculated. The user can define, whether both sides should be optimised or just one.

```
deltapstart1 = 0.0067;
deltapstart2 =-0.0044;
counter = 1;

check_tunesdeltap :  macro {
    deltap_start1= deltapstart1;
    deltap_start2= deltapstart2;

    twiss, deltap = deltap_start1;
    qpx1=table(summ,q1);
    qpy1=table(summ,q2);
```

```
    twiss, deltap = deltap_start1-0.0001;
    qpx2=table(summ,q1);
    qpy2=table(summ,q2);

    twiss, deltap =deltap_start2+0.0001;
    qnx2=table(summ,q1);
    qny2=table(summ,q2);
    twiss, deltap =deltap_start2;
    qnx1=table(summ,q1);
    qny1=table(summ,q2);

    penalty_xp=(abs(qpx1-qpx2))/0.0001;
    penalty_xn=(abs(qnx2-qnx1))/0.0001;
    penalty_yp=(abs(qpy1-qpy2))/0.0001;
    penalty_yn=(abs(qny2-qny1))/0.0001;


}
```

If the macro is executed from a while loop, the momentum acceptance can be increased iteratively until the current configuration of the sextupoles does not allow any further progress.

```
weiter=1;
while (weiter>0) {

match,use_macro;


    vary, name=knl_hilf_sf1.1, step=1.0E-10;
    vary, name=knl_hilf_sf1.2, step=1.0E-10;
    vary, name=knl_hilf_sf1.3, step=1.0E-10;
    vary, name=knl_hilf_sf1.4, step=1.0E-10;
    vary, name=knl_hilf_sf1.5, step=1.0E-10;
    vary, name=knl_hilf_sf1.6, step=1.0E-10;
    vary, name=knl_hilf_sf6.1, step=1.0E-10;
    vary, name=knl_hilf_sf6.2, step=1.0E-10;
    vary, name=knl_hilf_sf6.3, step=1.0E-10;
    vary, name=knl_hilf_sf6.4, step=1.0E-10;
    vary, name=knl_hilf_sf6.5, step=1.0E-10;
    vary, name=knl_hilf_sf6.6, step=1.0E-10;

    vary, name=knl_hilf_sd1.1, step=1.0E-10;
    vary, name=knl_hilf_sd1.2, step=1.0E-10;
    vary, name=knl_hilf_sd1.3, step=1.0E-10;
    vary, name=knl_hilf_sd1.4, step=1.0E-10;
    vary, name=knl_hilf_sd1.5, step=1.0E-10;
    vary, name=knl_hilf_sd1.6, step=1.0E-10;
    vary, name=knl_hilf_sd6.1, step=1.0E-10;
    vary, name=knl_hilf_sd6.2, step=1.0E-10;
    vary, name=knl_hilf_sd6.3, step=1.0E-10;
    vary, name=knl_hilf_sd6.4, step=1.0E-10;
    vary, name=knl_hilf_sd6.5, step=1.0E-10;
    vary, name=knl_hilf_sd6.6, step=1.0E-10;
```

```
use_macro, name=check_tunesdeltap;

    constraint, expr=penalty_xp=0;
    constraint, expr=penalty_xn=0;
    constraint, expr=penalty_yp=0;
    constraint, expr=penalty_yn=0;
    jacobian, calls=5, tolerance=1.0E-8, bisec=1;

endmatch;

    twiss, deltap=deltapstart1+0.0001;
    test1 = table(summ, q2);
    twiss, deltap=deltapstart2-0.0001;
    test2 = table(summ, q2);
    testweiter = test1+test2;

    if (test1>0) deltapstart1=deltapstart1+0.0001;
    if (test2>0) deltapstart2=deltapstart2-0.0001;

    if (testweiter<1) weiter=0;
    if (counter>5) weiter=0;
    value, counter;
    counter=counter+1;

    value, deltapstart1, deltapstart2;

}
```

Bibliography

[1] 16th Session of the European Strategy Council, "The European Strategy for Particle Physics Update 2013," no. CERN-Council-S/106, 2013. [Online]. Available: https://cds.cern.ch/record/1646092

[2] G. Aad *et al.*, "Observation of a new particle in the search for the Standard Model Higgs boson with the ATLAS detector at the LHC," *Physics Letters B*, vol. 716, no. 1, pp. 1 – 29, 2012. [Online]. Available: https://arxiv.org/abs/1207.7214

[3] S. Chatrchyan *et al.*, "Observation of a new boson at a mass of 125 GeV with the CMS experiment at the LHC," *Physics Letters B*, vol. 716, no. 1, pp. 30 – 61, 2012. [Online]. Available: https://arxiv.org/abs/1207.7235

[4] O. S. Brüning *et al.*, *LHC Design Report*. Geneva: CERN, 2004. [Online]. Available: https://cds.cern.ch/record/782076

[5] B. Haerer *et al.*, "Constraints on the FCC-ee Lattice from the Compatibility with the FCC Hadron Collider," 2015. [Online]. Available: http://cds.cern.ch/record/1982444

[6] J. Osborne, private communication.

[7] M. Benedikt *et al.*, "Challenges for highest energy circular colliders," no. CERN-ACC-2014-0153, p. 7 p, Jun 2014. [Online]. Available: http://cds.cern.ch/record/1742294

[8] T. Behnke *et al.*, "The International Linear Collider - Volume 1: Executive Summary," Geneva, Tech. Rep. CERN-ATS-2013-037, Jun 2013. [Online]. Available: http://cds.cern.ch/record/1601966

[9] M. Aicheler *et al.*, "A Multi-TeV Linear Collider Based on CLIC Technology: CLIC Conceptual Design Report," Geneva, Tech. Rep. CERN-2012-007, 2012. [Online]. Available: https://cds.cern.ch/record/1500095

[10] M. Bicer *et al.*, "First Look at the Physics Case of TLEP. First Look at the Physics Case of the FCC-ee (TLEP)," *J. High Energy Phys.*, vol. 01, no. arXiv:1308.6176,

p. 164. 50 p, Aug 2013, comments: 38 pages, 18 figures. [Online]. Available: http://cds.cern.ch/record/1595894

[11] M. Benedikt and F. Zimmermann, "Status and Challenges of the Future Circular Collider Study," CERN, Geneva, Tech. Rep. CERN-ACC-2016-0005, Jan 2016. [Online]. Available: http://cds.cern.ch/record/2120816

[12] F. Zimmermann and M. Benedikt, "Outline and Status of the FCC-ee Design Study," *ICFA Beam Dyn. Newsl.*, vol. 67, no. CERN-ACC-2015-0112, pp. 86–93. 8 p, Oct 2015. [Online]. Available: http://cds.cern.ch/record/2057708

[13] D. d'Enterria, "Physics case of FCC-ee," *Frascati Phys. Ser.*, vol. 61, p. 17, 2016. [Online]. Available: https://arxiv.org/pdf/1601.06640.pdf

[14] A. S. Müller, "Precision measurements of the LEP beam energy for the determination of the W boson mass," Ph.D. dissertation, Johannes Gutenberg University, Mainz, 2000. [Online]. Available: http://cds.cern.ch/record/492582

[15] J. Ellis and T. You, "Sensitivities of Prospective Future e+e− Colliders to Decoupled New Physics," *JHEP*, vol. 03, p. 089, 2016. [Online]. Available: https://arxiv.org/pdf/1510.04561v1.pdf

[16] J. Wenninger *et al.*, "Future Circular Collider Study, Lepton Collider Parameters (updated version)," FCC-1401201640-DSC, Jan. 2016.

[17] F. Willeke, "Commissioning of NSLS-II," in *Proc. of International Particle Accelerator Conference (IPAC'15), Richmond, VA, USA, May 3-8, 2015*, ser. International Particle Accelerator Conference. JACoW, May 2015, paper MOYGB3. [Online]. Available: http://accelconf.web.cern.ch/AccelConf/IPAC2015/papers/moygb3.pdf

[18] R. Dowd *et al.*, "Achievement of ultralow emittance coupling in the australian synchrotron storage ring," *Phys. Rev. ST Accel. Beams*, vol. 14, p. 012804, Jan 2011. [Online]. Available: http://link.aps.org/doi/10.1103/PhysRevSTAB.14.012804

[19] P. Raimondi, "The ESRF Low-emittance Upgrade," in *Proc. of International Particle Accelerator Conference (IPAC'16), Busan, Korea, May 8-13, 2016*, ser. International Particle Accelerator Conference, no. 7. Geneva, Switzerland: JACoW, June 2016, paper WEXA01, pp. 2023–2027, doi:10.18429/JACoW-IPAC2016-WEXA01. [Online]. Available: http://jacow.org/ipac2016/papers/wexa01.pdf

[20] W. Herr, "Beam-beam interactions," in *CAS - CERN Accelerator School: Intermediate Accelerator Physics: DESY, Zeuthen, Germany, September 15-26, 2003*, 2006, pp. 379–406. [Online]. Available: http://cds.cern.ch/record/941319

[21] K. Wille, *The physics of particle accelerators : an introduction*, repr. ed. Oxford [u.a.]: Oxford University Press, 2005.

[22] H. Wiedemann, *Particle Accelerator Physics*, 4th ed. Cham: Springer, 2015.

[23] A. S. Müller, "Description of Beam-Matter Interaction in the Covariance Matrix Formalism," CERN, Geneva, Switzerland, Tech. Rep. CERN/PS 2001-0013 (AE), 2001. [Online]. Available: http://cds.cern.ch/record/499590/files/ps-2001-013.pdf

[24] J. Buon, "Beam phase space and emittance," in *CAS - CERN Accelerator School: Fifth General Accelerator Physics Course: Jyväskylä, Finland, 7-18 September, 1992*, 1994, pp. 89–115. [Online]. Available: http://cds.cern.ch/record/242313

[25] *LEP design report*. Geneva: CERN, 1984. [Online]. Available: https://cds.cern.ch/record/102083

[26] A. W. Chao, Ed., *Handbook of accelerator physics and engineering*, 2nd ed. New Jersey [u.a.]: World Scientific, 2013.

[27] A. Wolski, "Low-emittance storage rings," in *CAS - CERN Accelerator School: Advanced Accelerator Physics Course: Trondheim, Norway, August 18-29, 2013*, 2014, pp. 245–294. [Online]. Available: https://inspirehep.net/record/1381963/files/arXiv:1507.02213.pdf

[28] K. W. Robinson, "Radiation Effects in Circular Electron Accelerators," *Phys. Rev.*, vol. 111, pp. 373–380, Jul 1958. [Online]. Available: http://link.aps.org/doi/10.1103/PhysRev.111.373

[29] M. Sands, "The physics of electron storage rings: an introduction," no. SLAC-121, 1971. [Online]. Available: https://cds.cern.ch/record/102780

[30] A. W. Chao, "Beam-beam instability," in *AIP Conf. Proc.*, vol. 127, 1983, pp. 201–242. [Online]. Available: http://inspirehep.net/record/192817/files/slac-pub-3179.pdf

[31] Website of the MAD project. [Online]. Available: http://mad.web.cern.ch/mad/

[32] H. Grothe *et al.*, *The MAD-X Program - User's Reference Manual*, 2016.

[33] J. Wenninger *et al.*, "Future Circular Collider Study, Lepton Collider Parameters," FCC-1401201640-DSC, Feb. 2014.

[34] D. Schulte, "Preliminary Collider Baseline Parameters: Deliverable D1.1," CERN, Geneva, Tech. Rep. CERN-ACC-2015-0132, Sep 2015. [Online]. Available: http://cds.cern.ch/record/2059230

[35] P. J. Bryant and K. Johnsen, *The principles of circular accelerators and storage rings*. Cambridge: Cambridge Univ. Press, 1993.

[36] B. J. Holzer, "Lattice design in high-energy particle accelerators," in *CAS - CERN Accelerator School: Intermediate Accelerator Physics: DESY, Zeuthen, Germany, September 15-26, 2003*, 2006, pp. 31–73. [Online]. Available: http://cds.cern.ch/record/941323

[37] L. Teng, "Minimizing the Emittance in Designing the Lattice of an Electron Storage Ring," Tech. Rep. FERMILAB-TM-1269, FERMILAB-TM-1269-A, Jun. 1984. [Online]. Available: http://inspirehep.net/record/204995/

[38] J. Jowett, private communication.

[39] F. Cerutti *et al.*, "Impact of Synchrotron Radiation in Lepton Collider Arcs," presentation at the FCC-ee Kick-off Meeting, Feb. 2014. [Online]. Available: https://indico.cern.ch/event/282344/contributions/1630742/

[40] C. Garion, TLEP project meeting, CERN, Geneva, Switzerland, Oct. 2013.

[41] R. Chasman, G. K. Green, and E. M. Rowe, "Preliminary design of a dedicated synchrotron radiation facility," *IEEE Trans.*, vol. NS-22, no. 3, 1975. [Online]. Available: http://cds.cern.ch/record/889821

[42] E. Huttel *et al.*, "Operation with a Low Emittance Optics at ANKA," in *Proc. of 2005 Particle Accelerator Conference, Knoxville, Tennessee*, May 2005, pp. 2467–2469. [Online]. Available: http://ieeexplore.ieee.org/document/1591147/

[43] E. Huttel *et al.*, "Low Beta Structure for the ANKA Storage Ring," in *Proc. of EPAC08, Genoa, Italy*, Jul 2008, paper WEPC024, pp. 2034–2036. [Online]. Available: http://accelconf.web.cern.ch/Accelconf/e08/papers/wepc024.pdf

[44] M. Streichert *et al.*, "Global optimisation of the ANKA lattice using Multiobjective Genetic Algorithms (MOGA)," in *Proceedings of ICAP2012, Rostock-Warnemünde, Germany*, Aug 2012, paper TUABC2, pp. 72–74. [Online]. Available: http://accelconf.web.cern.ch/accelconf/ICAP2012/papers/tuabc2.pdf

[45] A. Doblhammer, "master thesis," to be published.

[46] B. Haerer, A. Doblhammer, and B. Holzer, "Tapering Options and Emittance Fine Tuning for the FCC-ee Collider," in *Proc. of International Particle Accelerator Conference (IPAC'16), Busan, Korea, May 8-13, 2016*, ser. International Particle Accelerator Conference, no. 7. Geneva, Switzerland: JACoW, June 2016, paper

THPOR003, pp. 3767–3770, doi:10.18429/JACoW-IPAC2016-THPOR003. [Online]. Available: http://jacow.org/ipac2016/papers/thpor003.pdf

[47] M. Reiser, *Theory and Design of Charged Particle Beams*, ser. Wiley Series in Beam Physics and Accelerator Technology. Wiley, 2008.

[48] B. J. Holzer, private communication.

[49] F. Hinterberger, *Physik der Teilchenbeschleuniger und Ionenoptik*, 2nd ed. Berlin, Heidelberg: Springer Berlin Heidelberg, 2008.

[50] D. Missiaen, private communication.

[51] S. Aumon *et al.*, "Tolerance Studies and Dispersion Free Steering for Extreme Low Emittance in the FCC-ee Project," in *Proc. of International Particle Accelerator Conference (IPAC'16), Busan, Korea, May 8-13, 2016*, ser. International Particle Accelerator Conference, no. 7. Geneva, Switzerland: JACoW, June 2016, paper THPOR001, pp. 3759–3762, doi:10.18429/JACoW-IPAC2016-THPOR001. [Online]. Available: http://jacow.org/ipac2016/papers/thpor001.pdf

[52] A. Doblhammer, "Wigglers in FCC-ee - preliminary results," FCC-ee Optics Meeting, CERN, Geneva, Sep. 2015.

[53] A. Bogomyagkov, private communication.

[54] B. W. S. L. Montague, "Linear Optics For Improved Chromaticity Correction," CERN, Geneva, Tech. Rep. CERN-LEP-Note-165. LEP-Note-165, 1979. [Online]. Available: http://cds.cern.ch/record/443342

[55] A. Bogomyagkov, "Chromaticity correction of the interaction region," IAS Program on High Energy Physics, Hong Kong, Jan. 2016. [Online]. Available: http://ias.ust.hk/program/shared_doc/2016/201601hep/20160118_Bogomyagkov_LT.pdf

[56] M. Takao, "Formulation of nonlinear chromaticity in circular accelerators by canonical perturbation method," *Physical Review E*, vol. 72, no. 4, Oct. 2005. [Online]. Available: http://link.aps.org/doi/10.1103/PhysRevE.72.046502

[57] A. Bogomyagkov *et al.*, "Effect of the Sextupole Finite Length on Dynamic Aperture in the Collider Final Focus," Budker Institute of Nuclear Physics, Novosibirsk 630090, Russia, Tech. Rep., Sep. 2009. [Online]. Available: http://arxiv.org/abs/0909.4872

[58] R. Brinkmann and F. Willke, "Chromatic Corrections and Dynamic Aperture in the HERA Electron Ring II," Deutsches Elektronen-Synchrotron DESY, Hamburg, Tech. Rep. DESY 87-037, ISSN 0418-9833, May 1987. [Online]. Available: http://inspirehep.net/record/247313/files/desy87-037.kek.pdf

[59] A. Bogomyagkov and E. Levichev, "Momentum Acceptance Optimization in FCC-ee Lattice (CERN)," in *Proc. of International Particle Accelerator Conference (IPAC'16), Busan, Korea, May 8-13, 2016*, ser. International Particle Accelerator Conference, no. 7. Geneva, Switzerland: JACoW, June 2016, paper THPOR019, pp. 3814–3817, doi:10.18429/JACoW-IPAC2016-THPOR019. [Online]. Available: http://jacow.org/ipac2016/papers/thpor019.pdf

[60] K. Oide *et al.*, "Design of beam optics for the future circular collider e^+e^- collider rings," *Phys. Rev. Accel. Beams*, vol. 19, p. 111005, Nov 2016. [Online]. Available: http://link.aps.org/doi/10.1103/PhysRevAccelBeams.19.111005

[61] D. Shatilov, "FCC-ee parameter optimization," presentation at the FCC-ee progress meeting, Dec. 2014. [Online]. Available: https://indico.cern.ch/event/356596/

[62] A. Verdier, "Non-linear chromaticity correction with sextupole families." IEEE, 1995. [Online]. Available: http://cds.cern.ch/record/282841

[63] B. Haerer, "Correction of higher order chromaticity: an update," presentation at the 21st FCC-ee Optics Meeting, Jan. 2016. [Online]. Available: https://indico.cern.ch/event/486359/

[64] G. Roy, private communication.

[65] W. H. Press *et al.*, *Numerical Recipes in FORTRAN; The Art of Scientific Computing*, 2nd ed. New York, NY, USA: Cambridge University Press, 1993.

[66] P. Raimondi, M. Zobov, and D. Shatilov, "Suppression of beam-beam resonances in Crab Waist collisions," in *Proc. of EPAC08, Genoa, Italy*, 2008, pp. 23–27. [Online]. Available: https://accelconf.web.cern.ch/accelconf/e08/papers/wepp045.pdf

[67] S. D. Fartoukh, "Second order chromaticity correction of LHC V 6.0 at collision," CERN, Geneva, Switzerland, LHC Progres Report 308, 1999. [Online]. Available: http://cds.cern.ch/record/403591

Acknowledgements

I would like to express my sincere gratitude to everybody who supported and contributed to the work presented in this thesis. Especially I would like to thank

Prof. Dr. Anke-Susanne Müller for pointing out the possibility to contribute to the FCC Study and establishing the contact to my CERN supervisor Dr. Bernhard Holzer. I also would like to thank for her friendly supervision, the constant support and encouragement and the long discussions about my work.

Prof. Dr. Rüdiger Schmidt for his detailed feedback and suggestions to this thesis.

Dr. Bernhard Holzer for accepting me as his student and making my work at CERN to a fantastic and unforgettable experience. I extremely appreciate his support and the encouragement to pursue my work. I would not only like to thank for reading my thesis several times, but also for the countless discussions over coffee and the private lessons while sitting on his side-table.

Dr. Anton Bogomyagkov for sharing his expertise on higher-order chromaticity correction and providing his macros. I am really grateful for his constant advise and detailed explanations.

Dr. Sandra Aumon and Andreas Doblhammer for their contribution to this thesis and the very good working atmosphere.

Dr. Michael Benedikt and Dr. Frank Zimmermann, the project leaders of FCC, for giving me the opportunity to present my work on various conferences and workshops.

Dr. John Jowett, Dr. Jörg Wenninger and Dr. Katsunobu Oide for their friendly advise on any accelerator related issue.

The MAD-X team and especially Dr. Ghislain Roy for supporting me not only on MAD-X related issues.

Dr. Jimmy Garland for advising me on the subtleties of the English language.

Dr. Markus Schwarz and Dr. Marcel Schuh for taking the time to read my thesis and giving useful feedback.

Dr. Manuel Schedler for introducing me to the TikZ and PGFPlots modules, which allowed me generate the beautiful plots in this thesis.

The THz-Group at the KIT in Karlsruhe for including me despite the large distance to Geneva and making me feel welcome every time I was there.

Dr. Michael Hauschild for accepting me as a student of the Wolfgang Gentner Programme and supporting my travels to Germany.

Last but not least I would like to thank my family and my friends for their constant support and encouragement not only in context with this thesis.